

Masanobu Yoshikawa

Advanced Optical Spectroscopy Techniques for Semiconductors

Raman, Infrared, and
Cathodoluminescence Spectroscopy



Springer

Advanced Optical Spectroscopy Techniques for Semiconductors

This document is a comprehensive guide to advanced optical spectroscopy techniques used in the study of semiconductors. It covers various methods such as Raman scattering, photoluminescence, and absorption spectroscopy, along with their applications in understanding the electronic properties of semiconductors.

The guide includes detailed explanations of the underlying physical principles, experimental setup, and data analysis for each technique.

It also highlights the latest research findings and future directions in the field of optical spectroscopy for semiconductors.

Overall, this document provides a valuable resource for researchers, students, and professionals interested in the application of optical spectroscopy to semiconductor materials.

Table of Contents

I. Introduction to Optical Spectroscopy in Semiconductors

II. Raman Scattering in Semiconductors

III. Photoluminescence in Semiconductors

IV. Absorption Spectroscopy in Semiconductors

V. Advanced Applications and Future Directions

VI. Conclusion and Summary

Appendix A: Mathematical Derivations and Formulas

Appendix B: Experimental Setup and Data Analysis

Appendix C: References and Further Reading

Appendix D: Glossary of Terms and Symbols

Appendix E: Acknowledgments and Special Thanks

Appendix F: Index and Subject Headings

Appendix G: Additional Figures and Tables

Appendix H: Supplementary Information and Data

Appendix I: Detailed Calculations and Derivations

Appendix J: Advanced Theoretical Models and Simulations

Appendix K: Experimental Results and Data Analysis

Appendix L: Comparison with Previous Work and Results

Appendix M: Future Research Directions and Outlook

Appendix N: Additional Figures and Tables

Appendix O: Supplementary Information and Data

Appendix P: Detailed Calculations and Derivations

Appendix Q: Advanced Theoretical Models and Simulations

Appendix R: Experimental Results and Data Analysis

Appendix S: Comparison with Previous Work and Results

Appendix T: Future Research Directions and Outlook

Appendix U: Additional Figures and Tables

Appendix V: Supplementary Information and Data

Appendix W: Detailed Calculations and Derivations

Appendix X: Advanced Theoretical Models and Simulations

Appendix Y: Experimental Results and Data Analysis

Appendix Z: Comparison with Previous Work and Results

Appendix AA: Future Research Directions and Outlook

Appendix BB: Additional Figures and Tables

Appendix CC: Supplementary Information and Data

Appendix DD: Detailed Calculations and Derivations

Appendix EE: Advanced Theoretical Models and Simulations

Masanobu Yoshikawa

Advanced Optical Spectroscopy Techniques for Semiconductors

Raman, Infrared, and Cathodoluminescence
Spectroscopy



Springer

Masanobu Yoshikawa
Toray Research Center, Inc.
Otsu, Japan

ISBN 978-3-031-19721-5 ISBN 978-3-031-19722-2 (eBook)
<https://doi.org/10.1007/978-3-031-19722-2>

© The Editor(s) (if applicable) and The Author(s), under exclusive license to Springer Nature Switzerland AG 2023

This work is subject to copyright. All rights are solely and exclusively licensed by the Publisher, whether the whole or part of the material is concerned, specifically the rights of translation, reprinting, reuse of illustrations, recitation, broadcasting, reproduction on microfilms or in any other physical way, and transmission or information storage and retrieval, electronic adaptation, computer software, or by similar or dissimilar methodology now known or hereafter developed.

The use of general descriptive names, registered names, trademarks, service marks, etc. in this publication does not imply, even in the absence of a specific statement, that such names are exempt from the relevant protective laws and regulations and therefore free for general use.

The publisher, the authors, and the editors are safe to assume that the advice and information in this book are believed to be true and accurate at the date of publication. Neither the publisher nor the authors or the editors give a warranty, expressed or implied, with respect to the material contained herein or for any errors or omissions that may have been made. The publisher remains neutral with regard to jurisdictional claims in published maps and institutional affiliations.

This Springer imprint is published by the registered company Springer Nature Switzerland AG
The registered company address is: Gewerbestrasse 11, 6330 Cham, Switzerland

Preface

Toray Research Centre, Inc. (TRC) was founded in 1978 by incorporating the analytical groups of the Research and Development (R&D) division of Toray Industries, Inc. in Japan. Presently, TRC is one of the leading analytical service companies, engaging in providing technical support primarily for “cause analysis” and “problem solving” in the fields of research, development, and manufacturing by using analytical techniques and physical analyses.

I have studied cutting-edge materials using advanced Raman, infrared, photoluminescence, and cathodoluminescence spectroscopy. Vibrational spectroscopy has many applications, e.g., the characterisation of orientation, crystallinity, and chemical bonding structure of organic or inorganic materials, and provides solutions to a host of important and challenging analytical problems. Infrared and Raman spectroscopy are complementary techniques, and both techniques are usually required to fully measure the vibrational modes of a molecule, a solid, a solution or a specimen in solution.

On the other hand, cathodoluminescence (CL) spectroscopy has much potential for obtaining information about band structures, defects, and carrier densities of inorganic materials, particularly, semiconductor devices with spatial resolutions of less than 100 nm. If a scanning electron transmission microscope (STEM) is used as an excitation source, CL spectroscopy can yield much information not only about defects and dislocations but also regarding the carrier concentration and stress, with a spatial resolution of less than 30 nm. In this book, I would like to introduce advanced applications for semiconductors and related materials as the focus of recent research, using mainly cutting-edge Raman, infrared, and CL spectroscopy.

I would like to thank my colleagues, Dr. Masataka Murakami, Dr. Keiko Matsuda, Dr. Hirofumi Seki, Dr. Ryuichi Sugie, Dr. Naohiko Kawasaki, Mr. Takashi Miyamoto, Dr. Yasuhiko Fujita, Ms. Keiko Inoue, and Ms. Nevena Dokmanovic in addition to all employees of TRC. I dedicate this book to my late teacher, professor emeritus of Osaka university, Shinichi Nakashima who died on September 10th in 2022.

Otsu, Japan
December 2022

Masanobu Yoshikawa

Contents

1	Introduction	1
1.1	Introduction	1
2	Raman and Infrared (IR) Spectroscopy	3
2.1	Principle of Raman Spectroscopy	3
2.1.1	Crystal Orientation Characterization	6
2.1.2	Stress Characterization	9
2.2	Principle of IR Spectroscopy	11
2.3	Raman Instrumentations	13
2.3.1	Excitation Source	14
2.3.2	Grating [20, 21]	14
2.3.3	Spectrometer [21]	15
2.3.4	Detector	16
2.4	IR Instrumentations	18
2.4.1	IR Source	19
2.4.2	Michelson Interferometer	20
2.4.3	Detector	21
2.4.4	Microscopy and Imaging	23
References		24
3	Photoluminescence (PL) Spectroscopy	27
3.1	PL Imaging Technique	27
References		31
4	Overview of Cathodoluminescence (CL) Spectroscopy	33
4.1	Introduction	33
4.2	Principle of CL Spectroscopy	34
4.3	Instrumentations	34
4.3.1	Excitation Source	34
4.3.2	Optical System	37
4.3.3	Detector	38
4.3.4	Cryostat	39

4.3.5	Comparison of CL and Scanning Near-Field Optical Microscopy (SNOM)-PL Spectroscopy	40
References		44
5	Applications of Raman, IR, and CL Spectroscopy	47
5.1	Silicon and Silicon Dioxide (SiO_2)	47
5.1.1	Silicon	47
5.1.2	Silicon Dioxide	50
5.2	Strained Silicon	56
5.3	Silicon Processing of LSI Devices	60
5.4	Gallium Arsenide and Related Devices	63
5.5	Indium Phosphate and Related Devices	67
5.6	Wide-Gap Semiconductors: Gallium Nitride and Related Materials	70
5.7	Wide-Gap Semiconductors: Silicon Carbide and Related Materials	76
5.7.1	Silicon Carbide	76
5.7.2	Silicon Thermal Oxide Film (SiO_2)	86
5.8	Wide-Gap Semiconductor: Zinc Oxide	94
5.9	Wide-Gap Semiconductor: Diamond	99
5.9.1	Diamond Films	99
5.9.2	Fano Effect in Diamond	104
5.9.3	Nano-diamond	106
5.9.4	Amorphous Diamond	109
5.9.5	Resonant Raman Scattering from Si- and N-doped a-C:H Films	111
5.9.6	Infrared Spectra of a-C:H Films	115
5.9.7	CL of Diamond	116
5.10	Next-Generation Semiconductor: Ga_2O_3	117
5.11	Quantum Dots	126
References		130
6	STEM-CL	143
6.1	Setup	143
6.2	Application	143
6.2.1	Crystalline Characterisation of GaN Flake by STEM-CL	143
6.2.2	Crystalline Characterisation of Single Crystalline ZnO Nanowire by STEM-CL	146
6.2.3	Localised Surface Plasmon of Nanometre-Sized Metal by STEM-EELS and STEM-CL Spectroscopy	147
References		154

Contents	ix
7 Topics	157
7.1 DUV, UV, and NIR Raman Spectroscopy	157
7.2 AFM-Raman and AFM-IR Spectroscopy	163
7.2.1 AFM-Raman Spectroscopy	163
7.2.2 AFM-IR Spectroscopy	180
7.2.3 Optical Photothermal IR and Raman Spectroscopy	185
7.3 Terahertz Time-Domain Spectroscopy (THz-TDS)	187
7.4 SIMS-OES/-CL Spectroscopy	190
7.5 Time-Resolved CL Spectroscopy	192
References	199
Paper List	205
Index	217

About the Author



Dr. Masanobu Yoshikawa completed his doctorate in applied spectroscopy with the Fourier transform infrared (FT-IR) and Raman spectroscopy at the Osaka University in 1986. After his analytical study of the one-dimensionally conducting metal-tetracyanoquinodimethane (M-TCNQ) with FT-IR and Raman spectroscopy at the Osaka university, he joined Toray Research Center, Inc. in 1986, which is a leading analytical service company in Japan. He has mainly studied wide-gap semiconductors such as diamond, gallium nitride and silicon carbide, using FT-IR, Raman and cathodoluminescence. He worked for Fraunhofer-Institute in Freiburg in Germany for 6 months in 1998. Furthermore, he has served as the Japanese national project leader for development of the world-first scanning near field Raman spectroscopy (SNOM) from 2003–2007, entrusted by New Energy and Industrial Technology Development Organization (NEDO) in Japan and succeeded in stress characterization of Si devices with a spatial resolution of less than 100 nm. As a result, he was awarded the Advance Analytical Instrument Development prize from the Japan Society for Analytical Chemistry (JAIMA) in 2010. He is working for Toray Research Center, Inc. as a senior vice president and a senior fellow.

Chapter 1

Introduction



1.1 Introduction

Vibrational spectroscopy includes various techniques, specifically, infrared (IR), terahertz (THz), and Raman spectroscopy. In THz time-domain spectroscopy, short pulses of THz radiation are used to investigate the properties of materials. The generation and detection schemes are sensitive to the effects of the specimen on both the amplitude and phase of the THz radiation. Because measurements are made in the time domain, this technique can provide more information than conventional Fourier transform infrared (FT-IR) spectroscopy, which is sensitive only to the amplitude.

FT-IR and Raman spectroscopy are used to study a very wide range of specimen types, including both organic and inorganic materials, and their applications range from simple identification tests to in-depth, full-spectrum, qualitative and quantitative analyses.

FT-IR and Raman spectroscopy are complementary techniques, and it is usually necessary to apply both techniques to completely measure the vibrational modes of a molecule, a solid, or a specimen in solution. Although some vibrational modes may appear in both the FT-IR and Raman spectra, these spectroscopic techniques are based on different mechanisms and different selection rules. FT-IR spectroscopy is generally most effective for observing asymmetric vibrations of polar groups, whereas Raman spectroscopy is most effective for observing symmetric vibrations of nonpolar groups. Table 1.1 summarises the characteristics of FT-IR and Raman spectroscopy.

Table 1.1 Comparison of standard FT-IR and Raman spectroscopy

	IR	Raman
Characteristic	Functional group	Skeleton structure
	Side chain	Side chain (weak)
Spatial resolution	10 μm	10 nm (AFM-Raman)-500 nm
Disadvantages	Water vapour absorption	Interference from fluorescence
	(Huge database)	Few database
Observed object	Organic materials	Inorganic materials
	Inorganic materials	Organic materials
Information	Composition	Composition
	Orientation	Orientation
	Free carrier	Crystallinity, defect
	Inhomogeneity	Stress, carrier density

Chapter 2

Raman and Infrared (IR) Spectroscopy



2.1 Principle of Raman Spectroscopy

Rayleigh scattering was discovered in the nineteenth century. The weaker Raman effect is named after Raman [1], who discovered it in 1928 with assistance from his student Krishnan and Raman [2]. C. V. Raman was recognized the world-over and bestowed the Nobel Prize in 1930 for his discovery, although Grigory Landsberg and Leonid Mandelstam observed the effect in crystals in the same year in which Raman discovered the effect. The effect had been predicted theoretically by Adolf Smekal in 1923 [3].

When a specimen is irradiated with light, the light will interact with the specimen by some mechanisms, including reflection, absorption, or scattering. FT-IR spectroscopy is a method of detecting the reflected or directly absorbed energy in the IR region, which represents transitions from the initial (ground) state to the final (first excited) vibrational state, when the incident light is focused on a molecule or semiconductor. By contrast, Raman spectroscopy is a method of detecting the light scattered inelastically at a frequency different from the incident light (approximately only $1/10^7$ of the Rayleigh scattered light), which corresponds to a molecular vibration or lattice vibration in the specimen. The resulting line is called the Stokes or anti-Stokes Raman line. The elastic scattering is called Rayleigh scattering. Both FT-IR and Raman spectroscopy provides chemical and structural information about a specimen.

According to the principles of FT-IR and Raman spectroscopy, FT-IR spectroscopy is sensitive to heteronuclear functional group vibrations and polar bonds, especially C–H and OH bonds, whereas Raman spectroscopy is sensitive to homonuclear molecular bonds, especially Si–Si, C–C, C=C, and C≡C bonds.

We will look at vibrational and rotational Raman transitions. When a photon interacts with a semiconductor, it causes the electrons and protons to move, and this motion induces an oscillating dipole. The dipole then radiates photons of different frequencies. To find these frequencies, we consider a photon with the following electric field:

$$\mathbf{E} = \mathbf{E}_0 \cos(\omega_0 t) \quad (2.1)$$

The induced dipole is then expressed as

$$P_\rho = \alpha_{\rho\sigma} E_\sigma = \alpha_{\rho\sigma} E_{\sigma 0} \cos(\omega_0 t) \quad (2.2)$$

where $\alpha_{\rho\sigma}$ is the electronic polarisability tensor of the semiconductor. Throughout this section, one will be using Einstein notation (an implied sum over repeated indices). The term $\alpha_{\rho\sigma}$ does not have a constant value.

For small displacements, the electronic polarisability tensor can be expanded as a Taylor series in the normal coordinates of the semiconductor [4]:

$$\alpha_{\rho\sigma}(Q) = (\alpha_{\rho\sigma})_0 + \sum_k \left(\frac{\delta \alpha_{\rho\sigma}}{\delta Q_k} \right) Q_k + \dots \quad (2.3)$$

where $(\alpha_{\rho\sigma})_0$ is the polarisability tensor in the equilibrium configuration, and Q_k is the k th normal-mode coordinate of the semiconductor associated with the vibrational frequency ω_k . Because the normal modes are harmonic, Q can be written as [4]

$$Q_k = Q_{k0} \cos(\omega_k t) \quad (2.4)$$

Inserting this expression into Eq. (2.3) and then inserting the result into Eq. (2.2) gives the linear induced dipole vector $P_\rho(0)$ [4]:

$$\begin{aligned} P_\rho(0) &= (\alpha_{\rho\sigma})_0 \cos(\omega_0 t) + \\ &+ \sum_k \left(\frac{\delta \alpha_{\rho\sigma}}{\delta Q_k} \right)_0 Q_{k0} E_{\sigma 0} \cos(\omega_k t) \cos(\omega_0 t) \\ &= (\alpha_{\rho\sigma})_0 \cos(\omega_0 t) + \\ &+ \sum_k \left(\frac{\delta \alpha_{\rho\sigma}}{\delta Q_k} \right)_0 \frac{Q_{k0} E_{\sigma 0}}{2} \{ [\cos(t(\omega_0 - \omega_k))] + [\cos(t(\omega_0 + \omega_k))] \} \end{aligned} \quad (2.5)$$

This equation shows that the dipole has three frequencies: ω_0 , $\omega_0 - \omega_k$, and $\omega_0 + \omega_k$, which give rise to Rayleigh, Stokes, and anti-Stokes scattering, respectively [4].

The Stokes scattering peaks are stronger than the anti-Stokes scattering peaks. Their ratio depends on the temperature, and this dependence can therefore be exploited to measure it [4]:

$$\frac{I_{Stokes}}{I_{anti-Stokes}} = \frac{(\tilde{\nu}_0 - \tilde{\nu}_k)^4}{(\tilde{\nu}_0 + \tilde{\nu}_k)^4} \exp\left(\frac{hc\tilde{\nu}_k}{k_B T}\right) \quad (2.6)$$

where $\tilde{\nu}_0$ is the wavenumber of the laser, $\tilde{\nu}_k$ is the wavenumber of the vibrational transition, k_B is the Boltzmann factor, and T is the temperature. We can measure the temperature of electronic devices in situ during operation, for example, by applying an electrical current or a voltage, and combining Eq. (2.6) with the results of Raman measurement [4].

Light may be scattered in the following ways: Rayleigh scattering (no energy is exchanged; that is, the incident and scattered photons have the same energy), Stokes Raman scattering (an atom or a molecule absorbs energy, and the scattered photon has less energy than the incident photon), and anti-Stokes Raman scattering (an atom or a molecule loses energy, and the scattered photon has more energy than the incident photon) [5, 2].

The scattering intensity varies directly with the square of the induced dipole moment, $\mathbf{P} = \alpha\mathbf{E}$, where α is the electronic polarisability of the material, which is a volumetric measure of its electron cloud distortion in the path of the incident light relative to the nuclear framework. The electronic polarisability α is closely related to the structure and bonding properties of the materials and is *always* nonzero. The probability of fundamental transitions in the Raman spectrum is proportional to the square of the electronic polarisability gradient along the normal coordinate of the vibration, $(\partial \alpha / \partial Q_k)_0$.

If there is no net change in the electronic polarisability when the vibration occurs, i.e., $(\partial \alpha / \partial Q_k)_0 = 0$, the band in the Raman spectrum has zero intensity, and the vibration is said to be Raman-inactive. By contrast, the probability of a fundamental transition in IR absorption is proportional to the square of the dipole moment (μ) gradient along the normal coordinate of the vibration, $(\partial \mu / \partial Q_k)_0$. Therefore, if the dipole moment does not change when the vibration occurs, i.e., $(\partial \mu / \partial Q_k)_0 = 0$, the vibrational band in the IR spectrum has zero intensity, and the vibration is said to be IR-inactive. This is called the selection rule.

Czernuszewicz and Zaczek [6] considered how α varies not only with the normal modes of vibration but also with the frequency of the incident radiation that excites them [6]. Consider an atom initially in an energy state $|g\rangle$ that is perturbed by an electromagnetic wave of frequency ν_0 so that it passes into a final electronic state $|f\rangle$ while scattering light of frequency $\nu_0 \pm \nu_k$ ($\nu_k = \nu_f - \nu_g$). The matrix elements of α for the vibrational transition k , $[\alpha_{\rho\sigma}]_k$, are given by the Kramers–Heisenberg–Dirac (KHD) dispersion equation [5, 7]:

$$[\alpha_{\rho\sigma}]_k = \frac{1}{h} \sum_e \left(\frac{\langle f | M_\rho | e \rangle \langle e | M_\sigma | g \rangle}{\nu_{eg} - \nu_0 + ie} + \frac{\langle f | M_\sigma | e \rangle \langle e | M_\rho | g \rangle}{\nu_{eg} + \nu_0 + ie} \right) \quad (2.7)$$

where ρ and σ ($= x, y, z$), which independently refer to the semiconductor-fixed nonrotating Cartesian coordinate system, represent the polarisations of the scattered and incident light, respectively; $|g\rangle$ and $|f\rangle$ are the initial and final states of the semiconductor, respectively, and the summation is over all the excited electronic states $|e\rangle$ [5, 7]. The integrals $\langle f | M_\sigma | e \rangle$ and $\langle e | M_\rho | g \rangle$ are the electric dipole transition

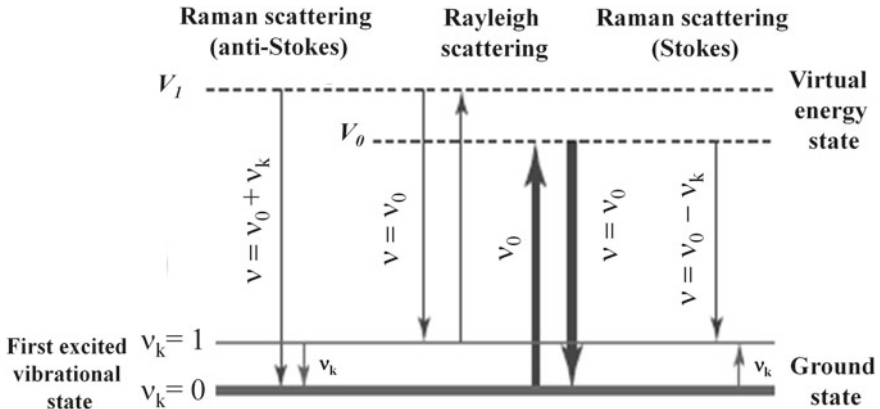


Fig. 2.1 Energy level diagram of Raman scattering

moments along the ρ and σ directions, respectively; M is the electron position operator; h_{ν_0} is the energy of the incident radiation; and Γ_e is a damping factor, which prevents the denominator at resonance from reaching zero and reflects the finite natural lifetime and sharpness of the excited state $|e\rangle$ [5, 7]. Far from resonance ($\nu_0 \ll \nu_{eg}$), the magnitude of $[\alpha_{\rho\sigma}]_k$ is independent of ν_0 ; many excited electronic states contribute to the polarizability [5, 7].

In this case, all the energy denominators in the KHD equation become large, and the scattering tensor $[\alpha_{\rho\sigma}]_k$ is thus small, resulting in very weak scattering (normal Raman scattering) [5, 7]. As the excitation energy (frequency), ν_0 , is tuned to the frequency of an electronic transition, ν_{eg} , the first (resonance) term of the KHD equation becomes dominant and large because $\nu_{eg} - \nu_0 \approx 0$ in its denominator, and the second (non-resonance) term becomes negligible [5, 7]. As a result, the intensity of Raman scattering is expected to increase dramatically (but not to infinity owing to the Γ_e term) when ν_0 is in the resonance region, if the resonant state $|e\rangle$ has a large enough transition dipole moment from the ground state [5, 7]. This phenomenon is called resonant Raman scattering. An energy level diagram of Raman scattering is shown in Fig. 2.1 [5, 7].

2.1.1 Crystal Orientation Characterization

The first-order Raman scattering intensity is expressed by [8]

$$I = \sum_j (e_i R_j e_s)^2 \quad (2.8)$$

where e_i and e_s are the unit polarisation vectors of the incident and scattered light, respectively, and R_j ($j = x, y, z$) is the Raman tensor of the F_{2g} mode.

Table 2.1 Phonon frequencies semiconductors with diamond-type and zinc blende-type crystal structures. Phonon frequencies are expressed in a unit of cm^{-1} (our work)

Diamond structure		F_{2g} mode (cm^{-1})
Germanium		380
Silicon		521
Diamond		1332
Zinc blende structure	TO phonon (cm^{-1})	LO phonon (cm^{-1})
ZnSe	213	253
GaAs	270	292
InP	300	340
GaP	362	400
3C-SiC	790	970

In general, familiar semiconductors such as silicon (Si), germanium (Ge), diamond, gallium arsenide (GaAs), gallium phosphate (GaP) and indium phosphate (InP), zinc selenide (ZnSe) are well-known to be consisted of diamond-type and zinc blende-type crystal structures. On the other hand, silicon carbide (SiC), gallium nitride (GaN), and gallium oxide (Ga_2O_3) exhibit wurtzite type crystal structures and they have various polytype crystal structures. Table 2.1 shows one phonon frequencies semiconductors with diamond-type and zinc blende-type crystal structures.

Diamond belongs to the space group O_h with two atoms per primitive cell. A triply degenerate optical phonon with F_{2g} symmetry has been observed at 1332 cm^{-1} in the first-order spectrum. The second-order Raman spectrum in diamond has been observed in the range $2000\text{--}3000 \text{ cm}^{-1}$. The origin of the second-order spectrum was studied in detail by Solin and Ramdas [9].

As an example, the configuration of Raman measurement with cartesian coordinate axes (x , y , z), and Raman tensors for diamond-type structures are depicted in Fig. 2.2.

In this backscattering geometry with the polarisation direction of the scattered light parallel to that of the incident light, Eq. (2.8) is simply given for diamond structure as follows [10, 11]:

$$\begin{aligned} I &= C \sin^2(2\varphi) && \text{for the (100) plane} \\ I &= C \sin^2 2\varphi + \sin^4 \varphi && \text{for the (110) plane} \\ I &\text{ is constant} && \text{for the (111) plane} \end{aligned} \quad (2.9)$$

where φ is the angle between the $<010>$ axis and the projection of the wave vector of the incident (scattered) light onto the (100) plane (e_i , e_s), and C is constant.

Figure 2.3 displays the Raman intensity variation versus rotation angle (in polar coordinates) of diamond structure for the (100), (110), and (111) planes, respectively. As seen in Fig. 2.3, the Raman intensity variation versus rotation angle for semiconductors yields us with information about the crystal structure of semiconductors.

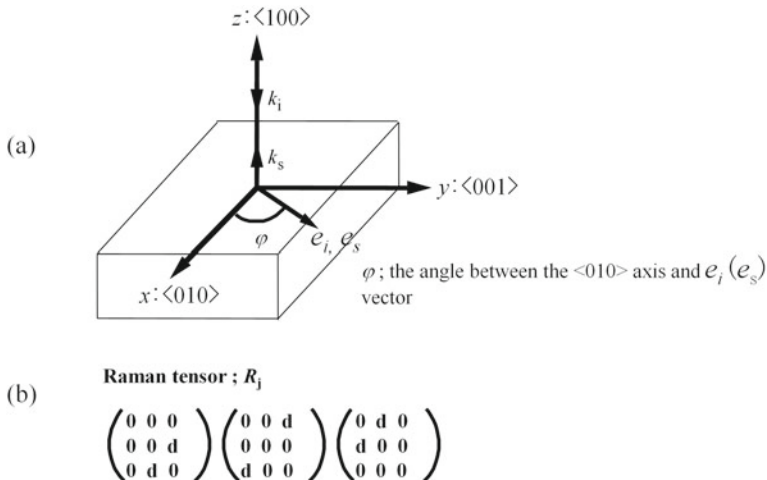


Fig. 2.2 The typical Raman measurement geometry: **a** the configuration of Raman measurement with cartesian coordinate axes (x , y , z), and **b** Raman tensors for diamond structure. The k_i and k_s express the wave vector of the incident and scattered light, respectively

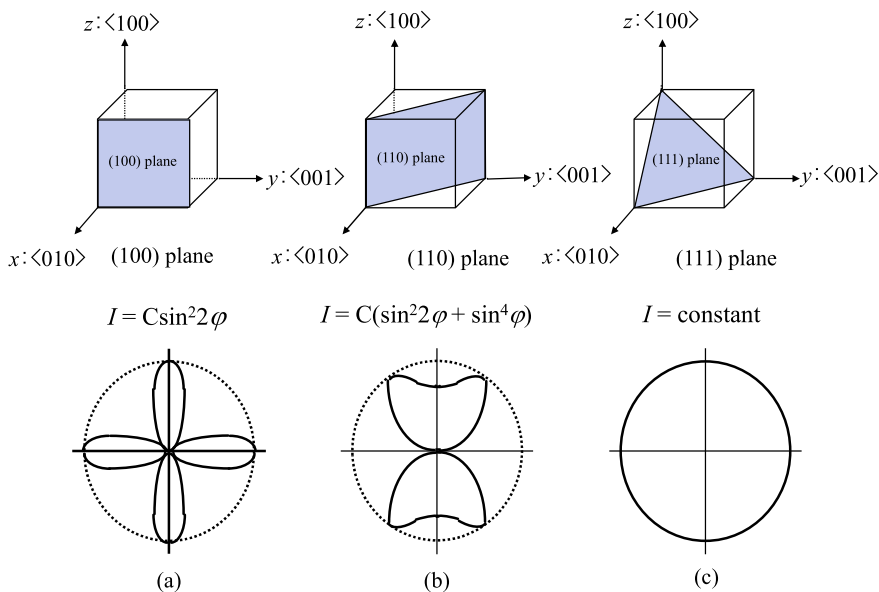


Fig. 2.3 The Raman intensity variation versus rotation angle (in polar coordinates) of the diamond plane: **a** (100), **b** (110), and **c** (111) plane, calculated by Eq. (2.9), respectively

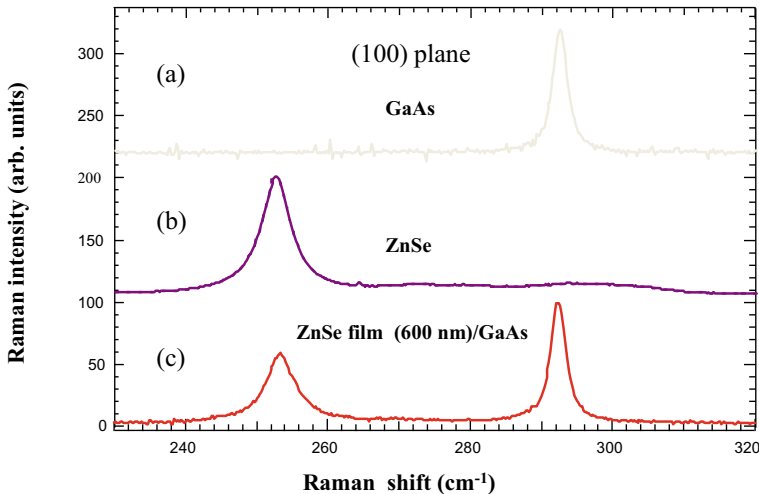


Fig. 2.4 Raman spectra **a** a GaAs substrate, **b** a ZnSe substrate, and **c** ZnSe film (600 nm-thick) on a GaAs substrate

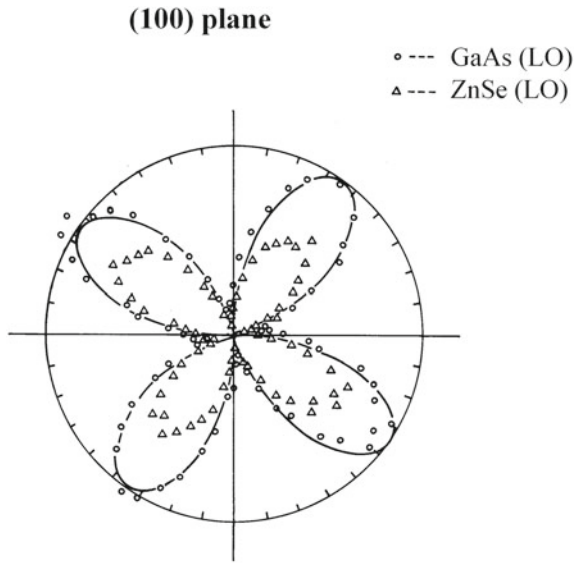
Figure 2.4 shows Raman spectra of a GaAs, ZnSe substrate, and ZnSe film (600 nm-thick) on a GaAs substrate. The longitudinal optical (LO) phonons of ZnSe, and GaAs are observed at 253 and 292 cm⁻¹, respectively.

Figure 2.5 displays the Raman intensity variation versus rotation angle (in polar coordinates) of a ZnSe film (600 nm-thick) grown on the (100) plane of a GaAs substrate measured in a backscattering geometry. The radial and angular coordinates are based on the intensity of the LO phonons of ZnSe and GaAs, and the rotation angle of the specimen, respectively. The angular dependence of the Raman intensity of ZnSe coincides well with that of the (100) plane of GaAs and the calculated curve for this plane in Fig. 2.5. This indicates that the crystallographic orientation of the ZnSe film is mostly the same as that of the (100) plane of GaAs substrate and that the ZnSe film grew heteroepitaxially on the GaAs plane.

2.1.2 Stress Characterization

The $k \approx 0$ optical phonons in a diamond-type semiconductor are triply degenerate (F_{2g} symmetry) by the cubic symmetry of the crystal in the absence of stress [12, 13]. Application of the stress removes this cubic symmetry and hence splits the triplet. The frequencies of the optical phonons in the presence of strain are determined by solving the following secular equation:

Fig. 2.5 Raman intensity variation versus rotation angle (in polar coordinates) of a ZnSe film (600 nm-thick) grown on the (100) plane of GaAs measured in a backscattering geometry



$$\begin{vmatrix} p\epsilon_{xx} + q(\epsilon_{yy} + \epsilon_{zz}) - \lambda & 2r\epsilon_{xy} & 2r\epsilon_{xz} \\ 2r\epsilon_{xy} & p\epsilon_{yy} + q(\epsilon_{zz} + \epsilon_{xx}) - \lambda & 2r\epsilon_{yz} \\ 2r\epsilon_{xz} & 2r\epsilon_{yz} & p\epsilon_{zz} + q(\epsilon_{xx} + \epsilon_{yy}) - \lambda \end{vmatrix} \equiv 0, \quad (2.10)$$

where $\lambda = \Omega^2 - \omega_0^2$ and $\Omega \approx \omega_0 + \lambda/2\omega_0$ is the strain dependent frequency of the optical phonons, and p , q , and r are deformation potential constants. The secular equation is referred to the crystallographic axes, $\mathbf{x} = [100]$, $\mathbf{y} = [010]$, and $\mathbf{z} = [001]$. Diagonalization of Eq. (2.10) yields the set of three eigenvectors of the optical phonons in the presence of strain.

In the presence of biaxial stress on a (100) surface, the triply degenerate F_{2g} mode splits into singlet and doublet modes. In the backscattering configuration from the (100) surface, only the singlet mode is Raman active and the relation between the peak-frequency shift ($\Delta\nu$) and isotropic biaxial stress (σ) is expressed as follows [12, 13]:

$$\sigma(\text{GPa}) = \sim 0.23 \times \Delta\nu(\text{cm}^{-1}) \quad \text{for (100)} \quad (2.11)$$

The peak-frequency shift of the modes split from the stress-free Raman line, $\Delta\nu$ is accurately measured, and then multiplied by the coefficient, $C = \sim 0.23$, in order to translate $\Delta\nu$ into local residual stress. The coefficient is a function of the elastic compliance constant and deformation potential constant, and strongly depends on the direction and distribution of the stress [13].

2.2 Principle of IR Spectroscopy

Infrared (IR) spectroscopy involves the interaction of IR radiation with materials. It includes various techniques, most of which are based on absorption spectroscopy. As with all spectroscopic techniques, they can be used to identify and study the chemical and physical structures of materials [14].

Specimens may be solids (for example, semiconductors), liquids, or gases. The IR spectrum is measured by an instrument called an IR spectrometer or spectrophotometer. This spectrum can be visualised in a graph of the IR light absorbance (or transmittance) on the vertical axis versus the frequency (or wavelength) on the horizontal axis [14]. The unit of frequency used in FT-IR spectra is the reciprocal centimetre (sometimes called the wavenumber), with the symbol cm^{-1} . An instrument that uses this technique is an FT-IR spectrometer [14].

The IR portion of the electromagnetic spectrum is usually divided into three regions, the near-IR (NIR), mid-IR (MIR), and far-IR (FIR), which are named for their relationship to the visible spectrum [14]. The higher-energy NIR, at approximately $14,000\text{--}4000\text{ cm}^{-1}$ (wavelengths of $0.7\text{--}2.5\text{ }\mu\text{m}$) can excite overtone or harmonic vibrations. The MIR, at approximately $4000\text{--}400\text{ cm}^{-1}$ ($2.5\text{--}25\text{ }\mu\text{m}$), may be used to study the fundamental vibrations and associated molecular or lattice vibration [14]. The FIR, at approximately $400\text{--}10\text{ cm}^{-1}$ ($25\text{--}1000\text{ }\mu\text{m}$), which is adjacent to the microwave region, has low energy and may be used for vibrational spectroscopy associated with THz phenomena [14].

Attenuated total internal reflectance (ATR) spectroscopy is a powerful technique for obtaining information about surface properties or conditions of a material [14]. The phenomenon of ATR was first observed by IR spectroscopy in 1959. It was observed that under certain conditions, IR radiation entering a prism made of a high-refractive-index IR-transmitting material (an ATR prism) is totally internally reflected (Fig. 2.6) [14].

This internal reflectance creates an evanescent wave that extends beyond the surface of the crystal into the specimen, which is held in contact with the crystal

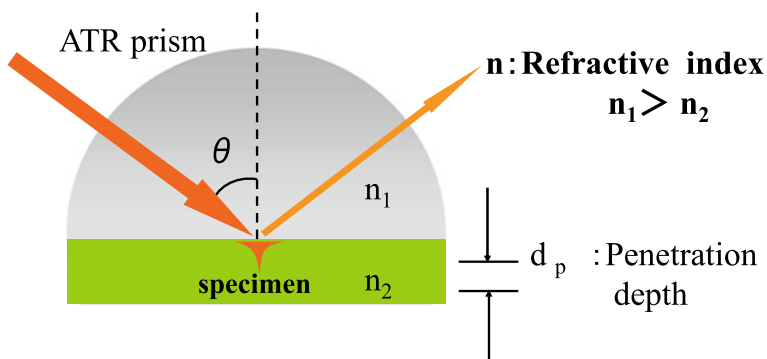


Fig. 2.6 Our setup for ATR measurement

[14]. In the regions of the IR spectrum where the specimen absorbs energy, the evanescent wave is attenuated. To obtain total internal reflectance, the angle of the incident radiation, θ , must exceed the critical angle, θ_c [14]. The critical angle is a function of the refractive indices of the specimen and ATR crystal, and is defined as [14]

$$\theta_c = \sin^{-1} \left(\frac{n_2}{n_1} \right) \quad (2.12)$$

where n_1 is the refractive index of the ATR crystal, and n_2 is the refractive index of the specimen. High-refractive-index materials are chosen for the ATR crystal to minimise the critical angle [14]. ATR is a powerful technique because the intensity of the evanescent wave decays exponentially with distance from the surface of the ATR crystal [14]. Because the distance is on the submicrometre order, ATR is generally insensitive to the specimen thickness, making it possible to analyse thick or strongly absorbing specimens [14].

A useful relationship in ATR spectroscopy, which can be used as a qualitative measure of the depth to which the evanescent wave penetrates the specimen, is the penetration depth d_p [14]. The penetration depth is defined as the distance from the crystal/specimen interface at which the intensity of the evanescent wave decays to $1/e$ (approximately 37%) of its original value. It is given by [14]

$$d_p = \frac{\lambda}{2\pi n_1 \sqrt{(\sin^2 \theta - n_{21}^2)}} \quad (2.13)$$

where λ is the wavelength of the incident light, and n_{21} is the ratio of the refractive indices of the specimen and the ATR crystal [14].

Many types of ATR accessories are available for FT-IR spectrometers [14]. They can be classified as ATR cells with a single reflection (one bounce) and cells with multiple reflections (multiple bounce) [14]. The material of the ATR crystal is chosen according to the application and the specimens to be measured. Typical materials for ATR crystals include germanium (Ge), thallium bromoiodide (KRS-5), and zinc selenide (ZnSe), whereas silicon (Si) is ideal for use in the FIR region of the electromagnetic spectrum [14]. The excellent mechanical properties of diamond make it an ideal ATR material, particularly for studying very hard solids, although the broad diamond phonon band between 2600 and 1900 cm^{-1} significantly decreases the signal-to-noise ratio in this region [14]. For specimens with very thin surfaces, Ge is used for the ATR prism, and the penetration depth d_p into the specimen is typically between 0.3 and 2 μm [14]. The shape of the crystal depends on the type of spectrometer and nature of the specimen. For dispersive spectrometers, the crystal is a rectangular slab with chamfered edges. Other geometries use prisms, half-spheres, or thin sheets [14].

Diffuse reflectance IR Fourier transform spectroscopy [14, 15] is an FT-IR spectroscopy sampling technique used on powder specimens without prior preparation. A

bulk specimen is added to a specimen cup, and data are collected. Under IR irradiation, the specimen reflects and transmits different amounts of the IR light depending on the bulk properties of the material [14, 15]. Incident light that is diffusely reflected by a specimen with a rough surface that reflects in all directions is collected using an ellipsoidal or parabolic mirror [14, 15]. The shape, compactness, refractive index, reflectivity, and absorption of the particles are all characteristics of the material being analysed. If the specimen is too absorbent, it can be diluted with a non-absorbent material such as potassium bromide (KBr) or potassium chloride (KCl) [14, 15]. The particle size should be smaller than the wavelength of the incident light to minimise Mie scattering; thus, it should be less than $5 \mu\text{m}$ for MIR spectroscopy [14, 15]. The spectra are plotted in units of the log inverse reflectance ($\log 1/R$) versus wavenumber [14, 15]. Another option is plots in Kubelka–Munk[16] units, which provide the relationship between the reflectance and the concentration using a scaling factor. A reflectance standard is needed to quantify the reflectance of the specimen because it cannot be determined directly [17, 18].

2.3 Raman Instrumentations

Raman spectroscopy can be used for microscopic analysis at a spatial resolution on the order of 500 nm. Such analysis is possible using a standard Raman microscope. A Raman microscope consists of a Raman spectrometer coupled to a standard optical microscope and affords visualisation of a specimen at high magnification and Raman analysis using a submicron laser spot. The Raman microanalysis setup is shown in Fig. 2.7.

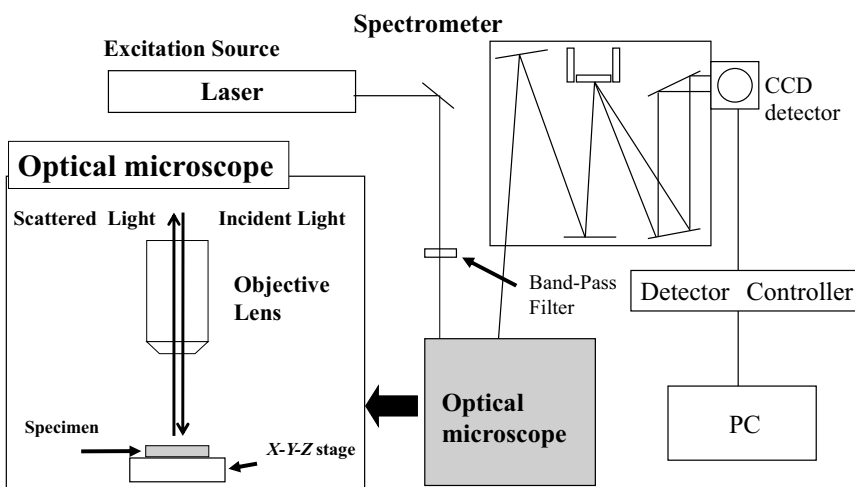


Fig. 2.7 Our Raman microanalysis setup

In a typical microanalysis, a specimen is placed on a stage under the microscope, the focus is adjusted, and the measurement is made. A confocal Raman microscope can be used to analyse particles or volumes with sizes on the order of micrometres. It can even be used to analyse different layers in multi-layered specimens (polymer films, etc.), contaminants and features beneath the surface of a transparent specimen (e.g., impurities within glass and fluid/gas inclusions in minerals).

A mapping stage makes it possible to generate Raman spectral images, which contain many thousands of Raman spectra acquired at different positions on the specimen [19]. Colour images based on the Raman spectra can be obtained and indicate the distributions of individual chemical components and variations in other characteristics of the specimen, such as the phase, polymorphism, stress/strain, and crystallinity [19]. To obtain high-quality Raman spectra of specimens, it is essential to select an incident laser with a suitable excitation wavelength [19].

2.3.1 *Excitation Source*

In modern Raman measurement, several laser wavelengths may be used to realise the optimal detection of the Raman spectra of specimens without inducing luminescence from the specimens. Lasers with excitation wavelengths ranging from the deep ultra-violet (DUV) to the NIR are used, for example, the 244 nm line (second harmonic) of an Ar⁺ laser, 266 nm line (fourth harmonic) of an Nd:YAG laser, 325 nm line of a He–Cd laser, 364 nm line of a Kr⁺ laser, 457.9–514.5 nm lines of an Ar⁺ laser, 532 nm line of a semiconductor laser, 633 nm line of a He–Ne laser (or semiconductor laser), 785 nm line of a semiconductor laser, 830 nm line of a semiconductor laser, and 1064 nm line of an Nd:YAG laser.

2.3.2 *Grating [20, 21]*

A diffraction grating is the most important element with a regular pattern, which diffracts light into each beam propagating in different directions [20]. The directions of these beams are dependent on the grating space and the wavelength of the light; thus, the grating acts as a dispersive element. The diffraction gratings are mainly used in spectrometers [20].

A photographic slide with a fine pattern of black lines forms a simple grating. For practical applications, gratings generally have grooves or rulings on their surface rather than dark lines. Such gratings can be either transparent or reflective [20]. Gratings that modulate the phase rather than the amplitude of the incident light are also produced, often by using holography [20].

The relation between the grating space and the angles of the incident and diffracted light beams is well-known as the grating equation [20]. When a wave travels, each

point on the wavefront acts as a point source, and the wavefront at any subsequent point is found by adding the contributions of the point sources [20].

An idealised grating consisting of a set of long and infinitely narrow slits of spacing d is considered here. When a plane wave of wavelength λ is normally incident on the grating, each of the slits in the grating acts as a set of point sources that propagate in all directions. The light moving in a particular direction θ consists of the interfering components of each slit [20, 21]. The waves from different slits will have different phases and will cancel each other out partially or entirely [20, 21]. Hence, when the path difference between the light from adjacent slits is equal to the wavelength λ , the waves will all be in phase. This occurs at angles θ_m that satisfy the relationship $d \sin \theta_m / \lambda = |ml|$, where m is an integer. Thus, the diffracted light will have maxima at angles θ_m given by [20, 21]

$$d \sin \theta_m = m\lambda \quad (2.14)$$

It is simply to show that if a plane wave is incident at an angle θ_i , the grating equation becomes [21]

$$d (\sin \theta_m + \sin \theta_i) = m\lambda \quad (2.15)$$

The light that corresponds to direct transmission (or specular reflection, in the case of a reflection grating) is called the zero order and is indicated as $m = 0$. The other maxima occur at angles that are labelled by nonzero integers m [21].

Gratings can be made that modulate various properties of the incident light in a regular pattern; these properties include the transparency (transmission amplitude gratings), the reflectance (reflection amplitude gratings), the refractive index (phase gratings), and the direction of the optical axis (optical axis gratings) [21].

2.3.3 Spectrometer [21]

The spectrometer plays an important role in separating an incident light source into its spectral components while measuring the outgoing light intensity emitted by a specimen over a broad spectral range [21]. It is widely used for spectroscopic analysis of materials [21]. The incident light from the light source can be transmitted through or absorbed or reflected by the specimen [21].

A monochromator produces a beam of light with a very narrow bandwidth, or light of a single colour. It is used in optical measuring instruments where tuneable monochromatic light is needed [21]. A spectrograph splits light from an object into its component wavelengths so that it can be recorded and analysed. It provides an image at a defined bandwidth and wavelengths. A spectrograph includes several instruments, such as an electronic detector, which records the spectrum for analysis [21].

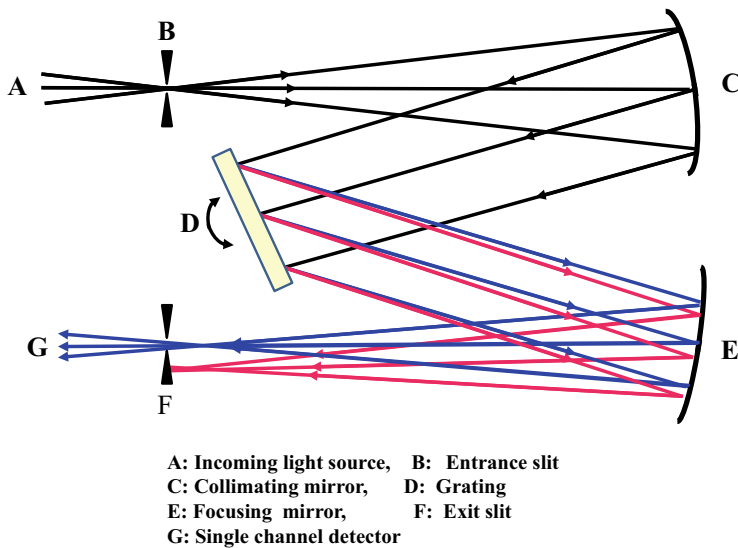


Fig. 2.8 CT monochromator configuration

A single, double, or triple monochromator is used in Raman measurement. Monochromator and spectrometer systems form an image of the entrance slit in the exit plane at the wavelengths present in the light source [21]. Many configurations can be used for this purpose, including plane grating systems and aberration-corrected holographic grating systems. The Czerny–Turner (CT) monochromator is a typical example. As shown in Fig. 2.8, the CT monochromator consists of two concave mirrors and one planar diffraction grating [21].

The CT configuration may be designed to produce a flattened spectral field and good coma correction at one wavelength. Spherical aberration and astigmatism will remain at all wavelengths.

2.3.4 Detector

Spectral imaging systems record a stack of monochromatic images on a 2D detector array, such as a charge-coupled device (CCD) detector. Multiple images are collected over many wavelengths, forming a spectral data cube. Spectral imaging systems incorporate various strategies to enable the collection of multiple monochromatic images.

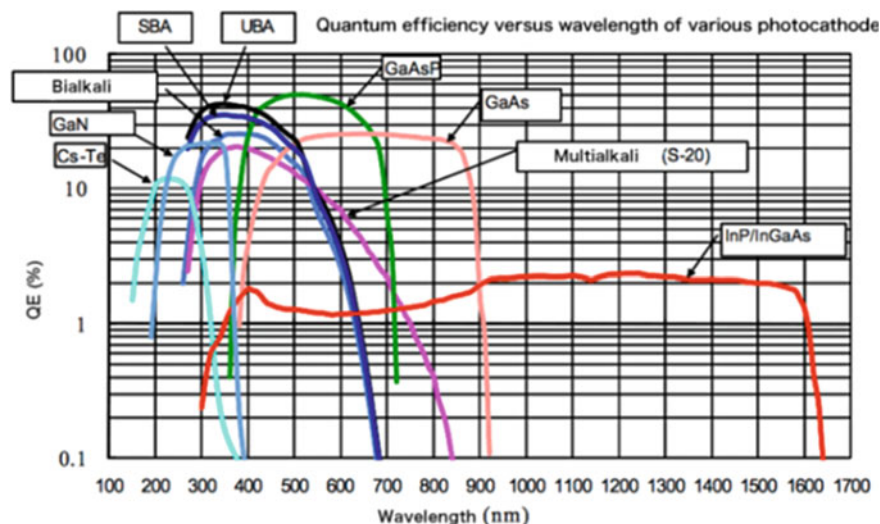
In spectroscopy mode, a spectrum of emitted light is obtained over a selected area under optical microscope observation. In imaging mode, a map of the photon intensity (energy resolved by a spectrograph) is acquired instead. Because these modes cannot operate simultaneously, information is inevitably lost. A Raman spectral imaging

Table 2.2 Typical detectors and their wavelengths of interest

	DUV (100–200 nm)	UV–Visible (200–900 nm)	NIR (900 nm–1.7 μm)
PMT	Cs–Te	GaAs	InP/InGaAs
CCD	Si	Si	Si
InGaAs Array	–	–	InGaAs

technique that combines the spectroscopy and imaging modes was recently developed using multichannel photodetectors. In brief, the spectral imaging technique acquires a spectrum for each pixel in the image by synchronising the scanning of the incident light with spectrum acquisition by a multichannel photodetector. A photomultiplier tube (PMT) [22], silicon CCD [23], or indium gallium arsenide (InGaAs) [24] photodetector array is selected for the Raman measurement, depending on the wavelength of interest (180–1800 nm). These cryo-cooled detectors offer high sensitivity and superior performance. Table 2.2 shows typical detectors and their wavelengths of interest.

Figures 2.9, 2.10, and 2.11 show the performance specifications of PMTs, CCDs, and InGaAs arrays, respectively.

**Fig. 2.9** Performance specifications of PMTs [22]

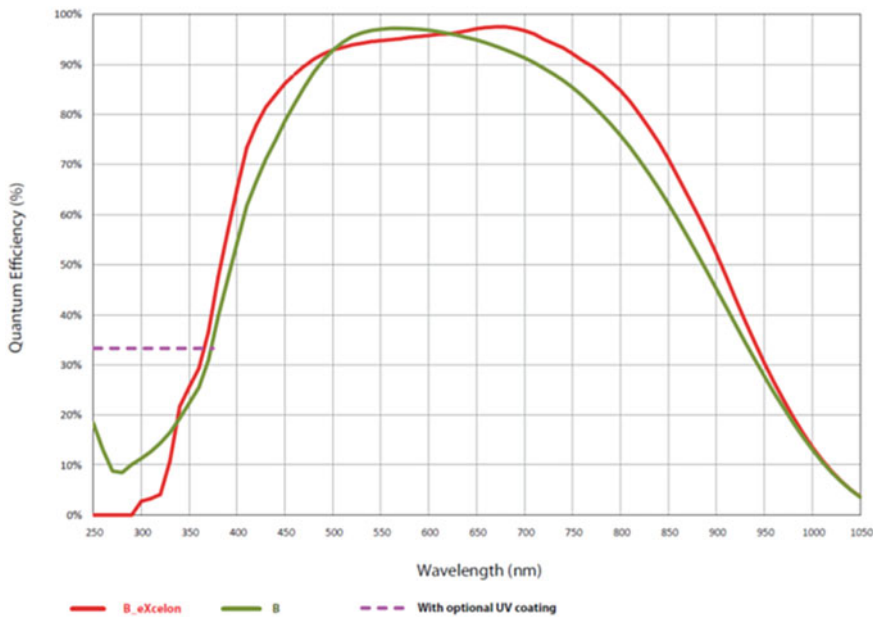


Fig. 2.10 Performance specifications of CCDs [23]

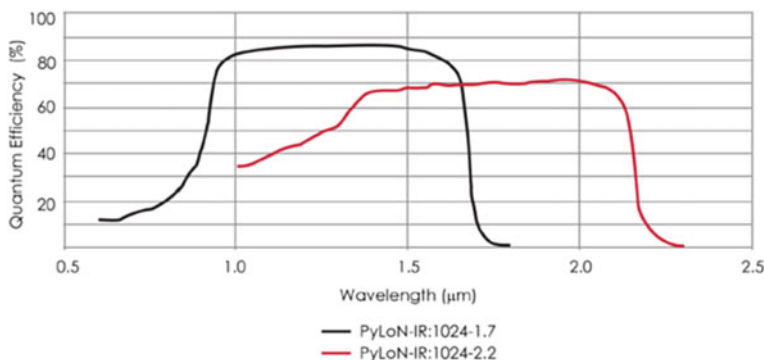


Fig. 2.11 Performance specifications of InGaAs arrays [24]

2.4 IR Instrumentations

FT-IR spectroscopy [25] is used to acquire the IR absorption spectra of solids, liquids, and gases. An FT-IR spectrometer can simultaneously obtain high-spectral-resolution data over a wide spectral range [25]. It thus has a significant advantage over a dispersive spectrometer, which measures the intensity over a narrow range of wavelengths in each measurement [25].

The first spectrophotometer that could record an IR spectrum was the Perkin-Elmer Infracord, which was introduced in 1957 [26]. This system covered wavelengths of 2.5–15 μm , which correspond to wavenumbers of 4000–660 cm^{-1} . The lower wavelength limit was imposed by the highest vibrational frequency of the fundamental molecular vibration [26]. The upper limit results from the fact that the dispersing element was a prism made from a single crystal of rock-salt (sodium chloride), which becomes opaque at wavelengths longer than approximately 15 μm ; this spectral region became known as the rock-salt region [26]. Later instruments used KBr and caesium iodide (CsI) prisms to extend the range to 25 μm (400 cm^{-1}) and 50 μm (200 cm^{-1}), respectively [26]. The region beyond 50 μm (200 cm^{-1}) became known as the FIR region; at very long wavelengths, it merges into the microwave region [26]. Measurements in the FIR region required the use of accurately ruled diffraction gratings instead of prisms as dispersing elements because salt crystals are opaque in this region [26]. Because of the low energy of the radiation in this region, detectors more sensitive than the bolometer were required, for example, the Golay detector [26]. An additional issue is the need to exclude atmospheric water vapour because it has an intense purely rotational, or lattice vibrational, spectrum in this region. FIR spectrophotometers are slow and expensive. The advantages of the Michelson interferometer were well-known, but considerable technical difficulties had to be overcome before a commercial instrument could be built [26]. An electronic computer was also needed to perform the necessary Fourier transform (FT), and this became practicable only with advances in minicomputers such as the PDP-8, which became available in 1965 [26]. Digilab pioneered the world's first commercial FT-IR spectrometer (Model FTS-14) in 1969 [25] (Digilab FT-IR spectrometers are now a part of the molecular product line of Agilent Technologies, which acquired the spectroscope business from Varian) [27].

FT-IR spectroscopy is used because an FT (a mathematical process) is necessary to convert raw data into a spectrum [28]. In practice, an interferogram consists of a set of intensities measured for discrete retardation values. The difference between successive retardation values is constant [28]. Thus, a discrete FT is needed. The fast FT algorithm is used. Figure 2.12 shows an example of our FT-IR spectrometer with an ATR attachment. THz spectroscopy was recently applied to measure the lattice vibration of semiconductors at wavenumbers below 33 cm^{-1} (10 THz) [29].

2.4.1 *IR Source*

FT-IR spectrometers are used mainly for measurements in the MIR and NIR regions. In the MIR (2–25 μm , 5000–400 cm^{-1}), the most common source is a silicon carbide (SiC) heated to approximately 1200 K (Globar) [29]. The output resembles that of a blackbody. For the shorter wavelengths of the NIR (1–2.5 μm , 10,000–4000 cm^{-1}), a higher-temperature source, typically a tungsten–halogen lamp, is used [29]. The long-wavelength output of these sources is limited to approximately 5 μm (2000 cm^{-1}) owing to the absorption of the quartz envelope. In the FIR, at wavelengths beyond

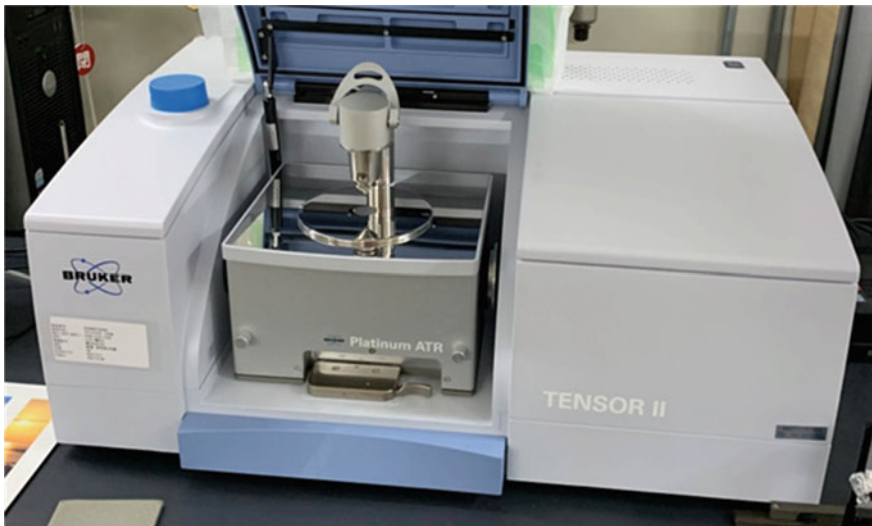


Fig. 2.12 Example of our FT-IR spectrometer with an ATR attachment (Tensor, Bruker Optik GmbH)

50 μm (200 cm^{-1}), a mercury discharge lamp has a higher output than a thermal source [29].

2.4.2 *Michelson Interferometer*

A Michelson interferometer is used for FT-IR measurement. Figure 2.13a shows a schematic of the Michelson interferometer.

In the Michelson interferometer, light from a polychromatic IR source, which is similar to that of a blackbody radiator, is collimated and directed into a beam splitter. Approximately 50% of the light is refracted towards the fixed mirror, and 50% is transmitted toward the moving mirror. Light is reflected from the two mirrors back into the beam splitter, and some fraction of the original light propagates into the specimen compartment. And then, the light is focused on the specimen. After it leaves the specimen compartment, the light is refocused on the detector.

The difference in optical path length between the two arms of the interferometer is well-known as the retardation (optical path difference). The light from the IR source is split into two beams that travel different optical paths and then are recombined, producing an interferogram. The interferogram shown in Fig. 2.13b was obtained by varying the retardation and recording the signal from the detector for various retardation values. The form of the interferogram when no specimen is present depends on factors such as the variation in the source intensity and splitter efficiency with wavelength. Consequently, there is a maximum at zero retardation, where there is

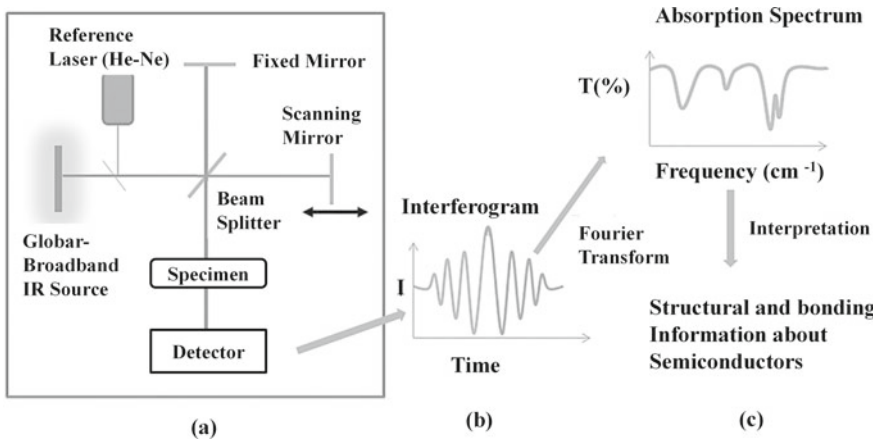


Fig. 2.13 **a** Schematic diagram of Michelson interferometer, **b** interferogram, and **c** absorption spectrum

constructive interference at all wavelengths. The position of zero retardation is determined accurately by finding the point of maximum intensity in the interferogram. When a specimen is present, the background interferogram is modulated by the presence of absorption bands from the specimen. By applying an FT to the background interferogram, we can obtain an FT-IR spectrum, that is, an absorption (or a transmission) spectrum of the specimen (Fig. 2.13c).

2.4.3 Detector

MIR spectrometers generally have pyroelectric detectors that respond to changes in temperature owing to variations in the IR radiation intensity falling on them [30]. The sensitive components in these detectors are made of either deuterated triglycine sulfate (DTGS) or lithium tantalate (LiTaO_3) [30]. These detectors operate at ambient temperatures and provide adequate sensitivity for most routine applications. Scan duration of a few seconds is usually used to obtain the best sensitivity [30]. Cooled photoelectric detectors are utilized when higher sensitivity or a faster response is required. Liquid-nitrogen-cooled mercury–cadmium–telluride (MCT) detectors are the most extensively employed in the MIR [30]. When these detectors are used, an interferogram can be obtained in as little as 10 ms. Uncooled InGaAs photodiodes or DTGS are commonly used in NIR systems. Very sensitive liquid-helium-cooled silicon or germanium (Ge) bolometers are used in the FIR, where both the sources and beam splitters are inefficient [30].

An ideal beam splitter transmits 50% and reflects 50% of the incident radiation. However, as any material has a limited range of optical transmittance, several beam splitters may be used interchangeably to cover a wide spectral range [30]. Beam

splitters for the MIR region are typically made of KBr with a Ge-based coating that makes them semireflective. KBr absorbs strongly at wavelengths beyond 25 μm (400 cm^{-1}); thus, CsI is sometimes used to extend the range to approximately 50 μm (200 cm^{-1}). ZnSe is an alternative for use where moisture vapour can be a problem, but it is limited to about 20 μm (500 cm^{-1}) [30]. CaF₂ is the most commonly used material for the NIR, as it is both harder and less sensitive to moisture than KBr, but it cannot be used beyond approximately 8 μm (1200 cm^{-1}). In a simple Michelson interferometer, one beam passes twice through the beam splitter, but the other passes through only once [30]. To correct this, an additional compensator plate of equal thickness is incorporated. Most FIR beam splitters are based on polymer films and cover a limited wavelength range [30].

IR focal plane arrays (FPAs) have advanced greatly since the first 2D arrays were produced in the 1970s. An FPA is a kind of bolometer and is widely utilized as one of the thermal detectors in IR region. It consists of a series of small thin-film bolometers arranged in a matrix in the focal plane of the detector. This configuration creates a planar pixel sensor, which has an improved price–performance ratio for various applications [31].

Vanadium oxide and amorphous silicon alternative technologies are utilised as materials in thin-film bolometers. Detector sizes are 160×120 , 320×240 , and 640×480 pixels etc. In the past, pixels were generally $35 \times 35 \mu\text{m}^2$ in size; by contrast, pixel sizes of $25 \times 25 \mu\text{m}^2$, $17 \times 17 \mu\text{m}^2$, or even $12 \times 12 \mu\text{m}^2$ are available now [31].

These arrays continue to grow in size; 16-megapixel IR imagers are becoming extensively used, and FPAs with hundreds of millions of pixels are under development. HgCdTe is utilised as an IR detector material [31]. This material is advantageous because its band gap—which depends on the mercury/cadmium ratio—can be adjusted by more than one order of magnitude, from less than 0.1 eV to more than 1 eV [31]. A more exact expression of this ternary compound is $\text{Hg}_{1-x}\text{Cd}_x\text{Te}$, where 50% of the atoms are tellurium, and the rest are a mixture of mercury and cadmium (when $x = 1$, HgCdTe reduces to CdTe). The longest wavelength of light that can be monitored by a detector is inversely proportional to the band gap; HgCdTe is typically grown with cutoff wavelengths between 1.7 and 16.5 μm [31].

The detector material in the Hyperion spectrometer produced by Bruker Optik GmbH (Fig. 2.14) is the highest-quality indium antimonide (InSb) because of its high sensitivity and low noise.

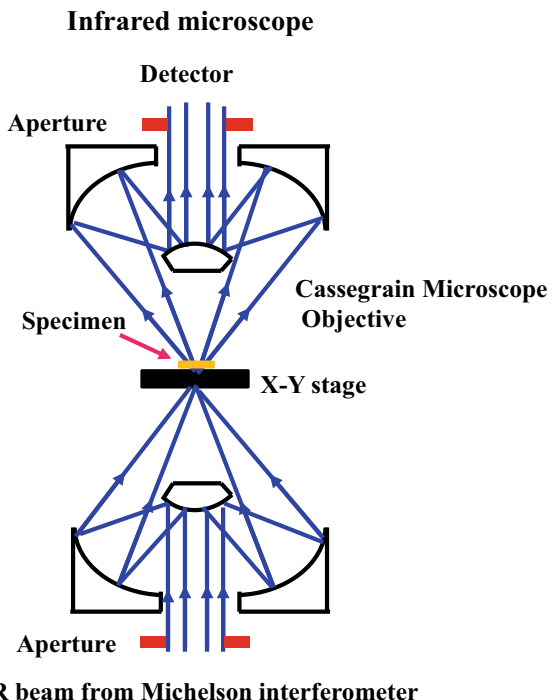


Fig. 2.14 Example of an FT-IR spectrometer with FPAs (Hyperion, Bruker Optik GmbH)

2.4.4 *Microscopy and Imaging*

An IR microscope can observe and obtain spectra from specimen regions with a size of $5 \mu\text{m}$, using a cassegrain objective lens in Fig. 2.15 [32]. Images can be generated by combining a microscope with linear or 2D array detectors. The spatial resolution can approach $5 \mu\text{m}$, if we use a 2D array detector with tens of thousands of pixels [32]. The images include a spectrum for each pixel and can be viewed as images depicting the intensity at any wavelength or combination of wavelengths. This makes it possible to observe the distribution of different chemical species within the specimen [32].

Fig. 2.15 Schematic diagram of a typical IR microscope [32]



References

1. Raman, C. V. (1928). A new radiation. *Indian Journal of Physics* 2.
2. Krishnan, K. S., & Raman, C. V. (1928). The negative absorption of radiation. *Nature*, 122, 12–13.
3. Smekal, A. (1923). Zur Quantentheorie der Dispersion. *Naturwissenschaften*, 11(43), 873–875.
4. Se non è vero, è molto ben trovato & Bruno, G. (2002). Classical theory of Rayleigh and Raman scattering. In D. A. Long (Ed.), *The Raman effect: A unified treatment of the theory of Raman scattering by molecules* (p. 31). Wiley Ltd.
5. Albrecht, A. C. (1961). On the theory of Raman intensities. *The Journal of Chemical Physics*, 34, 1476.
6. Czernuszewicz, R. S., & Zaczek, M. B. (2011). Resonance Raman spectroscopy. In Scott, R. A. (Ed.), *Encyclopedia of inorganic and bioinorganic chemistry*. Online © Wiley, Ltd.
7. Tang, J., & Albrecht, A. C. (1968). Studies in Raman intensity theory. *The Journal of Chemical Physics*, 49, 1144.
8. Loudon, R. (1964). The Raman effect in crystals. *Advances in Physics*, 13, 423.
9. Solin, S. A., & Ramdas, A. K. (1970). Raman spectrum of diamond. *Physical Review B*, 1, 1687.
10. Yoshikawa, M., Ishida, H., Ishitani, A., Murakami, T., Koizumi, S., & Inuzuka, T. (1990). Study of crystallographic orientations in the diamond film on cubic boron nitride using Raman microprobe. *Applied Physics Letters*, 57, 428.
11. Yoshikawa, M., Ishida, H., Ishitani, A., Koizumi, S., & Inuzuka, T. (1991). Study of crystallographic orientations in the diamond film on the (100) surface of cubic boron nitride using a Raman microprobe. *Applied Physics Letters*, 58, 1387.

12. Cerdaira, F., Buchenauer, C. J., I'ollak, F. H., & Cardona, M. (1972). Stress-induced shifts of first-order Raman frequencies of diamond- and zinc-blende-type semiconductors. *Physical Review B*, 5, 580.
13. Yoshikawa, M., Katagiri, G., Ishida, H., Ishitani, A., Ono, M., & Matsumura, K. (1989). Characterization of crystalline quality of diamond films by Raman spectroscopy. *Applied Physics Letters*, 55, 2608.
14. Harrick, N. J. (ed.). (1967). *Internal reflection spectroscopy*. Wiley Inc.
15. Hsu, C.-P. S. (1997). *Handbook of instrumental techniques for analytical chemistry* (p. 262). Prentice-Hall.
16. Kubelka, P., & Munk, F. (1931). Ein Beitrag zur Optik der Farbanstriche. *Zeitschrift für technische Physik*, 12(S), 593–601.
17. Fuller, M. P., & Griffiths, P. R. (1978). Diffuse reflectance measurements by infrared Fourier transform spectrometry. *Analytical Chemistry*, 50(13), 1906–1910. <https://doi.org/10.1021/ac50035a045.ISSN0003-2700>
18. Kortüm, G. (ed.). (1969). *Reflectance spectroscopy principles, methods, applications*. Springer. ISBN 9783642880711. OCLC 714802320.
19. Perkowitz, S. (Ed.). (1993). *Optical characterization of semiconductors*. Academic Press Limited.
20. https://www.newworldencyclopedia.org/entry/Diffraction_grating (Google 2021).
21. Born, M., & Wolf, E. (ed.). (1999). *Principles of optics: electromagnetic theory of propagation, interference and diffraction of light* (7th ed.). Cambridge University Press.
22. <https://underground.physics.berkeley.edu/JinPing/slides/Liu-HQEPMT.pdf> (Google 2022).
23. <https://www.princetoninstruments.com/products/sophia-cameras> (Google 2018).
24. <https://www.princetoninstruments.com/products/PyLoN-IR-InGaAs-camera> (Google 2018).
25. Griffiths, P., & de Hasseth, J. A. (ed.). (2007, 18 May). *Fourier transform infrared spectrometry* (2nd ed.). Wiley-Blackwell. ISBN 978-0-471-19404-0.
26. The Infracord double-beam spectrophotometer. *Clinical Science*, 16(2) (1957).
27. Agilent Technologies to Acquire Varian, Inc. for \$1.5 Billion. *Agilent*. July 27, 2009.
28. Peiponen, K.-E., Zeitler, J. A., & Kuwata-Gonokami, M. (Eds.). (2013). *Terahertz spectroscopy and imaging*. Springer.
29. Smith, D. R., Morgan, R. L., & Loewenstein, E. V. (1968). Comparison of the radiance of far-infrared sources. *Journal of the Optical Society of America*, 58(3), 433–434. <https://doi.org/10.1364/JOSA.58.000433>
30. Griffiths, P. R., & Holmes, C. (Eds.). (2002). *Handbook of vibrational spectroscopy* (Vol. 1). Wiley.
31. Wen, L., Jarek, A., & Lorenzo, F. (2015). Progress, challenges, and opportunities for HgCdTe infrared materials and detectors. *Physical Review Applied*, 2, 041303.
32. www.Bruker.com: please see “HYPERION Brochure”.

Chapter 3

Photoluminescence (PL) Spectroscopy



Photoluminescence (PL) spectroscopy is commonly used to characterise the opto-electronic properties of semiconductors and other materials [1]. It operates on the following principle [1]. When electrons are excited from the valence band to the conduction band of a semiconductor by a laser with an energy higher than the band-gap, the photoexcited carriers relax and then spontaneously recombine with holes in the conduction band [1]. In direct semiconductors, the excess energy is emitted in the form of light (spontaneous emission) [1]. By analysing the spectrum of the emitted light, it is possible to measure the semiconductor's response in terms of the intensity as a function of wavelength [1]. This measurement provides us with important information about the band structure, such as the band-gap width, relative light generation efficiency, quality of the material (inhomogeneous broadening), impurity, and about defect electronic states. PL spectroscopy systems are similar to Raman spectroscopy ones [1].

Table 3.1 shows a typical band-gap of semiconductors. Because PL spectroscopy uses a laser or a high-pressure mercury lamp as an excitation source, we can detect the PL from most semiconductors in addition to wide-gap semiconductors [2].

3.1 PL Imaging Technique

Figure 3.1 shows a typical PL imaging system, which employs a high-pressure mercury lamp as an excitation source. The light between 310 and 330 nm is focused on a specimen, often a wafer. The luminescence emitted by the specimen is collected by an objective lens, passed through a band-pass filter with a narrow bandwidth, and collected by a CCD detector. We can acquire a PL defect or band-gap image of a 2–8 in. wafer within a few seconds using a CCD detector. Further, we can obtain PL images of an 8 in. wafer with a high spatial resolution of less than 1 μm by scanning the wafer using an x – y stage.

Table 3.1 Typical bandgap of semiconductors [2]

Diamond type structure	Bandgap (eV)
Gerumanium (Ge)	0.7
Silicon (Si)	1.1
Diamond	5.5
<i>Zinc blende type structure</i>	
InN	0.53
GaAs	1.4
ZnSe	2.7
InP	1.35
GaP	2.26
3C-Silicon Carbide (c-SiC)	2.36
Cubic Boron Nitride (c-BN)	6.4
Cubic Garium Nitride (c-GaN)	3.22
<i>Wurtzite type strucure</i>	
InN	0.71
ZnO	3.37
GaN	3.39
<i>Hexiagonal (H) type structure</i>	
2H (hexiagonal)-SiC	3.30
4H-SiC	3.23
6H-SiC	3.00
15R-SiC (Rhombohedral)	2.99
AlN	6.20
h-BN	6.40

Figure 3.2 shows a PL image of a commercially available 3 in. 4H-polytype silicon carbide (4H-SiC) epitaxial wafer ($\sim 10 \mu\text{m}$ thick) measured using a high-pass filter ($>750 \text{ nm}$). A dark circle appears in the centre of the wafer. A comparison with a scanning capacitance microscope (SCM) image indicates that the dark circle has a higher carrier concentration than other areas.

Figure 3.3 shows a PL image of the same 4H-SiC epitaxial wafer measured using a band-pass filter at $417 \pm 30 \text{ nm}$ and a high-pass filter ($>750 \text{ nm}$). The PL peak, which is attributed to stacking faults (SFs), is observed at approximately 420 nm [3–5]. As shown in Fig. 3.3a, when the band-pass filter is used, we can observe a typical triangular SF in the commercial 4H-SiC epitaxial wafer in a short time, while the high-pass filter depicts only a triangular contour (Fig. 3.3b).

Figure 3.4 shows PL images at $\lambda > 325 \text{ nm}$ of a 4H-SiC epitaxial wafer ($\sim 10 \mu\text{m}$ thick) measured by the imaging system. Two types of defects appear in areas 1–2 on the wafer: triangular defects in area 1 (Fig. 3.4a), and linear defects in area 2 (Fig. 3.4b).

Fig. 3.1 Schematic diagram of PL imaging system

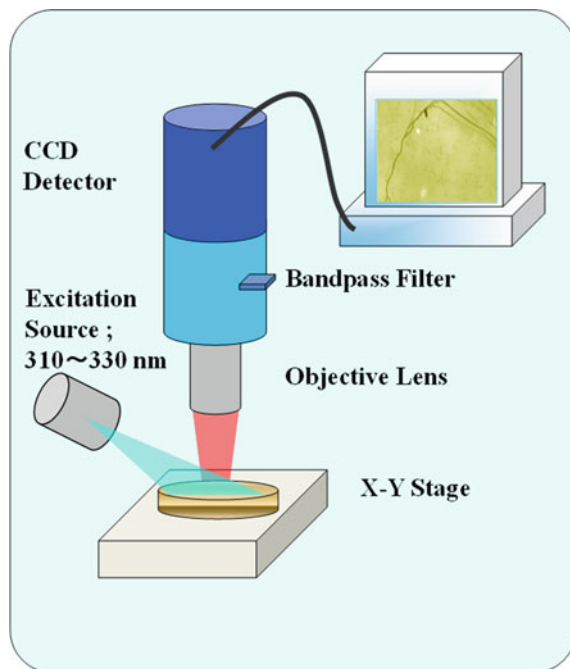
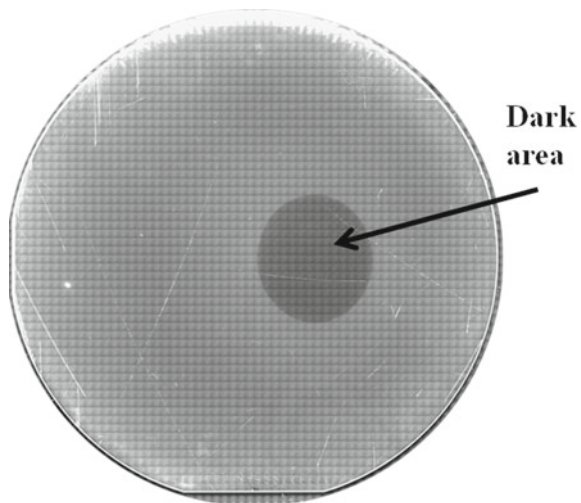


Fig. 3.2 PL image of commercially available 3 in. 4H-SiC epitaxial wafer measured using a high-pass filter (>750 nm)



To clarify the origin of the defects, the triangular defects in area 1 were observed using transmission electron microscopy (TEM). Figure 3.5a–c show a PL image, a magnified PL image, and a cross-sectional TEM image of area 1, respectively. As shown in Fig. 3.5c, area 1 contains an 8H-SiC polytype structure within the 4H-SiC

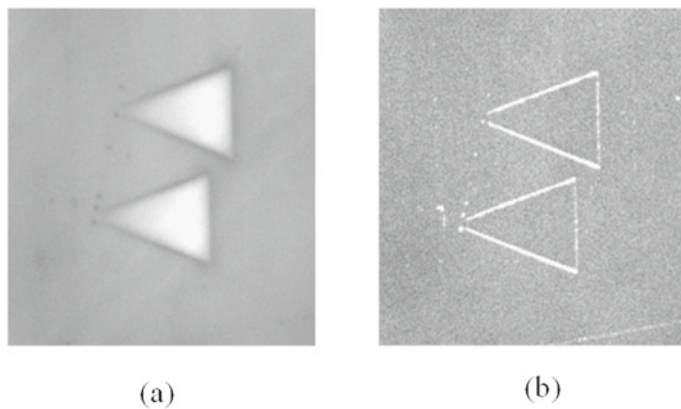


Fig. 3.3 PL images of commercially available 3 in. 4H-SiC epitaxial wafer obtained using **a** a band-pass filter at $417 \pm 30 \text{ nm}$ and **b** a high-pass filter ($>750 \text{ nm}$)

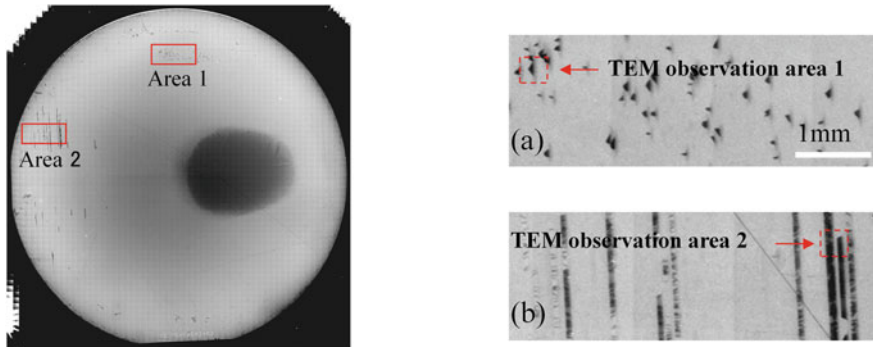


Fig. 3.4 PL images ($\lambda > 325 \text{ nm}$) of areas 1–2 on a 4H-SiC epitaxial wafer ($\sim 10 \mu\text{m}$ thick) measured by the imaging system

structures. Because it is similar to the triangular PL patterns reported in [3, 4], area 1 is considered to consist of in-grown Frank-type SFs containing 8H-SiC polytype structure.

The linear defects in area 2 were also observed by TEM. Figure 3.6a–c show a PL image at $\lambda > 325 \text{ nm}$, and plane-view and cross-sectional TEM images, respectively of area 2. As shown in Fig. 3.6c, area 2 contains 3C-SiC structure within the 4H-SiC structures. Furthermore, the PL pattern in Fig. 3.6a agrees well with that in [6]. This similarity indicates that area 2 consists of single Shockley SFs containing 3H-SiC polytype structure. The PL peak assigned to the single Shockley SFs is observed at 425 nm at room temperature [7].

PL imaging is a very powerful technique for quickly distinguishing many types of defects in 4H-SiC epitaxial wafers [8].

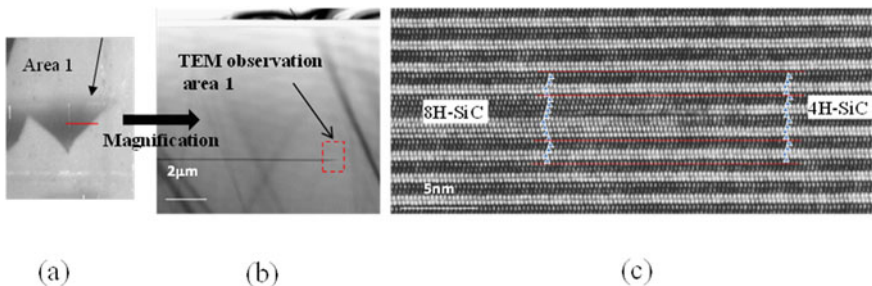


Fig. 3.5 Images of area 1: **a** PL image at $\lambda > 325$ nm, **b** magnification of **a**, and **c** cross-sectional TEM image

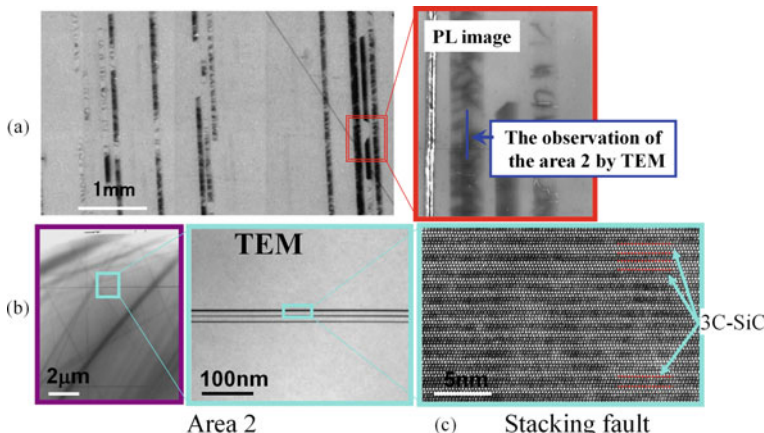


Fig. 3.6 **a** PL image at $\lambda > 325$ nm and **b** plane-view and **c** cross-sectional TEM images of area 2

References

1. Perkowitz, S. Ed. (1993). *Optical characterization of semiconductors*. University Printing House, Cambridge: Academic Press.
2. Adachi, S. Ed. (1999). *Optical constants of crystalline and amorphous semiconductors—numerical data and graphical information*. Massachusetts: Kluwer Academic Publishers.
3. Sridhara, S. G., Carlsson, F. H. C., Bergman, J. P., & Janzén, E. (2001). Luminescence from stacking faults in 4H SiC. *Applied Physics Letters*, 79, 3944.
4. Sugie, R., Yoshikawa, M., Harada, S., & Namikawa, Y. (2009). Expansion of stacking faults by electron-beam irradiation in 4H-SiC diode structure. *Materials Science Forum*, 600–603, 353–356.
5. Feng, G., Suda, J., & Kimoto, T. (2008). Characterization of stacking faults in 4H-SiC epilayers by room-temperature microphotoluminescence mapping. *Applied Physics Letters*, 92, 221906.
6. Hassan, J., & Bergman, J. P. (2010). Single Shockley stacking faults in as-grown 4H-SiC epilayers. *Materials Science Forum*, 645–648, 327–330.

7. Maeda, K., Murata, K., Tawara, T., Kamata, I., & Tsuchida, H. (2019). Suppressed expansion of single Shockley stacking faults at narrow widths in 4H-SiC. *Applied Physics Express*, *12*, 124002.
8. Kimoto, T. (2015). Material science and device physics in SiC technology for high-voltage power devices. *Journal of Applied Physics*, *54*, 040103.

Chapter 4

Overview of Cathodoluminescence (CL) Spectroscopy



4.1 Introduction

Luminescence in semiconductors occurs when an electron in the conduction band recombines with a hole in the valence band. The excess energy of this transition can be emitted in the form of a photon. The energy of the photon and the probability that a photon (not a phonon) will be emitted depends on the material, its purity, and the presence of defects. First, the electron has to be excited from the valence band into the conduction band.

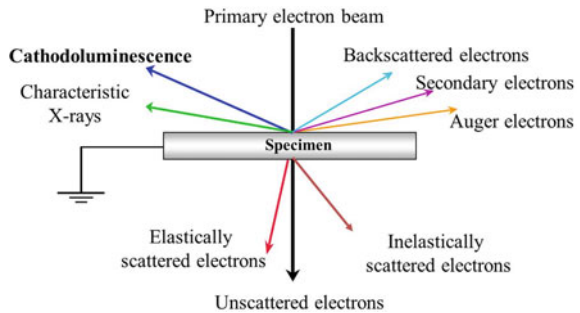
In cathodoluminescence (CL), this occurs as the result of colliding a high-energy electron beam onto a semiconductor. However, these primary electrons carry far too much energy to directly excite electrons. Instead, the inelastic scattering of the primary electrons in the crystal leads to the emission of secondary electrons (SEs), Auger electrons, and X-rays. Such a cascade of scattering events leads to the formation of up to 10^3 SEs per incident electron. These SEs can excite valence electrons into the conduction band when they have a kinetic energy of approximately three times the band-gap energy of the material [1]. The excess energy is transferred to phonons and, thus, heats the lattice. CL is one of the various processes that are created during the irradiation of a solid surface with an electron beam (Fig. 4.1).

CL spectroscopy has the following specific features:

- (i) One of the advantages of excitation with an electron beam is that the band-gap energy of materials that are investigated is not limited by the energy of the incident light, as in the case of photoluminescence (PL).
- (ii) High spatial resolution of less than 100 nm.
- (iii) Non-destructive technique.
- (iv) Penetration depth of sub-nm–μm, which is shallower than that of PL spectroscopy.

These advanced techniques are also useful for examining low-dimensional semiconductor structures, such as quantum wells (QWs) and quantum dots (QDs).

Fig. 4.1 Various interactions of a specimen surface by the irradiation of primary electron beam



4.2 Principle of CL Spectroscopy

The incident electrons are elastically or inelastically scattered by the specimen and spread in a certain volume. Elastic scattering only deflects an electron in a certain direction but does not modify its energy. On the other hand, inelastic scattering does not change the direction but transfers energy to the specimen and eventually reduces its energy to zero.

The irradiation of the electron beam generates electron–hole pairs in the range of the electron penetration, R_e .

The electron penetration, R_e , is defined as follows

$$R_e(\text{mm}) = (2.76 \times 10^{-2} A/rZ^{0.889})E^{1.67} \quad (4.1)$$

where A is the atomic weight in g/mol, ρ is the density in g/cm³, Z is the atomic number, and E is the acceleration voltage in keV [2]. These electron–hole pairs then diffuse into a crystal. Although the diffusion of the electron–hole pairs decreases the spatial resolution in CL spectroscopy, we can obtain spatial resolution at the sub-micrometre level by decreasing the acceleration voltage. The electrons may spread in a certain volume, which is illustrated by Monte Carlo simulations [3]. Figure 4.2 shows the trajectories of 4, 10, and 15 kV electrons in a GaAs wafer. The trajectories of 10 and 2 kV electrons in an Si wafer are shown in Fig. 7.2 in [4].

4.3 Instrumentations

4.3.1 Excitation Source

CL spectroscopy employs scanning electron microscopy (SEM) as an excitation source. SEM uses a focused beam of high-energy electrons to generate a variety of signals on the surface of solid specimens. The signals derived from electron–specimen interactions reveal information about the specimen, including the external

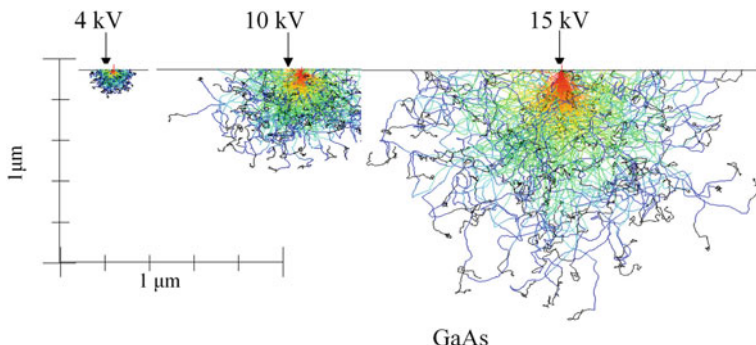


Fig. 4.2 Trajectories of 4, 10 and, 15 kV electrons in GaAs by Monte Carlo simulations

morphology (texture), chemical composition, crystalline structure, and orientation of materials constituting the specimen. In most applications, data are collected over a selected area of the surface of the specimen. Areas ranging from approximately 1 cm to 5 μm in width can be imaged in scanning mode using conventional SEM techniques (magnification ranging from 20-fold to approximately 30,000-fold and a spatial resolution of 100 nm).

SEM is also capable of performing analyses of selected point locations on the specimen. This approach is especially useful in qualitatively or semi-quantitatively determining chemical compositions using energy-dispersive X-ray spectrometry (EDS), crystalline structure, and crystal orientation using electron backscatter diffraction (EBSD). The design and function of the SEM are similar to the electron probe micro-analyser (EPMA), and considerable overlap in capabilities exists between the two instruments.

Figure 4.3 shows a photograph of SEM produced by JEOL. A typical SEM instrument consists of the electron column, specimen chamber, EDS detector, electronics console, and visual display monitors. Essential components of all SEMs contain the following:

- (1) Electron source (“Gun”)
- (2) Electron lenses
- (3) Specimen stage
- (4) Detectors for all signals of interest
- (5) Display/Data output devices
- (6) Infrastructure requirements:

power supply, vacuum system, cooling system, vibration-free floor, room free of ambient magnetic and electric fields etc.

SEMs always have at least one detector (usually a secondary electron detector), and most have additional detectors. The specific capabilities of a particular instrument are critically dependent on which detector it accommodates.



Fig. 4.3 Photograph of typical SEM (by courtesy of JEOL)

A field-emission (FE) gun is based on the emission of electrons from the surface of a sharply pointed tungsten tip. The field emission is induced by applying a voltage between the tip and a metal anode.

High brightness is made by the gun that consists of two electrodes: the first electrode contains the extraction voltage, and the second one contains the final accelerating voltage, required for the electron gun. There are two types of field-emission guns. Table 4.1 summarises the properties of their common elements [1].

In SEM, the spatial resolution is on the order of a few tens of nanometres, while in a scanning transmission electron microscope (STEM), nanometre-sized features can be resolved. Additionally, it is possible to conduct nanosecond- to picosecond-level time-resolved measurements if the electron beam can be chopped into nano- or picosecond pulses by a beam-blanker [5] or by photocathode plate with a pulsed electron source [6]. These advanced techniques are useful for examining low-dimensional semiconductor structures, such as quantum wells and quantum dots in Sect. 7.5 [6].

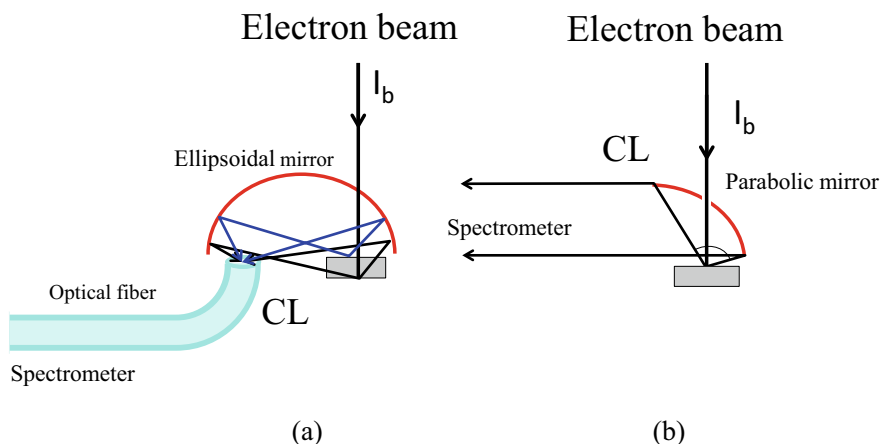
Table 4.1 The properties of several electron tips

	Units	Field emission (Schottky)	Field emission (cold)	LaB ₆	Tungsten
Cathode material	–	ZrO/W(100)	W(310)	LaB ₆	W
Minimum probe size	nm	1.8	1.8	3	4.5
Magnification		≤500,000	≤500,000	≤100,000	≤20,000
Brightness	A/cm ² sr (at 20 kV)	2×10^7 – 2×10^8	5×10^8	5×10^6	5×10^5
Energy spread	eV	0.3–1.0	0.2–0.3	2	4
Total emission current	μA	5–100	1–20	50	50
Max. probe current	nA	1–10	0.1	0.1	0.1
Drift		≤1%/h	≤5%/h	≤1%/h	≤1%/h

4.3.2 Optical System

Because the CL signal is often weak owing to the small excitation volume, it is necessary to design a light detection system with high efficiency for CL measurements. Several optical settings have been demonstrated in [1]. Ellipsoidal and parabolic mirrors are used to collect the CL light emitted from the specimen. The schematic diagram of ellipsoidal and parabolic mirrors is illustrated in Fig. 4.4.

An ellipsoidal mirror can transfer the light emitted from one focal point to another. The light is focused on the detector or on the slit of a monochromator. This system is

**Fig. 4.4** Schematic of **a** ellipsoidal and **b** parabolic mirror system for SEM-CL

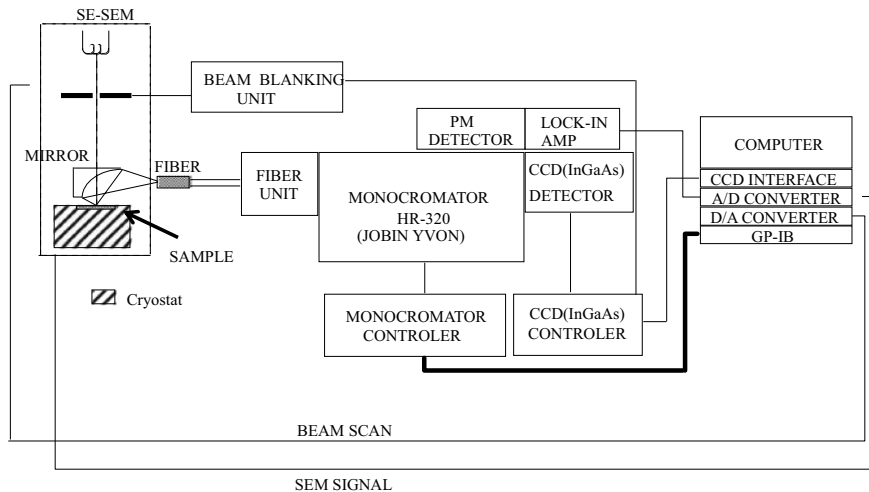


Fig. 4.5 Schematic of our optical system for SEM-CL

suitable for direct coupling or a fibre transfer system. A parabolic mirror can transfer the light from a focal point to a parallel light travelling along an axis. This setting is the standard for an optical light detection system.

When operating in low magnification, the electron beam may deviate from the focal point. The light from the off-focal point may be focused on the corresponding point near another focal point in the ellipsoidal mirror. The distance from the focal point is enlarged owing to the magnification of the mirror. Thus, this magnification of the optical system should be small.

Figure 4.5 shows the schematic of our SEM-CL system, which includes an ellipsoidal mirror and an optical fibre. We used the SEM equipped with the Schottky-emission (SE)-type gun as the excitation source for the CL measurement. An electron beam with a diameter of less than 5 nm was focused on the specimen through the aperture of the ellipsoidal mirror, and the CL emitted from the specimen was collected with the ellipsoidal mirror and focused on the inlet of an optical fibre. All CL spectra were measured using a single monochromator with a focal length of 0.32 m and a 2048-channel UV-coated CCD detector.

4.3.3 Detector

Detectors in CL Spectroscopy are almost the same as those in Raman spectroscopy. Please refer to Sect. 2.3.4 Detector.

4.3.4 Cryostat

Low-temperature measurements are also essential in CL study. In the case of the semiconductor crystal, the CL signal at low temperature tends to increase by at least over 100 times than the signal at less than 10 K and becomes sharp due to the suppression of thermal broadening, so that the identification of emission peaks becomes easy, and more information becomes available at low temperatures. Moreover, the suppression of non-radiative recombination may result in a significant increase in the CL signal. The specimen cooling is usually realised by a liquid helium (He) flow unit. A simple He flow system has several advantages: it can cool the specimen down to 10 K and suppress the extra vibration of an artificial cooling unit. In any case, the cooling system should be designed to avoid the specimen drift due to the thermal shrinkage of the stage.

Figure 4.6 shows a typical schematic of the He cooling cryostat setup, which is based on the Oxford Instruments CL302 light collector. The collected light is guided by free optics to a monochromator and detected by a photomultiplier.

Jahn et al. measured the temperature dependence of the CL intensity originating from GaAs-Al_{0.3}Ga_{0.7}As multiple QWs between 5 and 300 K [7]. They found that the CL intensity at 10 K was two orders of magnitude larger than that at room temperature. Furthermore, Xu et al. measured the temperature dependence of CL spectra on *n*-GaN grown on an Si (111) substrate, patterned by deep etching in the temperature range of 6–280 K [8]. The temperature dependence of the peak energy of a free exciton (FXA) and its 1LO and 2LO phonon replicas were observed. The stress distribution from corner to centre in the patterned mesa area at the low temperature of 10 K was estimated by the FXA energy, using a line scanning measurement of the CL spectra [8]. They indicated that the tensile stress reached a maximum at a

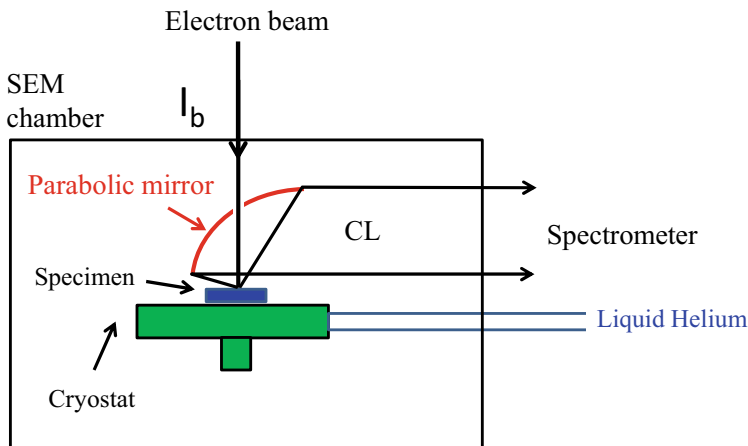


Fig. 4.6 Typical schematic of the He cooling cryostat setup

point far from the mesa edge at approximately 0.6 GPa and relaxed to 0.1 GPa at the corner [8].

4.3.5 Comparison of CL and Scanning Near-Field Optical Microscopy (SNOM)-PL Spectroscopy

GaN has been thoroughly studied and is commonly used for the fabrication of optoelectronic devices, such as ultraviolet, blue, and green light-emitting diodes (LEDs) and blue laser diodes (LDs) [9–11]. GaN is mainly prepared on sapphire substrates because of their low cost. The lattice mismatch between sapphire and GaN results in high threading dislocation (TD) densities in the material. The electrical properties of these devices are largely depending on the defects. These defects determine the reliability and durability of LEDs and LDs. It is important to study the defect distribution of GaN with a spatial resolution at the nanometre level because the distance between TDs is at this level.

For many years, TDs in GaN have been observed by transmission electron microscopy (TEM) [12, 13], atomic force microscopy (AFM)[13], scanning tunnelling microscopy (STM) [14], and CL spectroscopy [12–14]. However, there have been few reports on the defect distribution of GaN, using a SNOM-PL spectroscopic approach because of the following problems [15]:

- (1) Disturbance of the luminescence signal of GaN by the strong self-luminescence emitted from the SNOM-probe made of silicon dioxide
- (2) Low transmittance of the SNOM-probe (10^{-3})
- (3) Weakness of the near-field Raman signal because the optical penetration depth (OPD) of the near-field light is less than 100 nm

We have developed a SNOM-PL apparatus with the following specific features to overcome these problems [15]:

- (1) Adaptation of a SNOM-probe made of material with lower self-luminescence
- (2) Adaptation of a SNOM-probe with a high transmittance of 10^{-2}
- (3) Adaptation of an ultraviolet (UV) laser with an optical penetration depth of 100 nm

In the case of GaN, the direct band-gap at the Γ point is approximately 3.4 eV (~363.8 nm) [16]. The OPD becomes very shallow when the excitation energy is close to the electronic transition energy of materials. We measured the real and imaginary parts of the refractive index of Si-doped GaN by spectroscopic ellipsometry and calculated the OPD of the Si-doped GaN from $1/2\alpha$ [17], using the optical absorption coefficient (α). Indeed, the OPD of GaN at the excitation wavelength of 363.8 nm was estimated to be approximately 100 nm.

On the other hand, CL spectroscopy is an optical and electromagnetic phenomenon in which electrons impact a luminescent material such as a phosphor. It offers a higher spatial resolution than PL spectroscopy [1, 18, 19]. Irradiation by

an electron beam generates electron–hole pairs in the portion of the material that the electrons can penetrate: $\text{Re} (\mu\text{m}) = (2.76 \times 10^{-2} A/\rho Z^{0.889}) E^{1.67}$, given by Eq. (4.1). These electron–hole pairs then diffuse into a material [19]. This diffusion of the electron–hole pairs (EHPs) reduces the spatial resolution in CL spectroscopy. Recently, Schottky-emission scanning electron microscopy (SE-SEM), which uses a high electron beam current at a low acceleration voltage, has been developed. SE-SEM-CL spectroscopy offers a high spatial resolution of less than 100 nm [19]. In the case of dielectric materials such as GaN, its use enabled us to neglect the diffusion of the EHPs, and the spatial resolution of CL spectroscopy is less than 50 nm [19].

We developed a SNOM-PL apparatus with a pyramidal probe, using a UV Ar⁺ laser, and we measured the near-field PL (NFP) spectra of GaN. Detailed experimental conditions are written in [19]. The schematic diagram of SNOM-PL apparatus is shown in Fig. 4.7. We adopted a feedback system that detects the signal produced by a change in the amplitude of vibration of a micro-tuning fork [20, 21] mounted by a cantilever. A commercially available SNOM-probe with an aperture of 100 nm was used for our NFP measurement. The laser beam was focused on the aperture of the probe by a UV objective lens with a numerical aperture (N.A.) = 0.5 at a power of less than 1 mW, and the NFP was collected by the same objective lens through the aperture of the SNOM-probe. The NFP spectra were measured using a UV Raman microprobe [15]. The 363.8 nm line of a UV Ar⁺ laser was used as an excitation source.

Figure 4.8 shows the NFP spectra of GaN, measured by the SNOM-probe with a diameter of 100 nm. The NFP spectrum assigned to the band-to-band transition was observed near 3.4 eV (362 nm) at room temperature [16]. The NFP spectrum was very broad. For this reason, we used the UV Raman microprobe with a focal length of 1 m for the near-field PL measurement. We could detect the NFP signal of GaN only when the incident light was focused on the aperture of the SNOM-probe by the UV objective lens [15].

Figure 4.9a, b show the peak-intensity images of GaN at approximately 362 nm, measured without and with the SNOM-probe, respectively. The peak-intensity of each of the observed spectra was plotted as a function of the measured point [15]. Some dark spots (DSs) are observed in Fig. 4.9b, although there are no DSs in Fig. 4.9a. DSs with an average period of 100–300 nm are found to be spatially well resolved in Fig. 4.9b [15]. Irradiation by the UV laser beam generates EHPs in the Si-doped GaN film. The EHPs then diffuse into the film. The generation area of EHPs in Fig. 4.9b is less than that in Fig. 4.9a, and the diffusion length of these in Fig. 4.9b is shorter than that in Fig. 4.9a because of the excitation of the near-field incident light and of the collection of NFP. This is considered to induce improvements to the spatial resolution in Fig. 4.9b [15].

Figure 4.10a, b show the peak-intensity image at 362 nm in the Si-doped GaN film and the CL spectra at bright and dark spots, measured by CL spectroscopy, respectively [15]. Some DSs with an average period of 100–300 nm are observed in Fig. 4.10a, although the SEM image showed no change in morphology. CL spectra at bright and dark spots are shown in Fig. 4.10b [15]. The CL peaks at approximately 362 and 580 nm are ascribed to band-edge emission (BEE) and defect-related broad

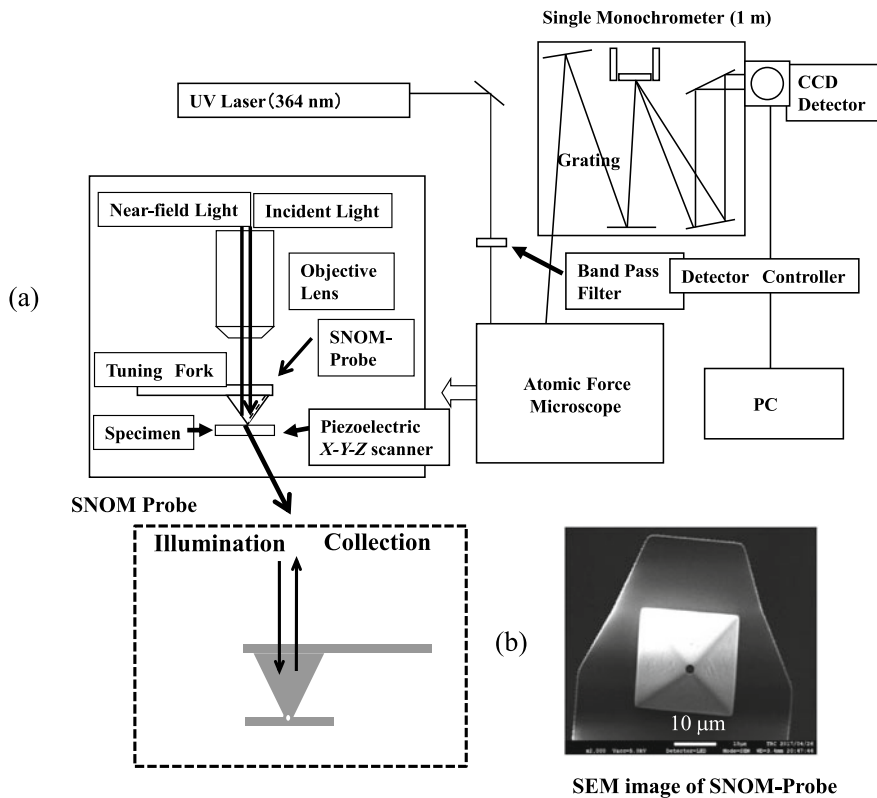
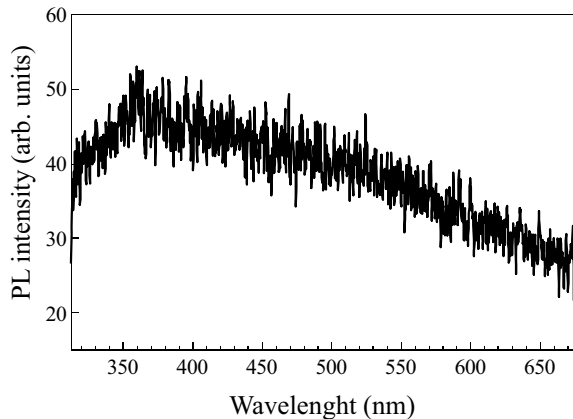


Fig. 4.7 Schematic diagram of SNOM-PL apparatus; **a** block diagram, and **b** SEM image of the SNOM-probe [15]

Fig. 4.8 NFP spectra of Si-doped GaN film, measured by the SNOM-probe with a diameter of 100 nm [15] (Reproduced with permission from [15]. ©AIP Publishing, 2006)



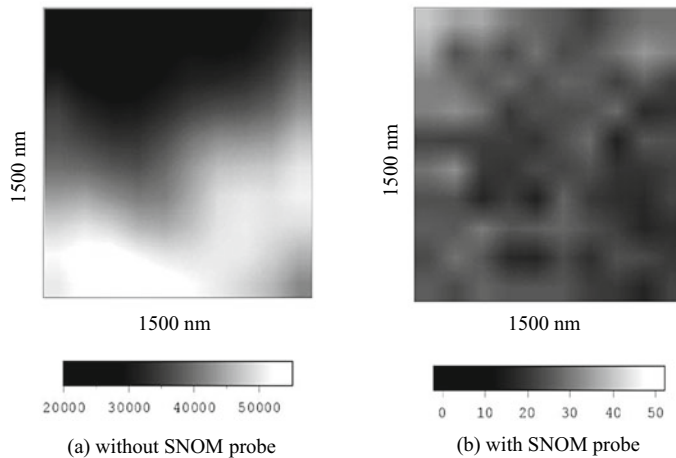


Fig. 4.9 The peak-intensity images in Si-doped GaN film at 362 nm; **a** the image without the SNOM-probe and **b** the image with the SNOM-probe, with a diameter of 100 nm [15] (Reproduced with permission from [15]. ©AIP Publishing, 2006)

luminescence, well known as YL, respectively [16, 22–24]. Beyond the Monte Carlo simulation [18], CL spectroscopy is thought to have the spatial resolution of at least 100 nm, as the DSs spatially separated by a distance of approximately 100 nm are clearly differentiated in Fig. 4.10a.

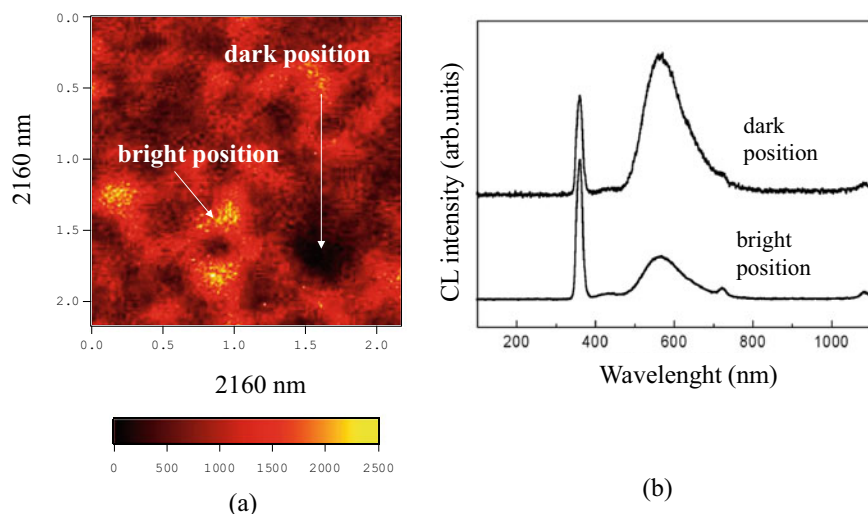


Fig. 4.10 **a** The peak-intensity image at 362 nm in Si-doped GaN film and **b** CL spectra at bright and dark spots [15] (Reproduced with permission from [15]. ©AIP Publishing, 2006)

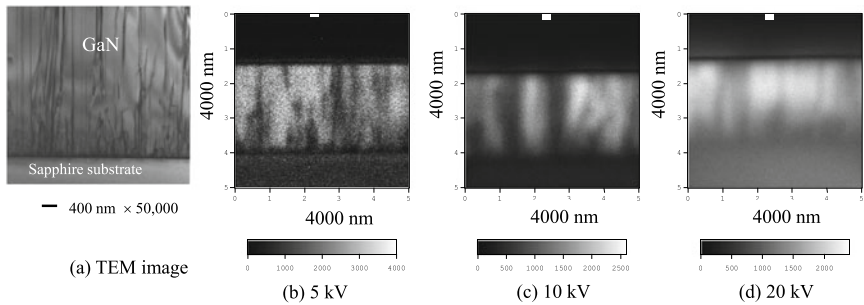


Fig. 4.11 **a** Cross-sectional TEM image of Si-doped GaN film and the peak-intensity image at 362 nm with acceleration voltages of **b** 5, **c** 10, and **d** 20 kV [15]

Figure 4.11a, b show cross-section TEM images of the Si-doped GaN film and the cross-sectional images of the 362 nm CL peak-intensity at various acceleration voltages, measured by CL spectroscopy. The CL intensity image becomes clear as the acceleration voltage decreases from 20 to 5 kV. Many TDs can be observed in the TEM image of Fig. 4.11a [15]. From the comparison of Fig. 4.11a, b, it was found that dark lines corresponding to the TDs are clearly observed in Fig. 4.11b. This indicates that the TDs in GaN films act as non-radiative recombination centres (NRRCs) [15]. Rosner et al. measured plane-view AFM and CL images of epitaxial GaN films and found that the TDs act as NRRCs in GaN films [14]. Their result coincides well with our result [14].

We measured all spectra of the imaging area of $5000 \times 5000 \text{ nm}^2$, scanning the electron beam in a step of 100 nm [22]. We obtained images of the peak-intensity in the BEE ($\lambda = 362 \text{ nm}$) and in YL at 580 nm in the Si-doped GaN film by fitting Gaussian lineshapes to the observed spectra, and we found that the peak-intensity image in the BEE agrees with that in YL. This means that the TDs act as NRRCs not only for the BEE but also for YL.

References

- Yacobi, R. G., & Holt, D. B. (Eds.). (1990). *Cathodoluminescence microscopy of inorganic solids*. Plenum Press.
- Kanaya, K., & Okayama, S. (1972). Penetration and energy-loss theory of electrons in solid targets. *Journal of Physics D*, 5, 43.
- Casino. <http://www.gel.usherbrooke.ca/casino/What.html>.
- Sekiguchi, T., & Chen, J. (2015). Defect characterization in silicon by electron-beam-induced current and cathodoluminescence techniques. In Y. Yoshida & G. Langouche (Eds.), *Defects and impurities in silicon materials*. Japan: Springer Japan.
- Moerland, R. J., Weppelman, I. G. C., Germing, M. W. H., Kruit, P., & Hoogenboom, J. G. (2016). Time-resolved cathodoluminescence microscopy with sub-nanosecond beam blanking for direct evaluation of the local density of states. *Optics Express*, 24(21), 24763.

6. Merano, M., Sonderegger, S., Crottini, A., Collin, S., Renucci, P., Pelucchi, E., Malko, A., Baier, M. H., Kapon, E., Deveaud, B., & Ganière, J.-D. (2005). Probing carrier dynamics in nanostructures by picosecond cathodoluminescence. *Nature Letter*, 438, 479.
7. Jahn, U., Menniger, J., Hey, R., & Grahn, H. T. (1994). Temperature dependence of cathodoluminescence from thin GaAs-AlGaAs multiple quantum wells. *Applied Physics Letters*, 64, 2382–2384.
8. Xu, J., Chen, L., & Lisheng, Y. (2007). Temperature dependence of cathodoluminescence spectra and stress analysis of a GaN layer grown on a mesa structured Si substrate. *Journal of Applied Physics*, 102, 104508.
9. Nakamura, S., Mukai, T., & Senoh, M. (1994). High-brightness InGaN/AlGaN double-heterostructure blue-green-light-emitting diodes. *Journal of Applied Physics*, 76, 8189.
10. Nakamura, S., Senoh, M., Iwasa, N., & Nagahama, S. (1995). High-brightness InGaN blue, green and yellow light-emitting diodes with quantum well structures. *Japanese Journal of Applied Physics*, 34, 794.
11. Nakamura, S., Senoh, M., Iwasa, N., Nagahama, S., Yamada, T., & Mukai, T. (1995). Super-bright green InGaN single-quantum-well-structure light-emitting diodes. *Japanese Journal of Applied Physics*, 34, 1332.
12. Sugahara, T., Sato, H., Hao, M., Naoi, Y., Kurai, S., Tottori, S., Yamashita, K., Nishino, K., Romano, L. T., & Sakai, S. (1998). Direct evidence that dislocations are non-radiative recombination centers in GaN. *Japanese Journal of Applied Physics*, 37, L398.
13. Evoy, S., Craighead, H. G., Keller, S., Mishra, U. K., & DenBaars, S. P. (1999). Scanning tunneling microscope-induced luminescence of GaN at threading dislocations. *Journal of Vacuum Science and Technology B*, 17, 29.
14. Rosner, S. J., Carr, E. C., Ludowise, M. J., Girolami, G., & Erikson, H. I. (1997). Correlation of cathodoluminescence inhomogeneity with microstructural defects in epitaxial GaN grown by metalorganic chemical-vapor deposition. *Applied Physics Letters*, 70, 420.
15. Yoshikawa, M., Sugie, R., Murakami, M., Matsunobe, T., Matsuda, K., & Ishida, H. (2006). Defect characterization of Si-doped GaN films by a scanning near-field optical microscope-induced photoluminescence. *Applied Physics Letters*, 88, 161905.
16. Yoshikawa, M., Kunzer, M., Wagner, J., Obloh, H., Schlotter, P., Schmidt, R., Herres, N., & Kaufmann, U. (1999). Band-gap renormalization and band filling in Si-doped GaN films studied by photoluminescence spectroscopy. *Journal of Applied Physics*, 86, 4400.
17. Holts, M., Duncan, W. M., Zollner, S., & Lie, R. (1999). Visible and ultraviolet Raman scattering studies of $\text{Si}_{1-x}\text{Ge}_x$ alloys. *Journal of Applied Physics*, 88, 2523.
18. Yoshikawa, M., Matsuda, K., Yamaguchi, Y., Matsunobe, T., Nagasawa, Y., Fjino, H., & Yamane, T. (2002). Characterization of silicon dioxide film by high spatial resolution cathodoluminescence spectroscopy. *Journal of Applied Physics*, 92, 7153.
19. Yoshikawa, M., Iwagami, K., & Ishida, H. (1998). Characterization of silicon dioxide film by high spatial resolution cathodoluminescence spectroscopy. *Journal of Applied Physics*, 51, 1693.
20. Karrai, K., & Grober, R. D. (1995). Piezoelectric tip-sample distance control for near field optical microscopes. *Applied Physics Letters*, 66, 1842.
21. Davydov, D. N., Shelimov, K. B., Haslett, T. L., & Moskovits, M. (1999). A near-field scanning optical microscope with a high Q -factor piezoelectric sensing element. *Applied Physics Letters*, 75, 1796.
22. Sugie, R., Yoshikawa, M., & Harima, H. (2003). Characterization of threading dislocation in Si-doped GaN films by high spatial resolution cathodoluminescence spectroscopy. In *International Conference on Solid State Devices and Materials*. Tokyo.
23. Calleja, E., Sanchez, F. J., Basak, D., Sanchez-Garcia, M. A., Munoz, E., Izpura, I., Calle, F., Tijero, J. M. G., Sanchez-Rojas, J. L., Beaumont, B., Lorenzini, P., & Gibart, P. (1997). Yellow luminescence and related deep states in undoped GaN. *Physical Review B*, 55, 4689.
24. Schubert, E. F., Goepfert, I. D., & Redwing, J. M. (1997). Evidence of compensating centers as origin of yellow luminescence in GaN. *Applied Physics Letters*, 71, 3224.

Chapter 5

Applications of Raman, IR, and CL Spectroscopy



5.1 Silicon and Silicon Dioxide (SiO_2)

5.1.1 Silicon

Silicon crystals show characteristic luminescence due to the dislocations observed by Dorozdov et al. [1, 2]. The dislocations are composed of 4 lines labelled by D1, D2, D3, and D4, whose peaks are located at 0.812, 0.875, 0.934, and 1.000 eV, respectively. This suggests that dislocations are related to some deep levels that act as radiative recombination centres (RRCs). Higgs et al. [3] measured CL images of slip lines in a plastically deformed specimen and found that the D3 and D4 lines were strong along slip lines, whereas the D1 and D2 lines were dominant in the regions between the slip lines. They ascribed the D1 and D2 lines to impurities incorporated in the dislocation core.

Sekiguchi and Sumino [4] measured CL spectra from a P-doped Si crystal with a resistivity of $0.4 \Omega \text{ cm}$, grown by the float-zone (FZ) method. They observed the peaks at 0.81, 0.88, 0.93, and 1.00 eV originated from D1, D2, D3, and D4 emissions, respectively. The peak at 1.09 eV is assigned to the transverse optical phonon (TO) replica of excitonic luminescence (EX(TO)) [4, 5]. CL spectrum of lightly deformed Si agrees well with that of PL, although the peaks are not so sharp. The lightly deformed Si generates only EX(TO). Because the PL and CL intensities of Si are rather weak, it has been difficult to directly detect D-line emission from individual dislocations until now [4].

Sauer et al. studied dislocated-related PL in Si under the temperature of 420–650 °C and the stress of 19–196 MPa in more detail. Usual deformation conditions of high temperature (approximately 650 °C) and low stress of approximately 30 MPa yielded sharp spectra of the D1 through D4 lines [6]. Further, they found that new lines D5 and D6 appeared for pre-deformation as above and subsequent low-temperature, high-stress deformation, in addition to another new sharp line of D12.

We measured CL spectra of Si wafers implanted at various fluences of 2×10^{10} to 2×10^{14} B ions/cm² at 80 keV. Figure 5.1 indicates the CL spectra of the B-ion-implanted Si wafer with a fluence of 2×10^{10} at a low temperature of 30 K. Based on Table 5.1, the weak D1 and strong D6 peaks observed at 1570 nm (0.79 eV) and 1224 nm (1.02 eV) were ascribed to geometrical kinks of dislocations, and stacking faults in Si, respectively. Sauer et al. assigned the D6 peak at 1224 nm to stacking faults [5, 6]. Our assignment agrees well with that of Sauer et al. [5, 6]

Figure 5.2 shows CL spectra of an Si wafer implanted at 80 keV with a fluence of 2×10^{10} to 2×10^{14} B ions/cm², measured at 30 K. The line labelled ‘I_{TO}’ at 1.02 eV (1230 nm) is the band-edge emission followed by a transverse optic (TO) phonon emission. As seen in Fig. 5.2, the relative D6 intensity normalised by the CL peak intensity (I_{TO}) increases with an increase in the ion implantation. This result suggests that the dislocations originating from stacking faults increase into the B-ion-implanted Si wafer in the order of 2×10^{10} to 2×10^{14} B ions/cm².

Figure 5.3 shows the TEM images of Si_{0.9}Ge_{0.1}, Si_{0.8}Ge_{0.2}, and Si_{0.7}Ge_{0.3} films, grown epitaxially on a Si substrate. As can be seen in Fig. 5.3, dislocations (dark lines) tend to increase as the Ge content increases and grow complexed dislocations at the interface of the SiGe film and Si substrate in Fig. 5.3c.

Fig. 5.1 The CL spectrum of a B-ion-implanted Si wafer with a fluence of 2×10^{10} at low temperature of 30 K [7]

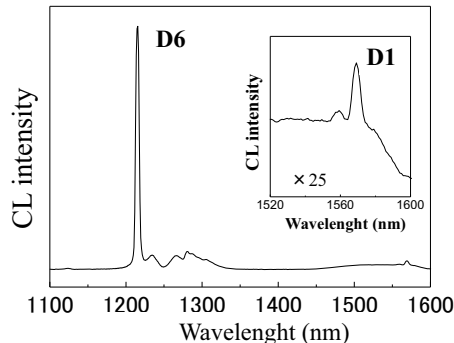


Table 5.1 Each peak energy (wavelength), and assignment of PL peaks related to the dislocations of Si [6]. PL spectra of a deformed Si were measured at 4.2 K

	Peak		Assignment
	eV	nm	
D1	0.812	1526.897	Geometrical kinks of dislocations
D2	0.875	1416.960	Geometrical kinks of dislocations
D3	0.934	1327.452	Dissociated glide dislocations
D4	1.000	1239.840	Dissociated glide dislocations
D5	0.953	1300.986	Straight dislocations
D6	1.012	1225.138	Stacking faults
D12	0.8443	1468.483	Straight and curved dislocations

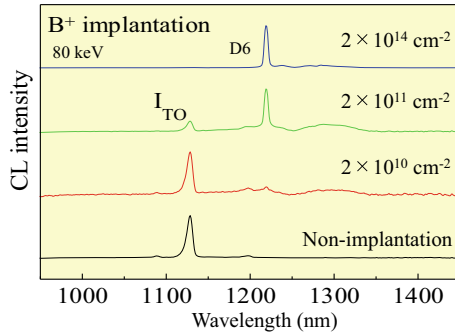


Fig. 5.2 CL spectra of the B-ion-implanted Si wafer as a function of B-ion implantation, measured at 30 K [7]

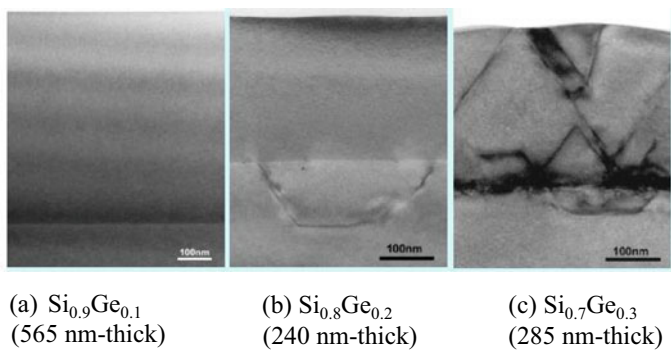


Fig. 5.3 TEM images of **a** $\text{Si}_{0.9}\text{Ge}_{0.1}$, **b** $\text{Si}_{0.8}\text{Ge}_{0.2}$, and **c** $\text{Si}_{0.7}\text{Ge}_{0.3}$ with various thicknesses, grown epitaxially on the Si substrate [7]

Figure 5.4 shows CL spectra of the same specimens (SiGe (10%): $\text{Si}_{0.9}\text{Ge}_{0.1}$, SiGe (20%): $\text{Si}_{0.8}\text{Ge}_{0.2}$, SiGe (30%): $\text{Si}_{0.7}\text{Ge}_{0.3}$) at acceleration voltages of 15 and 25 kV. Based on Eq. (4.1), the electron penetration (R_e) becomes deep with increasing the acceleration voltage (see Fig. 4.2 or Fig. 4.11). From the comparison of Fig. 5.4a, b, the intensities of D1, D2, D3, and D4 peaks relative to the CL peak (I_{TO}) at 1.02 eV, assigned to an Si substrate at 1.02 eV, become intense with increasing the acceleration voltage. This result suggests that the dislocations increase at the interface of SiGe film and Si substrate. Furthermore, new broad CL peaks at 1400 and 1550 nm are observed in the SiGe (20%), and SiGe (30%) films, respectively. A comparison of Figs. 5.3 and 5.4 indicates that new broad CL peaks at 1400 and 1550 nm observed in the SiGe (20%), and SiGe (30%) films are originating from the aggregations of dislocations.

Figure 5.5a depicts Raman spectra of the same specimens (SiGe (10%): $\text{Si}_{0.9}\text{Ge}_{0.1}$, SiGe (20%): $\text{Si}_{0.8}\text{Ge}_{0.2}$, SiGe (30%): $\text{Si}_{0.7}\text{Ge}_{0.3}$), measured at room temperature. In general, three main Ge–Ge, Si–Ge, and Si–Si Raman features assigned to Ge–Ge,

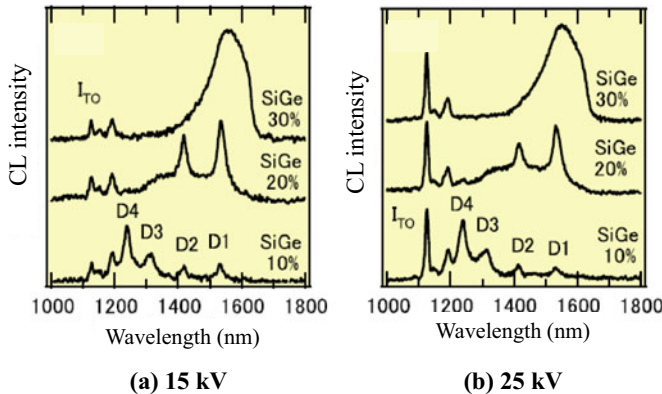


Fig. 5.4 CL spectra of SiGe (10%): Si_{0.9}Ge_{0.1}, SiGe (20%):Si_{0.8}Ge_{0.2}, and SiGe (30%):Si_{0.7}Ge_{0.3} layers with various thicknesses in Fig. 5.3, measured at acceleration voltages of **a** 15 kV and **b** 25 kV [7]

Ge–Si, and Si–Si bonds are observed at around 285–300, 395–410, and 460–520 cm^{−1}, respectively [8]. The Raman band ascribed to Si–Si bond is observed between 500–520 cm^{−1}. As seen in Fig. 5.5a, the Raman band ascribed to Si–Si bond shifts to low-frequency side with increasing the content of Ge. Arrows in Fig. 5.5a indicate the peak frequencies in the fully relaxed SiGe films [8]. By subtracting the peak frequencies of the fully relaxed SiGe films from the practically observed peak frequencies, we can estimate stresses in the SiGe films on the Si substrates. The results obtained are shown in Fig. 5.5b. Figure 5.5c illustrates the full width half maximum (FWHM) of each Raman band ascribed to the Si–Si band. As seen in Fig. 5.5b, the compressive stress in the SiGe films increases with an increase in the Ge content and finally decreases by the Ge content of 30%. On the other hand, the FWHM in Fig. 5.5c increases with increasing the Ge content. Combing TEM, CL, and Raman measurements, the crystalline quality of the SiGe films decreases with increasing the Ge content. From the comparison of TEM and CL measurements, the decrease of the compressive stresses in SiGe (30%) layer in Fig. 5.5b is considered to be caused by increase of an inhomogeneity of the compressive stresses in the SiGe (30%) layer with increasing the content of Ge.

5.1.2 Silicon Dioxide

Silicon dioxide (SiO₂) films are widely used for the gate oxide (GO), interlayer film, and passivation of junctions in a silicon device [9]. Silicon devices have been made more compact by increasing their density. Given the requirements for the lower operating power and the higher response speed, GO films have been made thinner, and the dielectric constant of the interlayer film has decreased [9]. Recently, thermally

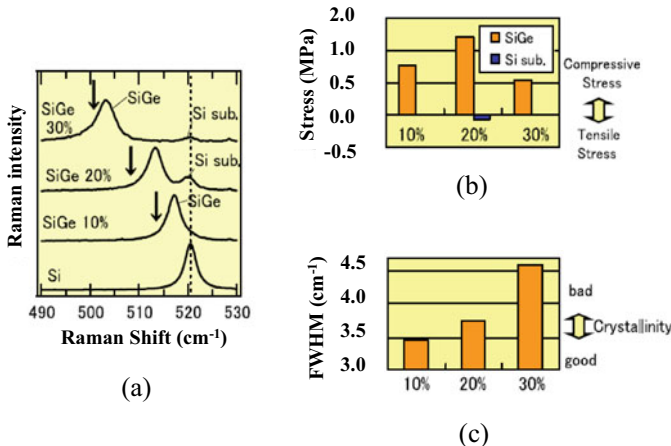


Fig. 5.5 **a** Raman spectra, **b** stress, and **c** FWHM of (SiGe (10%): $\text{Si}_{0.9}\text{Ge}_{0.1}$), (SiGe (20%): $\text{Si}_{0.8}\text{Ge}_{0.2}$), and (SiGe (30%): $\text{Si}_{0.7}\text{Ge}_{0.3}$) layers, measured at room temperature [7]

grown SiO_2 films have been used for the GO, while tetraethoxysilane (TEOS) films have been used for the interlayer films. High-quality SiO_2 films are most important for the GO film, as the number of defects in the GO film increases as the film becomes thinner [9].

An interlayer dielectric film with a low dielectric constant is essential for the fabrication of multilevel interconnections required by ultra-large-scale integrated (ULSI) circuits [9]. Hitherto, fluorine-doped silicon-dioxide (SiOF) films have been used for this purpose. The properties of these films depend on the fluorine to oxygen ratio (F/O ratio) [10–13]. The existence of thermal stress at the interface between the interlayer dielectric film and the Si substrate, as well as between it and the metal, gives rise to defects such as voids, oxygen vacancy centres (OVCs), three-fold and four-fold ring defects, and E' centres ($\text{O}_3\equiv\text{Si}$). These defects are regarded as some of the factors responsible for low reliability and device deterioration. Some fabrication processes for making good GO films have been proposed, for example, rapid thermal oxidation (RTO) and in situ steam generation (ISSG) [12, 13].

Nagai et al. characterised SiO_2 thin films prepared by rapid thermal oxidation (RTO) and in situ steam generation (ISSG) using FT-IR spectroscopy with gradient etching preparation (GEP) technique and grazing incidence X-ray reflectometry (GIXR) [14]. The GEP technique is an efficient method to investigate depth profiling of chemical structures with a high depth-resolution of sub-nanometer order, especially in the SiO_2/Si or SiO_2/SiC interface and with a combination of numerous characterising techniques, because the film thickness lengthens to an inclined plane direction of SiO_2 film, using GEP technique [14].

Figure 5.6a shows a schematic of IR measurement of thin SiO_2 film by GEP technique. The depth profile of thin SiO_2 film as a function of thickness is illustrated in Fig. 5.6b, measured by GIXR [14].

Fig. 5.6 **a** Schematic of FT-IR measurement of thin SiO₂ film by GEP technique, and **b** the depth profile of thin SiO₂ film as a function of thickness [14]

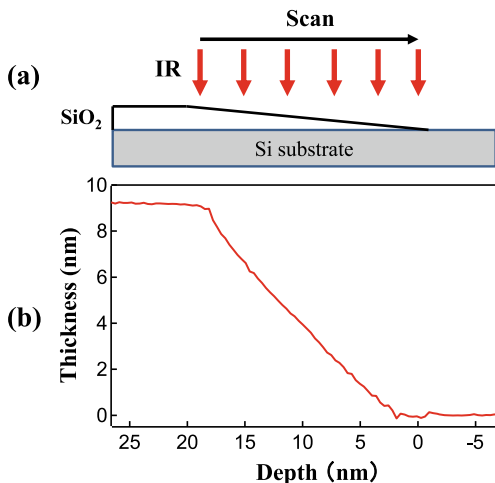


Figure 5.7a, b show FT-IR spectra of the SiO₂ films (RTO oxide, ISSG 33% H₂, and ISSG 5% H₂ films) and the peak-wavenumber dependence of phonons on the film thickness, prepared by the GEP technique, respectively. Transverse optical (TO) and longitudinal optical (LO) phonons in the SiO₂ films on a Si wafer are observed at 1072 and 1257 cm⁻¹, respectively, in Fig. 5.5a [15]. As the measured position comes closer to the interface, the peak intensities of LO and TO phonons decrease with a decrease in the film thickness [14]. The TO phonon shifts towards the lower wavenumber side in the RTO films as the incident light approaches the interface, whereas the peak-wavenumber shift of the 5% ISSG film cannot be observed in Fig. 5.7b [14]. Martinet and Devine [15] calculated the IR optical response of SiO₂/Si films by a phenomenological approach using the dielectric function, and the TO phonon shifts towards the lower wavenumber side as the film thickness decreases. Devine found the TO and LO phonon shift towards the lower wave number side in thermally grown oxides and concluded that these shifts are mainly caused by a change in stoichiometry [15]. Queeney et al. also studied TO and LO phonon shifts in ultrathin SiO₂ films and found that TO and LO phonon shifted to lower wavenumber side as the film thickness decreases from 3 to 0.5 nm [16]. Their result agrees well with Nagai et al.'s result [14]. The red-shifts in LO and TO phonons are considered to be caused by a change in stoichiometry in the SiO₂ films. Furthermore, weak broad bands are observed between LO and TO phonons in Fig. 5.7a. We assign these broad bands to the upper and lower branches of surface polaritons [17].

Figure 5.8 shows PL spectra of an Si substrate, RTO oxide, ISSG 33% H₂, and ISSG 5% H₂ films [18]. As seen in Fig. 5.8, a broad PL band is observed at around 2.9 eV. Kruchinin et al. measured the PL spectra of the SiO_x ($x < 2$) and assigned this PL peak to be originating from nonstoichiometric oxide of SiO_x < 2 [19]. The PL intensity of the broad band at around 2.9 eV in Fig. 5.8 decreases in the specimens in the order RTO oxide > ISSG 33% H₂ > ISSG 5% H₂ film. Based on Nagai et al.

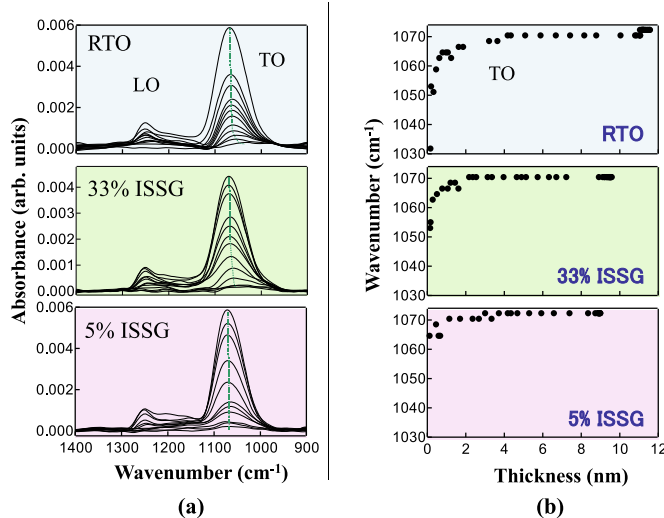


Fig. 5.7 **a** FT-IR spectra of thin SiO_2 film by GEP technique, and **b** change in TO phonon wavenumber as a function of the film thickness: RTO oxide, ISSG 33% H_2 , and ISSG 5% H_2 film [17]

and Kruchinin et al., we conclude that the red-shift of the TO phonon in Fig. 5.7b is caused by a deficit of oxygen in the SiO_2 films.

Furthermore, μ -FT-IR spectroscopy is a powerful technique for characterising Si devices. Seki et al. investigated process-induced damage in a Cu/low- k interconnect structure [20]. They applied μ -FT-IR spectroscopy to this structure using polarised

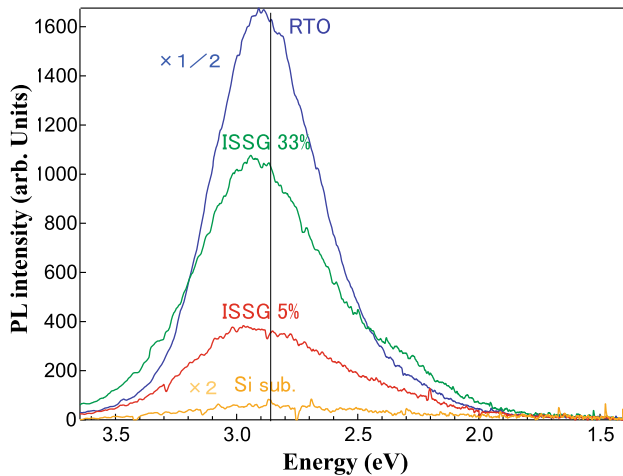


Fig. 5.8 PL spectra of an Si substrate, RTO oxide, ISSG 33% H_2 , and ISSG 5% H_2 films

IR light for the low- k spaces and Cu lines of different widths and for Cu lines of different heights formed on Si substrates [20]. Although the Cu lines and low- k regions were each 70 nm wide, which is considerably smaller than the wavelength of the IR light, they obtained the FT-IR spectra of the low- k film in the Cu/low- k interconnect structure [20].

Seki et al. measured the μ -FT-IR spectra of Cu/low- k specimens with different spacings and linewidths. They utilised the intensities of several bands relative to the intensity of an absorption band at 1050 cm^{-1} associated with the Si–O stretching mode, which is the main framework of the low- k film [20]. The relative Si–H/Si–O intensity is very similar for all the specimens, whereas the relative Si–CH₃/Si–O intensity decreases gradually with decreasing space width (S) [20]. However, the relative OH/Si–O intensity increases significantly with decreasing S . In an earlier report, they found that the number of Si–CH₃ groups decreased, and the structure changed to a SiO₂ network structure owing to plasma processes [21]. This result suggested that the generation of OH groups was related to process-induced damage; the volume fraction of the sidewall in the low- k film increased as the low- k space width decreased [20].

FT-IR spectroscopy can be used to measure several sidewalls of the low- k films simultaneously, and the Si–OH peak intensity is apparently amplified by the adsorption of water. This technique enabled highly sensitive measurement of the process-induced damage to the sidewall of the low- k film [20].

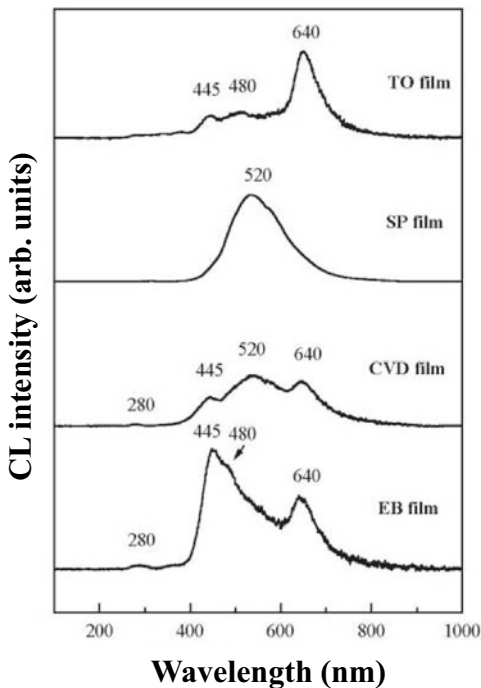
The electron spin resonance (ESR) provides us with some data on paramagnetic defects such as E' centres (O₃≡Si), Si clusters in SiO₂ films, and Pb centres between SiO₂ and the Si substrate [22]. In contrast, PL [23–27] and CL [28–32] spectroscopy yield us some information about non-paramagnetic defects such as OVCs in SiO₂ films, in addition to the non-bridging oxidation hole centres (NBOHC).

We measured CL spectra of SiO₂ films with a thickness of 500–1000 nm that were formed on Si substrates by thermal oxidation, electron beam, sputtering, and plasma chemical vapour deposition (PCVD) using TEOS [33]. The process conditions were those conventionally used for fabricating semiconductor devices. Additional details about the growth conditions are in Ref. [34, 33].

Figure 5.9 depicts the CL spectra of various SiO₂ films prepared on Si substrates by thermal oxidation (TO), electron beam (EB), sputtering (SP), and p-CVD using TEOS (CVD) [33]. CL peaks are observed at 445, 480, 520, and 640 nm. In Fig. 5.9, CL peaks at 445, 480, and 640 nm are observed in the TO film, whereas a broad peak at 520 nm is observed in the SP film [33]. On the other hand, CL peaks are observed at 280, 445, 520, and 640 nm in the CVD film. CL peaks are observed at 280, 445, 480, 520, and 640 nm in the EB film. The 480 nm peak is observed in both the TO and EB films. The relatively sharp 640 nm peak is attributed to the NBOHC or their precursors [33].

As seen in Fig. 5.9, the 520 nm peak is observed in the SP film, whereas it is not observed in the TO film [33]. We measured the impurities in the SP and TO films by X-ray fluorescence spectroscopy (XRF) and found that the TO and SP films contained negligible amounts (<50 and <200 ppm) of metal impurities [33]. We could find no significant difference in the concentration of impurities between the TO and SP

Fig. 5.9 CL spectra of SiO_2 films prepared on Si wafers by TO, EB lithography, SP, and p-CVD techniques using TEOS (CVD) [33]. (Reproduced with permission from Ref. [33]. © AIP Publishing, 1998.)



films. From this observation, it might be impossible that we assign the 520 nm peak to impurities [33]. Watanabe et al. measured PL excitation spectra and time-decay data in visible and near-infrared irradiated vitreous silica [26]. They concluded that the PL peaks at 283 and 558 nm were ascribed to the singlet–singlet transition of the oxygen vacancy and the oxygen vacancy–interstitial pairs, $(\text{V}_o;(\text{O}_2)_i)$, respectively, where V_o is the oxygen vacancy. The positions of the 280 and 520 nm peaks, which we observed in the SP, CVD, and EB films, are near the PL peak positions observed by Watanabe et al. [26]. The 280 and 520 nm peaks might be assigned to the singlet–singlet transition of the oxygen vacancy and the $\text{V}_o;(\text{O}_2)_i$, based on the coincidence between the CL and PL peak positions, respectively [33].

We measured the CL spectra of quartz glass implanted with a dose of $5 \times 10^{16} \text{ Si}^{28}$ ions/ cm^2 . We could see that the intensities of the 445 and 480 nm peaks become very high after ion implantation, suggesting that the defects related to these peaks increase after ion implantation [33]. The electron spin resonance (ESR) provides us with some data on paramagnetic defects such as E' centres ($\text{O}_3\equiv\text{Si}$), Si clusters in SiO_2 films, and Pb centres between SiO_2 and the Si substrate [14]. In contrast, PL [15–19] and CL [20–24] spectroscopy yield some information about non-paramagnetic defects such as OVCs in SiO_2 films, in addition to the non-bridging oxidation hole centres (NBOHC). We measured the spectral variations of the ESR spectrum and the CL peak as a function of annealing temperature (AT), respectively [33]. The ESR spectrum attributed to the E' centres is observed at approximately 336 mT in the ESR spectra

Table 5.2 The assignment of CL peaks for various SiO₂ films

	280 nm	445 nm	480 nm	520 nm	640 nm
TO film (thermal oxide)	—	OVC	OVC	—	NBOHC
SP film	—	—	—	V _o ;(O ₂) _I	—
CVD film	OVC	OVC	OVC	V _o ;(O ₂) _I	NBOHC
EB film	OVC	OVC	OVC	—	NBOHC

of the ion-implanted quartz glass [17]. Moreover, the shoulder peaks assigned to the peroxy radicals and Si clusters are observed in the low magnetic field side of the E' centres [33]. The ESR spectrum assigned to the E' centres falls dramatically as the AT increases. In contrast, the 445 and 480 nm peak intensities reach a maximum at 400 °C and then fall gradually as the AT increases [33]. In Fig. 3 of Ref. [33], the 445 nm and 480 nm peaks exhibited the same variation in intensity as in the AT. The comparison between ESR and CL measurements indicated that the 445 and 480 nm peaks were ascribed to the same luminescent centre, which is different from the E' centres [33]. Tohmon et al. [24] measured the absorption and PL excitation spectra of silica glass specimens with oxygen vacancies and concluded that the PL bands at 453 and 281 nm can be ascribed to the absorption due to the OVC. From our results and those of Tohmon et al. [24], we concluded that the 445 and 480 nm peaks were originating from OVC. The assignment of CL peaks is listed in Table 5.2.

5.2 Strained Silicon

Raman spectroscopy is a highly useful technique that provides structural information about both organic and inorganic materials; much like IR spectroscopy. However, IR bands arise from changes in the dipole moment of a molecule or an atom resulting from interaction with light, while Raman bands arise from changes in the electronic polarisability of the molecule or atom resulting from the same interaction. Raman spectroscopy has been applied to various materials and devices such as semiconductors, lithium-ion batteries, polymers, proteins, and biological specimens. In particular, Raman spectroscopy provides us with information about the crystal structure, crystalline quality, stress, electrical states, and carrier concentrations of semiconductors.

The local residual stress has an important effect on the electrical properties of electronic devices, such as large-scale integrated (LSI) circuits. Micro-Raman spectroscopy can be used to estimate the local residual stress in microstructures, such as local oxidation of silicon [35, 36] structures and isolation trench techniques [37, 38]:

$$\begin{vmatrix} p\varepsilon_{xx} + q(\varepsilon_{yy} + \varepsilon_{zz}) - \lambda & 2r\varepsilon_{xy} & 2r\varepsilon_{xz} \\ 2r\varepsilon_{xy} & p\varepsilon_{yy} + q(\varepsilon_{zz} + \varepsilon_{xx}) - \lambda & 2r\varepsilon_{yz} \\ 2r\varepsilon_{xz} & 2r\varepsilon_{yz} & p\varepsilon_{zz} + q(\varepsilon_{xx} + \varepsilon_{yy}) - \lambda \end{vmatrix} \equiv 0 \quad (5.1)$$

where $\lambda = \Omega^2 - \omega_0^2$ ($\Omega \approx \omega_0 + \lambda/2\omega_0$ is the strain-dependent frequency of the optical phonons), and p , q , and r are the deformation potential constants. The secular equation postulates the crystallographic axes $\mathbf{x} = [100]$, $\mathbf{y} = [010]$, $\mathbf{z} = [001]$. Diagonalisation of Eq. (5.1) yields a set of three eigenvectors of the optical phonons in the presence of strain [37, 38].

Under the presence of biaxial stress on a (100) surface, the triply degenerate F_{2g} mode splits into singlet and doublet modes. In the backscattering configuration from the (100) surface, only the singlet mode is Raman-active, and the relationship between the peak-frequency shift ($\Delta\nu$) and isotropic biaxial stress (σ) is expressed as follows [37, 38]:

$$\sigma(\text{GPa}) = 0.23\Delta\nu(\text{cm}^{-1}) \text{ for the (100) surface} \quad (5.2)$$

The peak-frequency shift $\Delta\nu$ of the modes split from the stress-free Raman line is accurately measured and then multiplied by the coefficient, C ($\text{GPa}/\text{cm}^{-1}$) ~ 0.23 , to convert $\Delta\nu$ into the local residual stress. The coefficient is a function of the elastic compliance constant and deformation potential constant, and depends largely on the direction and distribution of the stress [38].

Logic complementary metal oxide silicon (CMOS) devices achieve high performance from techniques such as strained silicon channels [39, 40] and transistors built in silicon-on-insulator (SOI) devices [41]. Both techniques enable a very high increase in performance with little change in the starting materials, and both techniques complement one another to provide maximum performance. Thus, it is even more exciting to combine both strained silicon and SOI techniques, although either technique is useful alone. The tensile strain in silicon channels in CMOS devices enhances the mobility of both electrons and holes. This has been theoretically predicted [42, 43] and experimentally validated [39, 41].

Higgs and Kittler measured CL and electron-beam induced current (EBIC) images of specimens consisting of a common structure: an Si capping layer ($3 \mu\text{m}$ thick) grown on top of an $\text{Si}_{1-x}\text{Ge}_x$ alloy layer ($2 \mu\text{m}$ thick) on an Si buffer layer ($2 \mu\text{m}$ thick) on top of a heavily doped Si (100) substrate [44]. Instead of detecting the weak D band luminescence image directly, the CL image assigned to the TO phonon replica of excitonic luminescence EX(TO) observed at 1.1 eV of the Si substrate was measured [44]. Monochromatic CL line scans revealed that these dark lines were a result of the reduction in CL intensity due to the Si substrate. They considered that the variation in the observed CL intensity occurred because the excitons were produced in the upper part of the specimen structure (top $2\text{--}3 \mu\text{m}$) and then diffused towards the Si substrate [44]. The exciton density was reduced as the excitons recombined non-radiatively at the misfit dislocations. Based on the reduction of the exciton density

upon reaching the Si substrate, they showed that there was a 1:1 correlation between the misfit dislocation pattern as measured by EBIC and the dark-line CL contrast [44].

We measured the atomic force microscopy (AFM) image ($10 \mu\text{m} \times 10 \mu\text{m}$) of a strained Si layer (25 nm thick) deposited onto an $\text{Si}_{0.67}\text{Ge}_{0.33}$ alloy layer (1 μm thick)/graded SiGe alloy layer (0–33%, 300 nm) on an Si substrate before and after Chemical Mechanical Polishing (CMP) treatment. A schematic of the multilayer structure of strained Si on a Si substrate is shown in Fig. 5.10.

Figure 5.11 shows the AFM image of multilayer structure of strained Si on a Si substrate in Fig. 5.10. The crosshatch pattern parallel to the $\langle 110 \rangle$ direction is clearly observed in Fig. 5.11. From a comparison of Fig. 5.11a, b, it is found that the topographic image by AFM after CMP treatment becomes smoother than that before CMP treatment.

We measured the Raman spectral image ($10 \mu\text{m} \times 10 \mu\text{m}$) of a strained Si layer (25 nm thick) deposited onto an $\text{Si}_{0.67}\text{Ge}_{0.33}$ alloy layer (1 μm thick) on an Si substrate. A typical Raman spectrum consists of two distinctive peaks: one at $\sim 516 \text{ cm}^{-1}$ ascribed to the Si phonon in the strained Si layer and another at $\sim 504 \text{ cm}^{-1}$ assigned to the Si–Si vibrational mode in the $\text{Si}_{0.67}\text{Ge}_{0.33}$ alloy layer [45]. Figure 5.12a, b show the strain distribution of the Raman peak due to the strained Si, and the Si–Si vibrational mode from the $\text{Si}_{0.67}\text{Ge}_{0.33}$ alloy layer, respectively. The crosshatch pattern parallel to the $\langle 110 \rangle$ direction is clearly observed in Fig. 5.12a, b. Furthermore, it is found that the strained Si layer is under tensile stress, whereas the $\text{Si}_{0.67}\text{Ge}_{0.33}$ alloy layer is under compressive stress [45].

Himcinschi et al. have measured strained Si (2 μm thick) layers deposited onto relaxed $\text{Si}_{0.78}\text{Ge}_{0.22}$ layers (4 μm thick) on silicon substrates by AFM and UV Raman spectroscopy (325 nm excitation wavelength), and they obtained the strain distribution determined from the Raman image on the strained Si layer [46]. Their

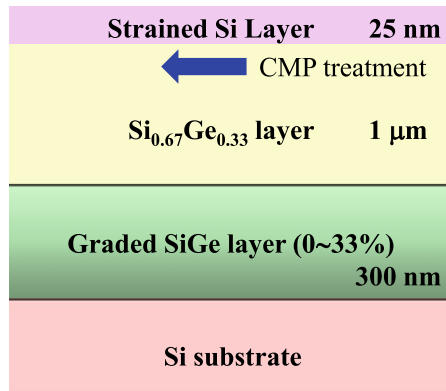


Fig. 5.10 Schematic of multilayer structure of strained Si on a Si substrate

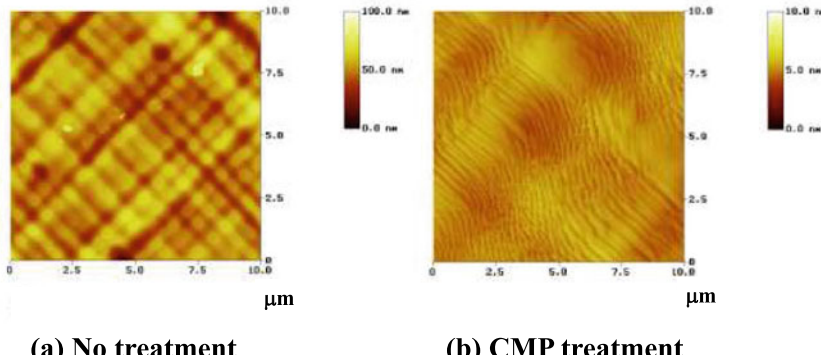


Fig. 5.11 AFM image ($10 \mu\text{m} \times 10 \mu\text{m}$) of a strained Si layer (25-nm thick) deposited onto an $\text{Si}_{0.67}\text{Ge}_{0.33}$ alloy layer (1 μm thick) on an Si substrate **a** before, and **b** after Chemical Mechanical Polishing (CMP) technique

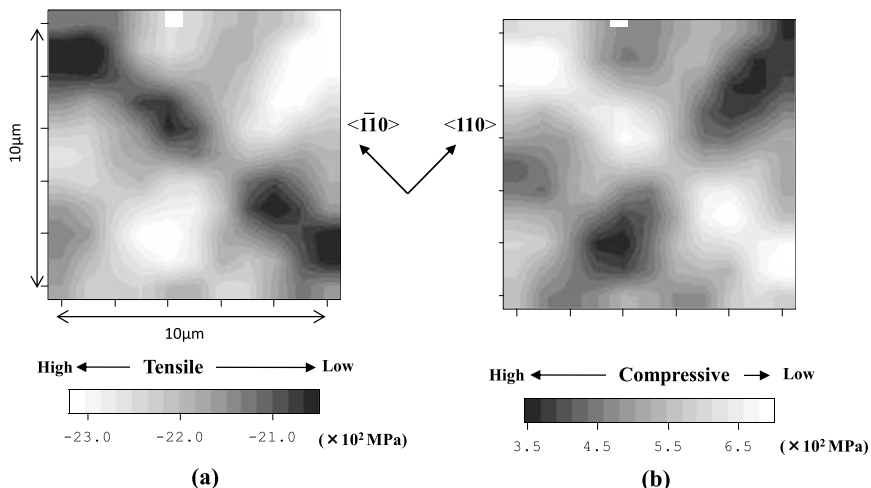


Fig. 5.12 **a** Strain distribution of the Raman peak of the strained Si, and **b** Si-Si vibrational mode from the $\text{Si}_{0.67}\text{Ge}_{0.33}$ alloy layer [45]

result agrees very well with our result (Fig. 5.12). Furthermore, Higgs et al. [47], measured CL imaging and spectroscopy of dislocations in Si and $\text{Si}_{1-x}, \text{Ge}_x$ alloys. The crosshatch pattern obtained from their CL image coincides well with that from our Raman and AFM images [45].

5.3 Silicon Processing of LSI Devices

The LSI devices are year by year improved by more characteristic processes, designs, and materials, such as the use of strained Si, low- k interconnection dielectric layer, and high- k gate dielectrics. Nevertheless, their reliability decreases and the risk of failure increases because of the complexity of cutting-edge technologies. The shallow trench isolation (STI) process techniques are necessary for accurately controlling stress and crystalline defects, because the differences in the thermal expansion coefficients among the Si substrate, thermal oxidation films, mask silicon nitride (SiN) films, and trench-filled oxides result in residual stresses, giving rise to the formation of crystalline defects [48–50].

CL spectroscopy is a powerful method to characterise crystalline defects in semiconductors. Although CL spectroscopy is effective for device characterisation, the low luminescence efficiency and the lack of a highly sensitive detector covering the near-infrared region have limited its application to Si devices [51]. However, Sauer et al. reported that plastically deformed Si gave characteristic luminescence, corresponding to dislocations, labelled D1 (1527 nm, 0.81 eV), D2 (1417 nm, 0.87 eV), D3 (1327 nm, 0.95 eV), and D4 (1240 nm, 1.0 eV) [52].

Raman spectroscopy is extensively used to study local residual stresses in Si devices because of high spatial resolution and high sensitivity to stress [38, 53–55]. The difference in thermal expansion coefficients between Si and silicon dioxide (SiO_2) or SiN films induces residual stresses, causing crystalline defects. Nevertheless, the relationship between residual stress and crystalline defects in the STI process has been unclear.

We have applied CL and Raman spectroscopy to STI characterisation in LSI to elucidate the relationship between stress and crystalline defects [56, 57]. We studied the generation mechanism of dislocations in more detail, by comparing the CL results with the residual stresses obtained from Raman measurements [57]. Furthermore, we found that the standby leakage current largely increased as the SiN film thickness becomes thicker from 190 to 230 nm [57].

Figure 5.13 shows a schematic of the STI processes [57]. Typical STI processes were used, consisting of trench patterning with a depth of ~400 nm, liner oxidation, and deposition of a high-density plasma chemical vapour deposition (HDP-CVD) film [57]. The thickness of the liner oxide film was ~30 nm. Chemical mechanical polishing (CMP) was used for surface planarisation. After the removal of SiN and SiO_2 films using chemical etching technique, sacrificial thermal oxidation (10 nm thick) was applied [57]. CL and Raman measurements were performed after each process. We conducted CL measurements at 30 K to study the crystalline defects in Si. The electron penetration depths at 10 and 15 kV were ~1.49 and ~2.93 μm , respectively, based on the Kanaya–Okayama model [58].

The measured regions were labelled as ‘Fuse,’ ‘S.A.,’ ‘Cell,’ ‘Dummy,’ and ‘W.D.’ according to the role of the specific region in the LSI, which correspond to the fuse circuit, sense amplifier, active memory cell, dummy memory cell, and word line driver, respectively (see Fig. 2 of Ref. [56]) [56]. The Cell and Dummy regions

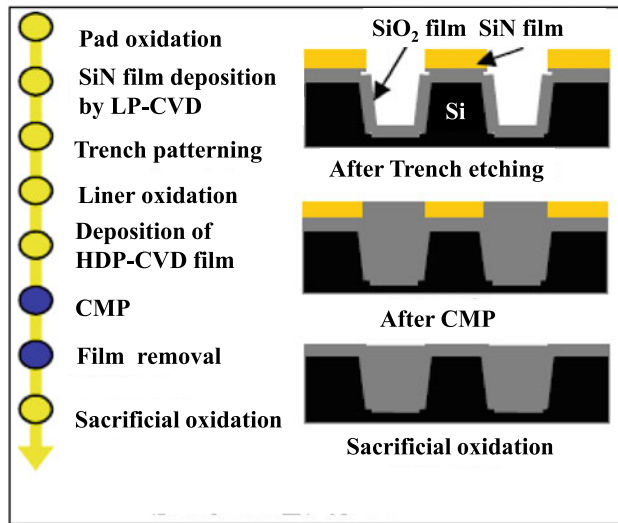


Fig. 5.13 Schematic of STI processes [57]

included periodic active and field areas with sizes of approximately 500 and 5000 nm, respectively. The Fuse, W.D., and S.A. regions, which are the surrounding circuits, named for simplicity' sake, included various sizes of active and field areas ranging from 500 to 5000 nm [57].

Figure 5.14 shows the CL spectra of the specimens with SiN thicknesses of 190 nm (normal product) and 230 nm (leakage product) after CMP and sacrificial oxidation [57]. The specimen with a thickness of 230 nm depicts several dislocation-related lines (D lines) at D1 (1527 nm, 0.81 eV), D2 (1417 nm, 0.87 eV), D3 (1327 nm, 0.95 eV), and D4 (1240 nm, 1.0 eV) in the Fuse and S.A. regions. The spectra at W.D., which do not appear in Fig. 5.14, are similar to the S.A. region [57]. As seen in Fig. 5.14, the regions with various sizes of active and field areas (Fuse, W.D., and S.A. regions) possess a high density of dislocations, while the regions with periodic active and field areas possess a low density of dislocations in all regions [57]. Moreover, the specimen (normal product, 190 nm thick) indicated no D lines during the STI process in any region. This revealed that the critical thickness of the SiN film was approximately 190 nm in these processes. The line labelled 'TO' at 1127 nm (1.1 eV) is the band-edge emission followed by a transverse optic (TO) phonon emission. The line labelled G at 1278 nm (0.97 eV) is observed in all regions in both specimens [57]. The G line was assigned to the transition of substitutional carbon and self-interstitial silicon (Cs-Sii) [59]. As can be seen in Fig. 5.14, the intensities of the D lines are depending on the SiN film thickness. This shows that dislocations in the surrounding circuits are the main factor of the large standby leakage current. The dislocations

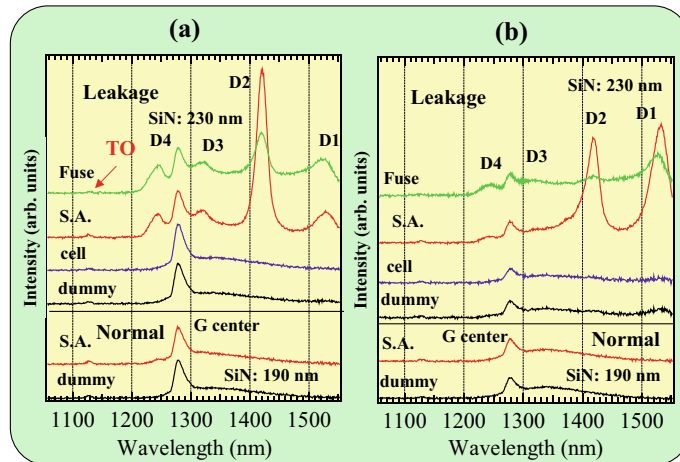


Fig. 5.14 CL spectra of the specimens with 190 nm thick and 230 nm thick SiN films after **a** CMP, and **b** sacrificial oxidation. The upper four spectra and lower two spectra were obtained from specimens (leakage product, 230 nm thick, and normal product, 190 nm thick, respectively) [57]

in the surrounding circuits in the 230 nm specimen are formed before the CMP process [57]. These D lines are observed in the same areas during the STI processes, indicating that the dislocations do not disappear, and new crystalline defects are not induced during these processes [57]. The relative intensities of the D lines change after the sacrificial oxidation. Some researchers reported that the intensity of the D1 line increases as the dislocation density increases [60, 61]. Thus, these spectral changes designate that the dislocations grow, with their densities reaching a high level after this thermal process. Controlling the SiN film thickness, the sizes of the active and field areas, and the process temperature is the most important factor for protecting the growth of dislocations [57].

An insulated-gate bipolar transistor (IGBT) is one of the key power semiconductor devices with highly efficient energy conversion systems in near future. The elimination or proper controlling of crystalline defects in power devices is most important to reduce switching losses and on-state losses [62]. IGBT is a three-terminal power semiconductor device mainly used as an electronic switch, which came to combine high efficiency and fast switching. It consists of four alternating layers (p–n–p–n) that are controlled by a metal–oxide–semiconductor (MOS) gate structure.

Figure 5.15a, b show a cross-sectional schematic device structure and the line profile of CL spectra along the n-drift region (solid arrow) in commercially available 600 V punch-through planar IGBTs. These IGBTs may be annealed at temperatures less than 400 °C before shipping to adjust and stabilise the electrical characteristics of such devices. We additionally annealed these devices at 200 °C for 1 h in a vacuum. CL spectra were measured at 30 K, by scanning the electron beam in steps of 5 μm in the depth direction along the solid arrow defined in Fig. 5.15a. Several sharp peaks labelled W (1218 nm, 1.018 eV), X (1201 nm, 1.032 eV), and C (1576 nm, 0.786 eV)

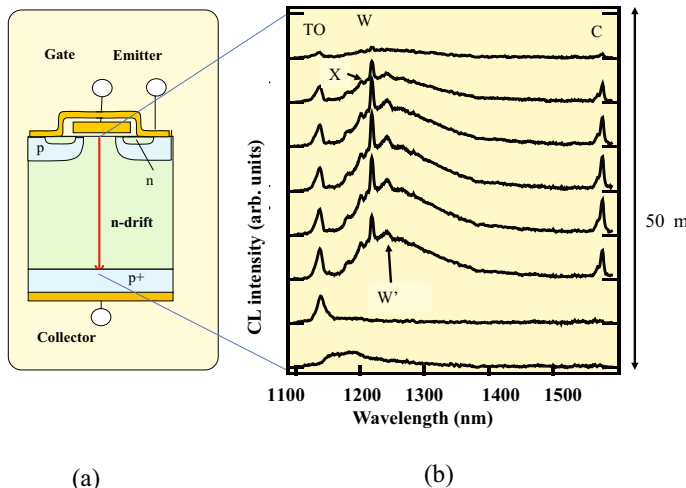


Fig. 5.15 **a** Cross-sectional schematic device structure, and **b** line profile of CL spectra along the n-drift region (solid arrow) in figure **(a)** in commercially available 600 V punch-through planar IGBTs

and a broad band around 1180–1370 nm are observed. The W' line at 1242 nm is a sum of the phonon replicas of the W line. The TO line at 1137 nm denotes the TO phonon replica of the band-to-band transition. The W and X centres are considered to be associated with small self-interstitial clusters, and the X centre is related to interstitial clusters larger than those of the W centre, since the X line appears at high temperatures accompanied by a decrease in the intensity of the W line [63, 64]. The C centre is well recognized as interstitial oxygen and carbon complexes in the form C_iO_i [64]. As seen in Fig. 5.15, each CL peak had a maximum value at the midpoint of the n-drift region, although electrons conventionally used to control carrier lifetime in power devices penetrated the entire device. One of the possible mechanisms for these distributions is probably caused by the interaction of the X, W, and C centres with other point-like defects and impurities near the surface and the interface, since the surface and interface of the device have tended to have many defects and impurities generated during its manufacturing process.

5.4 Gallium Arsenide and Related Devices

The FIR optical properties of group III–V zinc-blende semiconductors have been widely studied [65]. Within the reststrahlen region, the penetration depth of IR electromagnetic waves into a bulk crystal is only on the order of micrometres [65]. Conventional IR measurements of bulk semiconductors are generally performed in reflectance mode at near-normal angles of incidence and reflection [65]. The obtained

reflectance spectrum is then analysed using the conventional Kramers–Kronig transformation [66] to acquire information on the frequency dependence of the dielectric constant, and thus the optical phonon frequencies and damping. Group III–V compound semiconductors with zinc-blende structure have one transverse optical (TO) phonon and one longitudinal optical (LO) phonon. Their frequencies, ν_{TO} and ν_{LO} , are related to the Lyddane–Sachs–Teller (LST) equation [67]

$$\frac{\epsilon_0}{\epsilon_\infty} = \frac{\omega_{LO}^2}{\omega_{TO}^2} \quad (5.3)$$

where ϵ_0 and ϵ_∞ are the static and high-frequency dielectric constants, respectively.

Lockwood et al. measured the TO and LO optical phonons in AlAs, GaP, GaAs, InP, InAs, and InSb at room temperature by IR spectroscopy using an oblique-incidence reflectance technique [68]. The obtained spectra were fitted using a standard approach to determine the TO and LO phonon frequencies and damping. The results were found to be more precise than those of earlier reflectivity measurements using near-normal angles of incidence and provided information on the damping of both phonons [68]. The specimens, all of which were semi-insulating or low-doped, were studied by the oblique-incidence reflection technique under *p* polarisation, which has the advantage of producing a fairly uniform and low reflectivity at frequencies away from the reststrahlen band (see Fig. 1 of Ref. [69]). The reflectance spectra were analysed using a factorised model of the dielectric response [70, 71]

$$\epsilon(\omega) = \epsilon_\infty \frac{\omega_{LO}^2 - \omega^2 + i\gamma_{LO} \cdot \omega}{\omega_{TO}^2 - \omega^2 + i\gamma_{TO} \cdot \omega} \quad (5.4)$$

This model allows for different damping of the LO and TO phonons. Finally, excellent results were obtained by fitting the derivative of the reflectance using this model [72, 73], as will be discussed below. Lockwood et al. [68] adopted an approach that was developed for analysing thin films and that relies on the Berreman method [69–73].

Lockwood et al. [68] measured oblique-incidence reflectance spectra of GaAs and InP thin films, respectively, at 293 K under *p* polarisation. The fitted TO and LO mode frequencies were used, together with the literature values of ϵ_0 and ϵ_∞ , to calculate the dielectric response using Eq. (5.4). Their results are shown in Table 1 of Ref. [68]. Their room-temperature values for the TO and LO phonon linewidths are quite different from those predicted for AlAs, GaAs, GaP, and InP using ab initio calculations, except for the GaAs LO mode [74]. This demonstrates the need for further theoretical and experimental investigations of the temperature dependence of the phonon linewidths in zinc-blende semiconductors.

Semiconductor devices such as the metal–semiconductor field-effect transistor (MESFET) and heterojunction bipolar transistor (HBT) become smaller as the degree of density in these devices increases. Semiconductor devices consist of many components, such as a *p*–*n* junction, metal electrodes, and insulators. One of the most

important components is the *p*-*n* junction. The *p*- and *n*-type carriers are doped in the *p*-*n* junction. Heavy carrier doping and stress, which occur at the interface between the metal or oxide and the semiconductor, result in defects and dislocations in the semiconductor.

Raman spectroscopy has been used to estimate the carrier concentration and stress in semiconductors at the sub-micron level [38, 75]. However, Raman spectroscopy consumes a considerable amount of time to estimate the stress and carrier concentration in III-V compound semiconductor devices, such as GaAs, InP, and aluminium gallium arsenide (AlGaAs), on account of the weak Raman signal.

On the other hand, CL spectroscopy has a feature in which strong electron-beam irradiation causes an intense signal. Up to now, defects and dislocations of many kinds of semiconductors have been studied using CL spectroscopy [51, 76]. So far, there have been few studies using CL spectroscopy to estimate carrier concentration (*n*) and stress, although many studies have been conducted using PL spectroscopy [77–79]. CL spectroscopy provides us with much information not only about defects and dislocations, but also regarding *n* and stress. A luminescence peak shifts to the high energy side, and its intensity increases with an increase in *n*. The application of stress to a semiconductor produces a strain that reduces the symmetry of the material and subsequently results in significant changes in the electronic energy bands [80].

We have measured the CL spectra around the gate electrode in the cross-section of a GaAs MESFET with a charge coupled device (CCD) detector and proposed a new technique using CL spectroscopy to estimate *n* and stress in electronic devices [81]. A comparison between images of the peak intensity and peak-energy shift obtained from the CCD detector reveals that there is heavy carrier doping in the drain and source regions and that *n* is approximately 6×10^{17} atoms/cm³ [81]. Carrier concentration *n*, estimated from the peak-energy shift, agrees well with that obtained from the *C-V* method [81].

Furthermore, there is hardly any carrier doping, and stresses are relaxed at a distance of approximately 2 μm from the gate electrode. CL spectroscopy is a helpful technique for estimating the two-dimensional distribution of *n* and stress in electronic devices within a short amount of time, using the CCD detector [81].

The change in the band gap causes a shift in the CL peak. The CL peak generally also shifts to high and low energies under compressive and tensile stresses, respectively [81]. From these effects, we can estimate the carrier concentration and stress by CL spectroscopy [81]. Up to now, CL spectra have been measured using a photomultiplier; thus, we have only obtained an intensity map, fixing the spectrometer at the peak energy. The intensity map cannot reveal much information about *n* and stress, compared with the imaging technique using the CCD detector [81].

The plane-view SEM image of the GaAs MESFET device around the gate electrode is shown in Fig. 5.16.

Figure 5.17 depicts a typical CL spectrum at around under the gate electrode.

The CL peak ascribed to GaAs is observed at round 870 nm (1430 meV).

Figure 5.18a and b indicate the plain-view line profile of the intensity, and the peak shift at the CL peak at 870 nm (1430 meV), respectively. The CL peak intensity becomes intense under the gate and source electrode whereas weak under the gate

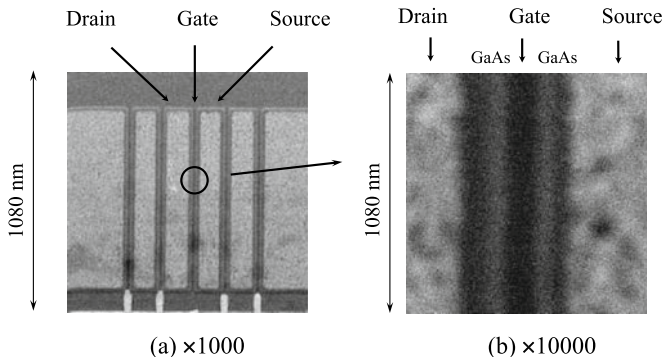
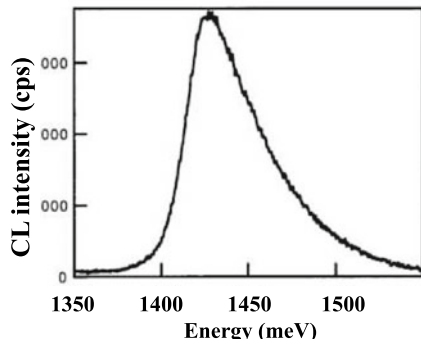


Fig. 5.16 The plane-view SEM image of the GaAs MESFET device around the gate **a** $\times 1000$, and **b** $\times 10,000$

Fig. 5.17 The CL spectrum around the gate in GaAs MESFET



electrode. On the other hand, the CL peak shifts to lower energy side under the gate but to higher energy sides under the drain and source electrodes.

Figure 5.19a, b, and c show the cross-sectional SEM image, the intensity, and the peak shift images for the CL peak at 1430 meV, respectively. As can be seen in Fig. 5.19, the CL peak at 1430 meV shifts to lower energy side by approximately -4 meV under the gate but to higher energy sides by approximately 5 meV under the drain and source electrodes. From this result, it is found that the GaAs substrate near the gate electrode is under tensile stresses whereas the areas near the drain and source electrodes are under compressive stresses.

Furthermore, we studied the change in the CL spectra as a function of the n -type carrier concentration (n) for Si-doped GaAs wafers. Figure 5.20 depicts the relationship between the CL peak shift at 1430 meV (870 nm) and carrier concentration (n). CL peak is observed around 1430 meV and assigned to the interband transition of GaAs. The CL peak shifts to dramatically higher energies, broadens, and intensifies with increase in n . This is called the Burstein–Moss shift [79]. As can be seen in

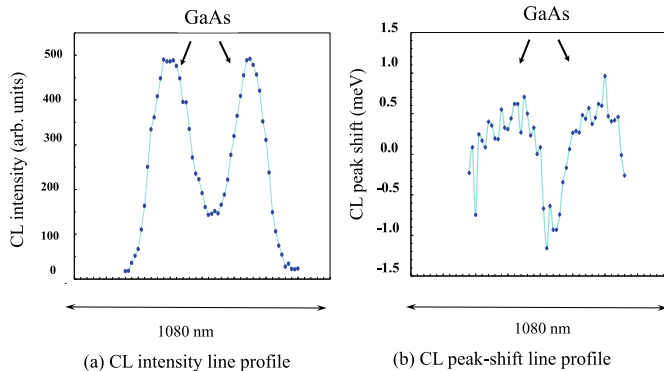


Fig. 5.18 The plain-view line profile of **a** the CL intensity, and **b** the CL peak shift at the CL peak at 870 nm (1430 meV)

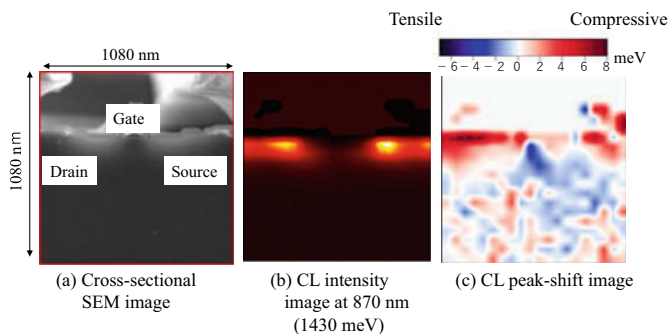


Fig. 5.19 **a** The cross-sectional SEM image, the images of **b** the intensity and **c** the peak shift for the CL peak at 1430 meV

Fig. 5.20, the CL peak shifts linearly with n in the range of 10^{16} – 10^{19} atoms/cm³ [81]. We can estimate n in GaAs devices, using Fig. 5.20.

5.5 Indium Phosphate and Related Devices

Indium phosphate (InP) and related devices, high-power, high-brightness single-mode semiconductor lasers and amplifiers, are of interest for a variety of applications, including pumping fibre amplifiers, free-space optical communications, and laser radar. Arrays of such lasers are also attractive for beam combining to attain even greater single-mode power. Power and brightness in single-mode semiconductor lasers are generally limited by catastrophic optical damage (COD) or thermal effects and two-photon absorption (TPA) [82].

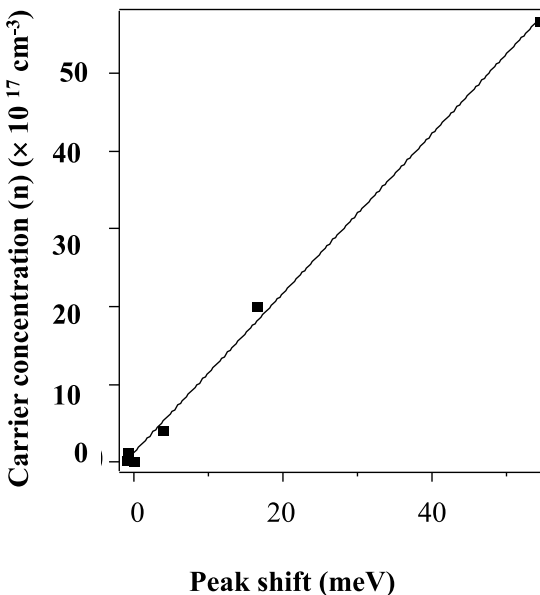


Fig. 5.20 Change in the n -type carrier concentration (n) as a function of CL peak shift for Si-doped GaAs wafers

The InGaAsP/InP multi-quantum-layer (MQW) laser diode, emitting at 1.3–1.5 μm , is of great interest as a light source for long-haul and undersea optical fibre transmission systems. Few studies on the degradation in these devices have been reported [83, 84]. However, rapid degradation and the appearance of self-sustained pulsation, which are associated with dark spot defects (DSDs) or $<1(0)$ dark-line defects in InGaAsP/InP double-heterostructure lasers, were reported.

The initial 1.5 μm InGaAsP/InP laser design was similar to that of the proof-of-concept 1.3 μm laser diode, with modifications to the QW active region to obtain emission at 1.5 μm . The laser devices were grown on n-type (100) InP substrates. The typical structure consists of an n-InP buffer layer and an n-InP cladding layer with a graded doping profile, a thick, lightly doped InGaAsP waveguide layer, a nominally undoped MQW active region, a p-InP cladding layer with a graded doping profile, a p-InP cap layer, and a p⁺-InGaAs contact layer.

Figure 5.21a–d show the cross-section SEM, CL peak intensity, CL linewidth, and CL peak wavelength images around the active layer of an InGaAsP/InP MQW laser diode (1.3 μm) [85]. All CL spectra were measured at 28 K to obtain intense CL signals. The acceleration voltage of the electron beam was 15 kV. As can be seen in Fig. 5.21b, the CL intensity is high at the centre of the active layer but declines to a low value at the right and left edges of the active layer [85]. Furthermore, the CL peak at the right and left edges of the active layer shifts to longer wavelengths,

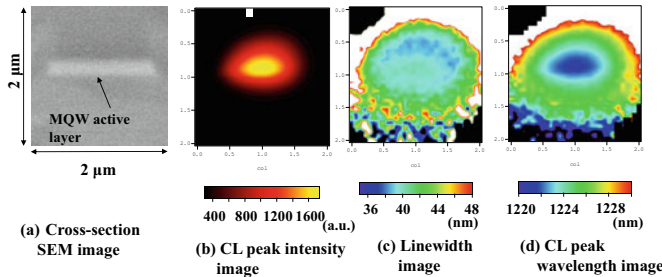


Fig. 5.21 **a** The cross-section SEM image, **b** CL peak intensity, **c** CL linewidth, and **d** CL peak wavelength images around the active layer of an InGaAsP/InP MQW laser diode [85]

compared with that at the centre, while the linewidth of the right and left edges of the active layer broadens, compared with that of the centre (Fig. 5.21c, d). These data suggest that the crystallinity at the edge of the active layer is lower than that at the centre [85].

Figure 5.22a, b show the cross-section SEM image and typical Raman spectra around the active layer, respectively [85]. In Fig. 5.22b, the peak frequency of TO phonon at points A and B around the active layer, observed at 304 cm^{-1} , shifts to higher frequencies, compared with that of a single crystalline InP (100) wafer. This shows that points A and B around the active layer are under compressive stress [85]. We can transform the peak-frequency shift of TO phonon from that of a single crystalline InP into the compressive stress by applying for the published value of 1.34 GPa/cm^{-1} [85].

Figure 5.23a–c show a schematic of the active layer, the line profile (10 μm in length) of stress, and linewidth in the direction perpendicular to the centre of the active layer (line A) and the position 5 μm from the active layer (line B), measured by steps of 0.5 μm from the top surface [85]. As shown in Fig. 5.23b, c, the compressive stress at the point near the active layer in line A is found to be stronger than that in

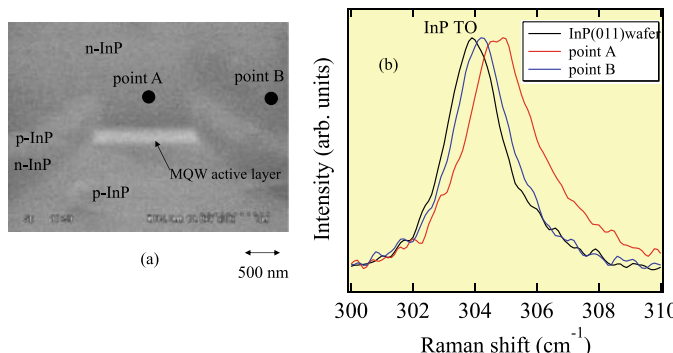


Fig. 5.22 **a** The cross-section SEM image and **b** typical Raman spectra around the active layer [85]

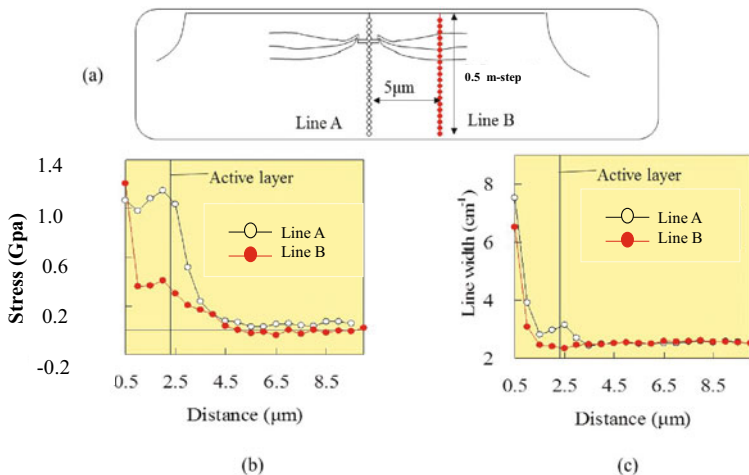


Fig. 5.23 **a** Schematic of the active layer, **b** the line profile (10 μm in length) of stress, and **c** linewidth in the direction perpendicular to the centre of the active layer (line A) and the position of 5 μm from the active layer (line B), measured in 0.5 μm steps from the top surface [85]

line B, and a decrease in crystallinity occurs in the active layer due to an increase in the linewidth at the point near the active layer in line A [85].

The comparison of Figs. 5.22 and 5.23 suggests that the decrease in the CL intensity at the right and left edges of the active layer is mainly caused by high compressive stresses in GPa order, originating from the fact that the active layer is confined by other layers, such as the current blocking layers [85].

5.6 Wide-Gap Semiconductors: Gallium Nitride and Related Materials

GaN, InN, AlN, and their alloys have been intensively studied as materials for the fabrication of light-emitting diodes (LEDs) and laser diodes (LDs) in the blue and UV regions [86]. It is important to characterise the basic physical properties of these materials so that the device quality can be improved. Resonant Raman scattering by phonons is one of the most important techniques for simultaneously obtaining information about the electronic and lattice vibrational properties of materials [87–95]. In particular, this technique is valuable for selective extraction of information about one thin layer that satisfies the resonant condition among individual layers in quantum wells (QWs).

GaN crystallises in a wurtzite structure whose Z-axis is perpendicular to the sapphire substrate plane (c axis). The space group belongs to C_{6v}^4 . Two formula units are contained in the unit cell. Based on the factor group analysis at the Γ point, optical phonons belong to the following irreducible representations [96]:

$$\Gamma_{\text{opt}} = A_1(Z) + 2B + E_1(X, Y) + 2E_2 \quad (5.5)$$

Figure 5.24a, b depict a schematic of polarised Raman measurement configuration, and depolarized and polarised Raman spectra of single crystalline GaN film ($4 \mu\text{m}$ thick) on a sapphire substrate. Especially, E_2 phonon is strongly observed at approximately 570 cm^{-1} in $X(Y, Y)\bar{X}$ configuration (the cross-sectional direction of the GaN film). We can estimate the depth profile of stresses at the interface between GaN film and sapphire substrate, measuring the peak-frequency shift of E_2 phonon [97].

Figure 5.25a, b show a schematic structure of single crystalline GaN film ($4 \mu\text{m}$ thick) on the sapphire substrate and the depth profile of the compressive stress as a function of a position [97]. We transformed the peak-frequency shift of E_2 phonon from that of a single crystalline GaN into the compressive stress by applying for the published value of $-4.1 \text{ cm}^{-1}/\text{GPa}$. The compressive stress tends to decrease with approaching to the sapphire substrate. This might be caused by a warpage of the substrate.

In a polar semiconductor, collective excitation of free carriers (plasmon) interacts with the LO phonon via their macroscopic electric fields, to form the longitudinal optical phonon–plasmon coupled (LOPC) mode. The LOPC modes are broad and their peaks shift to higher frequency with increasing free carriers. The carrier density dependence of LOPC modes has also been reported by Klein et al. in n-type GaAs, and GaP [98, 99]. Figure 5.26 shows the E_2 phonon frequency dependence of a Mg content for Mg-doped GaN films on sapphire substrates. The E_2 phonon shifts to high-frequency side with increasing the Mg content. Our result agrees well with that of Harima et al. [100]. We can estimate carrier concentrations of GaN films by measuring the frequency shift of E_2 phonon with the Mg content.

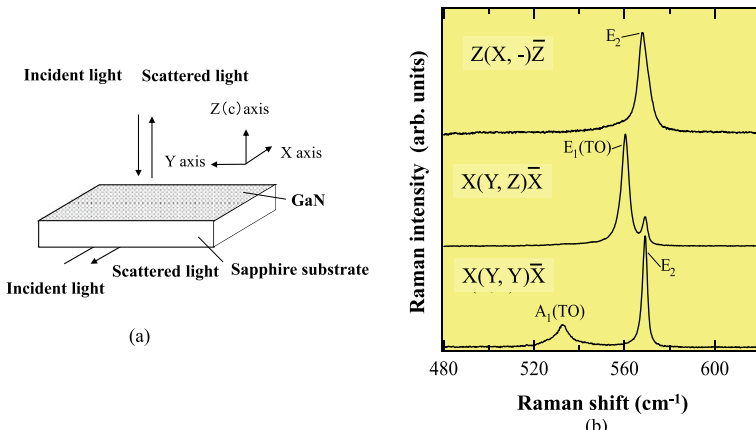


Fig. 5.24 **a** Schematic of polarised Raman measurement configuration, and **b** depolarized and polarised Raman spectra of single crystalline GaN film ($4 \mu\text{m}$ thick) on a sapphire substrate [97]

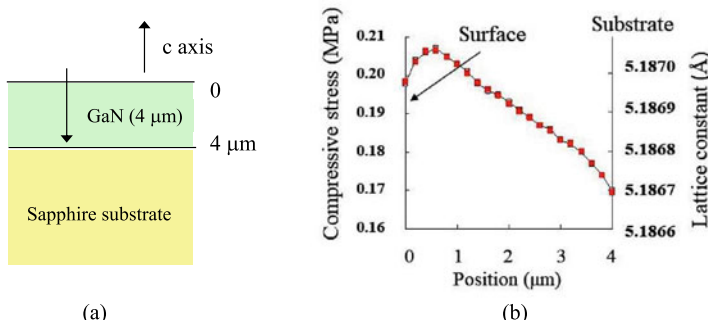


Fig. 5.25 **a** Schematic structure of single crystalline GaN film (4 μm thick) on the sapphire substrate, and **b** the depth profile of the compressive stress as a function of a position [97]

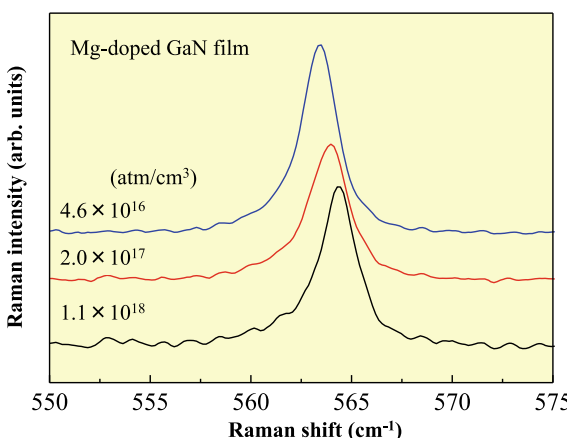


Fig. 5.26 The E_2 phonon frequency dependence of a Mg content for Mg-doped GaN films on sapphire substrates [97]

Figure 5.27 illustrates a schematic of blue light-emitting diode (LED). LED consists of p-type clad, InGaN active, and n-type clad layers on a sappier (or SiC) substrate [97].

In Sect. 2.1, the Stokes scattering peaks are stronger than the anti-Stokes scattering peaks. The intensity ratio of the Stokes scattering peak normalised by the anti-Stokes scattering peak is expressed by Eq. (2.6). Reversely, we can estimate the temperature of LED under operating conditions, in situ, by measuring the relative intensity of the Stokes and the anti-Stokes lines.

Figure 5.28 shows the principle of temperature measurement of LEDs by Raman spectroscopy, the Stokes, and the anti-Stokes Raman spectra of the active layer, respectively [97].

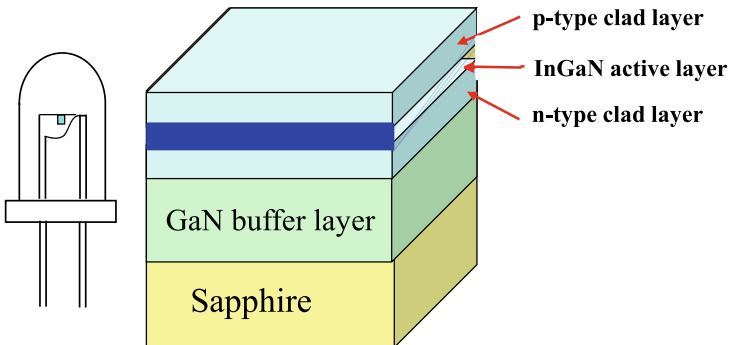


Fig. 5.27 A schematic of bule light-emitting diode (LED)

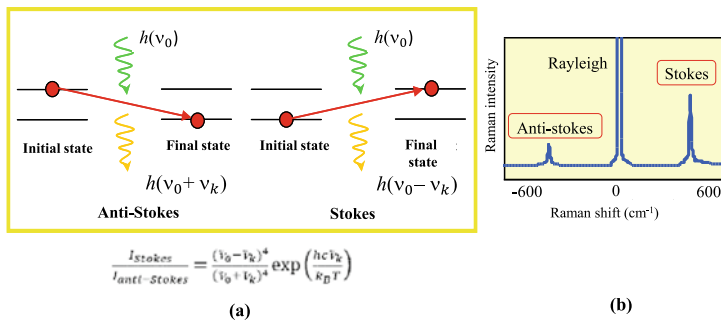


Fig. 5.28 **a** Principle of temperature measurement of LEDs by Raman spectroscopy, and **b** the Stokes, and the anti-Stokes Raman spectra of the active layer

Figure 5.29a–c show a schematic of blue-purple LED, the temperature dependence of the device on the current under the operation, and the temperature distribution of the device at a current of 150 mA as a function of distance from an active layer [97]. As seen in Fig. 5.29b, the temperature of the blue-purple LED at the active layer rises with an increase in the current. Furthermore, in Fig. 5.29c, during the operation with a current of 150 mA, the temperature goes down from 200 to 120 °C with increasing distance from the active layer to 10 μm [97].

Figure 5.30a–c depict the images at the CL 463 nm peak of the bule-purple LED under before operation, after operation, and CL spectra of the bule-LED under before operation, after operation, and after severe operating conditions [97]. From comparison of Fig. 5.30a, b, dark spots (DSs) originating from threading dislocations (TDs) are found to dramatically increase after the operation. Further, the CL peak at 463 nm is hardly observed in specimen degraded under severe operating conditions.

Figure 5.31a, b show the CL intensity image at 463 nm and the peak wavelength image of the cross-sectional active layer for the degraded blue-LED. For the degraded blue-purple LED, the CL intensity of the active layer is found to be scattered within

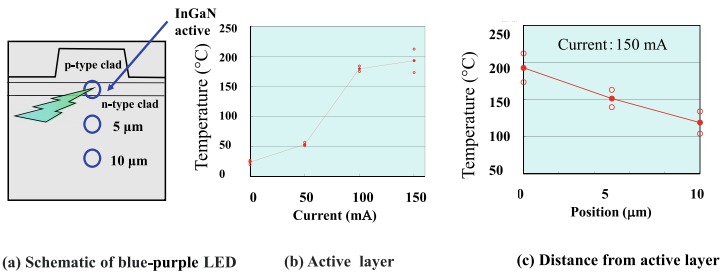


Fig. 5.29 **a** Schematic of blue-purple LED, **b** the temperature dependence of the device on the current under the operation, and **c** the temperature distribution of the device at the current (150 mA) as a function of distance from active layer [97]

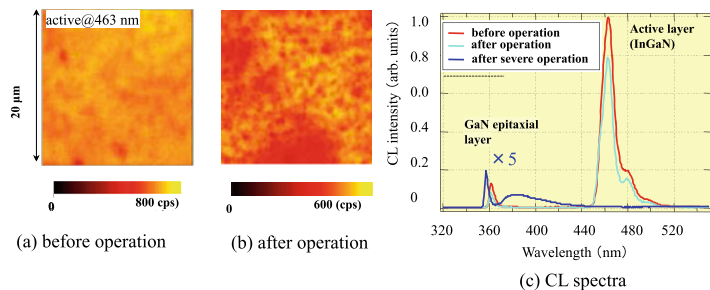


Fig. 5.30 The images at the CL 463 nm peak of the bule-purple LED **a** under before operation, **b** after operation, and **c** CL spectra of the bule-purple LED under before operation, after operation, and severe operating conditions [97]

the active layer [97]. Especially, the CL peak shifts to the longer wavelength at the positions where the CL peak intensity becomes weak. This means that the In content in InGaN active layer changes after the degradation of the LED.

Figure 5.32a-d depict the CL intensity and the peak wavelength images of the cross-sectional active layer before and after operating conditions for a blue-LED [97]. As seen in Fig. 5.32a-d, the CL intensity of the active layer is approximately distributed homogeneously and the CL peak is observed at around 405 nm before operation, whereas the CL intensity is distributed inhomogeneously within the active layer and the CL peak shifts from 409 to 415 nm after operation.

Figure 5.33a and b illustrate the resistance images of the cross-sectional LED tip, obtained by scanning spreading resistance microscopy (SSRM) before and after operating conditions, respectively [97]. Within an active layer of blue-LEDs, InGaN/GaN single quantum wells (SQWs) films and/or InGaN/GaN multiple quantum wells (MQWs) films have been used until now and known to have a typical defect, which is referred to as the ‘V-defect’ [101–105]. We studied the formation mechanism of V-defects by using our newly developed SE-SEM-CL [106]. We proposed a model of the formation of V-defects by selective termination of the threading defects (TDs)

Fig. 5.31 **a** CL intensity image at 463 nm and **b** the peak wavelength image of the cross-sectional active layer for the degraded blue-LED [97]

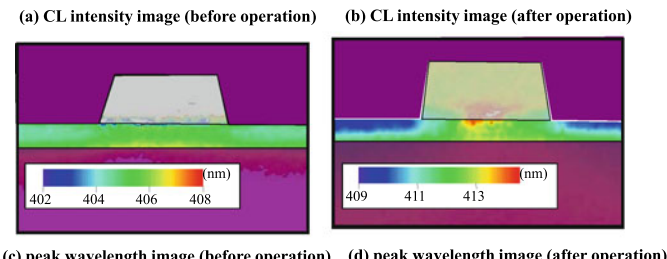
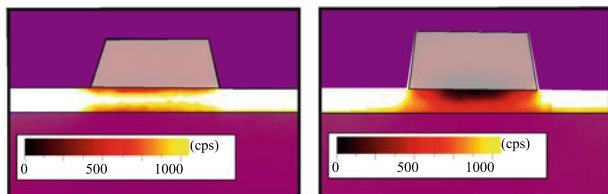
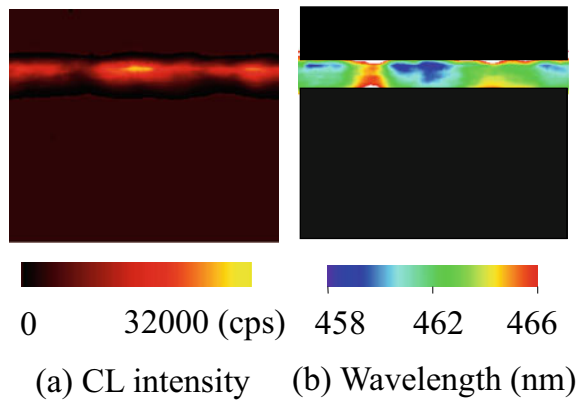


Fig. 5.32 **a** The CL intensity image before operation, **b** the CL intensity image after operation, **c** the peak wavelength image before operation, and **d** the peak wavelength image after operation for the cross-sectional active layer of the blue-LED [97]

on the (0001) surface of pseudomorphic InGaN SQW and GaN buffer layers by In. As seen in Fig. 5.33b, the V-defect increases with a deterioration of the active layer under operation. From comparison between Figs. 5.32 and 5.33, we believe that TDs in the active layer grow with the operation, and then the V-defects are formed in the active layer [97].

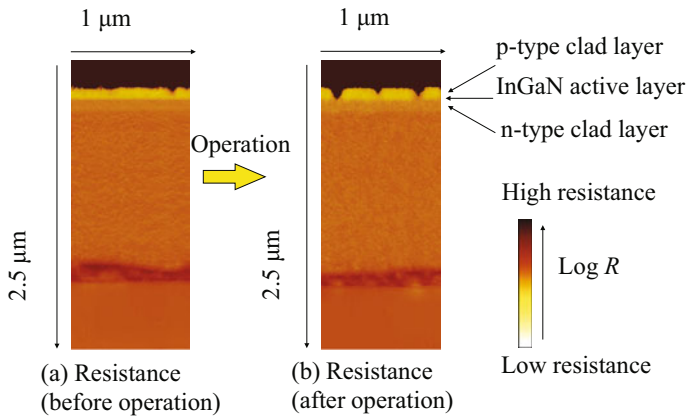


Fig. 5.33 Resistance image **a** before operation and **b** after operation for the cross-sectional blue-LED tip

5.7 Wide-Gap Semiconductors: Silicon Carbide and Related Materials

5.7.1 Silicon Carbide

Silicon carbide (SiC) is a wide-band-gap semiconductor containing native silicon dioxide (SiO_2), the presence of which makes SiC suitable for high-power, high-frequency metal–oxide–semiconductor (MOS) device applications. The high interface trap densities (D_{it}) at the SiO_2/SiC interface and the high effective fixed-charge densities (Q_{eff}), which are one to two orders of magnitude higher than those typically found at the SiO_2/Si interface [107], decrease the channel mobility (CM) [108–111]. The presence of interface traps in SiC MOS field-effect transistors is ascribed to (i) excess carbon [110, 112], (ii) interface defects due to the presence of three-fold coordinated O and C interstitial atoms [110, 112], and (iii) point defects such as Si and O vacancies, which expand into the SiC layer under the SiO_2/SiC interface [113, 114]. Although post-oxidation annealing (POA) in H_2 [108], NO [115, 116], or N_2O [109, 117–119] effectively increases the CM, the effect of POA on the microstructure of SiO_2 films on SiC wafers has not been sufficiently studied.

There are many polytypes of the SiC crystal. The SiC polytypes are uniaxial [hexagonal (H) or rhombohedral (R)], except for 3C-SiC, which is cubic. It is essential to control the polytype during crystal growth because the band-gap energy and electrical properties depend on the polytype. The recent development in crystal growth and device fabrication using SiC crystals requires polytype identification and qualitative characterisation of as-grown and processed SiC crystals. Figure 5.34 shows a schematic crystal structure of the SiC polytypes. The SiC polytypes can be described by different stacking of the Si–C double layers perpendicular to the direction of the

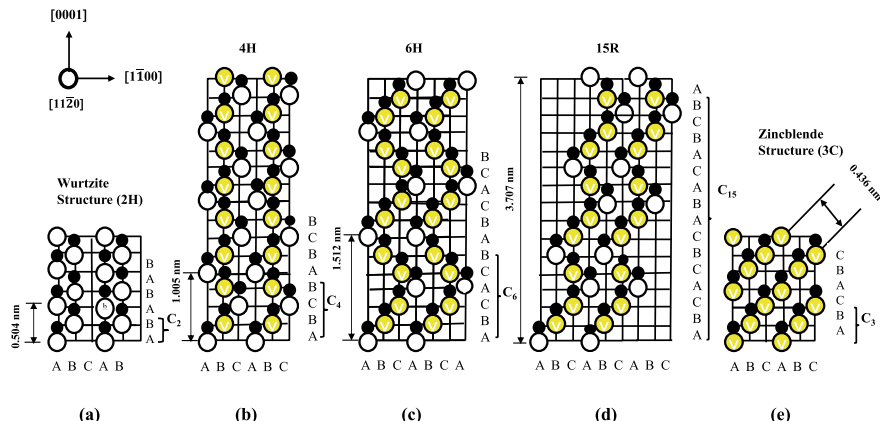


Fig. 5.34 A schematic crystal structure of the SiC polytypes [85]

closed-packed plane, that is, the cubic (111) or the hexagonal (0001). More than 200 different SiC polytypes are reported in the literature, and there are only one cubic (C), and several hexagonal (H) and rhombohedral (R) structures. The ideal face-centred cubic or 3C-structure follows an ABCABC... stacking sequence, whereas the stacking sequence in the [0001] direction, for example, of the hexagonal polytype 4H is ABCBAB..., where A, B, and C represent the three possible positions of the Si-C double layers in Fig. 5.34 [85, 120, 121].

Raman spectroscopy is a powerful technique for the characterisation of SiC polytypes because it is non-destructive and requires no special specimen preparation. Furthermore, because the Raman efficiency of this material is high owing to its strong covalent bonds, intense Raman signals are easily obtained. Raman parameters such as the intensity, width, peak frequency, and polarisation of the Raman bands provide important information on the crystalline quality.

As can be seen in Fig. 5.34, there are many SiC polytypes with different stacking sequences of the double atomic planes of Si-C along the *c* direction. The polytypes are regarded as natural superlattices. Figure 5.35 shows the entire Raman spectra of the 4H, 6H, and 15R polytypes, which are observed in backscattering geometry [85].

The simplest polytype with the shortest period is the 3C polytype which has a zinc-blende (cubic) structure [120, 121]. The type of SiC crystal is denoted by the number of Si-C double layers in the unit cell and the letter H or R, which specifies the lattice type. The primitive unit cell of *n*H or 3*n*R polytypes contains *n* formula units (Si-C) [120, 121]. The unit cell length of the polytypes along the *c* axis (which corresponds to the (111) direction of the zinc-blende structure) is *n* times that of the basic polytype (α -type SiC). Accordingly, the Brillouin zone in the Γ -L direction is reduced to 1/*n*th the size of the basic Brillouin zone; i.e., it is a minizone [120, 121]. The dispersion curves of the phonon modes propagating along the *c* direction in higher polytypes are approximated by folded dispersion curves in the basic Brillouin zone. Nakashima et al. observed the folded longitudinal optical (FLO) and acoustic

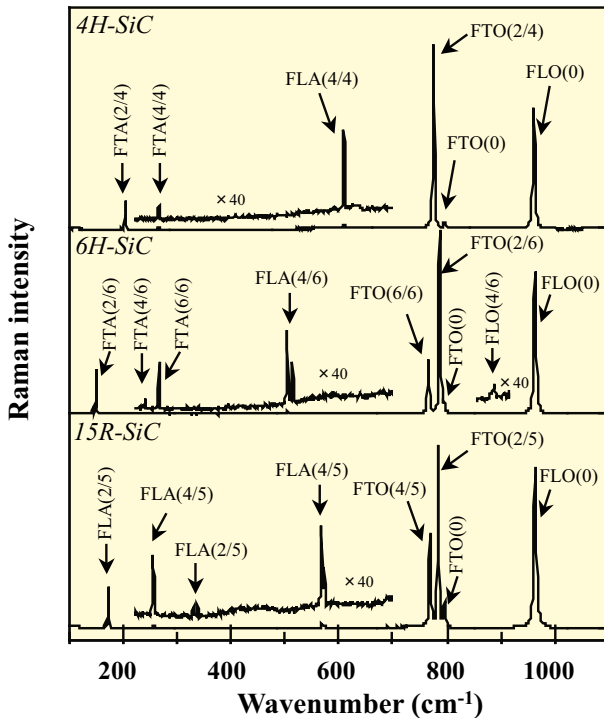


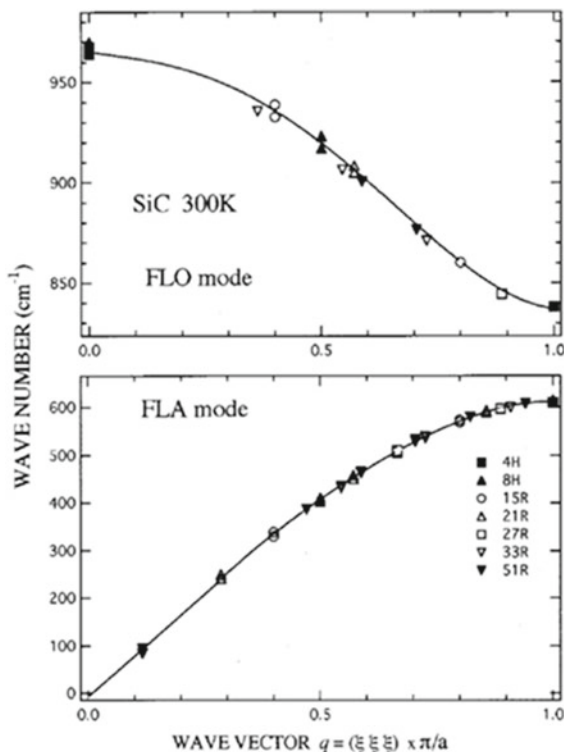
Fig. 5.35 Raman spectra of **a** 4H, **b** 6H, and **c** 15R polytypes [85]

(FLA) modes of various polytypes and obtained the phonon dispersion curves of 3C-SiC in the Γ -L direction, which were derived from the frequencies of the folded modes of various polytypes [120, 121]. The result is shown in Fig. 5.36.

Furthermore, Nakashima and Tahara performed quantitative structural analysis by measuring the Raman intensity profiles of SiC polytypes [120, 121]. They calculated these profiles using the force-constant parameters of a linear chain model that was obtained by fitting the experimentally observed phonon dispersions and Raman intensity profiles [120, 121]. Their result agreed quantitatively with the observed spectra of a number of polytypes. On the basis of this result, they suggested that the bond polarisability model could be applicable to the folded modes of both the acoustic and optical branches of any SiC polytype by using the set of force constants thus determined [120, 121].

In addition, Nakashima et al. measured the backscattering Raman spectra of SiC polytype crystals with SiC (0001) polar faces using deep ultraviolet (DUV), ultraviolet (UV), and visible excitation sources [120, 121]. The folded modes of the transverse acoustic (FTA), longitudinal acoustic (FLA), and longitudinal optical (FLO) branches of the SiC polytypes show sharp doublets for the folded modes that correspond to a phonon inside the Brillouin zone of the basic polytype (3C-SiC) [120, 121]. The zone-folded modes are characterised by the reduced wave vector, x (=

Fig. 5.36 Dispersion curves of the LO and LA modes, which transmit along the (111) direction in 3C-SiC and are estimated from the observed folded mode frequencies of various polytypes [121] (Reproduced with permission from Ref. [121]. © American Physical Society, 2000.)



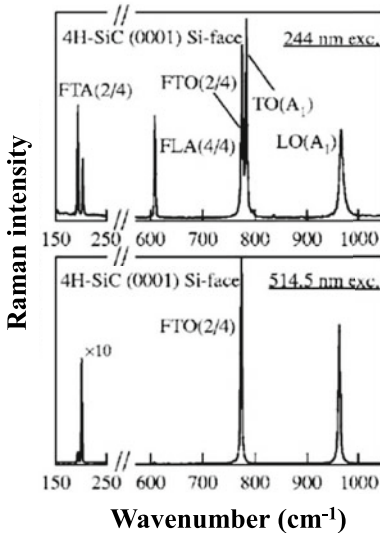
q/q_B); a folded mode corresponds to a phonon mode at a reduced wave vector in the Brillouin zone of the 3C polytype (zinc-blende structure). The doublets of the folded modes are denoted as FTA ($\pm x$) and FLO ($\pm x$), for example [120, 121].

Figure 5.37 shows Raman spectra measured from a 4H-SiC crystal with Si (0001) faces under 244 and 514.5 nm excitation [122]. Under DUV excitation, the resonance of the Raman bands of the FTA (2/4) mode at approximately 200 cm^{-1} , [122] the FLA (4/4) mode at 610 cm^{-1} , and the forbidden TO (A_1) band at 776 cm^{-1} were dramatically enhanced [122]. The FTA ($\pm 2/4$) mode constitutes a doublet in which the low- and high-frequency components exhibit markedly different relative intensities under DUV and visible excitation. These folded mode intensities are much weaker than the TO (E_2 , 778 cm^{-1}), and LO (A_1 , 960 cm^{-1}) mode intensities [122].

Figure 5.38 shows the DUV Raman spectra of several folded modes of the Si (0001) and C (000 $\bar{1}$) faces in 4H-, 6H-, and 15R-SiC under excitation at 244 nm [122]. These folded modes are formed by doublets in which the high- and low-frequency components are both very sharp (less than 2 cm^{-1} wide), although their intensities are much weaker than those of the TO (E_2) and LO (A_1) modes [122].

The relative intensities of the two components of the doublets are different for opposite faces. The intensity ratios of the components of the FTA ($\pm 2/4$) mode are opposite for the Si and C faces [122]. The Raman spectral profiles of the folded

Fig. 5.37 Raman spectra of 4H-SiC crystal under excitations at 244 and 514.5 nm [122]. (Reproduced with permission from Ref. [122]. © American Physical Society, 2000.)

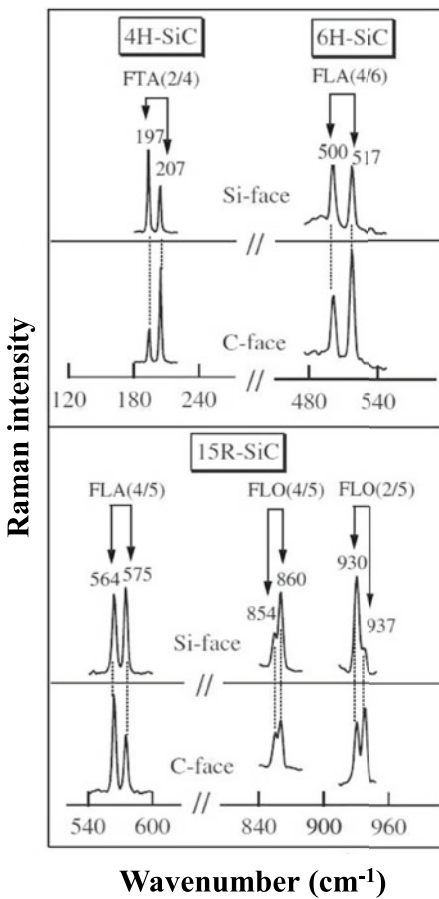


modes in the SiC polytypes were measured in detail under visible excitation and compared with the calculated results of travelling wave solutions for the atomic displacements [122]. Nakashima et al. reported that the calculated intensity ratio, $I (+)/I (-)$, of the FTA (2/4) mode in the 4H polytype under 514.5 nm excitation was approximately 11 [122]. The experimental intensity ratio was approximately 10, in agreement with the calculated value. Under 244 nm excitation, $I (+)/I (-)$ was 1.84 and 0.14 for the Si and C faces, respectively [122]. According to these results, the intensity profiles of these doublets change with the excitation wavelength, that is, with the optical penetration depth of the excitation light. Under DUV excitation, the intensity profiles of the zone-folded modes of the Si and C faces differ drastically [122]. This spectral feature is attributed to the presence of nonpropagating phonon modes confined in the near-surface region [122]. Nakashima et al. concluded that the surface-bound phonon modes created by a DUV photon field extend a few hundred nanometres in depth and that the displacements of the phonon modes are anisotropic in the direction of the polar axis [122]. They found that surface-orientation-dependent Raman measurement can be a useful method for identifying the surface polarity of SiC polytypes [122].

There have been still practical problems with high-power SiC devices such as reliability of gate oxide, quality, defect-formation mechanism of SiC epitaxial film, optimization of ion implantation, and packaging technology. These problems can be solved using scanning capacitance microscopy (SCM), cathodoluminescence (CL), Raman spectroscopy, and Fourier transform infrared spectroscopy (FT-IR).

The progress of SiC high-voltage p-i-n diodes is inhibited by degradation during forward carrier injection at room temperature. This phenomenon is considered as the expansion of Shockley-type stacking faults (SFs), in the process referred to as

Fig. 5.38 Raman intensity profiles of Si (0001) and C (000 $\bar{1}$) faces for typical folded modes in 4H-, 6H-, and 15R-SiC polytypes under excitation at 244 nm [122] (Reproduced with permission from Ref. [122]. © American Physical Society, 2007.)



‘recombination-enhanced dislocation motion’ [123]. Various techniques have been utilised to investigate the SFs in deteriorated diodes [123]. EL imaging is one of the most effective tools to observe the dislocation motion *in situ*.

However, an excitation region is confined in the junction region, and it is difficult to excite any region of interest by the EL method. If electron–hole recombination plays an important role in the motion of SFs, this SF motion can be detected in other carrier-injection techniques [123]. We investigated the influence of electron-beam irradiation on defects in 4H-SiC diode structures, using CL microscopy [124].

Two types of stacking faults (SFs), labelled SF1s and SF2s were observed in addition to threading-edge dislocations (TEDs) and threading-screw dislocations (TSDs). The SF1s at $\lambda = 425$ nm (2.92 eV) expand from the surface of basal plane dislocation with line direction [117–125] and change their geometric shape with the electron-beam irradiation, whereas the SF2s at $\lambda = 471$ nm (2.63 eV) are slightly influenced by electron-beam irradiation. The SF1s are considered to correspond to the

Shockley-type SFs observed in the degraded p-i-n diodes by Sridhara et al. [126]. On the other hand, the SF2s are assigned to in-grown SFs with 8H structure, which were reported by Harada et al. [127]. This result agrees with previous reports [128, 129].

We considered that the TSD surface was not the nucleation site because SF2 is located at a deep position far from the surface [124]. Although the precise depth of the nucleation site was not clear in our experiments, we concluded that the interface between the substrate and the epitaxial layer was not the nucleation site because of the penetration depth of the electron beam [124]. Panchromatic CL images suggest that there are non-radiative recombination (NRRCs) centres in the vicinity of Shockley-type SFs. We insisted that the NRRC of electron and hole was at least necessary to expand the SF. Panchromatic CL images provide us with information about NRRCs.

Ion implantation is a vital low-temperature process for SiC device fabrication to activate dopant atoms into an epitaxial SiC wafer as the ions, thereby changing its physical, chemical, or electrical properties. Activation of implanted ions and recovery of lattice damage are essential for SiC device fabrication. It is necessary to perform a post-implantation annealing process at a temperature higher than 1600 °C to activate an implanted ion as an impurity and to recover the ion implantation-induced lattice disorder. Many reports have been published on the ion implantation induced damage. For example, the generation of secondary defects after post-implantation annealing has been studied by TEM observation [130–132]. A significant reduction in the deep-level defects and an improvement in the carrier lifetime were observed in 4H-SiC epitaxial layer with shallow ion implantation layer and subsequent annealing above 1600 °C by Storasta et al. [133]. They concluded that the reduction in the deep-level defects after the implanted layer is attributable to the diffusion of carbon interstitials (C_i) from the shallow implanted layer. If one could see it from the opposite side, it might be possible to find the phenomenon that the point defect diffusing from the implanted area generates an intrinsic defect complex, such as D_I centre, in the deeper unimplanted area.

We investigated the depth distribution of optically active defect centres induced by Al ion implantation and subsequent annealing in 4H-SiC crystals, using cross-sectional CL spectroscopy.

Figure 5.39 shows cross-sectional SEM image, Q_0 , and L_1 intensity line profiles, and CL spectra obtained from Al ion-implanted SiC epitaxial layer (fluence of 1.8×10^{14} Al ions/cm², 12-μm thick), grown on an 8°-off 4H-SiC (0001) substrate after activation annealing at 1700 °C for 10 min [134]. The sharp CL band around 425 nm is the no-phonon L_1 line, which originates from the D_I defect [134–136]. The zero-phonon line of an N-bound exciton, labelled Q_0 , is observed at 382 nm [134]. The no-phonon L_1 line superimposed by the phonon-assisted structure is detected in SiC specimens, which underwent high-energy ion or electron bombardment and successive high-temperature annealing. The origin of the D_I defect was interpreted as a native-defect complex, possibly antisite pair, $C_{Si}-Si_C$ [136]. In Fig. 5.39, the L_1 line intensity increased with depth. The L_1 line was detected only at point 4 over 10 μm depth far from the end of the implanted layer (0.8 μm, point 1) [134]. The CL intensity in the implanted layer (point 1) is much lower than that in the area under the implanted layer. This means that the CL intensity is quenched in the implanted

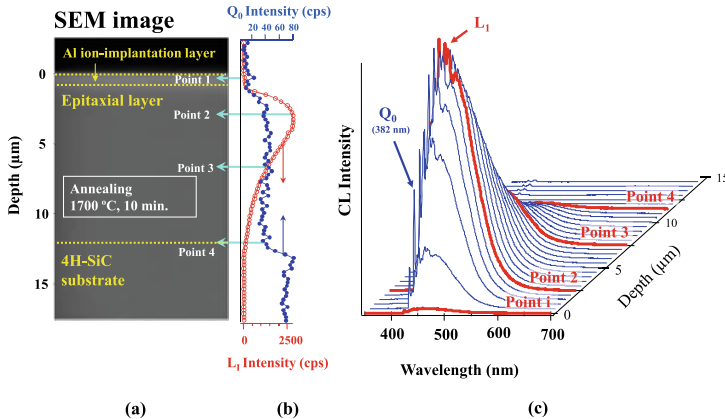


Fig. 5.39 **a** Cross-sectional SEM image, **b** Q_0 , and L_1 intensity line profiles, and **c** CL spectra obtained from Al ion-implanted SiC epitaxial layer (fluence of 1.8×10^{14} Al ions/cm 2 , 12 μ m thick), grown on an 8°-off 4H-SiC (0001) substrate after activation annealing at 1700 °C for 10 min

layer by the presence of high-density defects that serve as NRRCs [134]. The L_1 line intensity shows the maximum value at point 2 of a 3 μ m depth, which is deeper than the end of the implanted layer. It is worth recognising again that the 0.8 μ m thick box profile was confirmed by SIMS measurements [134]. Furthermore, we found that the strong L_1 luminescence that originates in the D_I defect was observed even in the deep region (point 4) where implanted ions could not penetrate. In the implanted layer, CL measurements showed that high-density non-radiative defects remained even after activation annealing up to 2000 °C. The generation of the D_I defect in the deep region is probably caused by the diffusion of point defects from a defective implanted layer.

Sugie et al. performed cross-sectional CL and scanning capacitance microscopy (SCM) measurements for SiC metal–oxide–semiconductor field-effect transistors (MOSFETs) to investigate process-induced defects [137]. Commercially available 1200 V SiC MOSFETs with a discrete package were used in their study. They mechanically cut the package and polished the cross-section, and finally finished the procedure using argon ion beams [137].

We measured FT-IR spectra of the SiO₂ and gate oxide layers of the SiC MOSFET [138]. Figure 5.40a–c depict SEM image, FT-IR spectra of the SiO₂ layers, which consist of phosphosilicate glass (PSG) and undoped silicate glass (USG) layers, and gate SiO₂ layer, after delamination of the SiC MOSFET. As can be seen in Fig. 5.40b, the FT-IR peak assigned to P=O stretching vibrational mode was 1320 cm $^{-1}$ in the upper PSG layer whereas its peak was not observed in the lower USG layer, although the TO phonons were observed at 1070 cm $^{-1}$. We can distinguish the different silicon oxide layers by measuring the FT-IR spectra of SiC MOSFETs. The gate oxide layer was thinned using dilute HF (0.05% HF) solution from 60 nm to a final thickness (8 nm).

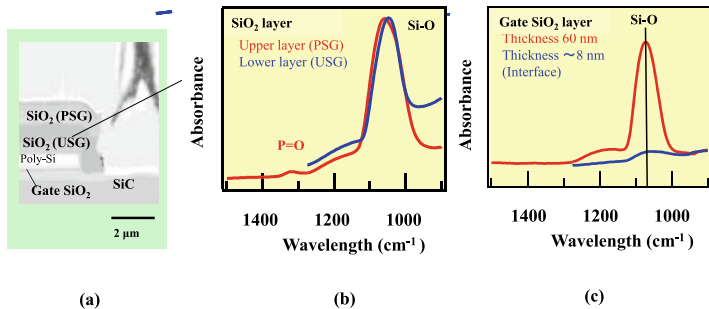


Fig. 5.40 a SEM image, FT-IR spectra of the SiO₂ layers, which consist of **b** phosphosilicate glass (PSG) and undoped silicate glass (USG) layers, and **c** gate SiO₂ layer, after delamination of the SiC MOSFET [138]. The gate oxide layer was thinned using dilute HF (0.05% HF) solution from 60 nm to a final thickness (8 nm)

In Fig. 5.40c, the TO phonon of a gate oxide film with a thickness of 60 nm is observed at 1070 cm^{-1} , whereas the TO phonon of gate oxide film with a thickness of approximately 8 nm shifts to the low wavenumber side. This indicates that the oxygen concentration (SiO_{2-x}) decreases near the interface between the gate oxide layer and electrode.

Figure 5.41 shows the cross-sectional dC/dV image measured by scanning capacitance microscopy (SCM), monochromatic CL image at L_1 line, and CL spectra of the SiC MOSFET at 35K [138]. The source region consists of a heavily doped n-type region surrounded by a p-type region. The drift layer is of the n-type and is formed by epitaxial growth, whereas the channel and source regions are formed by ion implantation and annealing. The n+-p-n junction is constructed in the device [138].

Figure 5.41b displays the monochromatic CL image of the SiC MOSFET at 35K [138]. In Fig. 5.41b, the CL intensity image is not uniform and low near the source region, which almost matches the implanted region as compared with Fig. 3 of Ref. [137]. Figure 5.41c shows the CL spectra at each point depicted in Fig. 5.41b [138]. A near-band-edge CL, several sharp peaks, and a broad CL peak are observed in all

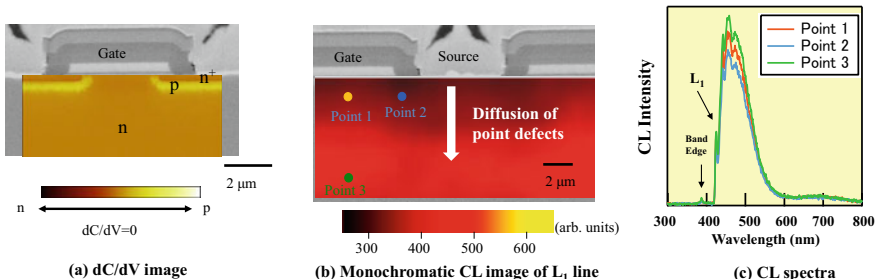


Fig. 5.41 (Color online) **a** Cross-sectional dC/dV image measured by SCM, **b** monochromatic CL image (L_1 line) of the SiC MOSFET at 35K, and **c** CL spectra at points 1, 2, and 3 at 35K [138]

spectra. The origin of the broad CL peak around 420–600 nm is not identified but is considered to be probably a kind of donor–acceptor pair (DAP) emission [137]. The sharp 426 nm peak is the D_I defect-related no-phonon line (L_I) and several CL peaks around 430–470 nm are its phonon replicas. The D_I centre is considered to be one of the intrinsic native point defects and is frequently observed in various kinds of SiC polytypes subjected to ion implantation or electron irradiation. The L_I line is the main D_I defect-related emission in 4H-SiC at temperatures lower than 10 K. But two new no-phonon lines labelled M_I and H_I were observed at slightly higher energies when the temperature is increased [135]. Therefore, it may be more appropriate to ascribe the sharp CL peak observed at 426 nm to the mixture of L_I, M_I, and H_I lines instead of the L_I line only because the temperature is 35 K in their experiment. The D_I centre is stable and observable even after annealing at 2000 °C [134]. Although the structure of the D_I centre is not fully identified, the antisite pair Sic–Csi and several variations are proposed for the structure of the D_I centre [139]. In Fig. 5.41b, a D_I defect-related line (L_I) is explicitly detected in all spectra, even though points 2 and 3 are located in the n-drift layer and not in the implanted region [138].

SCM can visualise the carrier distribution, while CL can evaluate crystalline defects in SiC MOSFETs. The L_I line originates from the point defect whose structure is the antisite pair of C and Si. The point defects generated by the ion implantation remain and diffuse into the epitaxial layer entirely.

From a comparison between the CL and SCM images, we concluded that L_I lines related to D_I centres existed even in the channel region near the gate and in the deep n-drift region located 10 μm far from the surface [138]. The cross-sectional CL spectroscopy can provide the visual defect distribution and is a useful method for the characterisation of the process-induced defects in SiC MOSFETs and other SiC-based devices [138].

Figure 5.42a–d illustrate a schematic, cross-sectional photograph of a commercially available SiC MOSFET, a change in compressive stress at points A–C, and local residual stress image of the SiC MOSFET [140]. The E₂ [folded transverse optical (FTO)] phonon mode is observed at 776 cm⁻¹. Generally, the E₂ phonon shifts to lower and higher wavenumber sides under tensile and compressive stresses, respectively. As a result, we can estimate the stresses of SiC devices, measuring the wavenumber shift of the E₂ phonon, using Raman spectroscopy. As seen in Fig. 5.42c, the compressive stresses are found to distribute within the cross-sectional SiC wafer (tip) and become large in the order point C < point B < point A and especially, the strong compressive stress of 120 MPa occurs at the corner of the SiC-chip, point A. Furthermore, because the E₂ phonon shifts to the high wavenumber side under the gate and source electrodes in Fig. 5.42d, we found that the compressive stresses occurred at the areas under the gate and source electrodes in the epitaxial SiC layer. On the other hand, the tensile stresses at the surrounding areas of the areas under the compressive stresses are attributed to a trade-off between the compressive and tensile stresses [140].

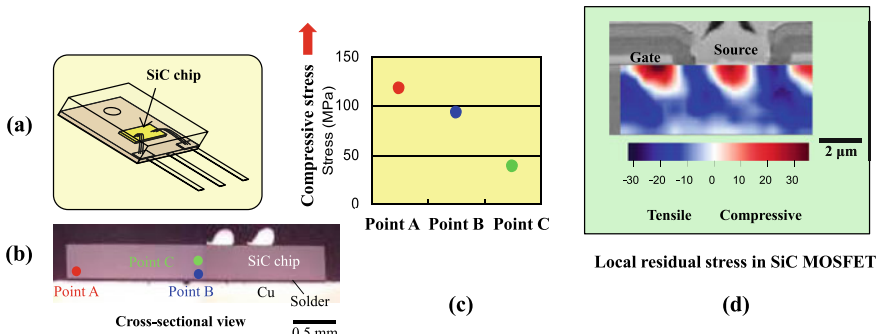


Fig. 5.42 **a** Schematic, **b** cross-sectional photograph of a commercially available SiC MOSFET, **c** change in compressive stress at points A–C, and **d** local residual stress image of the SiC MOSFET [140]

5.7.2 Silicon Thermal Oxide Film (SiO_2)

FT-IR spectroscopy is a powerful method for investigating chemical bonding structures in thin thermal oxide (SiO_2) films. However, transparent FT-IR spectra of SiO_2 films prepared on commercially available 4H-SiC substrates cannot be measured because of the strong absorption due to the free carriers in the substrates. Consequently, the attenuated total reflection (ATR) geometry is utilised as a sensitive technique for studying SiO_2 films. Transverse optical (TO) and longitudinal optical (LO) phonons in SiO_2 films on a Si wafer have been observed at around 1072 and 1257 cm^{-1} , respectively [114]. These phonons are assigned to the asymmetrical stretching of O in the intertetrahedral Si–O–Si bridge [141]. The peak frequency of these phonons is considered to shift depending on factors such as the electromagnetic phase shift, inhomogeneity, densification, porosity, and SiO_2 film thickness. However, because these factors are interdependent, it is difficult to elucidate the origin of this frequency shift in the TO and LO phonons. Although numerous studies using FT-IR spectroscopy have been undertaken with regard to SiO_2 films on Si wafers, no research has previously been published concerning the chemical bonding structures at the interface between SiO_2 films and SiC wafers [116, 117].

We reported abnormal behaviour of LO phonon in a SiO_2 film on a 4H–SiC bulk epitaxial substrate with the help of an ATR technique [17]. The LO-like phonon frequency with an asymmetric lineshape in the ATR spectrum was observed at around 1165 cm^{-1} and red-shifted by approximately 92 cm^{-1} relative to that at the grazing incidence angle (40°) [17].

Figure 5.43 shows the normal (transparent) and grazing incidence, and ATR spectra of a thick (100 nm) SiO_2 film on a bulk epitaxial 4H-SiC substrate (100 μm thick). The dominant features in the grazing incidence spectrum (40°) are LO and TO phonons arising from asymmetric Si–O stretching motions of the constituent SiO_4 tetrahedra, at 1257 and 1072 cm^{-1} , respectively, whereas only the TO phonon is observed in the normal incidence (transparent) FT-IR spectrum (Berreman effect

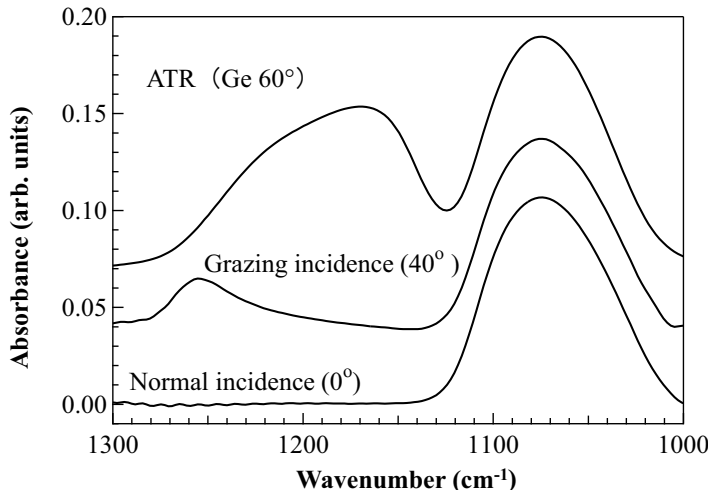


Fig. 5.43 The normal (transparent), grazing incidence (40°), and ATR spectra of a thick (100 nm) SiO_2 film on a bulk epitaxial 4H-SiC substrate (100 μm thick). The incident angle in the ATR spectrum was fixed at 60° , and a Ge crystal was used as an internal reflection element (ATR prism) [17] (Reproduced with permission from Ref. [17]. © SAGE Publications, 2013.)

[142]). This result shows that the polarisation property of the LO phonon to the incident light is maintained for the thick film (100 nm). The TO phonon in the ATR spectrum was observed at around 1072 cm^{-1} .

Surprisingly, despite of the same specimen, the peak frequency of the LO phonon in the ATR spectrum was observed at around 1165 cm^{-1} and red-shifted by approximately 92 cm^{-1} relative to that at the grazing incidence (40°), whereas the peak frequency of the TO phonon in the ATR spectrum agreed well with that at the grazing incidence. The peak frequency of the LO phonon did not depend on the change in the grazing incident angle, although its intensity changed with the grazing incident angle. Furthermore, the peak frequency of the TO phonon hardly depends on the change in the incident angle and thickness. This suggests that the microstructure of the specimen is homogeneous within a thickness of 100 nm. We considered that the asymmetric modes located between 1110 and 1250 cm^{-1} were ascribed to the upper and lower branches of surface polaritons (SPPs) [17]. Moreover, we divided the asymmetric modes between 1110 and 1250 cm^{-1} into two peaks with Lorentzian lineshapes and concluded that the two peaks divided could be attributed to the upper and lower branches of SPPs at the air- SiO_2 and SiO_2 -4H-SiC interfaces [17].

To confirm the assignment of the asymmetric modes located between 1110 and 1250 cm^{-1} , we measured the ATR spectra of thermal SiO_2 films (approximately 100 nm thick, or 50 nm thick) on an SiC and Si wafers, thinned using dilute HF (0.05% HF) solution to a final thickness (10 nm or 5 nm) [17, 143]. Figure 5.44a, b show the ATR spectra of (a) a thermal oxide SiO_2 film (10–100 nm thick) on an SiC substrate and a thermal oxide SiO_2 film (5–50 nm thick) on an Si substrate,

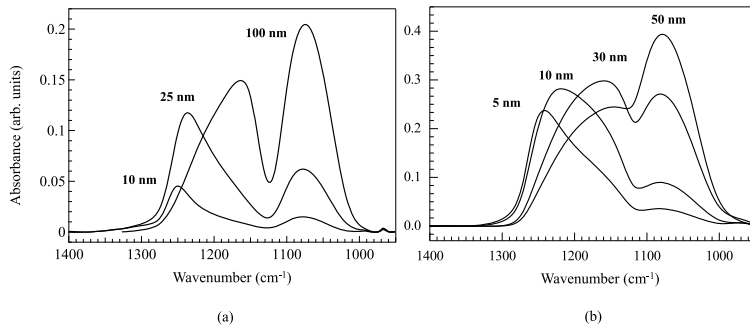


Fig. 5.44 The ATR spectra of **a** a thermal oxide SiO_2 film (10 – 100 nm thick) on an SiC substrate and **b** a thermal oxide SiO_2 film (5–50 nm thick) on an Si substrate, thinned using a dilute (0.05%) HF solution from 100 nm or 50 nm to a final thickness (10 nm or 5 nm). The incident angle was fixed at 60° with a Ge crystal [143] (Reproduced with permission from Refs. [17, 143]. © SAGE Publications, 2013, and 2014.)

thinned using a dilute (0.05%) HF solution from 100 nm or 50 nm to a final thickness (10 nm or 5 nm), respectively. The LO-like phonon frequency shifts to a higher frequency, from 1150 cm^{-1} to 1250 cm^{-1} , as the oxide-layer thickness decreases. Because the TO phonon frequency is independent of the oxide-layer thickness, the large blue-shift of the LO-like phonon frequency observed for the standard SiO_2 film on the Si wafer also cannot be interpreted with by any of the five factors such as (1) the electromagnetic phase shift, (2) inhomogeneity, (3) densification, (4) porosity, or (5) SiO_2 film thickness, previously discussed [17, 143].

The ATR spectra of the SiO_2 film on the SiC wafer coincide well with those on the Si substrate [17, 143]. From this work, we found that the SPPs were also observed in FT-IR spectra of a standard SiO_2 film on an Si wafer. Chen et al. have observed an SPP at approximately 1142 cm^{-1} ($8.76 \mu\text{m}$) in a $1 \mu\text{m}$ thick SiO_2 film on an Si wafer and yielded a propagation length of approximately $11 \mu\text{m}$ for the silicon dioxide SPP resonance at 1142 cm^{-1} [144]. This result and their work [144] support our observation [17] of SPPs in the SiO_2 films on 4H-SiC substrates. Furthermore, we found that the peak frequency of the upper branch of SPPs roughly shows a linear shift with oxide-layer thickness. This suggests that the frequency measurement of the upper branch of SPPs in the ATR configuration is used as a monitor for the oxide-layer thickness.

CL spectroscopy provides us with considerable information on defects in thin SiO_2 films [145–147]. In a prior study [147], SiO_2 films (41–47 nm thick) were grown on 4H-SiC (0001) Si, $(1\bar{1}00)$ M, and $(11\bar{2}0)$ A faces by post-oxidation annealing (POA) in ambient NO at 1250°C , and it was found that the SiO_2 film grown on the 4H-SiC $(11\bar{2}0)$ A face had a very large CM of $112 \text{ cm}^2/\text{Vs}$ [147]. To study the origin of this high CM, we investigated the variations in the CL spectra of SiO_2 films on 4H-SiC (0001) Si, $(1\bar{1}00)$ M, and $(11\bar{2}0)$ A faces, suffered from POA in ambient NO. For an acceleration voltage of 5 kV, the CL peak attributed to oxygen

vacancy centres (OVCs) became weak by POA, while the CL peak related to the Si–N bonding structures became intense with increasing CM [147]. This suggests that OVCs at the SiO_2/SiC interface are terminated by N. We indicated that NO-ambient POA increases the CM more effectively than that of ambient N_2O [147].

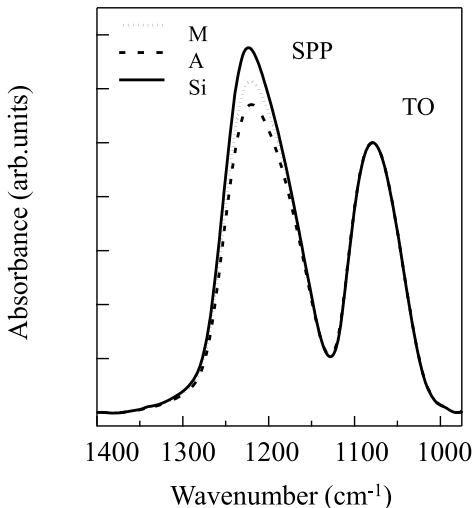
We prepared SiO_2 films with channel mobilities (CMs) of 35, 105, and $112 \text{ cm}^2/\text{Vs}$ on 4H-SiC (0001) Si, (1–100) M, and (11–20) A faces by post-oxidation annealing (POA) in NO ambient and measured FT-IR spectra. The preparation conditions of specimens were shown in more detail in Refs. [17] and [146] (we call those specimens Si, M, and A, respectively). The D_{it} values were obtained from high- (1 MHz) and low-frequency (quasi-static) capacitance–voltage (C – V) curves of n-type MOS capacitors, and the Q_{eff} values were calculated from the flatband voltage in the C – V curves. The thicknesses, oxidation conditions, D_{it} , Q_{eff} , and CM values of three specimens are listed in Table 5.3 [143].

Figure 5.45 shows the FT-IR spectra measured by the ATR geometry of thin (41–47 nm) SiO_2 films on 4H-SiC substrates, respectively. The peak frequency of SPPs in the SiO_2 films underwent the maximum red-shift by approximately $30\text{--}90 \text{ cm}^{-1}$ relative to the LO phonon at 1257 cm^{-1} in a grazing incidence of the thermally grown SiO_2 films on an Si substrate [143]. As seen in Fig. 5.45, because the TO phonon frequency in the ATR spectrum coincided well with that in the grazing incidence

Table 5.3 Thickness, thermal oxidation, POA condition, interface trap densities (D_{it}), effective fixed-charge densities (Q_{eff}), and channel mobility (CM) of thermally grown SiO_2 films on the 4H-SiC substrates [143] (Reproduced with permission from Ref. [143]. © SAGE Publications, 2014.)

Face	Thickness (nm)	Thermal oxidation condition	Post-oxidation annealing condition	$D_{it} (\text{cm}^2\text{eV})^{-1} (E_c - 0.2 \text{ eV})$	$Q_{eff} (\text{cm}^{-2})$	Mobility (cm^2/Vs)
Si	41(5)	1250 °C 60 min	NO anneal 1250 °C, 60 min Ar anneal 1250 °C, 60 min	5.0×10^{11}	1.5×10^{11}	35 ± 1
A	47(5)	1250 °C 10 min	NO anneal 1250 °C, 60 min Ar anneal 1250 °C, 60 min	3.4×10^{11}	1.8×10^{11}	112 ± 1
M	45(5)	1250 °C 10 min	NO anneal 1250 °C, 60 min Ar anneal 1250 °C, 60 min	3.6×10^{11}	1.7×10^{11}	105 ± 1

Fig. 5.45 FT-IR spectra measured using the ATR geometry of thin (41–47 nm) SiO_2 films (specimens Si, M, and A) on an 4H-SiC epitaxial substrate



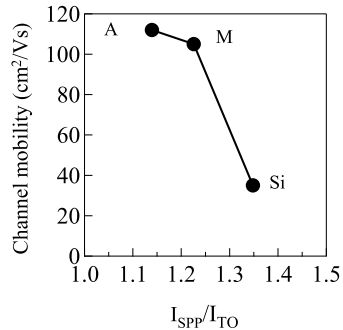
(or transparent) spectrum of typical SiO_2 films on an Si wafer, the maximum redshift of 30–90 cm^{-1} relative to that (1257 cm^{-1}) in thermally grown SiO_2 films on an Si substrate cannot be interpreted with any of the common factors, such as the electromagnetic phase shift, inhomogeneity, densification, porosity, or SiO_2 film thickness [143]. We concluded that the asymmetric modes located between 1110 and 1250 cm^{-1} were attributable to the upper and lower branches of SPPs, based on the model proposed by Mills and Maradudin [143].

Figure 5.46 depicts the relation between the relative intensity of the upper branch of SPPs normalised by that of TO phonon and the CM for specimens Si, M, and A, respectively [143]. As seen in Fig. 5.46, the relative intensity shows a tendency to increase as CM decreases. In general, SPPs are considered to be more intense with increasing film inhomogeneity because of a breakdown in the conservation of momentum between the incident photon and the phonon. This SPP feature indicates that the inhomogeneity of SiO_2 films increases in the specimens in the order A < M < Si in Fig. 5.46 [143].

We previously observed CL spectra of the SiO_2 films on epitaxial layers (approximately 5 μm thick), which were oxidised under the same deposition conditions, at acceleration voltages of 3 and 5 kV [146]. We found that for an acceleration voltage of 5 kV, CL peaks at 460 and 490 nm, attributed to OVCs, weaken through POA in ambient N_2O at 1300 °C, while the 580 nm CL peak, related to Si–N bonding structures, becomes stronger. Moreover, the peak ascribed to N– Si_3 configurations in X-ray photoelectron spectroscopy (XPS) spectra was observed at the SiO_2/SiC interface, only in specimens annealed in ambient N_2O . These results mean that D_{it} decreases and CM in n-type MOS capacitors increases with the termination of dangling bonds by the N atom at the SiO_2/SiC interface [143].

Figure 5.47a, b depict the CL spectra of SiO_2 films of the specimens Si, M, and A, thinned utilising dilute HF (0.05% HF) solution to a final thickness (5 nm) on the

Fig. 5.46 Relation between the relative intensity of the upper branch of SPPs normalized by that of the TO phonon and CM for specimens Si, A, and M [143] (Reproduced with permission from Ref. [143]. © SAGE Publications, 2014.)



epitaxial 4H-SiC substrates (approximately 5 μm thick), measured at acceleration voltages of 3 and 5 kV, respectively [143]. The 390 nm peak originates from a bound exciton of the epitaxial 4H-SiC substrates. The 540 nm peak is attributed to donor–acceptor pairs [146] or defect-related emission bands of the substrates. CL peaks were observed at 460, 490, 600, and 670 nm for the SiO₂ films on the 4H-SiC substrates. The 460 and 490 nm peaks were ascribed to OVCs, while the 600 and 670 nm peaks could be assigned to Si–N bonding structures and non-bridging oxidation hole centres (NBOHCs), respectively [145–147].

The weak 280 nm peak was assigned to OVCs [147]. The broad CL spectra of the SiO₂ films were decomposed into six CL peaks for quantitative analysis with Gaussian lineshapes [147]. In Fig. 5.47a, b, the 600 nm peak intensity tends to become intense in the specimens in the order Si < M < A when detected at acceleration voltages of both 3 and 5 kV [143].

Figure 5.48a, b illustrate the relation between the CM of the SiC MOSFET and the relative CL intensity at 600 nm, normalised by that at 670 nm, detected at acceleration voltages of 3 and 5 kV, respectively [143]. In Fig. 5.48, the relative intensity becomes more intense in the specimens in the order Si < M < A at 3 and 5 kV. This shows that the POA resulted in the decrease in the number of NBOHCs by N termination at the SiO₂/SiC interface in the specimens in the order Si > M > A, and that the inhomogeneity of SiO₂ films decreases in the specimens in the order Si > M > A, giving rise to an increase in CM [143].

In Fig. 5.46, we discovered that the relative intensity of the upper branch of the SPPs normalised by that of the TO phonon becomes intense with decreasing CM [143]. Based on a comparison between Figs. 5.46 and 5.48, we concluded that the SPP intensity correlates with the inhomogeneity of the SiO₂ films, which can be useful for monitoring the inhomogeneity at the SiO₂/SiC interface and of the CM in n-type MOS capacitors [143]. A combination of FT-IR and CL spectroscopy provides us with a large amount of data on the inhomogeneity, defect, and oxide thickness of SiO₂ films on 4H-SiC substrates [143].

We characterised the stress distribution of SiC epitaxial layer under the oxide layer of a cross-sectional 4H-SiC MOSFET, combining Raman spectroscopy and TEM analysis. For the TEM analysis, we used the nanobeam electron diffraction (NBD)

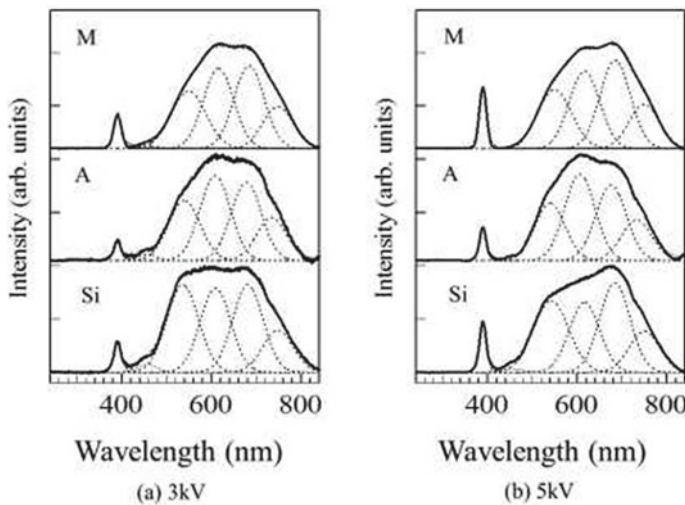


Fig. 5.47 The CL spectra for Si, M, and A SiO_2 films, **a** obtained at an acceleration voltage of 3 kV, **b** obtained at an acceleration voltage of 5 kV. The specimens were thinned using a dilute (0.05%) HF solution to a final thickness (5 nm) on the epitaxial 4H-SiC substrate (approximately 5 μm thick) [143] (Reproduced with permission from Ref. [143]. © SAGE Publications, 2014.)

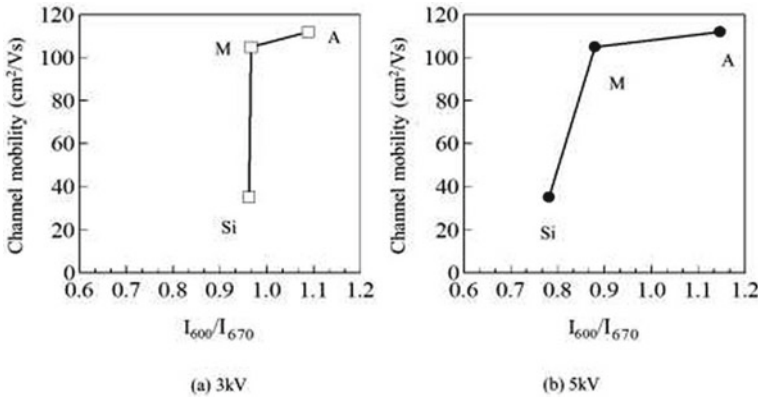


Fig. 5.48 Relation between the CM of the SiC MOSFET and the relative CL intensity at 600 nm, normalized by the intensity at 670 nm; **a** obtained at an acceleration voltage of 3 kV, **b** obtained at an acceleration voltage of 5 kV [143] (Reproduced with permission from Ref. [143]. © SAGE Publications, 2014.)

method [144]. NBD method consists of illumination of a nanometer-size area of the specimen with a parallel electron beam and acquiring diffraction patterns in the area of interest, and then measuring the distance between the diffracted spots within the diffraction patterns. The strain is calculated by comparing the diffraction pattern

acquired in the area of interest with the pattern acquired in an unstrained area as a reference.

Figure 5.49 depicts a schematic of a cross-sectional 4H-SiC MOSFET. We measured the diffraction pattern of the rectangular area (purple colour) by NBD method, and Raman spectra of the rectangular area ($50 \mu\text{m} \times 7 \mu\text{m}$, red colour), respectively [148].

Figure 5.50a, b show the electron diffraction pattern of the rectangular area (purple line) in Fig. 5.49, and the intensity profile along the arrow in Fig. 5.50a.

Figure 5.51a, b illustrate the cross-sectional TEM image and strain distribution at each position in Fig. 5.51a, calculated by NBD method. From 5.51b, it is found that each position in the epitaxial SiC layer under Al source electrode is at maximum applied with a compressive stress of approximately 1.0%, whereas each position in the epitaxial SiC layer under the oxide layer could hardly detect strains.

Figure 5.52a, b indicate the stress distribution of the rectangular area ($50 \mu\text{m} \times 7 \mu\text{m}$, red colour) in Fig. 5.49 and the line profile of the stress along the arrow

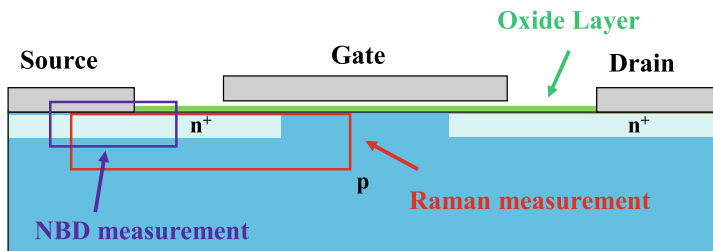


Fig. 5.49 Schematic of a cross-sectional 4H-SiC MOSFET

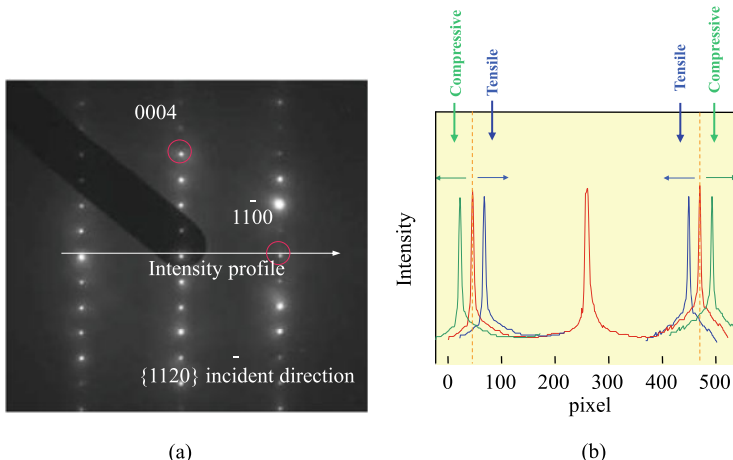


Fig. 5.50 **a** The electron diffraction pattern of the rectangular area (purple line) in Fig. 5.49, and **b** the intensity profile along the arrow in Fig. 5.50 a for 4H-SiC MOSFET [148]

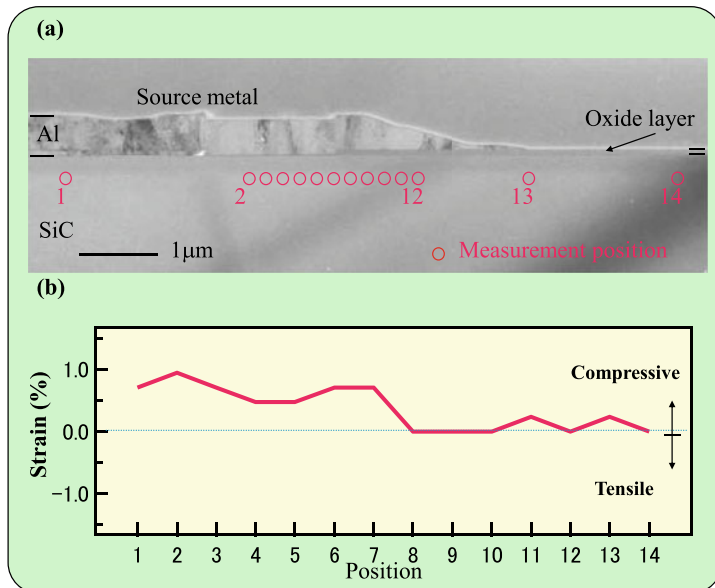


Fig. 5.51 **a** Cross-sectional TEM image and **b** strain distribution at each position in **(a)**, calculated by NBD method for 4H-SiC MOSFET [148]

depicted by Fig. 5.52a, respectively. We measured E_2 phonon frequency at each position and translate the E_2 phonon frequency shift into the stress using Eq. (6) in Ref. [142]. As can be seen in Fig. 5.52a, b, the epitaxial SiC layer near the source and gate electrodes is under compressive stresses of approximately 15 MPa whereas the epitaxial SiC layer near the oxide layer is under tensile stresses of approximately 15 MPa. This result means that Raman spectroscopy is more sensitive than the NBD method regarding stress (strain) characterisation [148].

5.8 Wide-Gap Semiconductor: Zinc Oxide

Zinc oxide (ZnO) is a candidate of wide-band-gap semiconductors for use in high-performance optoelectronic devices, such as UV LEDs, because of its wide band gap (3.37 eV). The optical properties of nanometre-scale devices can be controlled by adjusting the average size of nanometre-sized crystals [149–152]. Although perfect doping of ZnO has not yet been realised, ZnO has exhibited the largest charge-carrier mobility among the oxides and is thus used in UV LDs and several conventional electronic devices. Undoped ZnO exhibits n -type conduction, which is not clearly understood despite several theoretical and experimental studies. This makes p -doping, which is essential for the fabrication of transistors and LEDs, particularly difficult [149–152].

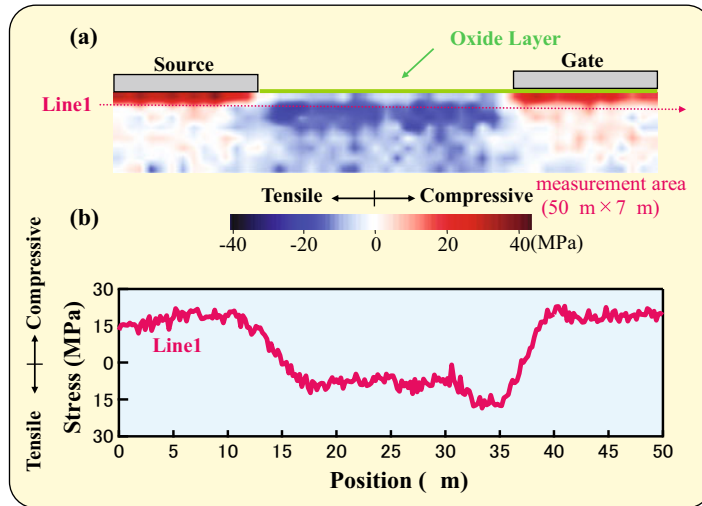


Fig. 5.52 **a** Stress distribution of the rectangular area ($50 \mu\text{m} \times 7 \mu\text{m}$, red colour) in Fig. 5.49 and **b** the line profile of the stress along the arrow depicted by (a) [148]

McCluskey et al. used IR spectroscopy to measure the local vibrational modes (LVMs) in ZnO annealed at 700°C for 120 h in hydrogen gas to study the microscopic structure of the hydrogen donors [153]. They measured the IR absorption spectra of an undoped, single-crystal ZnO specimen and observed an IR absorption peak at 3336.8 cm^{-1} with a full width at half-maximum (FWHM) of 8 cm^{-1} at room temperature [153]. The frequency of 3336.8 cm^{-1} is almost identical to the frequency of LVMs ascribed to O–H complexes in GaAs, which has a stretching mode at 3300 cm^{-1} at liquid helium temperature [154]. McCluskey et al. assigned this IR absorption peak to the stretching mode of O–H complexes in ZnO [153].

On the other hand, Raman spectroscopy is an important tool for characterising the crystallinity of semiconductors. The ZnO with a wurtzite structure belongs to the C_{6v}^4 ($P6_3mc$) space group and has six Raman-active optical phonon modes at the centre of the Brillouin zone [155]:

$$\Gamma_{\text{Opt}} = 2A_1 + 2E_1 + 2E_2 \quad (5.6)$$

The nonpolar E_2 modes have two frequencies, E_2^{low} and E_2^{high} , which are assigned to the Zn and O sublattice vibrations, respectively [155]. The A_1 and E_1 modes are polar; thus the TO and LO phonons have different frequencies because of the macroscopic electric field related to the LO phonons. The different scattering configurations allow different vibrational modes in the Raman spectra [155].

Figure 5.53 shows the visible Raman spectra of a ZnO film prepared on a glass substrate, excited by a 457.9 nm line of Ar^+ laser. Under the visible excitation wavelength, we cannot measure the Raman spectrum because of the obstruction by superimposed PL from the glass substrate.

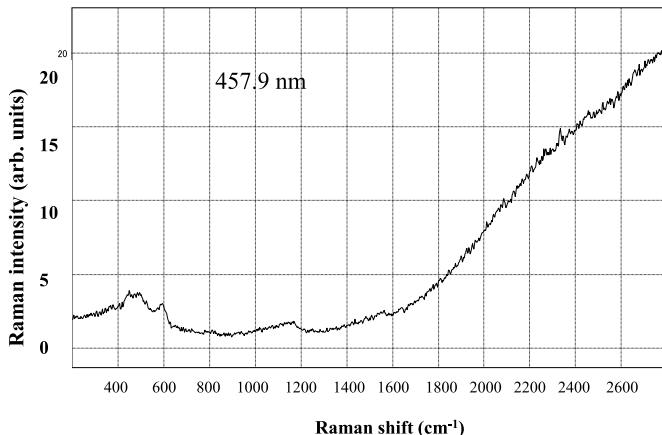


Fig. 5.53 Visible Raman spectra of a ZnO film prepared on a glass substrate, excited by a 457.9 nm line of Ar⁺ laser

Figure 5.54 shows the UV Raman spectra of ZnO films prepared for various growth rates on a glass substrate, exited by a 325 nm line of a He-Cd laser. The growth rate is fast in the specimens in the order $1 < 2 < 3 < 4$. For the 325 nm excitation wavelength, resonant Raman scattering from ZnO is observed and then the first-order (A_1 (LO)), second-order ($2A_1$ (LO)), third-order ($3A_1$ (LO)), and fourth-order ($4A_1$ (LO)) phonons can be detected in Fig. 5.54 [156]. In general, the higher order A_1 (LO) phonons tend to be observed with an increase of crystalline quality. As can be seen, The crystallinity of the ZnO film increases in the specimens in the order $1 < 2 < 3 < 4$.

Figure 5.55 shows the CL spectra of specimens 1, 2, 3, and 4. The CL peak at 360 nm is assigned to a band-edge emission whereas the broad CL band near 600–700 nm is ascribed to OVCs [156]. The intensity ratio of the below-band-gap CL peak at 600–700 nm normalised by the band-edge CL peak at approximately 360 nm becomes weak in the specimens in the order $1 < 2 < 3 < 4$. As a result, the OVC content decreases in the specimens in the order $1 < 2 < 3 < 4$. A comparison of Raman and CL measurements means that the crystalline quality becomes high in the specimens in the order $1 < 2 < 3 < 4$.

For nanometre-sized silicon, the peak frequency of the main Raman mode decreases (this decrease is named the crystallite size effect) as the crystallite size decreases. Moreover, it possesses an asymmetric lineshape and its main peak with some tailing towards low frequencies. Several groups have measured the Raman spectra of ZnO nanoparticles, but they have not observed a dramatical variation of Raman spectra with a decrease in the crystallite size of the ZnO nanoparticles [150, 157, 158]. On the other hand, CL spectroscopy is a useful method to observe luminescence that occurs when a specimen is irradiated by an electron beam [32, 159–161]. In general, the metal oxide possesses a CL peak in the visible region, due to the

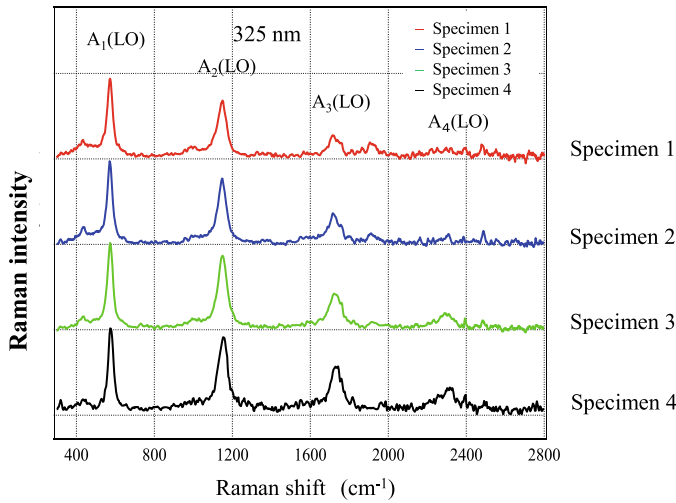


Fig. 5.54 UV Raman spectra of ZnO films (specimens 1, 2, 3, and 4) prepared for various growth rates on a glass substrate, exited by a 325 nm line of a He-Cd laser

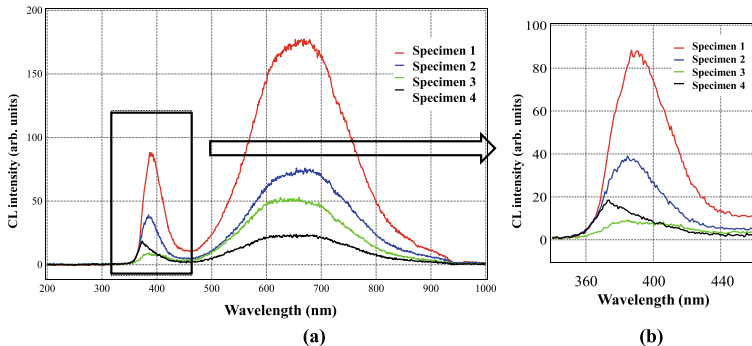


Fig. 5.55 CL spectra of specimens 1, 2, 3, and 4

presence of oxygen vacancy defects (OVDs) [32]. For example, ZnO nanorods show a broad CL peak at approximately 500–600 nm that was attributable to OVDs [32].

Figure 5.56 depicts the cross-sectional TEM images of specimens 1, 2, 3, and 4. As seen in Fig. 5.56a, ZnO nano-pillars with small sizes grow in a direction perpendicular to the film thickness. From a comparison between Fig. 5.56a–d, it is found that the ZnO nano-pillar size becomes large in the specimens in the order 1 < 2 < 3 < 4. From Raman, CL, and TEM measurements, we confirm that the crystalline quality becomes high in the specimens in the order 1 < 2 < 3 < 4.

Figure 5.57 shows Raman and CL spectra of ZnO nanoparticles with different crystallite sizes. The A₁ (LO) phonon at 574 cm⁻¹ is found to have an asymmetric lineshape, which tails towards low frequencies as the crystallite size decrease from

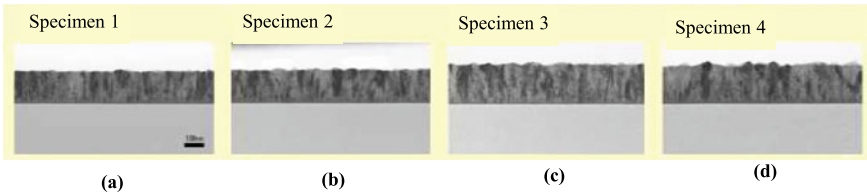


Fig. 5.56 Cross-sectional TEM images of specimens 1, 2, 3, and 4

59.6 to 11.0 nm [156]. Moreover, the peak frequency observed decreases owing to the reduction in crystallite size [156]. The decrease in the frequency at which the peak of the A_1 (LO) phonon is observed, displayed in [156], can be interpreted with the size effect [156]. The intensity ratio of the $2A_1$ (LO) (or higher order) phonon normalised by the A_1 (LO) phonon decreases as decreasing the crystallite size. As shown in Fig. 5.57, the $2A_1$ (LO) phonon peak frequency corresponds to the broad luminescence peak near 1200 cm^{-1} . This means that the $2A_1$ (LO) phonon energy coincides with the band-gap energy of the single-crystal ZnO, and the $2A_1$ (LO) phonon causes strong resonant Raman scattering. This variation in the intensity ratio suggests that the band-gap energy changes with a decrease in the crystallite size [156].

The CL spectra of the ZnO nanoparticles consist of a band-edge CL peak at 360 nm and a broad CL peak near 600 nm [156]. The CL spectra of the ZnO nanoparticles depend to a large extent on the crystallite size. Particularly, the intensity ratio of the below-band-gap CL peak at 600 nm normalised by the band-edge CL peak at approximately 360 nm becomes high as the crystallite size decreases. This indicates that the electronic structures in the ZnO nanoparticles change with the crystallite size [156].

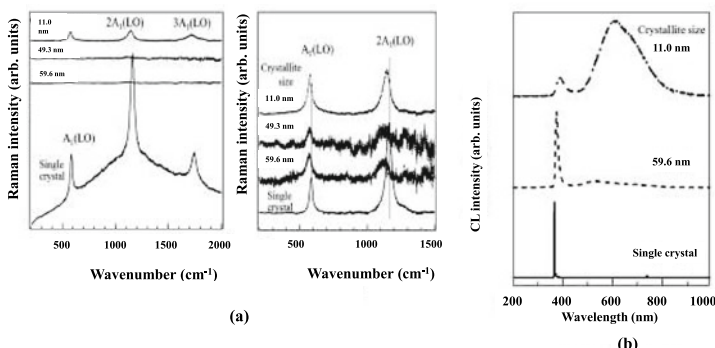


Fig. 5.57 **a** Raman spectra and those after the baseline correction, and **b** CL spectra of ZnO nanoparticles with the different crystallite sizes

The optical properties of nanometre-sized crystals, particularly the optical band gap, are dependent, to a large degree, on the crystallite size [156]. The number of defects tends to increase with decreasing crystallite size, because the surface volume increases with a reduction in the crystallite size, deteriorating the material quality and device performance [156]. From this viewpoint, it is worth investigating the variations in the crystalline quality and the number of defects in ZnO nanoparticles. By combining the resonant Raman scattering technique and CL spectroscopy, we can study the variations in the crystalline quality and the number of defects in ZnO nanoparticles [156].

5.9 Wide-Gap Semiconductor: Diamond

5.9.1 Diamond Films

Diamond films have been prepared by several methods, such as the glow discharge, plasma chemical vapour deposition (p-CVD), and the hot filament method [162–167]. They have excellent hardness, chemical inertness, optical transparency, and thermal conductivity. They are expected for many applications as heat sinks in electronic devices, protective films, and transistors operating at high temperature. Moreover, diamond films could be grown epitaxially only on diamond substrates and not on other types of substrates for various reasons, such as strain in the films and the formation of sp^2 carbons.

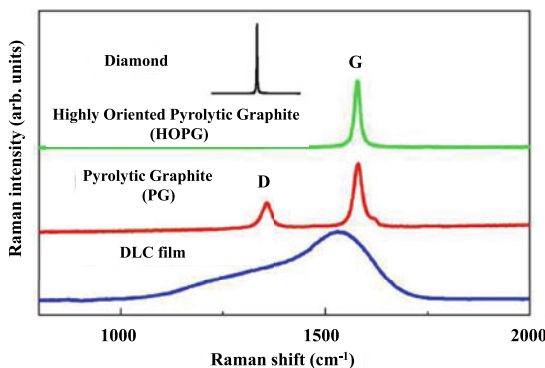
Raman spectroscopy is an important method for characterising carbon materials. For instance, single peaks are observed at 1332 cm^{-1} for diamond [166, 168] and at 1581 cm^{-1} (G band) for highly oriented pyrolytic graphite (HOPG) [169]. In glassy carbon and pyrolytic graphite(PG), which consist of amorphous sp^2 structures, two broad bands are detected at 1360 (disordered (D) band) and 1590 cm^{-1} [170]. An asymmetric broad band appears at approximately 1530 cm^{-1} in diamond-like amorphous carbon (DLC) films [171–173]. Figure 5.58 shows typical Raman spectra of diamond, HOPG, PG, and DLC films.

Diamond belongs to the space group O_h with two atoms per primitive cell. A triply degenerate optical phonon with F_{2g} symmetry is observed at 1332 cm^{-1} in the first-order spectrum, whereas the second-order Raman spectrum of diamond is observed between 2000 and 3000 cm^{-1} . The origin of the second-order spectrum was thoroughly investigated by Solin and Ramdas [174].

The first-order Raman scattering intensity is expressed by [175]

$$I = \sum_j (e_i R_j e_s)^2 \quad (5.7)$$

Fig. 5.58 Typical Raman spectra of diamond, HOPG, PG, and DLC film (unpublished.)

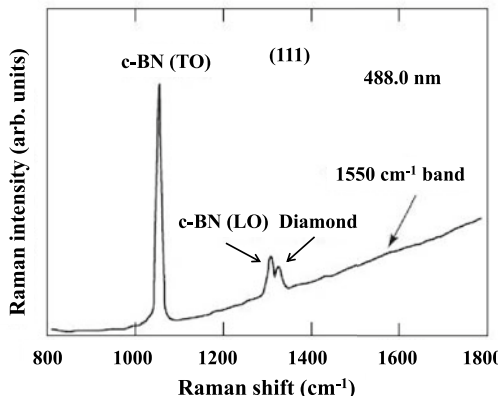


where e_i and e_s are the unit polarisation vectors of the incident and scattered light, respectively, and R_j ($j = x, y, z$) is the Raman tensor of the F_{2g} mode. In the backscattering geometry with the polarisation direction of the scattered light parallel to that of the incident light, Eq. (5.7) is simply given by Eq. (2.9) [176, 177].

Figure 5.59 indicates the Raman spectra of a diamond film prepared by the dc p-CVD method from a mixture of CH_4 and H_2 on the (111) surface of a cubic boron nitride (c-BN) microcrystal $\sim 100 \mu\text{m}$ in size [176]. A sharp diamond line overlapped with the background owing to luminescence appears at approximately 1325 cm^{-1} . A broad band at approximately 1550 cm^{-1} that is ascribed to sp^2 carbon clusters is not detected. Raman bands at 1306 and 1056 cm^{-1} were assigned to the LO and TO phonons of c-BN, respectively [176].

Figure 5.60a display the Raman intensity versus rotation angle (in polar coordinates) of the diamond film grown on the (111) surface of c-BN measured in backscattering geometry [176]. The radial and angular coordinates are based on the intensity of the Raman lines of diamond and c-BN, and the rotation angle of the specimen, respectively. The angular dependence of the Raman intensity of diamond coincides

Fig. 5.59 Raman spectrum of a diamond film on the (111) surface of c-BN under 488.0 nm excitation [176] (Reproduced with permission from Ref. [176]. © AIP Publishing, 1990.)



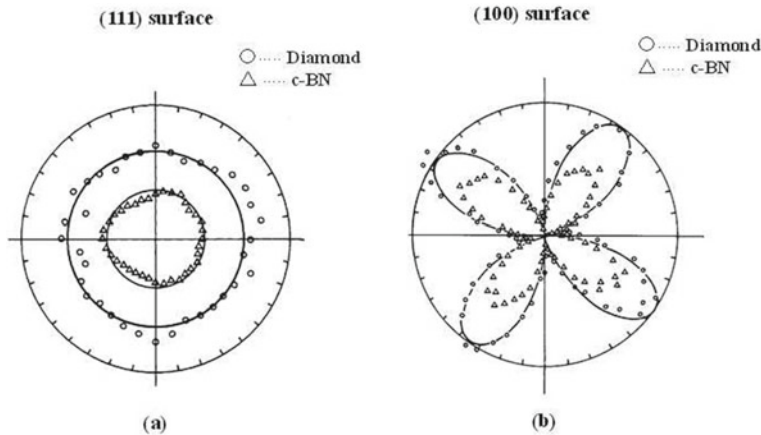


Fig. 5.60 Angular dependence of the Raman intensity of a diamond layer on **a** the (111) surface and **b** the (100) surface of c-BN. The open circles, triangles, and solid lines are experimental data for the lines of diamond and the LO phonon of c-BN, and the calculation curves for the (111) and (100) surfaces of c-BN, respectively [176, 178] (Reproduced with permission from Refs. [176, 178]. © AIP Publishing, 1990, 1991.)

well with that of the (111) surface of c-BN and the calculated curve for this surface [176]. This indicates that the crystallographic orientation of the diamond film is mostly the same as that of the (111) surface of c-BN and that the diamond film grew heteroepitaxially on the c-BN surface [176]. The deviation of the angular dependence of the observed Raman intensity from the calculated curve is attributed to the presence of strains, defects, sp^2 carbon, etc. [176, 177].

The crystallographic orientation of this specimen was also determined by the electron diffraction method [168]. Observation of the diffraction spots means that the diamond film is neither polycrystalline nor amorphous. Furthermore, the diffraction pattern indicates that the diamond prepared on c-BN has cubic rather than hexagonal symmetry [176]. The similarity between the diffraction patterns of the diamond film on the (111) surface of c-BN and the (111) surface of c-BN itself proved that the crystallographic orientation of the diamond film is almost the same as that of c-BN [176].

Figure 5.60b displays the intensity versus rotation angle of the specimen for the diamond film grown on the (100) surface of c-BN [176, 178]. The radial and angular coordinates are based on the intensity of the Raman bands of diamond and c-BN, and the rotation angle of the specimen, respectively [178]. The angular dependence of the Raman intensity of diamond coincides also well with that of the (100) surface of c-BN. This means that the diamond film grew heteroepitaxially on not only the (111) surface but also the (100) surface of c-BN [178].

We studied the Raman spectra of a diamond film deposited on a silicon substrate under various excitation wavelengths [179]. A sharp diamond line at $\sim 1332 \text{ cm}^{-1}$ and an asymmetric broad band centred at $\sim 1530 \text{ cm}^{-1}$ are observed in the spectra

measured under 514.5 nm excitation. The spectral profile of the diamond film agrees well with that of amorphous carbon (a-C) films except for the sharp diamond line [171–173].

The position of the sharp diamond line does not depend on the excitation wavelength, while that of the asymmetric broad band shifts to a lower frequency with increasing excitation wavelength. The spectral variation of the diamond film with the excitation wavelength except for the sharp diamond line coincides well with that of a-C films [179].

The Raman spectral variation of a-C films can be interpreted with resonant $\pi-\pi^*$ Raman scattering from π^* -bonded (sp^2) carbon clusters with various sizes [171–173]. A comparison of the Raman spectra of the diamond film with those of a-C films confirms that the asymmetric broad band at $\sim 1530\text{ cm}^{-1}$ in the spectra of the diamond film is originating from sp^2 carbon clusters with various sizes. We measured the Raman spectra of diamond films prepared using various ethanol concentrations [179]. The intensity of the asymmetric broad band assigned to sp^2 carbon clusters increases relative to that of the sharp diamond line with increasing ethanol concentration [179].

Furthermore, we investigated the high-resolution Raman spectra of diamond in diamond films. The Raman band of natural diamond was measured for comparison [179]. The Raman line of diamond in diamond films was $1\text{--}3\text{ cm}^{-1}$ higher in frequency than that of natural diamond [179]. Furthermore, the Raman line had a dramatically larger linewidth than the natural diamond line. These results mean that the crystalline quality of diamond films is not as good as that of natural diamond [179].

The Raman band of silicon shifts to higher and lower frequency under compressive and tensile stresses, respectively, in silicon films [180]. The degree of stress is obtained by measuring the peak frequency shift. In addition, the Raman bands of diamond reportedly shift to higher frequencies with increasing compressive stress [178].

According to the above results, the peak frequency shift of the Raman line of diamond here means the presence of compressive stress. The lattice constants of diamond and silicon are 0.3567 and 0.5430 nm, respectively [179]. When a diamond film is formed on a silicon substrate, the lattice constant of diamond layers is considered to increase and that of silicon layers is considered to decrease because of the lattice mismatch [179]. As a result, a diamond film on a silicon substrate should be under tensile stress. Hence, the compressive stress in diamond films cannot be interpreted in terms of the difference in the lattice constants [179].

This $1\text{--}3\text{ cm}^{-1}$ shift to higher frequency compared to that of natural diamond, as well as the relative intensity, which indicates the diamond/non-diamond content ratio tends to decrease with increasing degree of stress [179]. These findings suggest a close relationship between the formation of non-diamond material and the presence of strain in the diamond structures. The formation of sp^2 carbon clusters might give rise to the strain and vice versa [179].

Under uniaxial stress parallel to either the $<100>$ or $<111>$ direction, the $k \approx 0$ triply degenerate optical phonon in diamond-type materials is split into a doublet and a singlet mode. According to the selection rule, only the singlet mode can be

observed in the backscattering configuration. The frequency of the singlet mode is expressed by [179, 180]

$$\begin{aligned} v_s &= v_0 + 2v_H - (2/3)v_U \\ v_H &= (p + 2q)(s_{11} + 2s_{12})X/6v_0 \end{aligned} \quad (5.8)$$

$$\begin{aligned} v_U &= (p - q)(s_{11} - s_{12})2v_o \text{ for the (100) plane} \\ v_U &= rs_{44}X/8v_0 \text{ for the (111) plane} \end{aligned} \quad (5.9)$$

where s_{11} , s_{12} , and s_{44} are the elastic compliance constants, X is the stress, and p , q , and r are the changes in the spring constant by strain. The peak frequency shift $\Delta v_s = v_s - v_0$ has a linear relationship with the stress X . The values of s_{11} , s_{12} , s_{44} , p , q , and r in Refs. [181, 182] are

$$\begin{aligned} s_{11} &= 9.524 \times 10^{-14} \text{ cm}^2/\text{dyn}, & p &= -1.071 \times 10^{28} \text{ s}^{-2}, \\ s_{12} &= -0.9913 \times 10^{-14} \text{ cm}^2/\text{dyn}, & q &= -5.260 \times 10^{28} \text{ s}^{-2} \\ s_{44} &= 1.736 \times 10^{-13} \text{ cm}^2/\text{dyn}, & r &= -7.707 \times 10^{28} \text{ s}^{-2} \end{aligned} \quad (5.10)$$

By using these values, the following equation is given [179, 180]:

$$\begin{aligned} X(\text{dyn/cm}^2) &= -1.08 \times 10^{10} \Delta v(\text{cm}^{-1}) \text{ for the (100) plane} \\ &\quad - 2.63 \times 10^{10} \Delta v(\text{cm}^{-1}) \text{ for the (111) plane} \end{aligned} \quad (5.11)$$

We measured the Raman band of diamond in a back scattering configuration because of the weakness of the Raman band and the surface roughness of the films; although the singlet and doublet modes are generally detected in this configuration, the coefficient for the doublet mode is not significantly different from that for the singlet mode in Eq. (5.11) [179, 180]. Further, because the films are polycrystalline, Eq. (5.11) cannot be directly utilised. However, the compressive stress for these specimens can be roughly estimated as being on the order of GPa, and the corresponding strain is estimated to be $\varepsilon = 0.1\text{--}0.2\%$ using the relation [179, 180]

$$e = (s_{11} + s_{12})X \quad (5.12)$$

The lattice constants of the films, as determined by XRD analysis, ranged from 0.3562 to 0.3566 nm [179]. Although the lattice constants of the films did not differ significantly, the peak frequency of the Raman band of diamond changed remarkably with the specimens. This shows that Raman spectroscopy is a sensitive technique for studying crystalline quality, in particular, the strain fields of diamond films [179, 180].

5.9.2 Fano Effect in Diamond

Heavy acceptor doping is well-known to influence the peak frequency and linewidth of the first-order Raman spectra of Ge and Si [183, 184]. The LO phonon lineshape is greatly broadened and deformed by interactions with free holes in heavily doped *p*-type silicon. The effect was investigated by Cerdeira et al. [185] and is reported as Fano-type interference between the LO phonon line and an electronic continuum [186].

Furthermore, the lineshape becomes derivative-like as the excitation wavelength increases [186]. The Fano lineshape can be expressed as [186]

$$I(\varepsilon, q) = A(q + \varepsilon)^2 / (1 + \varepsilon^2) \quad (5.13)$$

$$\varepsilon = \eta(\omega - \omega_0 - \Delta\omega_0) / \Gamma \quad (5.14)$$

where ω_0 is the phonon frequency of the undoped material, $\Delta\omega_0$ is the renormalisation of ω_0 due to the electron–phonon interaction in the doped material, Γ is the broadening due to interference, and q is the Fano asymmetry parameter, which is presented by the electron–phonon matrix and Raman matrix elements between the ground and excited states of the phonon and electron [186]. The strongest asymmetry, with the derivative-like lineshape, can be for $q = 1$, while the lineshape becomes Lorentzian and the asymmetry vanishes as $q \rightarrow \infty$. Cerdeira et al. discovered that the Raman spectral profile of the heavily doped *p*-type Si was depending on the excitation wavelength and that the dependence of q on the laser photon energy E_L was well approximated by $q \approx (3.3 \text{ eV} - E_L)^{-1}$, except under excitation at 647.1 nm [185].

There have been few reports of Raman spectra from heavily doped single crystalline diamond [187]; the Raman spectra of B-doped diamond films have been studied by Locher et al. [188] and Ager et al. [189].

We measured the Raman spectra of the (111) face of B-doped diamond for various carrier concentrations excited with different excitation wavelengths. Figure 5.61a, b show the Raman spectra of the (111) face of B-doped diamond with a carrier concentration of $2 \times 10^{19} \text{ cm}^{-3}$ under 514.5 nm excitation wavelength by an Ar⁺ laser, and 785.0 nm excitation wavelength by a semiconductor laser [190]. The 1332 cm^{-1} band shifts to a lower frequency, broadens and develops a derivative-like lineshape as the B concentration increases [190]. The background in the low-frequency side of the first-order Raman band at approximately 1332 cm^{-1} becomes lower than that in the high-frequency side, which coincides with a reported result for heavily doped *p*-type Si [184].

The Fano parameters obtained by a fitting of each Raman spectrum into the Fano lineshape expressed in Eqs. (5.13) and (5.14) are listed in Table 5.4.

As seen in Table 5.4, the difference in the asymmetry of the lineshapes at excitation wavelengths of 514.5 and 785.0 nm is ascribed to a change from positive to negative q . This result indicates that the interaction between the zone centre phonon and

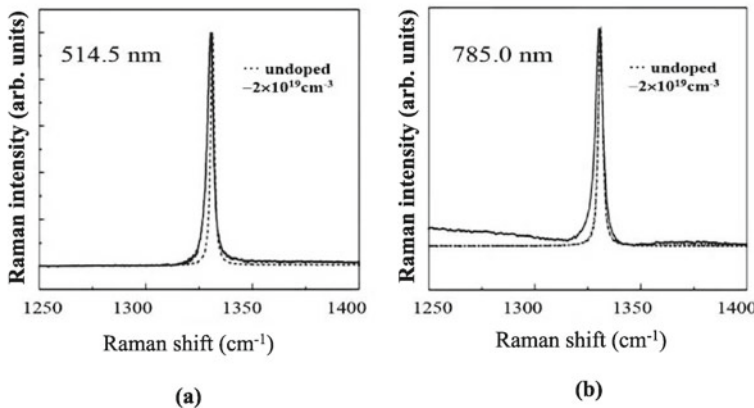


Fig. 5.61 Raman spectra of (111) face of B-doped diamond (carrier concentration of $2 \times 10^{19} \text{ cm}^{-3}$) under **a** 514.5 nm excitation wavelength by an Ar^+ laser, and **b** 785.0 nm excitation wavelength by a semiconductor laser [190] (Reproduced with permission from Ref. [190]. © Trans Tech Publications, 2015.)

Table 5.4 Excitation wavelength and parameters $\Delta\omega_0$, Γ , and q of B-doped diamond obtained by curve fitting of the experimental spectra to Eqs. (5.13) and (5.14)

nm	$\Delta\omega_0$	Γ	q
364.0	-0.46	1.46	0.15
514.5	-0.96	1.63	0.02
785.0	-0.69	1.83	-0.01
1064.0	-0.05	1.32	-17.29

the electric excitation continuum is different at excitation wavelengths of 514.5 and 785.0 nm [190]. Burke et al. also measured the Raman spectra of *p*-doped silicon and found that the variation in the asymmetry of the lineshape due to the change from negative to positive q occurred at an excitation wavelength of 325.0 nm [191].

Ohta et al. calculated the density of states (DOS) of periodic B dopants with a random alloy of substitutional B in diamond using several supercells and the coherent potential approximation for the random alloy case [192]. They showed that the DOS possesses a peak at approximately 2.0 eV in B-doped diamond. This is in good agreement with the peak value of approximately 2.0 eV [190]. Hence, the difference in the abnormal Raman line shapes at excitation wavelengths of 514.5 and 785.0 nm in Fig. 5.61a, b is ascribed to a difference in the DOS in the valence band [190].

5.9.3 Nano-diamond

Nanometre-sized diamond (nano-diamond) has attracted interest because it is expected to have outstanding properties different from those of crystalline diamond [193, 194]. Particularly, nano-diamond particles produced by detonation of trinitrotoluene explosives are expected to be used for various applications, such as abrasives for semiconductors, reinforcers for polymers, rubber, a lubricating material for hard disks, and life science field [193, 194].

Figure 5.62 shows the Raman spectra of nano-diamond under 514.5 nm excitation wavelength by an Ar⁺ laser [194]. A weak broad band ascribed to sp² clusters is detected at approximately 1600 cm⁻¹, and the Raman band of diamond appears at approximately 1322 cm⁻¹. Because the Raman scattering cross-section of diamond is approximately 1/60th that of graphite [195], the nano-diamond is thought to contain a small number of sp² clusters. Additional bands appear at approximately 600 and 800 cm⁻¹ in Fig. 5.62 [194].

The Raman spectra of amorphous materials generally indicate the vibrational density of states (DOS), which is similar to that of the crystals [196]. The peak

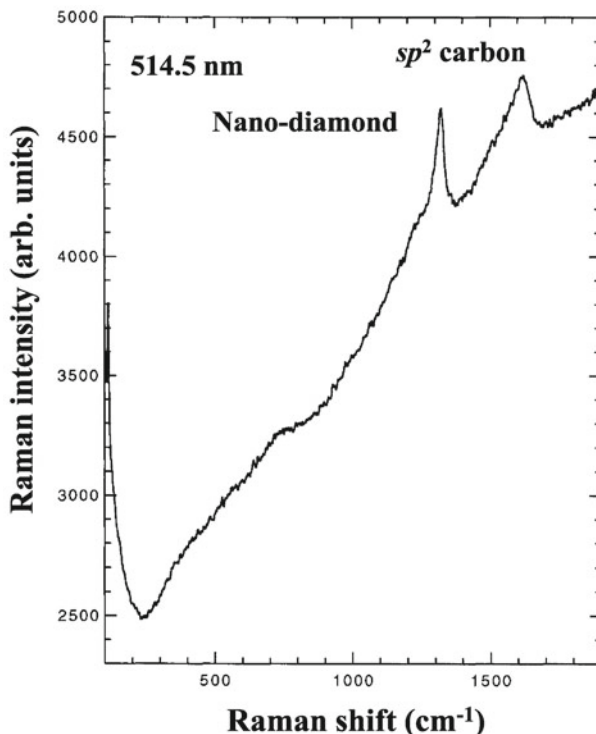


Fig. 5.62 Raman spectra of nano-diamond [194] (Reproduced with permission from Ref. [194]. © AIP Publishing, 1995.)

frequencies of the additional bands are near maxima in the vibrational DOS of graphite [197]. A comparison of the vibrational DOSs indicates that the additional Raman bands are mainly originating from amorphous sp^2 clusters [194]. The Raman spectra of diamond particles of 0.1–2 μm size exhibit a broad Raman band at approximately 800 cm^{-1} ; this band originates from the transverse acoustic (TA) phonon near the Brillouin zone boundary, which is activated by the relaxation of the wave vector selection rule in small particles [193]. On the other hand, this 600 cm^{-1} band is thought to be obscured by the additional bands assigned to sp^2 clusters because of the difference between the Raman scattering cross-sections of sp^2 and sp^3 clusters and its weakness.

Figure 5.63 depicts the high-resolution Raman spectra of a nano-diamond from 1200 to 1400 cm^{-1} [194]. The nano-diamond demonstrates an asymmetric lineshape with the main peak at approximately 1322 cm^{-1} and some tailing towards lower frequencies. Its spectrum can be interpreted in terms of a phonon confinement effect [198–201]. This confinement model is based on the fact that, in an infinite crystal, only phonons in the vicinity of the centre of the Brillouin zone ($q \equiv 0$) make a contribution to the Raman spectrum because of momentum conservation between the phonons and incident light. By contrast, in a finite crystal, phonons can be confined in space by crystal boundaries or defects. This behaviour results in uncertainty in the phonon momentum, permitting phonons with $q \neq 0$ to contribute to the Raman spectrum [198–201].

The Raman spectrum of nano-diamonds with sizes of less than 100 nm is calculated by superimposing Lorentzian lineshapes centred at $\omega(q)$, which are weighted by the wave vector q uncertainty induced by confinement [194, 200].

$$\mathbf{I}(\omega) \approx \int_0^1 \frac{\exp(-\mathbf{q}^2 L^2/4) 4\pi q^2 d\mathbf{q}}{[\omega - \omega(\mathbf{q})]^2 + (\Gamma/2)^2} \quad (5.15)$$

where $\omega(q)$ is the approximate one-dimensional (1D) phonon dispersion curve. Here, q is expressed in units of $2\pi/a$, and the crystallite size L is in units of a , where $a = 0.3567 \text{ nm}$ is the lattice constant of diamond. We used the Gaussian confinement function and assumed that L is equal to the particle size of a nano-diamond [194]. The 3D Brillouin zone integration in Eq. (5.15) is approximated by 1D integration in a spherical Brillouin zone [194]. The dispersion curve $\omega(q)$ is postulated to have the following form [194]:

$$\omega(q) = A + B \cos(q\pi) \quad (5.16)$$

where $A = 1193.75 \text{ cm}^{-1}$, and $B = 139.25 \text{ cm}^{-1}$. A and B were determined so that $\omega(q)$ could produce the TO phonon dispersion curve [194]. In addition, the Lorentzian linewidth Γ was postulated to depend on the particle size; it is expressed by [194]

$$\Gamma = 2.990 + 0.052/L \quad (5.17)$$

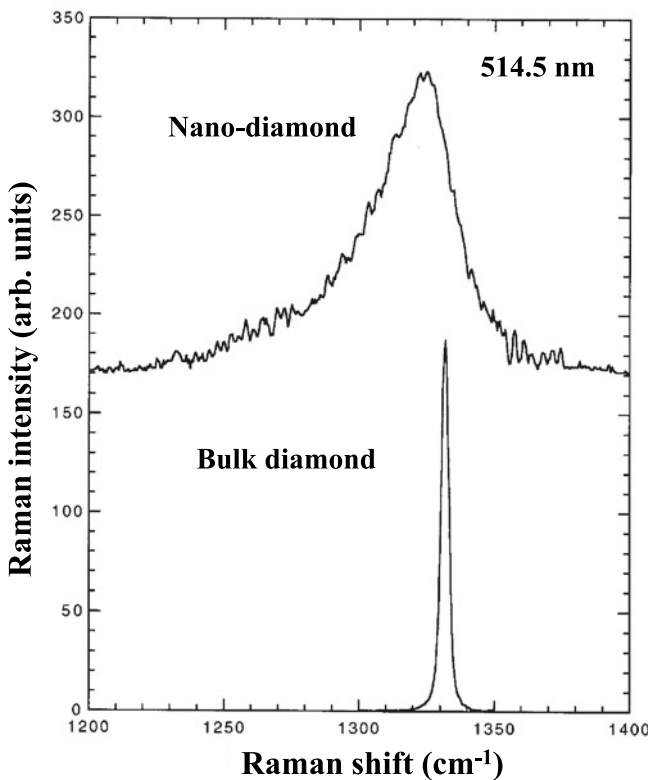
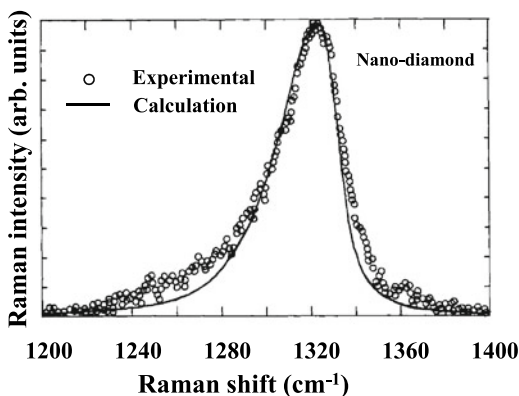


Fig. 5.63 High-resolution Raman spectrum of nano-diamond from 1200 to 1400 cm^{-1} . The spectra were adjusted by subtracting the background. The Raman line of bulk diamond is depicted for comparison [194] (Reproduced with permission from Ref. [194]. © AIP Publishing, 1995.)

where the coefficients were determined from the least-squares fit to the data in Ref. [194].

Figure 5.64 illustrates the Raman spectrum of nano-diamond with a size of 5.5 nm as calculated by Eqs. (5.15)–(5.17). Open circles and a solid line indicate experimental data and the calculated result, respectively [194]. The experimental and calculated results are in good agreement. The asymmetric lineshape, with some tailing towards lower frequencies, is well interpreted with the confinement model. The calculated result indicates that the Raman spectrum of nano-diamond with a size of 5.5 nm is asymmetric, with a shift of -10 cm^{-1} and a linewidth of 32 cm^{-1} [194]. The experimental result is in good agreement with Fig. 3 in Ref. [179]. Moreover, the crystallite size of nano-diamond estimated using the phonon confinement model coincides approximately with that estimated by X-ray measurement [194]. The crystallite size of a nano-diamond can be easily estimated only by measuring the Raman spectra of the diamond particles without the X-ray measurement. Finally, this calculation result predicts that the Raman band of amorphous diamond with sizes

Fig. 5.64 Calculated Raman spectrum of nano-diamond with a size of 5.5 nm [194] (Reproduced with permission from Ref. [194]. © AIP Publishing, 1995.)



of less than 5 nm will be very broad and appear at approximately 1100 cm^{-1} , being introduced in the next section (Sect. 5.9.4).

5.9.4 Amorphous Diamond

Hydrogenated diamond-like amorphous carbon (a-C:H) films consist of a mixture of sp^3 and sp^2 carbon clusters. These films are prepared by various methods, such as p-CVD and sputtering, and are used as protective films for hard disks (HDs), the magnetoresistance (MR) heads of HD drives, and an engine for motor vehicles. Amorphous Si, SiN, or SiC film is used as spacers. Si–C bonds are formed at the interface between these spacers and the surface of the a-C:H films. For HDs, multi-layer structures consisting of nitrogen-doped and undoped a-C:H films are adopted for use in increasing the lubrication between the HD and the MR head. Moreover, there was little information on the CN bonding structures in N-doped a-C:H films. Because the bonding structure at the interface significantly affects the durability of HD drives, it is most important to clarify the bonding states between silicon and carbon atoms, and between nitrogen and carbon atoms.

Raman spectroscopy is also a powerful technique for characterising the microstructures of a-C:H films because of the intense signal due to resonant Raman scattering and the high spatial resolution [202, 203]. The Raman spectra of boron-ion-implanted glassy carbon (GC) with a crystallite size of $\sim 2.5\text{ nm}$ and a-CH films have been measured [204]. The E_{2g} (G) mode at 1590 cm^{-1} shifts to a lower frequency, while the disordered (D) mode [204] at 1360 cm^{-1} shifts to a higher frequency with increasing B ion implantation. The Raman spectral profile of heavily implanted GC resembles that of an a-C:H film [204]. The Raman spectral profiles of a-C:H films and heavily implanted GC have been found to show similar variation with the excitation wavelength [204]. The spectral variation with an excitation wavelength of a-C:H

films and heavily implanted GC have been explained by $\pi-\pi^*$ resonant Raman scattering from sp^2 carbon clusters [204]. We found that the Raman bands observed in a-C:H films originate from sp^2 carbon clusters; moreover, the position of the main peak in the a-C:H films is related to the sp^2 cluster size and shifts to a lower frequency with decreasing sp^2 cluster size. Moreover, we found that the relative intensity of the Raman bands was correlated with the sp^3 content of a-C:H films [204].

Because the amorphous mode ascribed to the C=C bond stretching mode is very weak in FT-IR spectra, and only a broad emission band is observed in the visible region by CL spectroscopy, it is difficult to analyse the microstructure of amorphous diamond. By contrast, Raman spectroscopy is a useful method of studying the microstructure of diamond crystals and amorphous diamond because of the strong intensity of their spectra.

The electron energy loss spectroscopy (EELS) is a method of measuring the energy lost by the interaction of electrons with atoms as they pass through a thin specimen using TEM or STEM. In a-C:H films, two peaks are seen, a weak one of approximately 6.7 eV due to plasma oscillations of π electrons, and a strong peak from $(\pi + \sigma)$ valence electrons at about 25 eV. We can estimate sp^2/sp^3 ratio of a-C:H films by measuring their relative intensity.

The absorption spectra of a-C:H films prepared on glass substrates at various temperatures are obtained with the relation [205]

$$(\alpha E)^{1/2} \approx (E - E_g) \quad (5.18)$$

where α and E are the absorptivity and energy, respectively. Extrapolation of the straight line to the abscissa gave the optical gap E_g . The optical gaps of the films range from 1.2 to 1.5 eV and decrease with increasing substrate temperature [204]. Generally, the absorption features assigned to the $\pi-\pi^*$ transition in π -bonded materials are observed between 10,000 and 45,000 cm^{-1} (for example, at approximately 16,000 and 43,000 cm^{-1} for transpolyacetylene and benzene, respectively) [206].

We prepared a-C:H films on silicon glass substrates from CH_4 gas by electron cyclotron resonance (ECR) p-CVD. Several specimens labelled No. 1 to No. 3 were formed by varying the substrate temperature between 150 and 250 °C. Figure 5.65 shows Raman, EELS spectra, and optical gaps of a-C:H films prepared at 150 °C (specimen No. 1), 200 °C (specimen No. 2), and 250 °C (specimen No. 3) [204]. In Fig. 5.65c, the absorption at approximately 20,000 cm^{-1} increases with increasing substrate temperature [204].

Figure 5.65a illustrates the Raman spectra of a-C:H films obtained at an excitation energy of approximately 20,000 cm^{-1} (19,435 cm^{-1} , 514.5 nm) [204]. The intensity of the D band increases with increasing the substrate temperature. Furthermore, in Fig. 5.65b, two peaks appear in the EELS spectra of the a-C:H films: a weak peak at approximately 6.7 eV assigned to plasma oscillations of π electrons and a strong peak ascribed to $(\pi + \sigma)$ valence electrons at approximately 25 eV [204]. The intensity of the weak peak, which is associated with the π plasmon, increases with increasing substrate temperature [204]. A comparison of the EELS, $(\alpha E)^{1/2}$, and Raman spectra confirms that the variation in the strong peak of the a-C:H films with the excitation

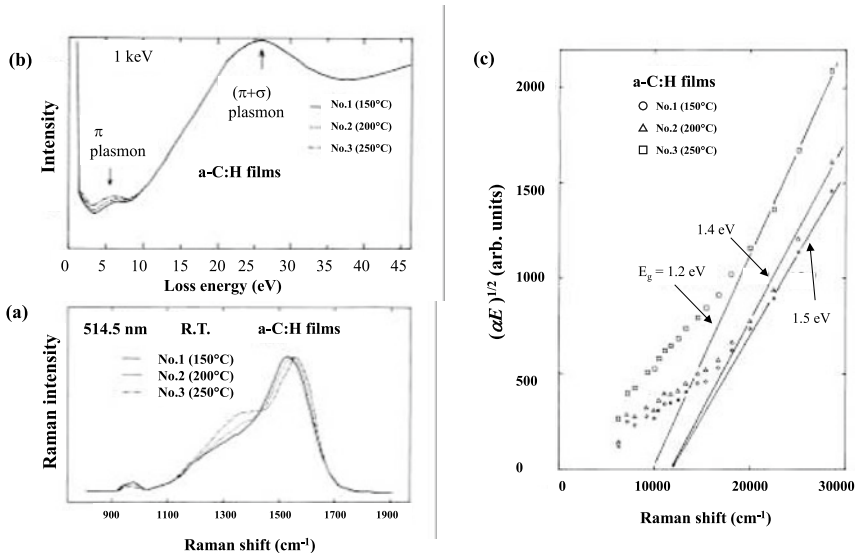


Fig. 5.65 Raman, EELS spectra, and optical gaps of a-C:H films prepared at 150 °C (specimen No. 1), 200 °C (specimen No. 2), and 250 °C (specimen No. 3)

wavelength is caused by $\pi-\pi^*$ resonant Raman scattering from sp^2 carbon clusters of various sizes [204].

Based on these results, we found a method to characterise the ratio between sp^3 and sp^2 carbon clusters of a-C:H films. Figure 5.66a, b illustrate a photograph of a commercially available hard disk drive (HDD), and a schematic method to characterise the ratio between sp^3 and sp^2 clusters of a-C:H films, using Raman spectroscopy.

Figure 5.67 shows Raman spectra of an unused, and deterioration of commercially available HDD. As can be seen, the main broad band at around 1530 cm^{-1} shifts to high-frequency side and the relative intensity ratio, I_D/I_G , becomes intense with the deterioration of HDD. We can non-destructively estimate the relative intensity ratio, I_D/I_G , of a-C:H films, using Raman spectroscopy.

5.9.5 Resonant Raman Scattering from Si- and N-doped a-C:H Films

Si-doped a-C:H films were prepared on silicon glass substrates from CH_4 and SiH_4 gases by the ECR p-CVD method. N-doped a-C:H films were prepared by sputtering a graphite target at a power of 1 kW onto a silicon substrate, which was held at approximately 300 K in a mixture of Ar, H₂, and N₂ gas. All measurements were

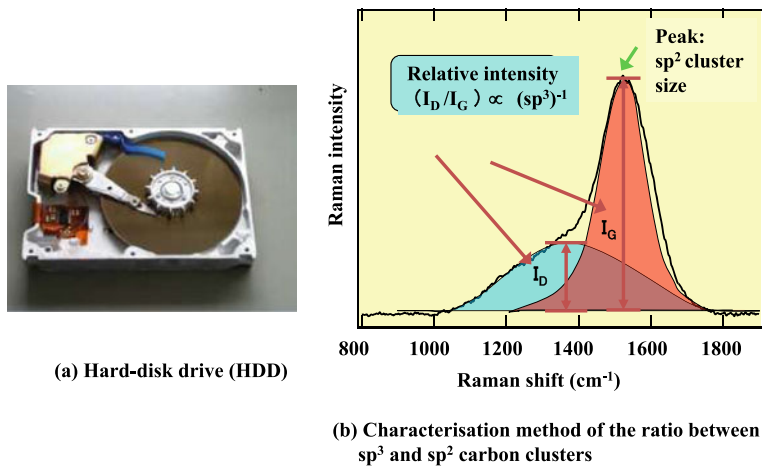
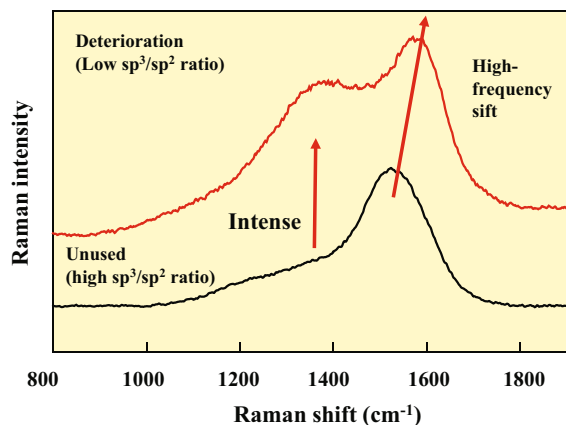


Fig. 5.66 **a** Photograph of a commercially available hard disk drive (HDD), and **b** a schematic method to characterise the ratio between sp^3 and sp^2 clusters of a-C:H films, using Raman spectroscopy

Fig. 5.67 Raman spectra of an unused, and deterioration of commercially available HDD



shown in Ref. [207]. The composition and optical gaps are listed in Table I of Ref. [207].

We have studied the Raman spectra of the Si-doped and N-doped a-C:H films prepared by the ECR p-CVD method [207]. The Raman spectra were measured using Ar^+ and He–Ne lasers at several excitation energies. The Raman bands at 1390 and 1550 cm^{-1} are attributed to sp^2 carbon clusters [207]. The relative Raman intensity of the D band (1360 cm^{-1}) normalised by that of the 1550 cm^{-1} band decreases dramatically with the Si concentration. Table I of Ref. [207] shows that the optical band gap and film density of the Si-doped a-C:H films increase with increasing Si concentration and approach to those of bulk diamond [207].

The main band at approximately 1550 cm^{-1} starts to shift dramatically with increasing excitation wavelength and decreasing Si concentration [207]. From Ref. [204], and because of the decrease in optical band gap with decreasing Si concentration, it is considered that $\pi-\pi^*$ resonant Raman scattering from sp^2 carbon clusters with various sizes is detected in the Si-doped a-C:H films [207].

The 1550 cm^{-1} band shifts dramatically to a lower frequency with increasing Si concentration. The E_{2g} mode (1590 cm^{-1}) has been found to shift towards lower frequency with decreasing sp^2 cluster size owing to B ion implantation [204]. The optical band gap and film density of the Si-doped a-C:H films increase with an increase in the Si concentration. These results indicate that the sp^2 carbon cluster size decreases with increasing Si concentration in the Si-doped a-C:H films and that the incorporation of Si into the C–C bonds assists the formation of sp^3 carbon clusters. An analogous decrease in the main peak was observed by Wagner et al. in an- $\text{Si}_{1-x}\text{C}_x:\text{H}$ films ($x = 0.5\text{--}1.0$) [208].

We measured the Raman spectra of the N-doped a-C:H films under excitation by Ar^+ and He–Ne lasers at several excitation energies [207]. The main band (approximately 1570 cm^{-1}) shifts towards a lower frequency as the excitation wavelength increases. The relative intensity varies drastically with an increasing excitation wavelength and N concentration [207]. The decrease in optical band gap with increasing N concentration suggests that $\pi-\pi^*$ resonant Raman scattering from sp^2 carbon clusters of various sizes is also detected in the N-doped a-C:H films [207].

Furthermore, we measured Raman spectra of the Si-doped and N-doped a-C:H films excited by the 1064 nm line of a Nd: YAG laser in Fig. 5.68. Surprisingly, the G bands at approximately 1550 cm^{-1} observed under 514.5 nm excitation by an Ar^+ laser were detected at around 1300 cm^{-1} under the 1064 nm excitation by a Nd: YAG laser [207]. The D bands of the Si-doped and N-doped a-C:H films, which are observed at 1390 cm^{-1} in the visible region, are becoming more intense than the main band at approximately 1300 cm^{-1} under the 1064 nm excitation by a Nd: YAG laser [209]. As a result, almost one broad band is observed at approximately 1300 cm^{-1} for the Si-doped and N-doped a-C:H films in the Raman spectra excited by the 1064 nm line. This result indicates that the resonant Raman scattering from sp^2 cluster carbons with larger sizes dominates Raman spectra of the Si-doped and N-doped a-C:H films in near-infrared (NIR) region [209].

Gilkes et al. measured the Raman spectra of tetrahedral amorphous carbon (ta-C) films on a Si substrate, which contain approximately 20% sp^2 clusters, under 244 nm excitation [210]. The ta-C films were grown using the filtered cathodic vacuum arc method, which can be used to obtain ta-C films with a range of sp^3 contents by varying the ion energy of the plasma beam used for deposition. The sp^3 contents of the films were estimated by carbon K-edge EELS [210].

Figure 5.69 shows the first-order DUV Raman spectra of commercially available four ta-C specimens, A1, A2, B1, and B2 with sp^3 cluster excited by the 266 nm (fourth harmonic) line of a Nd: YAG laser, using Raman apparatus we developed. The peak positions of the ta-C specimens were determined by fitting the spectra with a Gaussian lineshape [209]. A2 and B2 ta-C:H specimens mean that they contain hydrogen in the films.

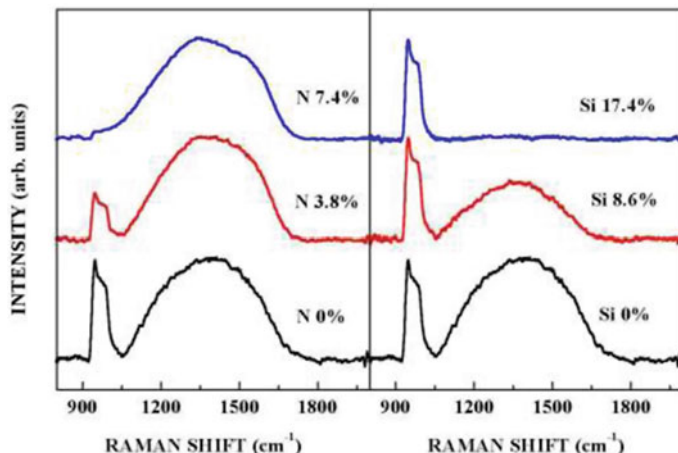
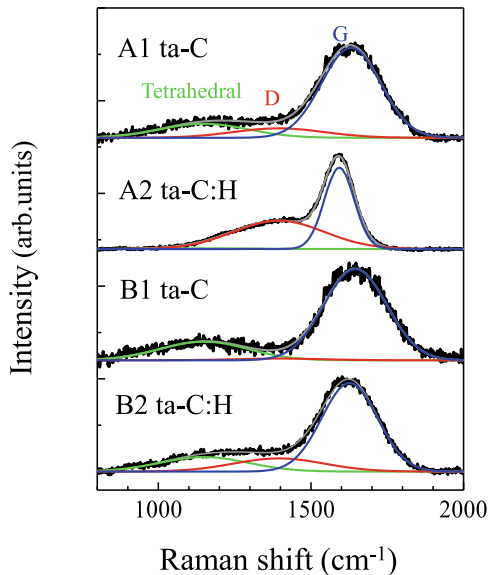


Fig. 5.68 Raman spectra of Si-doped and N-doped a-C:H films excited by the 1064 nm line of a Nd:YAG laser (our original data). A broad Raman band at approximately 970 cm^{-1} is the second order line of an Si substrate [209]

Fig. 5.69 Raman spectra (solid curves in black colour) of ta-C specimens A1, A2, B1, and B2 under 266 nm excitation (our original data). The solid curves in blue, green, and red colour are Gaussian fits to the experimental ta-C spectra. A2 and B2 ta-C:H specimens mean that they contain hydrogen in the films [209]



The ta-C spectra consist of two broad peaks centred around 1100 cm^{-1} and 1650 cm^{-1} , which are referred to as the tetrahedral (T) sp^3 clusters and G peaks, respectively. The Raman spectra of specimens A1, A2, B1, and B2 were normalised to have the same maximum G peak intensities above the background. Our observation coincides well with one by Gilkes et al. [210].

As seen in Fig. 5.69, A1 and B1 specimens without almost containing hydrogen (H) apparently show the T bands at 1100 cm^{-1} whereas A2 ta-C:H specimen with containing H does not the T band, and the D band at 1390 cm^{-1} becomes stronger. Moreover, the G bands at 1570 cm^{-1} of A2 and B2 ta-C:H specimens tend to become sharper than those of A1 and B1. This result shows that the microstructure of ta-C:H films is different from that of ta-C films. Maybe ta-C:H films might contain many C sp³-H bands compared with ta-C films, as discussed in the next session Sect. 5.9.6.

These observations of the Raman bands at approximately 1100 cm^{-1} are in good agreement with a prediction based on a confinement model of nano-diamond, calculated with the crystallite size L much smaller than 5.5 nm in Eq. (5.15). DUV Raman spectroscopy is the most powerful technique for characterising amorphous diamond-like carbon, nano-diamond, and crystalline diamond.

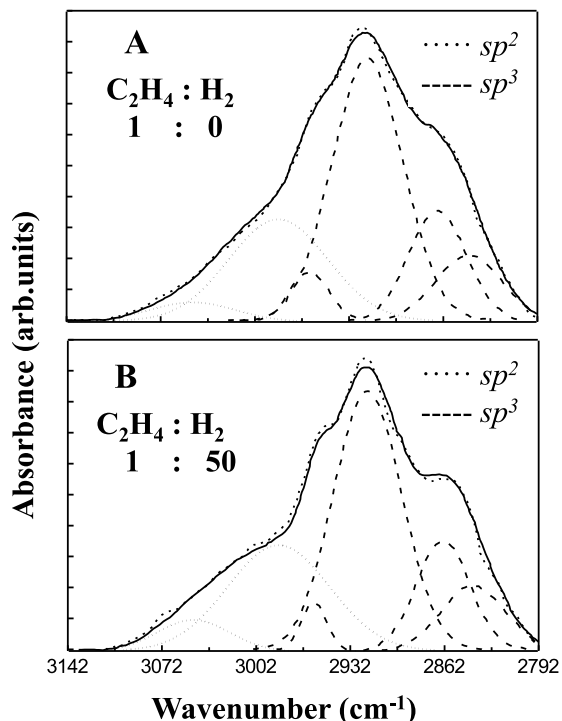
5.9.6 Infrared Spectra of a-C:H Films

Figure 5.70 displays the FT-IR absorption spectra of a-C:H films prepared by p-CVD with no H_2 and a $\text{C}_2\text{H}_4/\text{H}_2$ ratio of 1:50 (specimens A and B, respectively) [211]. The relative Raman intensity of the 1390 and 1550 cm^{-1} bands was estimated to be 0.9 and 1.2 for specimens A and B, respectively. C-H stretching absorption bands assigned to hydrogens bonded to sp² and sp³ carbons (C sp²-H and C sp³-H bands) are detected at approximately 3000 and 2900 cm^{-1} , respectively [211]. The ratio of sp² carbon to sp³ carbon was estimated from the relative intensity of the C sp²-H and C sp³-H bands [211]. The absorption spectra were fitted to six bands with Gaussian lineshapes. The relative intensity of the C sp³-H and C sp²-H bands showed that 72 and 69% of the carbon atoms were sp³-bonded in specimens A and B, respectively [211]. A comparison of the Raman and FT-IR spectra indicated that the relative intensity of the Raman bands was correlated to the relative intensity of the C sp²-H and C sp³-H absorption bands. The relative intensity of these bands measured by FT-IR spectroscopy, in addition to the relative Raman intensity, can be used as an indicator of the sp³/sp² carbon ratio [211].

In GC with a crystallite size of $L \sim 2.5\text{ nm}$, two Raman bands are observed at 1590 and 1360 cm^{-1} , while asymmetric broad Raman bands ascribed to sp² carbon clusters with various sizes are observed at approximately 1530 cm^{-1} in a-C:H films [204]. A comparison of the Raman spectra of the ion-implanted GC and a-C:H films speculates that the sp² clusters in the a-C:H films are less than 2.5 nm in diameter. On the basis of a calculation of the electronic structure of a-C:H films, Robertson and O'Reilly stated that the absorption edge of these films is decided by the sp² carbon cluster size and that the optical gap changes inversely with the cluster size [212]. Their interpretation means that the a-C:H films, which possess an optical gap of $\sim 1\text{ eV}$, consist of sp² carbon clusters with a crystallite diameter of approximately 1.5 nm .

A schematic of the microstructure of the a-C:H films is presented in Fig. 5.71 [211]. The a-C:H films are formed by sp³ and sp² carbon clusters, where the ratio

Fig. 5.70 FT-IR spectra of a-C:H films prepared by p-CVD



depends on the deposition conditions. The sp^2 carbon cluster size is approximately 1.5 nm on average. Most of these clusters are formed by aromatic rings, and the others may be polyenes or polymers. We believe that the connection of those sp^2 carbon clusters and the content of sp^3 carbon clusters decides the hardness of the a-C:H films. The hydrogen atoms are bonding to the terminals of these clusters. For the a-C:H film of $E_g \sim 1.0$ eV, approximately 66% of the carbon atoms were estimated to be sp^3 -bonded.

5.9.7 CL of Diamond

Figure 5.72 shows cathodoluminescence (CL) spectra of diamond (specimens A, B, and C) measured at 30 K. Nitrogen is well-known as a dominant impurity in diamond. The sharp CL peaks at approximately 575 and 637 nm are assigned to the nitrogen-vacancy (NV)⁰ centre and the negatively charged nitrogen-vacancy (NV)⁻ centre with zero-phonon lines, respectively [213, 214]. Furthermore, the CL peaks at around 503 nm are considered to be originating from H3 series defects like H3 (N-V-N or V-N-N-V complex) or N3 (N3V complex) and are mainly observed in type-Ia diamond. The negatively charged nitrogen-vacancy (NV)⁻ centre at 637 nm

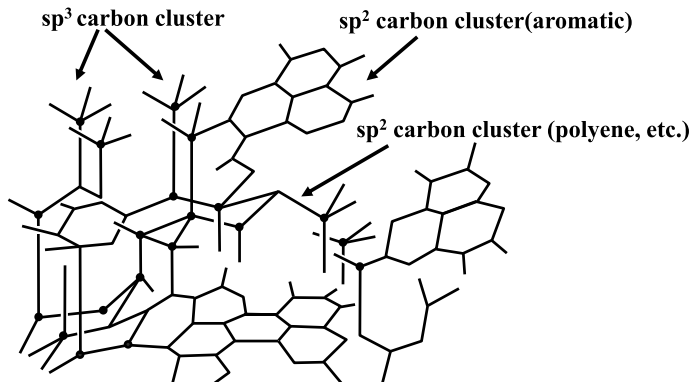
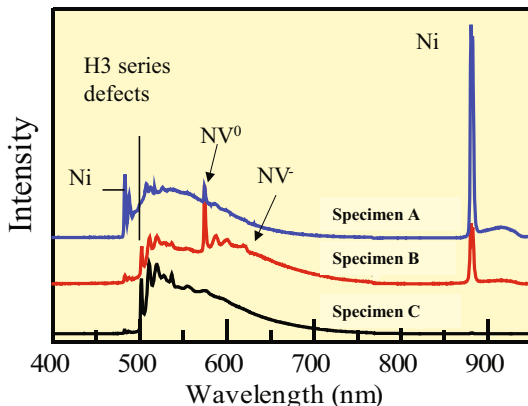


Fig. 5.71 Schematic of the microstructure of a-C:H films [211]

Fig. 5.72 CL spectra of various diamonds measured at 30 K



has attracted significant attention and will be expected as a single photon source with a long spin lifetime at room temperature which is utilised in quantum cryptography and quantum computing. The CL peaks at 484 and 885 nm are related to Ni and observed in all type-Ib synthetic diamonds and are particularly intense in specimens using a nickel-based solvent-catalyst [213, 214]. Based on these results, we can distinguish types of diamonds using CL spectroscopy.

5.10 Next-Generation Semiconductor: Ga₂O₃

Monoclinic gallium oxide (β -Ga₂O₃) is a wide-band-gap semiconductor material that has a direct band gap of approximately 4.9 eV [215, 216]. Because β -Ga₂O₃ has a higher dielectric constant ($\epsilon \sim 10\text{--}14$) than SiO₂ ($\epsilon \sim 4$) and unique transparency from the visible into the UV region, it is a very good candidate for industrial

applications, for example, in solar cells and optoelectronic devices operating at short wavelengths, as a gate dielectric material for complementary MOS devices, and next-generation high-power devices [216]. In addition, metal/ β -Ga₂O₃/semiconductor hydrogen sensor diodes with β -Ga₂O₃ reactive oxide films are very useful for hydrogen gas sensing because the reactive oxide intermediate layer between the metal and the semiconductor in the Schottky barrier diodes could improve the hydrogen gas sensing performance [216]. Ga₂O₃ has five crystalline forms (α , β , γ , δ , and ϵ), and the β form is the most stable from room temperature to the melting point. Plasma-enhanced atomic layer deposition (ALD) is widely used as an alternative to conventional ALD [216]. The plasma source creates ions and radicals that enhance the chemical reactions; thus a wider range of materials can be deposited at low temperatures by this method [216].

The unit cell of the stable phase, β -Ga₂O₃, contains two crystallographically different Ga atoms in the asymmetric unit, one with tetrahedral and the other with octahedral coordination geometry [217]. The unit cell is composed of two types of gallium ions (Ga_I and Ga_{II}) and three types of oxygen ions (O_I, O_{II}, and O_{III}). Consequently, the physical, optical, and electrical properties are anisotropic [217], as predicted theoretically and observed experimentally [218–220]. For example, the thermal conductivity of Ga₂O₃ shows a strong anisotropy, as it is 2.5 times higher in the [010] direction than in the [100] direction [216], although theory and experiment both suggest that there is little anisotropy in the electron effective mass [216, 220]. The highest thermal conductivity is approximately 29 W/m K in the [010] direction. The thermal conductivity of Sn- and Fe-doped specimens was lower than that of undoped specimens owing to a larger phonon–impurity scattering contribution.

Nakata studied the crystalline structures of Sn-doped Ga₂O₃ films on a sapphire substrate (the *c* plane) [221]. Figure 5.73 depicts a cross-sectional TEM image of a Ga₂O₃ film obtained at a Sn fluence of 0.1%, and Fig. 5.74 shows the XRD patterns of the upper and lower surfaces of ~400-nm thick Ga₂O₃ films obtained at various Sn fluences. The Ga₂O₃ film obtained at a Sn fluence of 0.1% consists mainly of the β forms with a small amount of the ϵ form [221].

In addition, Fig. 5.75 illustrates the measured Raman spectra of Ga₂O₃ films fabricated at various Sn fluences on a sapphire substrate. The penetration depth of the incident light was approximately 1 μm . The peaks assigned to the ϵ form did not appear in the Raman spectrum of the Ga₂O₃ film fabricated at a Sn fluence of 0.1%, which is not consistent with the XRD patterns [221]. This inconsistency is considered to be caused by the difference in penetration depths between the Raman and X-ray measurements.

Figure 5.76 shows the CL spectra of Ga₂O₃ films obtained at various Sn fluences on a sapphire substrate, which were measured at an acceleration voltage of 3 keV [221]. The electron penetration depth (Re) was calculated to be approximately 80 nm using the following equation:

$$\text{Re}(\mu\text{m}) = (2.76 \times 10^{-2} A / \rho Z^{0.889}) E^{1.67} \quad (5.19)$$

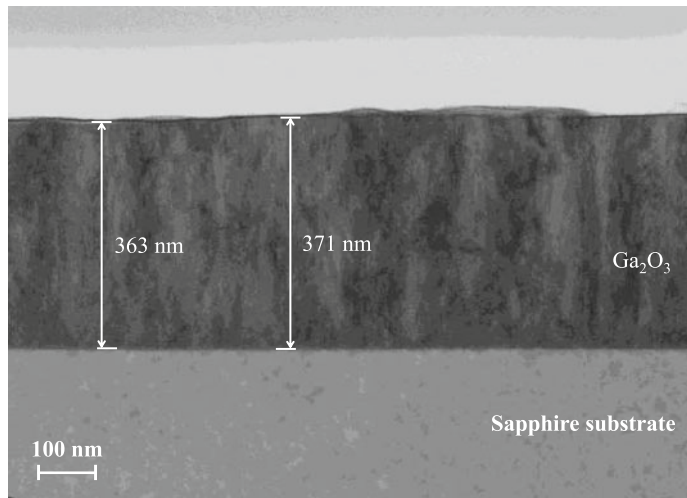


Fig. 5.73 Cross-sectional TEM image of Ga_2O_3 film obtained at a Sn fluence of 0.1% [221]

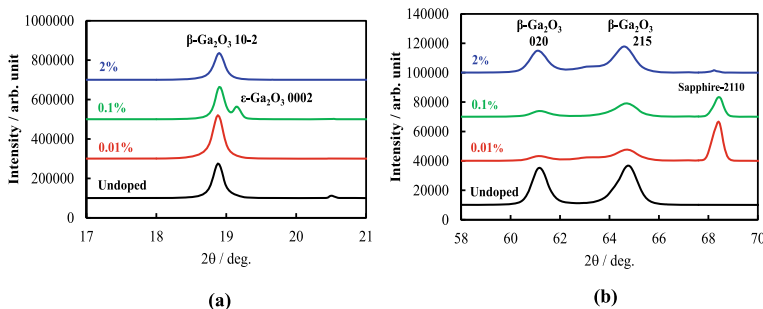


Fig. 5.74 XRD patterns of **a** upper and **b** lower surfaces of ~400-nm thick Ga_2O_3 films obtained at various Sn fluences

where A is the atomic weight in g/mol, ρ is the density in g/cm³, Z is the atomic number, and E is the acceleration voltage in keV. On the basis of the Re value, the CL spectrum in Fig. 5.76 is thought to include information from the top layer of the Ga_2O_3 films fabricated at various Sn fluences on the sapphire substrate [221].

The broad CL peak at approximately 400–500 nm is ascribed to donor–acceptor pair emission [222, 223]. Although the assignment of the broad CL peak at approximately 800 nm is unclear, it might be attributable to the second-order emission of the broad CL peak at approximately 400–500 nm or to point defects [221]. As shown in Fig. 5.76, the CL peak at 740 nm originating from point defects in the specimen deposited at a Sn fluence of 0.1% is much stronger than those of the undoped specimen and the specimens fabricated at Sn fluences of 0.01 and 2% [221]. This result

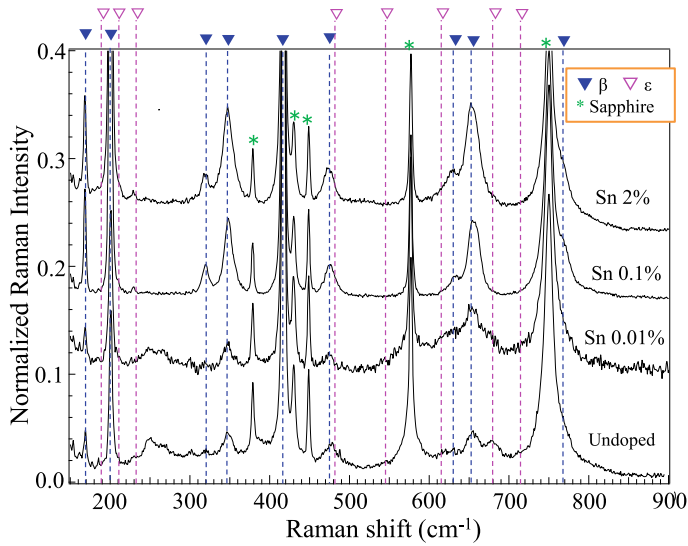


Fig. 5.75 Raman spectra of Ga_2O_3 films fabricated at various Sn fluences on a sapphire substrate [221]

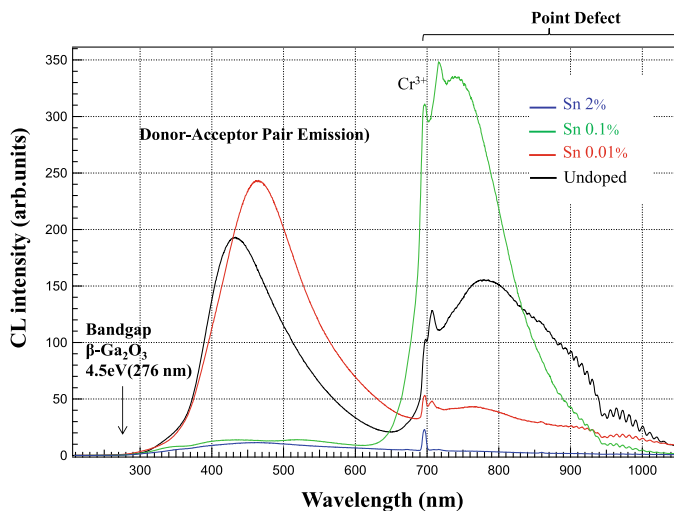


Fig. 5.76 CL spectra of Ga_2O_3 films fabricated at various Sn fluences on a sapphire substrate, which were measured at an acceleration voltage of 3 keV [221]

suggests that the specimen fabricated at a Sn fluence of 0.1% has lower crystalline quality than the other specimens.

Further, the structural changes in a commercially available *n*-type β-Ga₂O₃ bulk wafer [(201) face] resulting from Si ion implantation were studied using secondary ion mass spectrometry (SIMS), TEM, scanning capacitance microscopy (SCM), and Raman and CL spectroscopy [224]. The β-Ga₂O₃ bulk wafer was implanted at 60 keV and a fluence of $2 \times 10^{12} - 1 \times 10^{15}$ Si ions/cm². The specimens were annealed at 800 or 1000 °C.

Figure 5.77 depicts the depth profile of the β-Ga₂O₃ bulk wafer measured by SIMS analysis [224]. The Si ions show a peak of the region approximately 0.1 μm from the surface of the β-Ga₂O₃ bulk wafer. Furthermore, the β-Ga₂O₃ bulk wafer itself indicates Si impurities of 1×10^{17} atoms/cm³ at the background level by SIMS analysis [224].

Figure 5.78a, b show the depth profiles of Si ions after annealing at 800 and 1000 °C.

A comparison of Figs. 5.77 and 5.78 indicates that Si ions diffused from 0.1 μm into the interior of the wafer after annealing at 1000 °C (Fig. 5.78b), whereas the depth profile of Si ions after annealing at 800 °C (Fig. 5.78a) is similar to the depth profile in Fig. 5.77 [224]. As seen in Fig. 5.78b, the depth profiles of Si ions in the specimens show inflection points instead of a simple diffusion pattern. This result suggests that a structural change occurs at approximately 0.2–0.4 μm position far from the surface of the wafer [224].

Figure 5.79 shows the Raman spectra of the Si-doped β-Ga₂O₃ wafers implanted at various Si fluences and annealed at 1000 °C. Because the Raman measurement revealed no structural changes, TEM and CL measurements were performed [224].

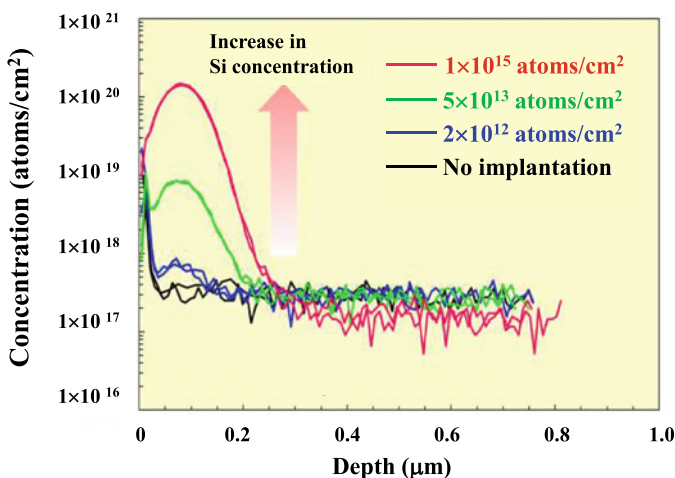


Fig. 5.77 SIMS depth profiles of Si ions in β-Ga₂O₃ bulk wafers implanted at various Si fluences [224]

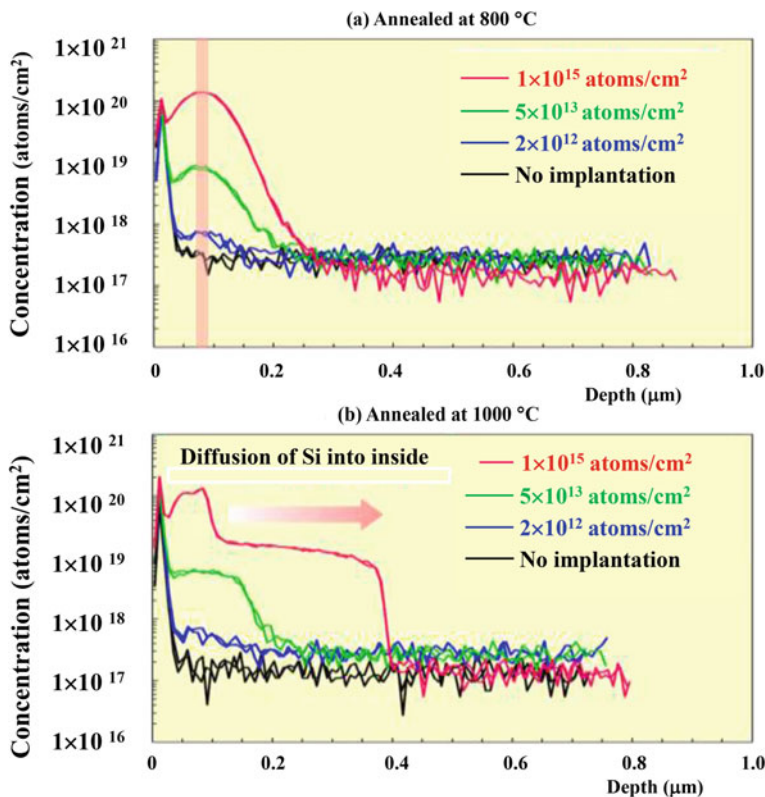


Fig. 5.78 Depth profiles of Si ions after annealing at **a** 800 °C and **b** 1000 °C [224]

Figure 5.80 shows cross-sectional TEM images of the specimen implanted at a fluence of 1×10^{15} Si ions/cm² [224]. Variations in the contrast appear in the TEM image in Fig. 5.80b, indicating damage due to ion implantation. The location of the damaged region is in good agreement with the high-fluence region in Fig. 5.78a. By contrast, after annealing (Fig. 5.80c), many defects remain, although the crystalline quality is somewhat improved [224].

Figure 5.81 shows CL spectra of specimens implanted at various Si ion fluences after annealing [224]. The CL peak at 400 nm is assigned to donor–acceptor pair emission. The intensity of the CL peak decreases with increasing Si fluence, indicating an increase in defects [224]. Figure 5.82 shows the annealing temperature dependence of the CL intensity of the specimens. For all the specimens, the CL intensity at 400 nm increases with increasing the annealing temperature. These results indicate that CL spectroscopy is a sensitive method of estimating the degree of recovery of the crystalline quality of β -Ga₂O₃ bulk wafers [224].

Finally, SCM measurements of the specimen implanted at a fluence of 1×10^{15} Si atoms/cm² were made after the specimen was annealed at 800 and 1000 °C [224]. The

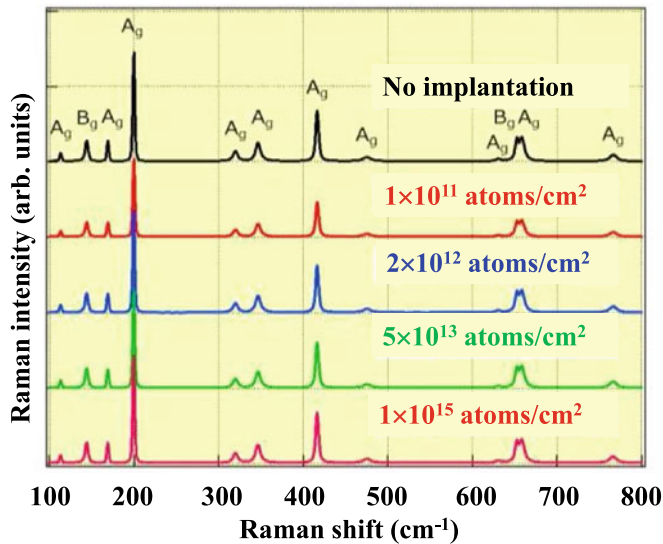
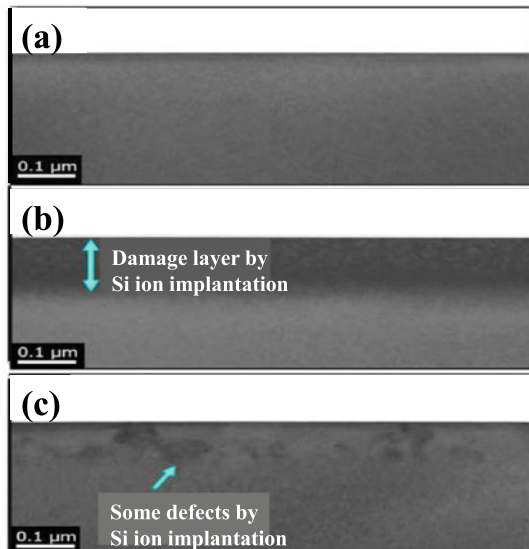


Fig. 5.79 Raman spectra of Si-doped β -Ga₂O₃ wafers implanted at various Si fluences after annealing at 1000 °C [224]

Fig. 5.80 Cross-sectional TEM images of Si-doped β -Ga₂O₃ specimen implanted at a fluence of 1×10^{15} Si ions/cm² **a** before implantation, **b** after implantation, and **c** after annealing at 1000 °C [224]



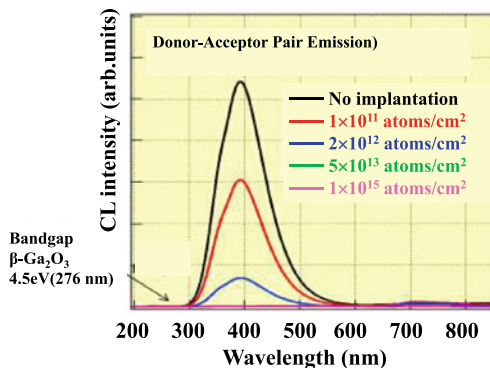


Fig. 5.81 CL spectra of Si-doped $\beta\text{-Ga}_2\text{O}_3$ specimens implanted at various Si ion fluences after annealing [224]

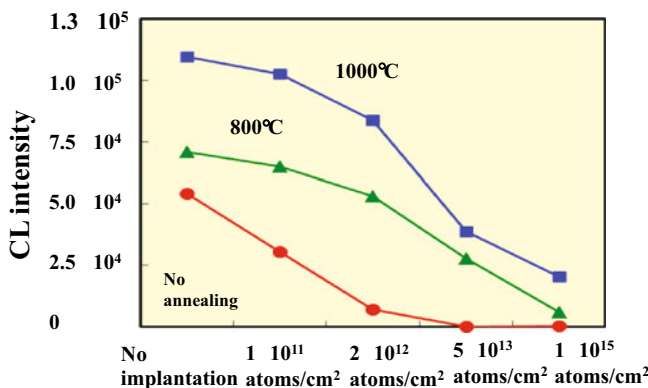


Fig. 5.82 Annealing temperature dependence of the CL intensity at 400 nm of Si-doped $\beta\text{-Ga}_2\text{O}_3$ specimens implanted at various Si ion fluences [224]

results are illustrated in Fig. 5.83a, b. The location of the n+ layer in Fig. 5.83a shifted inwards compared to that in Fig. 5.83b, resulting in greater diffusion of Si into the interior of the wafer [224]. This result is consistent with that of SIMS measurement in Fig. 5.78. Furthermore, a comparison of Fig. 5.83a, b shows that, although the SCM signal intensity of the n-typed area in the specimen annealed at 1000 °C did not change in the region with a high n concentration, the SCM signal intensity in the specimen annealed at 800 °C decreased in this area (approximately 0.05 μm). There was no difference between the specimens annealed at 800 and 1000 °C in the area more than 0.4 μm apart from the upper surface [224]. There is generally a relationship between the SCM signal (dC/dV) and the carrier concentration n in high concentration regions of n-typed specimens in Fig. 5.84 [225]. These results indicate that the n-type carriers in the area 0.05 μm from the upper surface of the specimen

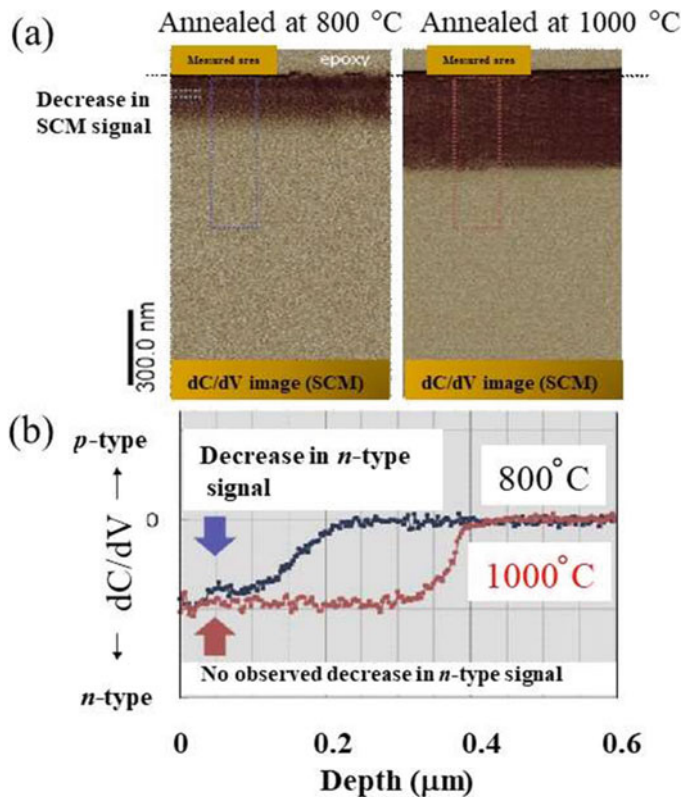


Fig. 5.83 **a** SCM signal images for, and **b** depth profiles of dC/dV signal for specimen implanted at a fluence of 1×10^{15} Si atoms/cm² after annealing at 800 °C and 1000 °C [224]

annealed at 1000 °C were not activated, in contrast to those in the specimen annealed at 800 °C [224].

Rao et al. synthesised β -Ga₂O₃ nanowires using a microwave plasma reactor with H₂/CH₄/O₂ and performed SEM, TEM, FT-IR, and Raman measurements [226]. They found that the Raman bands of the [110] nanowires were significantly blue-shifted compared with those of the bulk [226]. Further, they measured the corresponding FT-IR transmittance spectra of the same specimens using a Bruker IFS 66 v/s spectrometer and pressed KBr pellets containing dispersions of either powdered or nanowire forms of β -Ga₂O₃ [226].

The IR modes in the nanowire spectrum, like the Raman bands, were also blue-shifted in frequency relative to those of the bulk [226]. For example, the IR mode frequencies above 600 cm⁻¹ in the β -Ga₂O₃ nanowires were blue-shifted by as much as 50 cm⁻¹ [226]. A first-principles calculation of the strain dependence of the Raman mode frequencies of bulk β -Ga₂O₃ indicated that the phonon frequency shifts of the β -Ga₂O₃ nanowires were caused by internal strains [226].

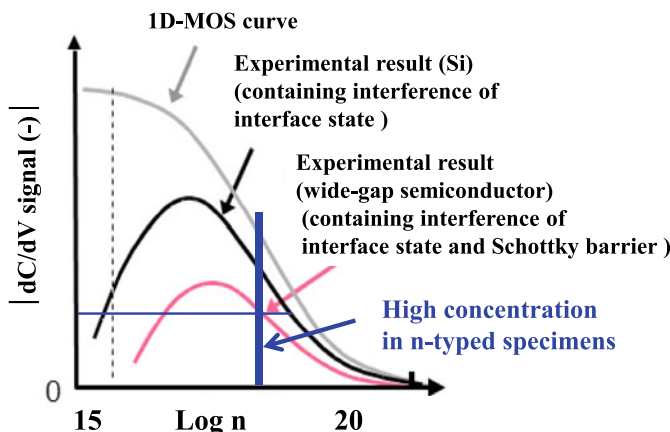


Fig. 5.84 Relationship between the SCM signal (dC/dV) and carrier concentration n in regions of high n concentration [225]

5.11 Quantum Dots

Semiconductor quantum dots (QDs) have attracted much interest in various scientific fields owing to their unique optical, electronic, and electrochemical properties. These properties, in particular the broad absorption spectra with narrow emission bands, excellent photostability, high quantum yield, and size-dependent PL, make them suitable for use as fluorescence probes for biological specimens [227–230].

Milekhin et al. reported an experimental work that compared InAs/AlAs periodical structures with InAs and AlAs QDs using Raman spectroscopy [231]. The confined LO frequencies of the QDs measured using Raman scattering were compared with those calculated from an analysis of the IR spectra under the dielectric function approximation [231].

Milekhin et al. prepared the QD structures AlAs QDs consisting of 50 periods of AlAs [2.4 monolayers (ML, 1 ML = 0.283 nm)] embedded in InAs and InAs (12-nm thick) layers (specimen A), grown by MBE on GaAs (011) substrates [231]. They measured the Raman spectra of specimen A in different scattering configurations, in which confined optical and/or interface (IF) phonons were detected. They assigned the strong peaks at 219 and 240 cm^{-1} to the TO and LO phonons of the InAs layers [231]. Raman bands at 270 and 294 cm^{-1} in both spectra are originating from the TO and LO phonons of the GaAs substrate. Dramatic features at 339 and 367 cm^{-1} , which are assigned, respectively, to the TO and LO phonons localised in the AlAs QDs, are a shift from their bulk positions caused by the tensile strain in AlAs QDs [231].

Moreover, they found Raman spectra in additional features located at 232 cm^{-1} and 351 cm^{-1} , between the TO and LO phonon modes of AlAs QDs and InAs layers [231]. They assigned these modes to InAs- and AlAs-like IF phonons attributed to

the QD/matrix interface. Their peak-frequency positions were calculated using the dielectric continuum model [232]. Based on the calculation, they assumed that AlAs QDs surrounded by InAs possess a shape of an oblate ellipsoid with a ratio of the ellipsoid axes 2:1 corresponding to the value induced from HRTEM images [231]. The calculated results are coincident with the experimental data. In their model, each IF mode is determined by two quantum numbers, l ($l \geq 0$) and m ($|m| \leq l$) [232]. The IF modes with small quantum numbers strongly contribute to Raman spectra for QDs, since the modes with large l are strongly localised at the interface while coupled weakly to charge carriers [232]. The calculated frequency positions of the first three InAs- and AlAs-like IF phonons (with quantum numbers $l = 1, m = 0$ (230 and 352 cm^{-1}) and $m = 1$ (235 and 346 cm^{-1}); and $l = 2, m = 0$ (232 and 350 cm^{-1}), respectively) are shown in Fig. 2 of Ref. [231] by closed triangles [231]. Only IF modes with $l = \text{even integer}$ and $m = 0$ are allowed in Raman scattering selection rule by Comas et al. [233]. The major contribution to the IF modes observed in the Raman spectra at 232 and 350 cm^{-1} is most likely owing to the IF modes with $l = 2, m = 0$ (the middle-closed triangles in Fig. 2 of Ref. [231]) [231]. For comparison, the frequency positions of the IF mode with quantum number $l = 1$ calculated for the structure with spherical QDs are depicted by open triangles in Fig. 2 of [231]. Their calculations for the ellipsoidal QDs agree well with the observed IF mode positions. They demonstrated that Raman spectroscopy was sensitive to the preferential shape of QDs [231].

CdSe quantum dots (QDs) on ZnSe are desirable as a material for green LDs [234]. The lattice mismatch between CdSe and ZnSe is approximately 7%. This value resembles that between InAs and GaAs, whose QDs structures are more actively studied [234]. CdSe QDs can be formed on ZnSe by the self-assembling method through the Stranski–Krastanov (S–K) mode [234].

Luminescence emitted from single QDs was studied by μ -PL through a narrow window on the metal mask or by near-field PL [235, 236]. On the other hand, CL spectroscopy can be conducted without a metal mask or sharp metal tip, differently from the two techniques presented above. CL spectra can be measured at any point on the specimen. The spatial resolution in CL spectroscopy is determined not by the diameter of an exciting electron beam (EB) but by the spreading of an e-beam in the specimen and the diffusion of the excited carriers.

We prepared for the CdSe QD/ZnSe/GaAs structures by molecular beam epitaxy (MBE) [237]. Elemental Zn, Cd, and, Se with 6-N purity were used as the source materials. The ZnSe buffer layer (50 nm thick) was first grown on a GaAs (100) substrate and then the CdSe QDs were grown on the ZnSe/GaAs substrate [237]. The amount of supply was 2.6 monolayers (ML), and the supply rate was 0.1 ML/s. The ZnSe cap layer (30 nm thick) was formed on it without interruption. The growth temperature was 330 °C. A bright PL was observed at 14 K in this specimen [237]. SEM-CL spectra were measured at 30 K, and the acceleration voltage and the current of the exciting EB were 10 kV and 4 nA, respectively. The beam diameter was approximately 30 nm [237]. With a scanning area of $1 \times 1\text{ }\mu\text{m}^2$ or less, sharp CL peaks from the single QDs structures were observed on a broad envelope-like emission [237]. The CL image of QDs structures was successfully obtained by measuring the

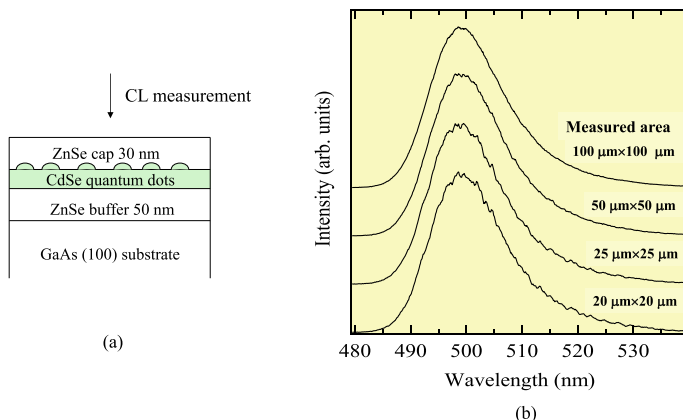


Fig. 5.85 **a** Schematic of QD structures and **b** μ -CL spectra measured decreasing the scanning region of the exciting e-beam from $100 \times 100 \mu\text{m}^2$ to $20 \times 20 \mu\text{m}^2$ (our original data) [7]

CL intensity at each fixed wavelength, decreasing the scanning region of the exciting EB from $100 \times 100 \mu\text{m}^2$ to $2 \times 2 \mu\text{m}^2$. CL peaks assigned to the single QDs structures were observed at different positions and at different wavelengths [237]. With the EB fixed every 70 nm in a region of $2 \times 2 \mu\text{m}^2$, 30 × 30 CL spectra were obtained for 2D CL image measurement of the CdSe QDs structures.

Figure 5.85 illustrates a schematic of QDs structures and CL spectra measured, decreasing the scanning region of the exciting EB from $100 \times 100 \mu\text{m}^2$ to $20 \times 20 \mu\text{m}^2$. A broad CL spectrum was observed at the scanning region of $20 \times 20 \mu\text{m}^2$. The peak wavelength was 500 nm (2.48 eV), and the FWHM was 61 meV. Sharp CL peaks appeared on the broad envelope-like emission at a scanning region of $20 \times 20 \mu\text{m}^2$.

Figure 5.86 depicts many CL spectra among them, measured every 125 nm along a $2 \mu\text{m}$ length. The spectral resolution of this measurement was approximately 1 meV [7]. Many sharp CL peaks from single QDs structures were detected at each point. The FWHM of the sharpest CL peaks was approximately 2.5 meV [7]. The FWHM values of 200 μeV at 5 K and 900 μeV at 60 K [238], or 320 μeV at 8 K [239], were reported for the CdSe QDs structures. The origin of the larger FWHM value in our specimen is not clear at this stage. The broad envelope-like spectrum differs at each point in their peak wavelength and FWHM. It means that the QD distribution fluctuates at each position in size and space [7].

The number of sharp peaks in Fig. 5.86 was estimated to be 60 at maximum under the excitation energy of the fixed EB. The diameter of the EB was approximately 30 nm, but the EB expands laterally inside the ZnSe buffer and cap layers, exciting electrons, and holes [7]. It is generally reported that the excited carriers are trapped in a short time on the order of 10 ps. Hence, they do not diffuse significantly in the lateral direction in ZnSe but diffuse laterally in the CdSe QDs after being trapped [240, 241]. The excited region is larger than the EB diameter in CL measurement.

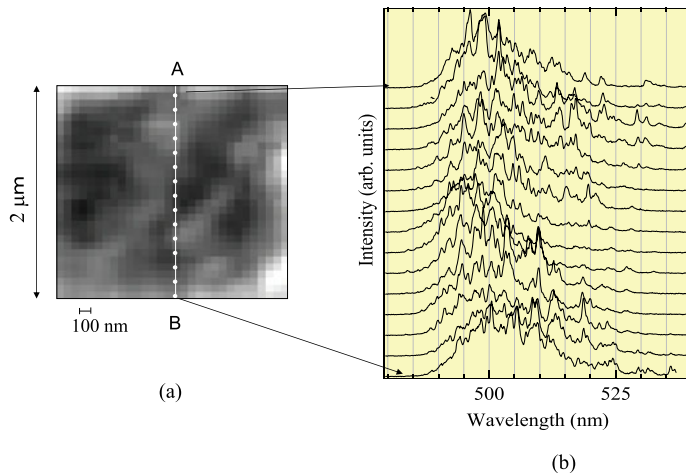


Fig. 5.86 **a** SEM image of CdSe QD structures and **b** CL spectra of CdSe QD structures, with the exciting EB fixed every 125 nm along line A-B (2- μm length) (our original data) [7]

The excited region in this specimen can be estimated from the number of sharp CL peaks and the QD density [7].

Figure 5.87 depicts a plane-view STEM image. The QD density was evaluated to be approximately 10^{10} cm^{-2} from the plane-view STEM image in Fig. 5.87 [237]. The shape and the size (approximately 20 nm) of QDs resembled those reported by Maehashi et al. [241]. The excited region was calculated to be approximately $0.45 \times 0.45 \mu\text{m}^2$. Thus, the spatial resolution was approximately $0.45 \mu\text{m}$ in the CL measurement. The spread of the EB is evaluated to be approximately $0.1 \mu\text{m}$, and the diffusion length in the two-dimensional (2D) CdSe quantum well (QW) is reported to be $0.498 \mu\text{m}$ [237]. The sum of these values ($\sim 0.6 \mu\text{m}$) resembles our value, $0.45 \mu\text{m}$, although the diffusion length may be different between the QDs layer and the 2D QW. Under strong excitation energy by the EB, a single QD may illustrate several CL peaks, namely, the ground-state exciton, excited-state exciton, biexciton, trion, and phonon-related CL peaks. Therefore, 60 is the maximum number of single QD structures that exist in the excited region. The value of the spatial resolution, approximately $0.45 \mu\text{m}$, is also the maximum value evaluated [237].

Figure 5.88 depicts CL intensity images of CdSe QDs, measured at arbitrarily selected wavelengths in a $2 \times 2 \mu\text{m}^2$ area [7]. As seen in Fig. 5.88, a different CL image is observed at a different wavelength in the same $2 \times 2 \mu\text{m}^2$ region. This means that QDs with different sizes are distributed in the same $2 \times 2 \mu\text{m}^2$ region [7]. The diameter of the dot size was approximately $0.4 \mu\text{m}$. This size is not the one of the QD itself (approximately 20 nm) but rather the carrier excitation region mentioned above. The $0.4\text{-}\mu\text{m}$ size coincides well with the $0.45\text{-}\mu\text{m}$ spatial resolution calculated above [7].

STEM-CL, which has been recently developed, discussed in Sect. 6, provides us with direct information about the size of single QDs and their distribution.

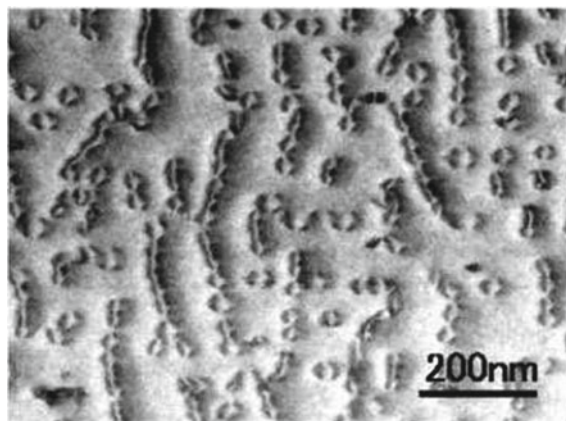


Fig. 5.87 A plane-view STEM image [237] (Reproduced with permission from Ref. [237]. © John Wiley and Sons, 2004.)

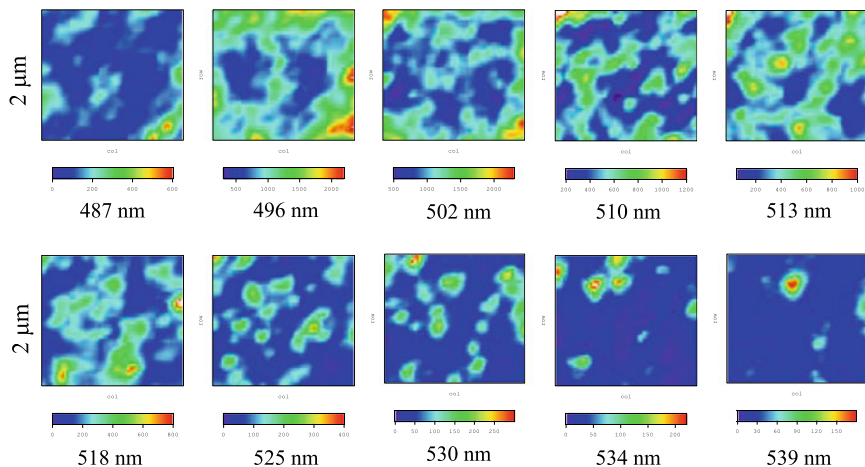


Fig. 5.88 CL intensity images ($2 \mu\text{m} \times 2 \mu\text{m}$) of CdSe QD structures, measured at arbitrarily selected wavelengths (our original data) [7]

References

1. Drozdov, N. A., Patrin, A. A., & Tkachev, V. D. (1976). Recombination radiation on dislocations in silicon. *JETP Letters*, 23, 597.
2. Drozdov, N. A., Patrin, A. A., & Tkachev, V. D. (1977). On the nature of the dislocation luminescence in silicon. *Physica Status Solidi B*, 83, K137.
3. Higgs, V., Lightowers, E. C., Norman, C. E., & Kightley, P. C. (1992). Characterisation of dislocations in the presence of transition metal contamination. *Materials Science Forum*, 83–87, 1309.

4. Sekiguchi, T., & Sumino, K. (1996). Cathodoluminescence study on dislocations in silicon. *Journal of Applied Physics*, 79(6), 15.
5. Yoshida, Y., & Langouche, G. (2015). Defect characterization in silicon by electron-beam-induced current and cathodoluminescence techniques. In Y. Yoshida & G. Langouche (Eds.), *Defects and impurities in silicon materials* (pp. 343–372). Springer.
6. Sauer, R., Weber, J., & Stoltz, J. (1985). Dislocation-related photoluminescence in silicon. *Applied Physics A*, 36, 1–13.
7. Sugie, R., & Yoshikawa, M. (unpublished).
8. Pages, O., Souhabi, J., Torres, V. J. B., Postnikov, A. V., & Rustagi, K. C. (2012). Re-examination of the SiGe Raman spectra: Percolation/one-dimensional-cluster scheme and ab initio calculations. *Physical Review B*, 86, 045201.
9. Zhao, B., Wang, S.-Q., Fiebig, M., Anderson, S., Vasudev, P. K., & Seidel, T. E. (1996). *Reliability and electrical properties of new low dielectric constant interlevel dielectrics for high performance ULSI interconnect* (p. 156). IEEE.
10. Kim, J.-H., Seo, S.-H., Yun, S.-M., Chang, H.-Y., Kwang-Man, & Choi, C.-K. (1996). The deposition of SiOF film with low dielectric constant in a helicon plasma source. *Applied Physics Letters*, 68, 1507.
11. Nakano, T., Mura, N., & Tsuzumitani, A. (1995). Raman study of ring structures of chemical vapor deposited SiO₂ thin films. *Japanese Journal of Applied Physics*, 34, L1064.
12. Lee, S., & Park, J. W. (1996). Effect of fluorine on dielectric properties of SiOF films. *Journal of Applied Physics*, 80, 5260.
13. Yoshikawa, M., Iwagami, K., Morita, N., Matsunobe, T., & Ishida, H. (1997). Characterization of fluorine-doped silicon dioxide film by Raman spectroscopy. *Thin Solid Films*, 310, 167.
14. Nagai, N., Terada, K., Muraji, Y., Hashimoto, H., Maeda, T., Maeda, Y., Tahara, E., Tokai, N., & Hatta, A. (2002). Infrared absorption study of rapid thermal oxidation and in situ steam generation of thin SiO₂ films by gradient etching preparation. *Journal of Applied Physics*, 91, 4747.
15. Martinet, C., & Devine, R. A. B. (1995). Analysis of the vibrational mode spectra of amorphous SiO₂ films. *Journal of Applied Physics*, 77, 4343.
16. Queeney, K. T., Weldon, M. K., Chang, J. P., Chabal, Y. J., Gurevich, A. B., Sapjeta, J., & Opila, R. L. (2000). Infrared spectroscopic analysis of the Si/SiO₂ interface structure of thermally oxidized silicon. *Journal of Applied Physics*, 87, 1322.
17. Yoshikawa, M., Seki, H., Yamane, T., Nanen, Y., Kato, M., & Kimoto, T. (2013). Abnormal behavior of longitudinal optical phonon in silicon dioxide films on 4H-SiC bulk epitaxial substrate using Fourier transform infrared (FT-IR) spectroscopy. *Applied Spectroscopy*, 67, 542–545.
18. Nagai, N., Seki, H., & Yoshikawa, M. (unpublished).
19. Kruchinin, V. N., Perevalov, T. V., Aliev, V. Sh., Iskhakzai, R. M. Kh., Spesivtsev, E. V., Gritsenko, V. A., & Pustovarov, V. A. (2020). Optical properties of the SiO_x (x < 2) thin films obtained by hydrogen plasma processing of thermal silicon dioxide. *Optics and Spectroscopy*, 128, 1467.
20. Seki, H., Hashimoto, H., & Ozaki, Y. (2016). Characterization of process-induced damage in Cu/low-k interconnect structure by microscopic infrared spectroscopy with polarized infrared light. *Journal of Applied Physics*, 120, 095301.
21. Seki, H., Inoue, K., Nagai, N., Shimada, M., Inukai, K., Hashimoto, H., & Ogawa, S. (2004). Characterization of ashing damage in depth in low-k dielectric films by micro beam IR method. In *Proceedings of Advanced Metallization Conference* (pp. 34–37).
22. Conley, Jr., J. F., & Lenahan, P. M. (1996). A review of ESR studies of MOS systems. In H. Z. Massoud, E. H. Poindexter, & C. R. Helms (Eds.), *The physics and chemistry of SiO₂ and the Si-SiO₂ interface-3* (Vol. 96, No. 1, p. 214). The Electrochemical Society.
23. Skuja, L. N., Strelets, A. N., & Paakovich, A. B. (1984). A new intrinsic defect in amorphous SiO₂: Twofold coordinated silicon. *Solid State Communications*, 50, 1069.
24. Tohmon, R., Shimogaichi, Y., Mizuno, H., & Ohki, Y. (1989). 2.7-eV luminescence in as-manufactured high-purity silica glass. *Physical Review Letters*, 62, 1388.

25. Zhang, J.-Y., Bao, X.-M., Li, N.-S., & Song, H.-Z. (1998). Photoluminescence study of defects in Si⁺ ion implanted thermal SiO₂ films. *Journal of Applied Physics*, 83, 3609.
26. Watanabe, M., Juodkazis, S., Sun, H., Matsuo, S., & Misawa, H. (1999). Luminescence and defect formation by visible and near-infrared irradiation of vitreous silica. *Physical Review B*, 60, 9959–9964.
27. Sakurai, Y. (2000). The 3.1 eV photoluminescence band in oxygen-deficient silica glass. *Journal of Non-Crystalline Solids*, 271, 218–223.
28. Mitchell, J. P., & Denure, D. G. (1973). A study of SiO layers on Si using cathodoluminescence spectra. *Solid-State Electronics*, 16, 825–839.
29. Koyama, H. (1980). Cathodoluminescence observation of SiO₂ layers in a semiconductor device. *Journal of Applied Physics*, 51, 2304.
30. McKnight, S. W., & Palik, E. D. (1980). Cathodoluminescence of SiO₂ films. *Journal of Non-Crystalline Solids*, 40, 595.
31. Kalceff, M. A. S., & Phillips, M. R. (1995). Cathodoluminescence microcharacterization of the defect structure of quartz. *Physical Review B*, 52, 3122–3144.
32. Yacobi, R. G., & Holt, D. B. (Eds.). (1990). *Cathodoluminescence microscopy of inorganic solids*. Plenum Press.
33. Yoshikawa, M., Matsuda, K., Yamaguchi, Y., Matsunobe, T., Nagasawa, Y., Fujino, H., & Yamane, T. (2002). Characterization of silicon dioxide film by high spatial resolution cathodoluminescence spectroscopy. *Journal of Applied Physics*, 92, 7153.
34. Yamane, T., Nagai, N., Katayama, S., & Todoki, M. (2002). Measurement of thermal conductivity of silicon dioxide thin films using a 3ω method. *Journal of Applied Physics*, 92, 9772–9776.
35. Cerdeira, F., Buchenauer, C. J., Pollak, F. H., & Cardona, M. (1972). Stress-induced shifts of first-order Raman frequencies of diamond- and zinc-blende-type semiconductors. *Physical Review B*, 5, 580.
36. Wolf, I. D., Maes, H. E., & Jones, S. K. (1996). Stress measurements in silicon devices through raman spectroscopy: Bridging the gap between theory and experiment. *Journal of Applied Physics*, 79, 7148.
37. Yoshikawa, M., & Nagai, N. (2002). Vibrational spectroscopy of carbon and silicon materials. In J. M. Chalmers & P. R. Griffiths (Eds.), *Handbook of vibrational spectroscopy* (Vol. 4, pp. 2593–2620). Wiley.
38. Yoshikawa, M., Maegawa, M., Katagiri, G., & Ishida, H. (1995). Characterization of anisotropic stress around Si trenches by polarized Raman spectroscopy. *Journal of Applied Physics*, 78, 941.
39. Welser, J., Hoyt, J. L., Takagi, S., & Gibbons, J. F. (1994). Strain dependence of the performance enhancement in strained-Si n-MOSFETs. In *IEDM Technical Digest* (pp. 373–376).
40. Rim, K., Welser, J. J., Hoyt, J. L., & Gibbons, J. F. (1998). Transconductance enhancement in deep submicron strained-Si n-MOSFETs. In *IEDM Technical Digest* (p. 707).
41. Shahidi, G. G. (2002). SOI technology for the THz era. *IBM Journal of Research and Development*, 46, 121–131.
42. Oberhuber, G., Zandler, G., & Vogel, P. (1998). Subband structure and mobility of two dimensional holes in strained Si/SiGe MOSFETs. *Physical Review B*, 58, 9941.
43. Takagi, S., Hoyt, J. L., Welser, J. J., & Gibbons, J. F. (1996). Comparative study of phonon limited mobility of two-dimensional electrons in strained and unstrained Si metal-oxide-semiconductor field-effect transistors. *Journal of Applied Physics*, 80, 1567.
44. Higgs, V., & Kittler, M. (1993). Investigation of the recombination activity of misfit dislocations in Si/SiGe epilayers by cathodoluminescence imaging and the electron beam induced current technique. *Applied Physics Letters*, 63, 11.
45. Yoshikawa, M., & Sugie, R. (unpublished).
46. Hincinschi, C., Radu, I., Singh, R., Erfurth, W., Milenin, A. P., Reiche, M., Christiansen, S. H., & Gosele, U. (2006). Relaxation of strain in patterned strained silicon investigated by UV Raman spectroscopy. *Materials Science and Engineering B*, 135, 184–187.

47. Higgs, V., Lightowers, E. C., Tajbakhsh, S., & Wright, P. J. (1992). Cathodoluminescence imaging and spectroscopy of dislocations in Si and $\text{Si}_{1-x}\text{Ge}_x$ alloys. *Applied Physics Letters*, 61, 1087.
48. Steegen, A., Lauwers, A., de Potter, M., Badenes, G., Rooyackers, R., & Maex K. (2000). In *Symposium on VLSI Technology Digest* (p. 180). IEEE.
49. Damiano, J., et al. (1998). In *Symposium on VLSI Technology Digest* (p. 212). IEEE.
50. Park, M. H., Hong, S. H., Hong, S. J., Park, T., Song, S., Park, J. H., Kim, H. S., Shin, Y. G., Kang, H. K., & Lee, M. Y. (1997). Stress minimization in deep sub-micron full CMOS devices by using an optimized combination of the trench filling CVD oxides. In *Technical Digest—International Electron Devices Meeting* (pp. 669–672).
51. Yacobi, B. G., & Holt, D. B. (Ed.). (1990). *Cathodoluminescence microscopy of inorganic solids*. Plenum Press.
52. Sauer, R., Weber, J., Stolz, J., Weber, E. R., Kusters, K. H., & Alexander, H. (1985). Dislocation-related photoluminescence in silicon. *Applied Physics A*, 36, 1.
53. Kambayashi, S., Hamasaki, T., Nakakubo, T., Watanabe, M., & Tango, H. (1986). In *Extended Abstracts of the 18th Conference on Solid State Devices and Materials, Tokyo* (pp. 415–418).
54. Kobayashi, K., Inoue, Y., Nishimura, T., Nishioka, T., Arima, H., Hirayama, M., & Matsukawa, T. (1987). In *Extended Abstracts of the 19th Conference on Solid State Devices and Materials, Tokyo* (p. 323).
55. Wolf, I. D., Vanhellemont, J., Romano-Rodriguez, A., Norström, H., & Maes, H. E. (1992). Micro-Raman study of stress distribution in local isolation structures and correlation with transmission electron microscopy. *Journal of Applied Physics*, 71, 898.
56. Mizukoshi, T., Shibusawa, K., Yo, S., Sugie, R., & Ajioka, T. (2005). An application of cathodoluminescence to optimize the shallow trench isolation process. *IEEE Transactions on Semiconductor Manufacturing*, 18, 546–553.
57. Sugie, R., Matsuda, K., Ajioka, T., Yoshikawa, M., Mizukoshi, T., Shibusawa, K., & Yo, S. (2006). Investigation of stress-induced defects in shallow trench isolation by cathodoluminescence and Raman spectroscopies. *Journal of Applied Physics*, 100, 064504.
58. Kanaya, K., & Okayama, S. (1972). Penetration and energy-loss theory of electrons in solid targets. *Journal of Physics D*, 5, 43–58.
59. Thonke, K., Klemisch, H., Weber, J., & Sauer, R. (1981). New model of the irradiation-induced 0.97-eV (G) line in silicon: A $\text{C}_S\text{—Si}^*$ complex". *Physical Review B*, 24, 5874.
60. Kveder, V. V., Steinman, E. A., Shevchenko, S. A., & Grimmeiss, H. G. (1995). Dislocation-related electroluminescence at room temperature in plastically deformed silicon. *Physical Review B*, 51, 10520–10526.
61. Pizzini, S., Acciarri, M., Leoni, E., & Donne, A. L. (2000). About the D1 and D2 dislocation luminescence and its correlation with oxygen segregation. *Physica Status Solidi B*, 222, 141–150.
62. Sugie, R., Inoue, K., & Yoshikawa, M. (2012). Semi-quantitative analysis of the depth distribution of radiative recombination centers in silicon power devices by cross-sectional cathodoluminescence. *Journal of Applied Physics*, 112, 033507.
63. Giri, P. K., Coffa, S., & Rimini, E. (2001). Evidence for small interstitial clusters as the origin of photoluminescence W band in ion-implanted silicon. *Applied Physics Letters*, 78, 291.
64. Davies, G. 1989. "The optical properties of luminescence centres in silicon". *Phys. Rep.* 176: 83.
65. Palik, E. D. (1985). *Handbook of optical constants of solids* (Vols. I and II). Academic Press.
66. Burns, G. (1985). In *Solid state physics* (p. 458). Academic Press.
67. Burns, G. (1985). In *Solid state physics* (p. 469). Academic Press.
68. Lockwood, D. J., Yu, G., & Rowell, N. L. (2005). Optical phonon frequencies and damping in AlAs, GaP, GaAs, InP, InAs, and InSb studied by oblique incidence infrared spectroscopy. *Solid State Communications*, 136, 404–409.
69. Rowell, N. L., Shin, H. K., Lockwood, D. J., & Poole, P. J. (2002). Polarized infrared spectroscopy at oblique incidence of optical phonons in $\text{In}_{1-x}\text{Ga}_x\text{As}$ epilayers on InP. *Journal of Applied Physics*, 92, 629.

70. Gervais, F., & Piriou, B. (1974). Anharmonicity in several-polar-mode crystals: Adjusting phonon self-energy of LO and TO modes in Al_2O_3 and TiO_2 to fit infrared reflectivity. *Journal of Physics C*, 7, 2374.
71. Born, M., & Wolf, E. (Eds.). (1975). *Principles of optics* (p. 68). Pergamon Press.
72. Yu, G., Rowell, N. L., Lockwood, D. J., & Wasilewski, Z. R. (2003). Infrared reflectivity of $(\text{GaAs})_m/(\text{AlAs})_n$ superlattices. *Applied Physics Letters*, 83, 3683.
73. Rowell, N. L., Yu, G., Lockwood, D. J., & Poole, P. J. (2003). Phonons in $\text{In}_{0.53}\text{Ga}_{0.47}\text{As}/\text{InP}$ (100) superlattices by infrared reflectance. *Physical Review B*, 68, 165320.
74. Debernadi, A. (1998). Phonon linewidth in III-V semiconductors from density-functional perturbation theory. *Physical Review B*, 57, 12847–12858.
75. Klein, M. V. (1983). In M. Cardona (Ed.), *Light scattering in solids* (p. 147). Springer.
76. Rich, D. H., George, T., Pike, W. T., Maserjian, J., & Grunthaner, F. J. (1992). Cathodoluminescence and transmission electron microscopy study of dark line defects in thick $\text{In}_{0.2}\text{GaOsAs}/\text{GaAs}$ multiple quantum wells. *Journal of Applied Physics*, 72, 5834–5839.
77. Asai, H., & Oe, K. (1983). Energy band-gap shift with elastic strain in $\text{Ga}_x\text{In}_{1-x}\text{P}$ epitaxial layers on (001) GaAs substrates. *Journal of Applied Physics*, 54, 5834.
78. Landa, G., Carles, R., Fontaine, C., Bedel, E., & Munoz-Yague, A. (1989). Optical determination of strains in heterostructures: GaAs/Si as an example. *Journal of Applied Physics*, 66, 196.
79. De-Sheng, J., Makita, Y., Ploog, K., & Queisser, H. J. (1982). Electrical properties and photoluminescence of Te-doped GaAs grown by molecular beam epitaxy. *Journal of Applied Physics*, 53, 999.
80. Pollak, F. H., & Cardona, M. (1968). Piezo-electroreflectance in Ge, GaAs, and Si. *Physical Review B*, 172, 816.
81. Yoshikawa, M., Iwagami, K., & Ishida, H. (1998). Characterization of carrier concentration and stress in GaAs metal-semiconductor field-effect transistor by cathodoluminescence spectroscopy. *Journal of Applied Physics*, 84, 1693–1696.
82. Coleman, J. J., Bryce, A. C., & Jagadish, Ch. (2012). *Advances in Semiconductor Lasers*. Academic Press.
83. Matsui, T., Ohtsuka, K., Sugimoto, H., Abe, Y., & Ohishi, T. (1990). 1.5 μm GaInAsP/InP buried-heterostructure laser diode fabricated by reactive ion etching using a mixture of ethane and hydrogen. *Applied Physics Letters*, 56, 1641.
84. Chung, T., Hosoda, N., Suga, T., & Takagi, H. (1998). 1.3 μm InGaAsP/InP lasers on GaAs substrate fabricated by the surface activated wafer bonding method at room temperature. *Applied Physics Letters*, 72, 1565.
85. Yoshikawa, M., & Matsuda, K. (unpublished).
86. Giehler, M., Ramsteiner, M., Brandt, O., Yang, H., & Ploog, K. H. (1995). Optical phonons of hexagonal and cubic GaN studied by infrared transmission and Raman spectroscopy. *Applied Physics Letters*, 67, 733–735.
87. Lawaetz, P. (1972). Stability of the Wurtzite structure. *Physical Review B*, 5, 4039.
88. Brandt, O., Yang, H., Jenichen, B., Suzuki, Y., & Daweritz, L., & Ploog, K. H. (1995). Surface reconstructions of zinc-blende GaN/GaAs(001) in plasma-assisted molecular-beam epitaxy. *Physical Review B*, 52, R2253.
89. Lei, T., Ludwig, K. F., Jr., & Moustakas, T. D. (1993). Heteroepitaxy, polymorphism, and faulting in GaN thin films on silicon and sapphire substrates. *Journal of Applied Physics*, 74, 4430.
90. Manchon, D. D., Jr., Barker, A. S., Jr., Dean, P. J., & Zetterstrom, R. B. (1970). Optical studies of the phonons and electrons in gallium nitride. *Solid State Communications*, 8, 1227–1231.
91. Barker, A. S., Jr., & Illegems, M. (1973). Infrared lattice vibrations and free-electron dispersion in GaN. *Physical Review B*, 7, 743.
92. Sobotta, H., Neumann, H., Franzheld, R., & Seifert, W. (1992). Infrared lattice vibrations of GaN. *Physica Status Solidi B*, 174, K57.
93. Cingolani, A., Ferrara, M., & Lugara, M., & Scamarcio, G. (1986). First order Raman scattering in GaN. *Solid State Communications*, 58, 823–824.

94. Hayashi, K., Itoh, K., Sawaki, N., & Akasaki, I. (1991). Raman scattering in $\text{Al}_x\text{Ga}_{1-x}\text{N}$ alloys. *Solid State Communications*, 77, 115–118.
95. Perlin, P., Jauberthie-Carillon, C., Itie, J. P., Miguel, A. S., Grzegora, I., & Polian, A. (1992). Raman scattering and X-ray-absorption spectroscopy in gallium nitride under high pressure. *Physical Review B*, 45, 83–89.
96. Azuhata, T., Sota, T., Suzuki, K., & Nakamura, S. (1995). Polarized Raman spectra in GaN. *Journal of Physics: Condensed Matter*, 7, L129–L135.
97. Sugie, R., & Yoshikawa, M. (unpublished).
98. Klein, M. V., Ganguly, B. N., & Colwell, P. J. (1972). Theoretical and experimental study of Raman scattering from coupled LO-phonon-plasmon modes in silicon carbide. *Physical Review B*, 6, 2380.
99. Klein, M. V. (1982). In M. Cardona (Ed.), *Light scattering in solids* (p. 147). Springer.
100. Harima, H., Inoue, T., Nakashima, S., & Furukawa, K., & Taneya, M. (1998). Electronic properties in p-type GaN studied by Raman scattering. *Applied Physics Letters*, 73, 2000.
101. Sun, C. J., Zubair Anwar, M., Chen, Q., Yang, J. W., Asif Khan, M., Shur, M. S., Bykhovski, A. D., Liliental-Weber, Z., Kisielowski, C., Smith, M., Lin, J. Y., & Xiang, H. X. (1997). Quantum shift of band-edge stimulated emission in InGaN–GaN multiple quantum well light-emitting diodes. *Applied Physics Letters*, 70, 2978.
102. Wu, X. H., Elsass, C. R., Abare, A., Mack, M., Keller, S., Petroff, P. M., DenBaars, S. P., Speck, J. S., & Rosner, S. J. (1998). Structural origin of V-defects and correlation with localized excitonic centers in InGaN/GaN multiple quantum wells. *Applied Physics Letters*, 72, 692.
103. Kim, I.-H., Park, H.-S., Park, Y.-J., & Kim, T. (1998). Formation of V-shaped pits in InGaN/GaN multiquantum wells and bulk InGaN films. *Applied Physics Letters*, 73, 1634.
104. Chen, Y., Takeuchi, T., Amano, H., Akasaki, I., Yamada, N., Kaneko, Y., & Wang, S. Y. (1998). Pit formation in GaInN quantum wells. *Applied Physics Letters*, 72, 710.
105. Northrup, J. E., Romano, L. T., & Neugebauer, J. (1999). Surface energetics, pit formation, and chemical ordering in InGaN alloys. *Applied Physics Letters*, 74, 2319.
106. Yoshikawa, M., Murakami, M., Ishida, H., & Harima, H. (2009). Characterizing nanometer-sized V-defects in InGaN single quantum well films by high-spatial-resolution cathodoluminescence spectroscopy. *Applied Physics Letters*, 94, 131908-1–131908-3.
107. Sze, S. M. (2002). Semiconductor devices. In *Physics and technology* (2nd ed., Chap. 6, p. 182). Wiley.
108. Fukuda, K., Kato, M., Kojima, K., & Senzaki, J. (2004). Effect of gate oxidation method on electrical properties of metal-oxide-semiconductor field-effect transistors fabricated on 4H-SiC C (000̄1) face. *Applied Physics Letters*, 84, 2088.
109. Kimoto, T., Kanzaki, Y., Noborio, M., Kawano, H., & Matsunami, H. (2005). Interface properties of metal-oxide-semiconductor structures on 4H-SiC 0001 and (1120) formed by N_2O oxidation. *Japanese Journal of Applied Physics*, 44, 1213.
110. Afanasev, V. V., Bassler, M., Pensl, G., & Schulz, M. (1997). Intrinsic SiC/SiO₂ interface states. *Physica Status Solidi A*, 162, 321.
111. Cosper, J. A., Jr. (1997). Advances in SiC MOS technology. *Physica Status Solidi A*, 162, 305.
112. Zheleva, T., Lelis, A., Duscher, G., Liu, F., Levin, I., & Das, M. (2008). Transition layers at the SiO₂/SiC interface. *Applied Physics Letters*, 93, 022108.
113. Luo, T. Y., Laughery, M., Brown, G. A., Al-Shareef, H. N., Watt, V. H. C., Karamcheti, A., Jackson, M. D., & Huff, H. R. (2000). Effect of H₂ content on reliability of ultrathin *in-situ* steam generated (ISSG) SiO₂. *Electron Device Letter*, 21(9), 430–432.
114. Nagai, N., Terada, K., Muraji, Y., Hashimoto, H., Maeda, T., Maeda, Y., Tahara, E., Tokai, N., & Hatta, A. (2002). Infrared absorption study of rapid thermal oxidation and *in situ* steam generation of thin SiO₂ films by gradient etching preparation. *Journal of Applied Physics*, 87, 4747–4750.
115. von Bardeleben, H. J., Cantin, J. L., Vickridge, I. C., Song, Y., Dhar, S., Feldman, L. C., Williams, J. R., Ke, L., Shishkin, Y., Devaty, R. P., & Choyke, W. J. (2005). Modification

- of the oxide/semiconductor interface by high temperature NO treatments: A combined EPR, NRA and XPS study on oxidized porous and bulk n-type 4H-SiC. *Materials Science Forum*, 483–485, 277–282.
116. Jamet, P., Dimitrijer, S., & Tanner, P. (2001). Effects of nitridation in gate oxides grown on 4H-SiC. *Journal of Applied Physics*, 90, 5058–5063.
 117. Lipkin, L. A., Das, M. K., & Palmour, J. W. (2002). N₂O processing improves the 4H-SiC: SiO₂ interface. *Materials Science Forum*, 389–393, 985.
 118. Kanzaki, Y., Kinbara, H., Kosugi, H., Suda, J., Kimoto, T., & Matsunami, H. (2004). High channel mobilities of MOSFETs on highly-doped 4H-SiC (11–20) face by oxidation in N₂O ambient. *Materials Science Forum*, 457–460, 1429.
 119. Das, M. K. (2004). Recent advances in (0001) 4H-SiC MOS device technology. *Materials Science Forum*, 457–460, 1275–1280.
 120. Nakashima, S., Okumura, H., Yamamoto, T., & Shimidzu, R. (2004). Deep-ultraviolet raman microspectroscopy: Characterization of wide-gap semiconductors. *Applied Spectroscopy*, 58, 224.
 121. Nakashima, S., Harima, H., Tomita, T., & Suemoto, T. (2000). Raman intensity profiles of folded longitudinal phonon modes in SiC polytypes. *Physical Review B*, 62, 16605.
 122. Nakashima, S., Mitani, T., Tomita, T., Kato, T., Nishizawa, S., Okumura, H., & Harima, H. (2007). Observation of surface polarity dependent phonons in SiC by deep ultraviolet Raman spectroscopy. *Physical Review B*, 75, 115321.
 123. Skowronski, M., & Ha, S. (2006). Degradation of hexagonal silicon-carbide-based bipolar devices. *Journal of Applied Physics*, 99, 011101.
 124. Sugie, R., Yoshioka, M., Harada, S., & Namikawa, Y. (2009). Expansion of stacking faults by electron-beam irradiation in 4H-SiC diode structure. *Materials Science Forum*, 600–603, 353–356.
 125. Sumakeris, J. J., Bergman, J. P., Das, M. K., Hallin, C., Hull, B. A., Janzén, E., Lendenmann, H., O'Loughlin, M. J., Paisley, M. J., Ha, S., Skowronski, M., Palmour, J. W., & Carter, C. H., Jr. (2006). Techniques for minimizing the basal plane dislocation density in SiC epilayers to reduce V_f drift in SiC bipolar power devices. *Materials Science Forum*, 527–529, 141–146.
 126. Sridhara, S. G., Carlsson, F. H. C., Bergman, J. P., & Janzén, E. (2001). Luminescence from stacking faults in 4H SiC. *Applied Physics Letters*, 79, 3944.
 127. Harada, S., Namikawa, Y., & Sugie, R. Submitted to this conference.
 128. Izumi, S., Tsuchida, H., Kamata, I., & Tawara, T. (2005). Structural analysis and reduction of in-grown stacking faults in 4H-SiC epilayers. *Applied Physics Letters*, 86, 202108.
 129. Fujiwara, H., Kimoto, T., Tojo, T., & Matsunami, H. (2005). Characterization of in-grown stacking faults in 4H-SiC (0001) epitaxial layers and its impacts on high-voltage Schottky barrier diodes. *Applied Physics Letters*, 87, 051912.
 130. Persson, P. O. A., & Hultman, L. (2002). On the nature of ion implantation induced dislocation loops in 4H-silicon carbide. *Journal of Applied Physics*, 92, 2501.
 131. Ohno, T., & Kobayashi, N. (2001). Structure and distribution of secondary defects in high energy ion implanted 4H-SiC. *Journal of Applied Physics*, 89, 933.
 132. Heera, V., Mucklich, A., Dubois, C., Voelkskow, M., & Skorupa, W. (2004). Layer morphology and Al implant profiles after annealing of supersaturated, single-crystalline, amorphous, and nanocrystalline SiC. *Journal of Applied Physics*, 96, 2501.
 133. Storasta, L., & Tsuchida, H. (2007). Reduction of traps and improvement of carrier lifetime in 4H-SiC epilayers by ion implantation. *Applied Physics Letters*, 90, 062116.
 134. Mitani, T., Hattori, R., & Yoshioka, M. (2009). Depth profiling of Al ion-implantation damage in SiC crystals by cathodoluminescence spectroscopy. *Materials Science Forum*, 600–603, 615–618.
 135. Egilsson, T., Bergman, J. P., Ivanov, I. G., Henry, A., & Janzén, E. (1999). Properties of the D1 bound exciton in 4H–SiC. *Physical Review B*, 59, 1956.
 136. Gali, A., Deak, P., Rauls, E., Son, N. T., Ivanov, I. G., Carlsson, F. H., Janzen, E., & Choyke, W. J. (2003). Correlation between the antisite pair and the DI center in SiC. *Physical Review B*, 67, 155203.

137. Sugie, R., Uchida, T., Kosaka, K., & Matsumura, K. (2016). Characterization of process-induced defects in SiC MOSFETs by cross-sectional cathodoluminescence. *Journal of Applied Physics*, 55, 04ER03.
138. Sugie, R., Baden, N., & Yoshikawa, M. (unpublished).
139. Eberlein, T. A. G., Jones, R., Öberg, S., & Briddon, P. R. (2006). Density functional theory calculation of the DI optical center in SiC. *Physical Review B*, 74, 144106.
140. Sugie, R., Uchida, T., & Yoshikawa, M. (unpublished).
141. von Bardeleben, H. J., Cantin, J. L., Vickridge, I. C., Song, Y., Dhar, S., Feldman, L. C., Williams, J. R., Shishkin, L., Ke, Y., Devaty, R. P., & Choyke, W. J. (2005). Modification of the oxide/semiconductor interface by high temperature NO treatments: A combined EPR, NRA and XPS study on oxidized porous and bulk n-type 4H-SiC. *Materials Science Forum*, 483–485, 277–280.
142. Harbecke, B., Heinz, B., & Grosse, P. (1985). Optical properties of thin films and the Berreman effect. *Applied Physics A*, 38(4), 263–267.
143. Yoshikawa, M., Seki, H., Inoue, K., Nanen, Y., & Kimoto, T. (2014). Characterization of inhomogeneity in silicon dioxide films on 4H-silicon carbide epitaxial substrate using a combination of Fourier transform infrared and cathodoluminescence spectroscopy. *Applied Spectroscopy*, 65, 1176–1180.
144. Chen, D. A., & Chen, G. (2007). Measurement of silicon dioxide surface phonon-polariton propagation length by attenuated total reflection. *Applied Physics Letters*, 91, 121906.
145. Yoshikawa, M., Seki, H., Inoue, K., Matsuda, K., Tanahashi, Y., Sako, H., Nanen, Y., Kato, M., & Kimoto, T. (2011). Characterization of silicon dioxide films on a 4H-SiC Si (0001) face by fourier transform infrared (FT-IR) spectroscopy and cathodoluminescence spectroscopy. *Applied Spectroscopy*, 65, 543–548.
146. Yoshikawa, M., Ogawa, S., Inoue, K., Seki, H., Tanahashi, Y., Sako, H., Nanen, Y., Kato, M., & Kimoto, T. (2012). Characterization of silicon dioxide films on 4H-SiC Si (0001) face by cathodoluminescence spectroscopy and X-ray photoelectron spectroscopy. *Applied Physics Letters*, 100, 082105.
147. Yoshikawa, M., Inoue, K., Seki, H., Nanen, Y., Kato, M., & Kimoto, T. (2013). Characterization of silicon dioxide films on 4H-SiC (0001) Si, (1–100) M, and (11–20) A faces by cathodoluminescence spectroscopy. *Applied Physics Letters*, 102, 051612.
148. Itoh, T., Kosaka, K., & Yoshikawa, M. (unpublished).
149. Demangeot, F., Paillard, V., Chassaing, P. M., Pages, C., Kahn, M. L., Maisonnat, A., & Chaudret, B. (2006). Experimental study of LO phonons and excitons in ZnO nanoparticles produced by room-temperature organometallic synthesis. *Applied Physics Letters*, 88, 071921.
150. Bergman, L., Chen, X.-B., Huso, J., Morrison, J. L., & Hoeck, H. (2005). Raman scattering of polar modes of ZnO crystallites. *Journal of Applied Physics*, 98, 093507.
151. Ursaki, V. V., Tiginyanu, I. M., Zalamai, V. V., Masalov, V. M., Samarov, E. N., Emelchenko, G. A., & Briones, F. (2004). Photoluminescence and resonant Raman scattering from ZnO-opal structures. *Journal of Applied Physics*, 96, 1001.
152. Dinh, L. N., Schildbach, M. A., Balooch, M., & Mclean, W. II. (1999). Pulsed laser deposition of ZnO nanocluster films by Cu-vapor laser. *Journal of Applied Physics*, 86, 1149.
153. McCluskey, M. D., Jokela, S. J., Zhuravlev, K. K., Simpson, P. J., & Lynn, K. G. (2002). Infrared spectroscopy of hydrogen in ZnO. *Applied Physics Letters*, 81, 3807.
154. Pajot, B., & Song, C. (1992). OH bonds in gallium arsenide grown by the liquid-encapsulated Czochralski crystal-growth method. *Physical Review B*, 45, 6484.
155. Damen, T. C., Porto, S. S. P., & Tell, B. (1966). Raman effect in zinc oxide. *Physical Review*, 142, 570.
156. Yoshikawa, M., Inoue, K., Nakagawa, T., Ishida, H., Hasuike, N., & Harima, H. (2008). Characterization of ZnO nanoparticles by resonant Raman scattering and cathodoluminescence spectroscopies. *Applied Physics Letters*, 92, 113115.
157. Demangeot, F., Paillard, V., Chassaing, P. M., Pages, C., Kahn, M. L., Maisonnat, A., & Chaudret, B. (2006). Experimental study of LO phonons and excitons in ZnO nanoparticles produced by room-temperature organometallic synthesis. *Applied Physics Letters*, 88, 2006.

158. Thakur, J. S., Auner, G. W., Naik, V. M., Sudakar, C., Kharel, P., Lawes, G., Suryanarayanan, R., & Naik, R. (2007). Raman scattering studies of magnetic Co-doped ZnO thin films. *Journal of Applied Physics*, 102, 093904.
159. Yoshikawa, M., Iwagami, K., & Ishida, H. (1998). Resonant Raman scattering of diamondlike amorphous carbon films. *Journal of Applied Physics*, 51, 1693.
160. Yoshikawa, M., Matsuda, K., Yamaguchi, Y., Matsunobe, T., Nagasawa, Y., Fjino, H., & Yamane, T. (2002). Characterization of ZnO nanoparticles by resonant Raman scattering and cathodoluminescence spectroscopies. *Journal of Applied Physics*, 92, 7153.
161. Yoshikawa, M., Sugie, R., Murakami, M., Matsunobe, T., Matsuda, K., & Ishida, H. (2006). Defect characterization of Si-doped GaN films by a scanning near-field optical microscope-induced photoluminescence. *Applied Physics Letters*, 88, 161905.
162. Chang, C.-P., Flamm, D. L., Ibbotson, D. E., & Mucha, J. A. (1988). Diamond crystal growth by plasma chemical vapor deposition. *Journal of Applied Physics*, 63, 1744.
163. Suzuki, K., Sawabe, A., Yasuda, H., & Inuzuka, T. (1987). Growth of diamond thin films by dc plasma chemical vapor deposition. *Applied Physics Letters*, 50, 728.
164. Kamo, M., Sato, Y., Matsumoto, S., & Setaka, N. (1983). Diamond synthesis from gas phase in microwave plasma. *Journal of Crystal Growth*, 62, 642–644.
165. Akatsuka, F., Hirose, Y., & Komaki, K. (1988). Rapid growth of diamond films by arc discharge plasma CVD. *Japanese Journal of Applied Physics*, 27, L1600.
166. Kobashi, K., Nishimura, K., Kawate, Y., & Horiuchi, T. (1988). Synthesis of diamonds by use of microwave plasma chemical-vapor deposition: Morphology and growth of diamond films. *Physical Review B*, 38, 4067.
167. Celli, F. G., Pehrsson, P. E., Wang, M.-T., & Butler, J. E. (1988). Infrared detection of gaseous species during the filament-assisted growth of diamond. *Applied Physics Letters*, 52, 2043.
168. Krishnamurti, D. (1954). The Raman spectrum of diamond. *Proceedings of the Indian Academy of Sciences Section A*, 40, 211–216.
169. Dresselhaus, M. S., & Dresselhaus, G. (Ed.). (1982). *Light scattering in solids III* (p. 3). Springer.
170. Nemanich, R. J., & Solin, S. A. (1979). First- and second-order Raman scattering from finite-size crystals of graphite. *Physical Review B*, 20, 392.
171. Yoshikawa, M., Katagiri, G., Ishida, H., Ishitani, A., & Akamatsu, T. (1988). Raman spectra of diamondlike amorphous carbon films. *Solid State Communications*, 66, 1177.
172. Yoshikawa, M., Katagiri, G., Ishida, H., Ishitani, A., & Akamatsu, T. (1988). Resonant Raman scattering of diamondlike amorphous carbon films. *Applied Physics Letters*, 52, 1639.
173. Yoshikawa, M., Katagiri, G., Ishida, H., Ishitani, A., & Akamatsu, T. (1988). Raman spectra of diamondlike amorphous carbon films. *Journal of Applied Physics*, 64, 6464.
174. Solin, S. A., & Ramdas, A. K. (1970). Raman spectrum of diamond. *Physical Review B*, 1, 1687.
175. Loudon, R. (1964). The Raman effect in crystals. *Advances in Physics*, 13, 423–482.
176. Yoshikawa, M., Ishida, H., Ishitani, A., Murakami, T., Koizumi, S., & Inuzuka, T. (1990). Study of crystallographic orientations in the diamond film on cubic boron nitride using Raman microprobe. *Applied Physics Letters*, 57, 428.
177. Yoshikawa, M., & Nagai, N. (2002). Vibrational spectroscopy of carbon and silicon materials. In J. M. Chalmers, P. R. Griffiths (Eds.), *Handbook of vibrational spectroscopy* (Vol. 4, pp. 2593–2620). Wiley.
178. Yoshikawa, M., Ishida, H., Ishitani, A., Koizumi, S., & Inuzuka, T. (1991). Study of crystallographic orientations in the diamond film on the (100) surface of cubic boron nitride using a Raman microprobe. *Applied Physics Letters*, 58, 1387.
179. Yoshikawa, M., Katagiri, G., Ishida, H., Ishitani, A., Ono, M., & Matsumura, K. (1993). Raman scattering from diamond particles. *Applied Physics Letters*, 62, 3114.
180. Cerdaira, F., Buchenauer, C. J., I'ollak, F. H., & Cardona, M. (1972). Stress-induced shifts of first-order raman frequencies of diamond- and zinc-blende-type semiconductors. *Physical Review B*, 5, 580.

181. Ganesan, S., Maradudin, A. A., & Oitmaa, I. (1970). A lattice theory of morphic effects in crystals of the diamond structure. *Annals of Physics*, *56*(2), 556–594.
182. Grimsditch, M. H., & Ramdas, A. K. (1975). Brillouin scattering in diamond. *Physical Review B*, *11*, 3139.
183. Abstreiter, G., Cardona, M., & Pinczuk, A. (1984). In M. Cardona & G. Güntherodt (Eds.), *Light scattering in solids IV* (p. 5). Springer.
184. Klein, M. V. (1982). Electronic Raman scattering. In M. Cardona (Ed.), *Light scattering in solids I* (p. 147). Heidelberg GmbH.
185. Cerdeira, F., Fjeldly, T. A., & Cardona, M. (1973). Effect of free carriers on zone-center vibrational modes in heavily doped p-type Si. II. Optical modes. *Physical Review B*, *8*, 4734.
186. Fano, U. (1961). Effects of configuration interaction on intensities and phase shifts. *Physical Review B*, *124*, 1866.
187. Gheeraert, E., Gonon, P., Deneuville, A., Abello, L., & Lucaleau, G. (1993). Effect of boron incorporation on the “quality” of MPCVD diamond films. *Diamond and Related Materials*, *2*, 742.
188. Locher, R., Wagner, J., Fuchs, F., Wild, C., Hiesinger, P., Gonon, P., & Koidl, P. (1995). Boron doped diamond films: “Electrical and optical characterization and the effect of compensating nitrogen.” *Materials Science and Engineering B*, *29*, 211.
189. Ager, J. W., III., Walukiewicz, W., & McCluskey, M. (1995). Fano interference of the Raman phonon in heavily boron-doped diamond films grown by chemical vapor deposition. *Applied Physics Letters*, *66*, 616.
190. Yoshikawa, M. (2015). Abnormal Raman spectral variation with excitation wavelength in boron-doped single-crystalline diamond. *Materials Science Forum*, *858*, 1158–1161.
191. Burke, B. G., Chean, J., Williams, K. A., Wu, Z., Puretzky, A. A., & Geohegan, D. B. (2010). Raman study of fano interference in p-type doped silicon. *Journal of Raman Spectroscopy*, *41*, 1759.
192. Ohta, Y. (2007). Theoretical aspects of superconductivity in boron-doped diamond. *New Diamond and Frontier Carbon Technology*, *17*, 33.
193. Yoshikawa, M., Mori, Y., Maegawa, M., Katagiri, G., Ishida, H., & Ishitani, A. (1993). Raman scattering from diamond particles. *Applied Physics Letters*, *62*, 3114.
194. Yoshikawa, M., Mori, Y., Obata, H., Maegawa, M., Katagiri, G., Ishida, H., & Ishitani, A. (1995). Raman scattering from nanometer-sized diamond. *Applied Physics Letters*, *67*, 694.
195. Wada, N., & Solin, S. A. (1981). Pressure dependent X-ray studies of alkali-graphite intercalation compounds. *Physica B+C*, *105*, 353.
196. Brodsky, M. H. (1983). Raman scattering in amorphous semiconductor. In M. Cardona (Ed.), *Light scattering in solids I* (pp. 205–251). Springer.
197. Dresselhaus, M. S., & Dresselhaus, G. (1982). Light scattering in graphite intercalation compounds. In M. Cardona & D. Güntherodt (Eds.), *Light scattering in solids II* (pp. 3–57). Springer.
198. Richter, H., Wang, Z. P., & Ley, L. (1981). The one phonon Raman spectrum in microcrystalline silicon. *Solid State Communications*, *39*, 625.
199. Campbell, I. H., & Fauchet, P. M. (1986). The effects of microcrystal size and shape on the one phonon Raman spectra of crystalline semiconductors. *Solid State Communications*, *58*, 739.
200. Fauchet, P. M., & Campbell, I. H. (1988). Raman spectroscopy of low-dimensional semiconductors. *Critical Reviews in Solid State and Materials Sciences*, *14*, S79–S101.
201. Ager, J. W., III., Veirs, D. K., & Rosenblatt, G. M. (1991). Spatially resolved Raman studies of diamond films grown by chemical vapor deposition. *Physical Review B*, *43*, 6491.
202. Yoshikawa, M. (2018). Infrared spectroscopy and raman spectroscopy of semiconductor. In *Encyclopedia of analytical chemistry*. Wiley.
203. Yoshikawa, M., & Nagai, N. (2006). Vibrational spectroscopy of carbon and silicon materials. In *Handbook of vibrational spectroscopy I*. Wiley.
204. Yoshikawa, M., Nagai, N., Matsuki, M., Fukuda, H., Katagiri, G., Ishida, H., Ishitani, A., & Nagai, I. (1992). Raman scattering from sp² carbon clusters. *Physical Review B*, *46*, 7169.

205. Tamor, M. A., Haire, J. A., Wu, C. H., & Hass, K. C. (1989). Correlation of the optical gaps and Raman spectra of hydrogenated amorphous carbon films. *Applied Physics Letters*, *54*, 123.
206. Harada, I., Furukawa, Y., Tasumi, M., Shirakawa, H., & Ikeda, S. (1980). Spectroscopic studies on doped polyacetylene and *p* carotene. *The Journal of Chemical Physics*, *73*, 4746.
207. Yoshikawa, M., Iwagami, K., Matsunobe, T., Morita, N., Yamaguchi, Y., & Izumi, Y. (2004). Resonant Raman scattering from N-doped and Si-doped diamondlike amorphous carbon films. *Physical Review B*, *69*, 045410(R).
208. Ramsteiner, M., Wagner, J., Wild, Ch., & Koidl, P. (1988). Raman scattering of amorphous carbon/semiconductor interface layers. *Solid State Communications*, *67*, 15–18.
209. Yoshikawa, M., & Murakami, M. (unpublished).
210. Gilkes, K. W. R., Sands, H. S., Batchelder, D. N., Robertson, J., & Milne, W. I. (1997). Direct observation of bonding in tetrahedral amorphous carbon using ultraviolet Raman spectroscopy. *Applied Physics Letters*, *70*, 1980.
211. Yoshikawa, M. (1990). Raman spectra of diamondlike amorphous carbon films. *Materials Science Forum*, *52–53*, 365–386.
212. Robertson, J., & O'Reilly, E. P. (1987). Electronic and atomic structure of amorphous carbon. *Physical Review B*, *35*, 2946.
213. Jadidi, M. F., Özer, H. Ö., Goel, S., Kilpatrick, J. I., McEvoy, N., McCloskey, D., Donegan, J. F., & Cross, G. L. W. (2020). Distribution of shallow NV centers in diamond revealed by photoluminescence spectroscopy and nanomachining. *Carbon*, *167*, 114–121.
214. Pezzagna, S., Rogalla, D., Wildanger, D., Meijer, J., & Zaitsev, A. (2011). Creation and nature of optical centres in diamond for single-photon emission—overview and critical remarks. *New Journal of Physics*, *13*, 035024.
215. Tippins, H. H. (1965). Optical and microwave properties of trivalent chromium in β -Ga₂O₃. *Physical Review*, *140*, A865.
216. HuiWen, X., QiMing, H., GuangZhong, J., ShiBing, L., Tao, P., & Ming, L. (2018). An overview of the ultrawide bandgap Ga₂O₃ semiconductor-based schottky barrier diode for power electronics application. *Nanoscale Research Letters*, *13*, 290.
217. Pearson, S. J., Yang, J., Cary IV, P. H., Ren, F., Kim, J., Tadjer, M. J., & Mastro, M. A. (2018). A review of Ga₂O₃ materials, processing, and devices. *Applied Physics Reviews*, *5*, 011301.
218. Gao, Y. H., Bando, Y., Sato, T., Zhang, Y. F., & Gao, X. Q. (2002). Synthesis, Raman scattering and defects of β -Ga₂O₃ nanorods. *Applied Physics Letters*, *81*(12), 16.
219. Paskaleva, A., Spassov, D., & Terziyska, P. (2017). Electric, dielectric and optical properties of Ga₂O₃ grown by metal organic chemical vapour deposition. *Journal of Physics: Conference Series*, *794*, 012017.
220. Tadjer, M. J., Mastro, M. A., Mahadik, N. A., Currie, M., Wheeler, V. D., Freitas, Jr., J. A., Greenlee, J. D., Hite, J. K., Hobart, K. D., Eddy, Jr., C. R., & Kub, F. J. (2016). Structural, optical, and electrical characterization of monoclinic β -Ga₂O₃ grown by MOVPE on sapphire substrates. *Journal of Electronic Materials*, *45*, 2031.
221. Nakata, Y. Private communication (The TRC News 201901-01, 2019 in Japanese).
222. Villora, E. G., Yamaga, M., Inoue, T., Yabasi, S., Masui, Y., Sugawara, T., & Fukuda, T. (2001). Optical spectroscopy study on β -Ga₂O₃. *Solid State Communications*, *120*, 455–458.
223. Suzuki, K., Kuroki, Y., Okamoto, T., & Takata, M. (2006). Effect of growth conditions on the cathodoluminescence of β -Ga₂O₃ crystals grown by electric current heating method. *Key Engineering Materials*, *301*, 181–184.
224. Hashimoto, A., & Yoshikawa, M. (unpublished) (Hashimoto, A. The TRC News 202001-02, 2020 in Japanese).
225. Stephenson, R., Verhulst, A., Wolf, P. D., Caymax, M., & Vandervorst, W. (1998). Contrast reversal in scanning capacitance microscopy imaging. *Applied Physics Letters*, *73*, 2597.
226. Rao, R., Raoa, A. M., Xu, B., Dong, J., Sharma, S., & Sunkara, M. K. (2005). Blueshifted Raman scattering and its correlation with the (110) growth direction in gallium oxide nanowires. *Journal of Applied Physics*, *98*, 094312.

227. Hu, M., Tian, J., Lu, H. T., Weng, L., & Wang, L. H. (2010). H₂O₂-sensitive quantum dots for the label-free detection of glucose. *Talanta*, *82*, 997–1002.
228. Frasco, M. F., & Chaniotakis, N. (2009). Semiconductor quantum dots in chemical sensors and biosensors. *Sensors*, *9*, 7266–7286.
229. Jaiswal, J. K., Mattoussi, H., Mauro, J. M., & Simon, S. M. (2003). Long-term multiple color imaging of live cells using quantum dot bioconjugates. *Nature Biotechnology*, *21*, 47–51.
230. Huang, S., Xiao, Q., Li, R., Guan, H. L., Liu, J., Liu, X. R., He, Z. K., & Liu, Y. (2009). A simple and sensitive method for l-cysteine detection based on the fluorescence intensity increment of quantum dots. *Analytica Chimica Acta*, *645*, 73–78.
231. Milekhin, A. G., Toropov, A. I., Bakarov, A. K., Tenne, D. A., Zanelatto, G., Galzerani, J. C., Schulze, S., & Zahn, D. R. T. (2004). Interface phonons in InAs and AlAs quantum dot structures. *Physical Review B*, *70*, 085314.
232. Knipp, P. A., & Reinecke, T. L. (1992). Classical interface modes of quantum dots. *Physical Review B*, *46*, 10310.
233. Comas, F., Trallero-Giner, C., Studart, N., & Marques, G. E. (2002). Interface optical phonons in spheroidal dots: Raman selection rules. *Physical Review B*, *65*, 073303.
234. Klude, M., Passow, T., Kroger, R., & Hommel, D. (2001). Electrically pumped lasing from CdSe quantum dots. *Electronics Letters*, *37*, 1119–1121.
235. Kim, J. C., Rho, H., Smith, L. M., Jackson, H. E., Lee, S., Dobrowolska, M., Merz, J. L., & Furdyna, J. K. (1998). Spectroscopic characterization of the evolution of self-assembled CdSe quantum dots. *Applied Physics Letters*, *73*, 3399.
236. Matsuda, K., Saiki, T., Nomura, S., Mihara, M., & Aoyagi, Y. (2002). Near-field photoluminescence imaging of single semiconductor quantum constituents with a spatial resolution of 30 nm. *Applied Physics Letters*, *81*, 2291.
237. Saraie, J., Matsumura, N., Sugie, R., & Yoshikawa, M. (2004). Observation of emissions from CdSe single quantum dots and spatial mapping by micro-cathodoluminescence measurement. *Physica Status Solidi (c)*, *1*(4), 759–762.
238. Kim, J. C., Rho, H., Smith, L. M., Jackson, H. E., Lee, S., Dobrowolska, M., & Furdyna, J. K. (1999). Temperature-dependent micro-photoluminescence of individual CdSe self-assembled quantum dots. *Applied Physics Letters*, *75*, 214.
239. Makino, T., Andre, R., Gerard, T.-M., Romestain, R., Dang, L. S., Bartels, M., Lischka, K., & Shikora, D. (2003). Single quantum dot spectroscopy of CdSe/ZnSe grown on vicinal GaAs substrates. *Applied Physics Letters*, *82*, 2227.
240. Logue, F. P., Fewer, D. T., Hewlett, S. J., Heffeman, J. F., Jordan, C., Rees, P., Donegan, J. F., McCabe, E. M., Hegarty, J., Taniguchi, S., Hino, T., Nagano, K., & Ishibashi, A. (1997). Optical measurement of the ambipolar diffusion length in a ZnCdSe–ZnSe single quantum well. *Journal of Applied Physics*, *81*, 536.
241. Maehashi, K., Yasui, N., Murase, Y., Ota, T., Noma, T., & Nakashima, H. (2000). Formation and characterization of self-organized CdSe quantum dots. *Journal of Electronic Materials*, *29*, 542–548.

Chapter 6

STEM-CL



6.1 Setup

STEM-CL is an analytical tool which is similar to well-known techniques: SEM-CL, PL, and EELS. The schematic of the STEM-CL that we developed is shown in Fig. 6.1 [1]. We used a STEM (JEOL H2100F) as an excitation source for the CL measurement. The CL from specimens was collected by an ellipsoidal mirror (3.4-mm thick), passed through an optical fibre and a Jobin Yvon HR-320 single monochromator, and was detected by a 1024-charge coupled device (CCD) detector [1].

Losquin et al. composed a STEM-CL spectroscopic system using a STEM with EELS detection and a high-efficiency CL detection system, as shown in Fig. 6.2 [2]. A microscope generates a sub-nanometre electron beam that scans over the region of interest. At each sampling point, a morphological (high angle annular dark field, HAADF) signal is detected simultaneously with an EELS or CL spectrum [2]. At the end of the scan, both an HAADF image and a complete set of spatially resolved CL spectra are acquired and available for accurate comparison. To obtain highly sensitive CL intensity mapping of specimens, an energy filter was adopted [2].

6.2 Application

6.2.1 *Crystalline Characterisation of GaN Flake by STEM-CL*

Figure 6.3a–d show STEM, STEM-CL intensity (365-nm peak) images ($1.5 \mu\text{m} \times 1.5 \mu\text{m}$), STEM-CL spectra from 300 to 800 nm, and STEM-CL spectra from 325 to 465 nm of a piece of GaN crystal flake at points 1–6 with a thickness less than 100 nm measured by an acceleration voltage of 120 keV, respectively [1]. The CL

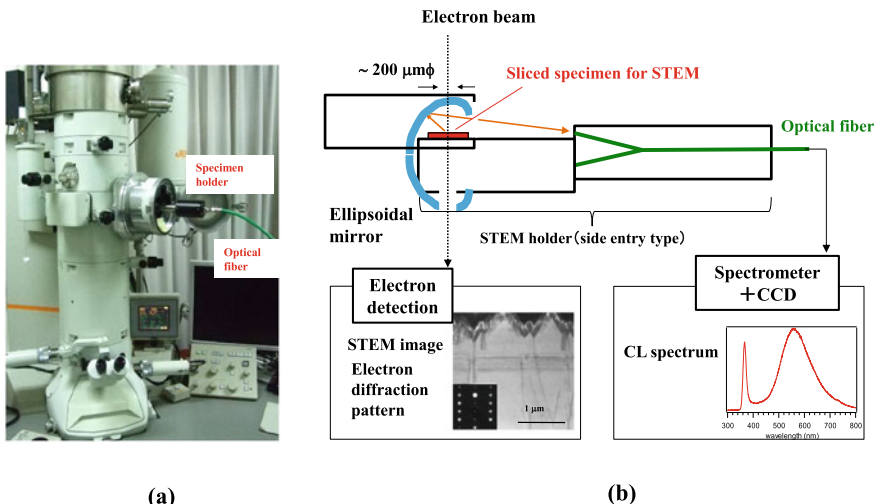
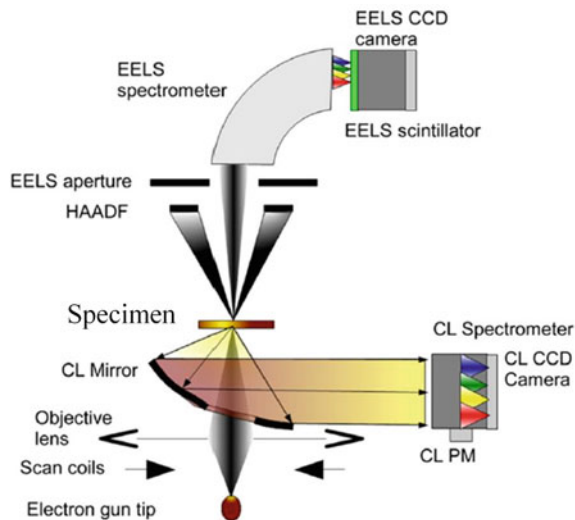


Fig. 6.1 **a** photograph of typical STEM (JEOL H2100F) and **b** schematic diagram of our optical system for STEM-CL [1]

Fig. 6.2 STEM-CL system setup, equipped with EELS detection and a high-efficiency CL detection system [2]. (Reprinted with permission from Ref. [2]. Copyright (2015) American Chemical Society.)



peaks at approximately 365 and 580 nm are assigned to band-edge emission and defect-related broad luminescence, known as yellow luminescence (YL), respectively [3–6]. As seen in Fig. 6.3d, the CL peak ascribed to the band-edge emission shifts by 5 nm (-46 meV) from 365 nm (3.397 eV) to 370 nm (3.351 eV), depending on each position. Rieger et al. studied the influence of biaxial stress on the optical

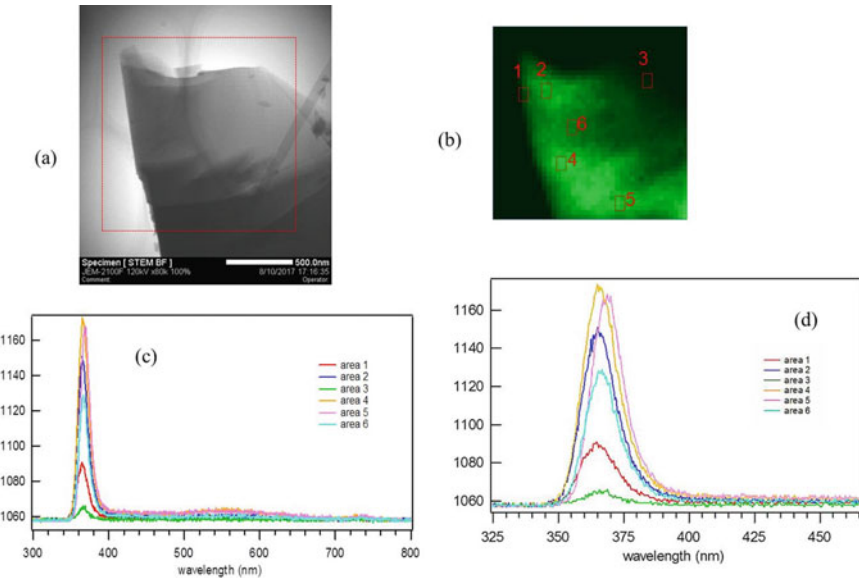


Fig. 6.3 **a** STEM and **b** STEM-CL intensity images (365-nm peak) in a scanning area of $1.5 \mu\text{m} \times 1.5 \mu\text{m}$, and STEM-CL spectra at points 1–6 **c** from 300 to 800 nm and **d** from 325 to 465 nm of a piece of GaN crystal flake with a thickness of less than 100 nm, measured by an acceleration voltage of 120 keV. The electron beam diameter is about 0.2 nm [1]

properties of thin GaN films by using X-ray diffraction, and Raman and photoluminescence spectroscopy. They estimated that the linear coefficient for the near band gap luminescence shift due to biaxial compressive strain yields a value of 24 meV/GPa [7]. Using their coefficient to translate the 5-nm shift into stress, we concluded that the crystal flake is under tensile or compressive stress by approximately 1.9 GPa [1].

Figure 6.4a shows a STEM image in the vicinity of dislocations of a GaN crystal flake, measured by an acceleration voltage of 120 keV [1]. Furthermore, Fig. 6.4b indicates the CL intensity image at 365 nm ($1 \mu\text{m} \times 2 \mu\text{m}$). As can be seen in Figs. 6.4a, b, the STEM image in the vicinity of dislocations of the GaN crystal flake in Fig. 6.4a, coincides well with the CL intensity image at 365 nm in Fig. 6.4b. In general, the CL intensity attributable to band-edge emission (BEE) decreases in the vicinity of dislocations, because the dislocations in GaN act as non-radiative recombination centres (NRRCs). Decrease in the CL intensities at points 1, 2, and 3 near the dislocations in Fig. 6.4b implies that the crystalline quality of GaN decreases in the area near the dislocations [1].

Figure 6.4c displays the CL intensity image at 405 nm in the area of $1 \mu\text{m} \times 2 \mu\text{m}$. As seen in Fig. 6.4d, the CL peak at 405 nm is found to shift to the longer wavelength side near point 3. Figure 6.4e exhibits CL spectra from 325 to 480 nm, as a magnification of Fig. 6.4d; [1]. The 405-nm CL peak becomes broader than the CL peak assigned to BEE. Generally, GaN does not exhibit a special peak near 405 nm [8]. Furthermore, when In is incorporated into the GaN crystal, the CL peak

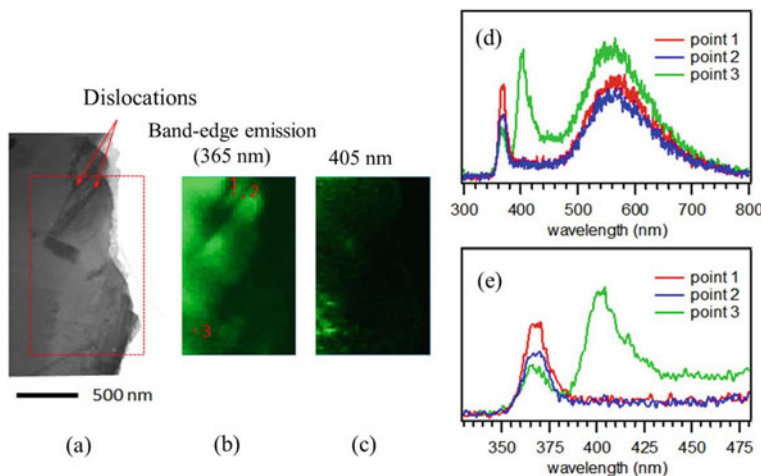


Fig. 6.4 **a** STEM image, **b** CL image at 365 nm, and **c** CL image at 405 nm in the scanning area of $1 \mu\text{m} \times 2 \mu\text{m}$, and **d** the CL spectra at points 1–3 from 300 to 800 nm and **e** from 325 to 480 nm of a GaN crystal flake with thickness less than 100 nm, measured by an acceleration voltage of 120 keV. The electron-beam diameter is about 0.2 nm [1]

assigned to BEE tends to shift to longer wavelengths [9]. Although the origin of the CL peak at 405 nm is unclear, we suggest that In is mostly segregated into point 3 of the GaN flake [1].

Based on these data and the change in the CL spectrum at each point in Fig. 6.4d, e, the STEM-CL apparatus we developed has a spatial resolution of less than 30 nm [1].

6.2.2 Crystalline Characterisation of Single Crystalline ZnO Nanowire by STEM-CL

Kawasaki et al. studied the crystalline quality of a single ZnO nanowire (NW) by STEM-CL we developed [10]. Figure 6.5a–c show BF(Bright field)-STEM, STEM-CL images, and STEM-CL spectra at different positions in the single ZnO NW, respectively [10]. The STEM-CL spectra of the ZnO single crystal consist of a band-edge emission (BEE) at 380–385 nm and a broad CL peak near 620 nm assigned to the oxygen vacancy centre (OVC) [10].

Figure 6.5b shows CL images at various wavelengths in the ZnO NW, measured by an acceleration voltage of 120 keV [10]. As can be seen in Figs. 6.5b, the CL intensity image at 380–385 nm, which is assigned to BEE, tends to become weak, approaching to the tip of NW [10]. In general, the CL intensity attributable to BEE decreases in the vicinity of dislocations or defects, because the dislocations and defects in ZnO act as non-radiative recombination centres (NRRCs) like GaN [10].

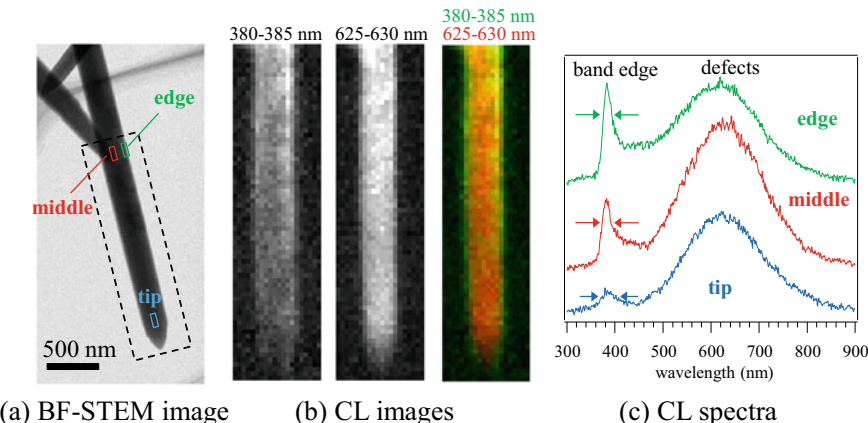


Fig. 6.5 **a** BF-STEM, **b** STEM-CL images at various wavelengths, and **c** STEM-CL spectra of ZnO NW [10]

Decrease in the CL intensity at the tip of NW implies that the crystalline quality of NM decreases near the tip [10].

Figure 6.5c depicts the CL spectra at the tip, middle, and edge in the single ZnO NW. As shown in Fig. 6.5c, the intensity ratio of the band-edge CL peak at approximately 380–385 nm normalised by the CL peak at 620 nm decreases as the measured position approached from the edge to the tip [10]. This implies that the crystalline quality decreases, approaching from the edge to the tip [10].

Figures 6.6a–d show ADF (Annular Dark Field)-STEM, TEM images, selected area diffraction patterns, and schematic of crystal structure [10]. ADF imaging is a useful technique to observe specimens in a STEM. This image is formed by collecting scattered electrons with an ADF detector [11]. As seen in Fig. 6.6a, the low-density area is observed near a middle of ZnO NW, suggesting the existence of voids. From a comparison of the diffraction patterns at the middle and tip positions, it is found that the tip position is rotating along the c-axis by two degrees compared with the middle position of ZnO NW. The schematic model structures of the tip and middle position are depicted in Fig. 6.6d [10].

6.2.3 Localised Surface Plasmon of Nanometre-Sized Metal by STEM-EELS and STEM-CL Spectroscopy

With the development of the STEM-CL system, its technique has been applied to metallic nanoparticles, which gave rise to new optical phenomena, such as quasi-one-dimensional surface plasmon resonances (SPRs). Electron energy-loss spectroscopy (EELS) and CL are effective tools for investigating surface plasmons (SPs) with high spatial resolution [13].

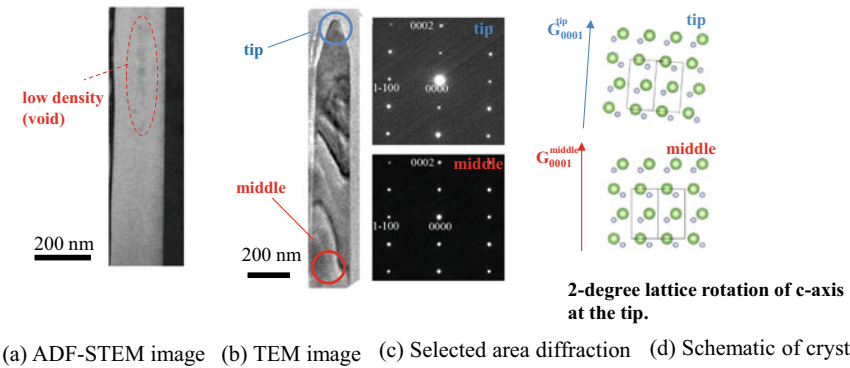


Fig. 6.6 **a** ADF-STEM image, **b** TEM image, **c** selected area diffraction patterns, and **d** schematic of crystal structure of ZnO NW [10]

EELS determines the atomic structure and chemical properties of the materials, including the type and quantity of the atoms present, atomic chemical state, and the collective interactions of atoms with their neighbours, such as SPs. A typical energy loss spectrum includes several regions [13]. When an electron beam is incident to a specimen, a part of the electrons is inelastically scattered and loses a part of the energy [13]. The elemental composition and atomic bonding state of the materials can be clarified by analysing the EELS spectra [13]. The first peak, the most intense for a very thin specimen, occurs at 0 eV loss (equal to the primary beam energy) and is called the zero-loss peak (ZLP), representing electrons that did not undergo inelastic scattering. The zero-loss peak width mainly reflects the energy distribution of the electron source [12].

SPRs in metal nano-particles are an outstanding technology base for nano-optics applications. The electromagnetic near-field related to these resonances originates from modes determined by the shape, size, and metal nano-particle composition [12]. When coupled with the electromagnetic near field, multiple resonant modes interact to induce interference effects and provide a fine control of both the spectral response and spatial distribution of fields near the nano-particle [12].

Collins et al. [13] compared experimental EELS and CL results in plasmonic Ag nano-rods with their simulations and performed discrete dipole approximation (DDA) simulations for electron beam excitation, using a customised version of e-DDA.

They observed higher-order multipolar longitudinal resonance modes in Ag nano-rods in the visible energy region for rods with a length of approximately 500 nm [13]. Longitudinal modes $m = 2-6$ of SPRs in Ag nano-rods were labelled by the number of nods ($m = 1, 2, 3, 4, 5, 6, \dots$) [13]. Figure 6.7 depicts STEM-EELS images of such modes for a 540-nm-long rod on a 30-nm SiN membrane substrate (Rod A) and a 490-nm-long rod on an ultrathin carbon film (Rod B) measured by Collins et al. [13].

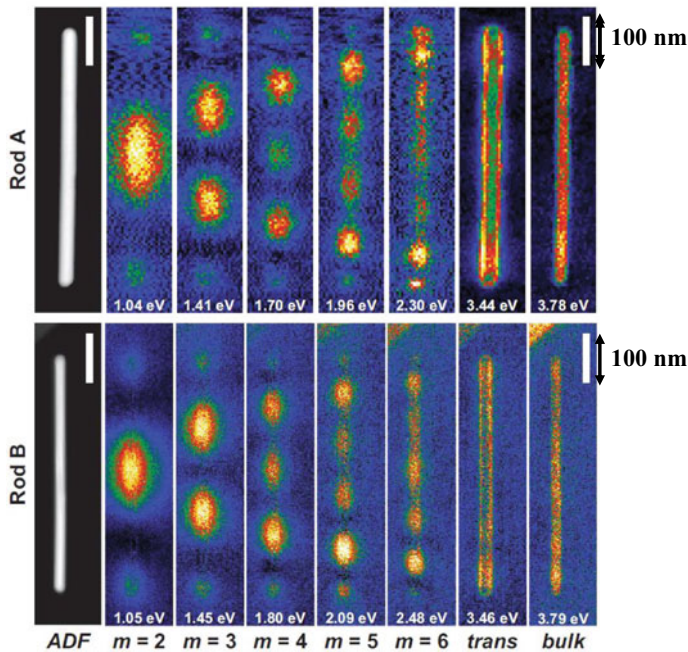


Fig. 6.7 STEM-EELS images for two Ag nanorods approximately 540 nm (Rod A) and 490 nm (Rod B) in length. Longitudinal modes $m = 2$ –6 are indicated and then, the images due to the transverse (*trans*) and bulk excitations are shown for comparison. Annular dark field (ADF) micrographs are shown for reference [13] (Reproduced with permission from Ref. [13]. © American Physical Society, 2014.)

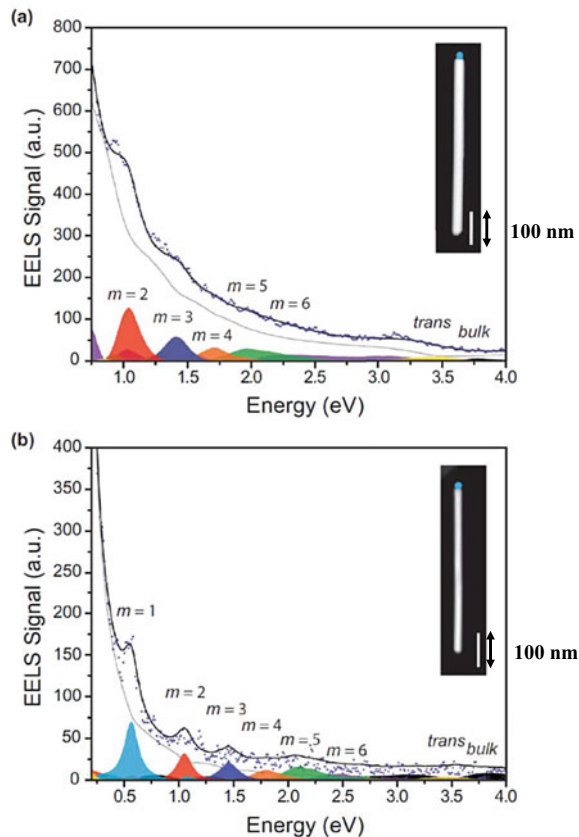
These images were prepared by non-negative matrix factorisation (NMF) of the experimental data set into two positive matrices, the images and related spectral components [14, 15]. An NMF decomposition technique was utilised to EELS measurements of hybridised SPs in Ag nanocubes [16]. They utilised analogous multivariate statistical modal decomposition techniques, independent of the analysis of modes of Ag nano-rods [17] or Ag cubes [18]. Spectral decomposition technique significantly divides overlapping spectral characteristics and does not suppose any particular lineshape. Especially, the components clarified by NMF processing agree with those already observed in energy-filtered data sets (Ref. [19] and Fig. 6.7). STEM-EELS spectra of Rod A and B were acquired with a ZLP of approximately 180 meV FWHM and with a ZLP of approximately 90 meV FWHM, respectively. To explain the differences in the ZLP tail intensity for electrons propagating through the Ag particles and those propagating outside the nano-rod, these images were divided by the component image related with the tail of the ZLP. The unprocessed

NMF results are contained in the SM (supplemental material in Ref. [20]) alongside results acquired by dividing the component images to the ZLP at each pixel in the original spectrum image [20]. Explaining varying ZLP intensity is essential for replicating a signal for comparison with the simulated energy loss probabilities [21].

The STEM-EELS spectra related to each of the images in Fig. 6.7 are depicted in Fig. 6.8 for a single-electron trajectory at the rod tip where all longitudinal resonances are strongly excited [13]. By contrary, the transverse (*trans*) and bulk excitations are weakly excited for the selected trajectory [13].

The unprocessed spectrum (blue dots) is depicted with the spectral components for the ZLP (grey solid line), the longitudinal resonances $m = 2\text{--}6$ (Rod A) and $m = 1\text{--}6$ (Rod B), transverse (*trans*) mode excitations, and the Ag bulk plasmon [13]. The sum of the spectral components is indicated (solid black line). These peaks exhibit a

Fig. 6.8 STEM-EELS spectra for **a** Rod A and **b** Rod B, at the position indicated by the blue marker in the inset [13]. (Reproduced with permission from Ref. [13]. © American Physical Society, 2014.)



dominant amplitude at the particular energies noted in Fig. 6.7; [13]. Furthermore, the unprocessed data (blue dots) are well reproducible by NMF decomposition technique but with significantly reduced noise (black solid line) [13]. The effect of the ZLP is pronounced in Fig. 6.8, as the EELS peaks are scarcely visible as modulations of the ZLP tail, particularly for Rod A, obtained with a broader ZLP than for Rod B [13]. The NMF decomposition technique makes use of the entire spectrum image and explains the Poissonian noise present in the data, being effective for characteristic extraction even at pixels where the EELS signals are weak [13].

On the other hand, Losquin et al. [2, 13] investigated the optical properties of an Au triangular nano-prism with a length of 60 nm, and a thickness of 30 nm, deposited on a graphene sheet through combined nanometre-resolved EELS and CL measurements, and showed that only CL detected the radiative modes, compared with EELS, which showed dark modes [2, 13]. The combination of both techniques on the same particles provides us with complementary information. Furthermore, they indicated that, although the radiative modes cause similar spatial distributions when detected by EELS or CL, their resonant energies are different [2, 13].

Kawasaki et al. [22] studied the optical properties of localised surface plasmons (LSPs) with different orders in the individual Ag nanotriangles with different sizes by STEM-EELS and -CL. Both techniques showed the first two-order modes possessed similar spatial distributions. Moreover, it was confirmed that both lower- and higher-order plasmon modes showed the slightly different resonant energies [22]. For the first two lower-order modes, the resonant energy in CL spectra was blue-shifted compared to that in EELS spectra, which can be explained by a simple damped oscillator model [22]. This coincides well with the experimental and theoretical observations recently performed on dipolar plasmons in Au, also extending to the second-order modes [22].

Figure 6.9 illustrates STEM-EELS and -CL spectra from the corner (area 1) and the middle (the centre between two corners) (area 2) of (a) 160-nm, (b) 360-nm, and (c) 555-nm Ag triangles [22]. STEM-EELS and -CL spectra were normalised by the intensity of the dipolar ($m = 1$) mode for the 160-nm triangle and hexapolar ($m = 2$) mode for the 360- and 555-nm triangles [22]. STEM-EELS and -CL energy-filtered images near the resonant energy positions are also shown. In the EELS energy-filtered images, the intensity inside the particles was lower than that outside, because fewer electrons were transmitted when they pass through the Ag nano-particles [22]. In addition, their CL detection system has very low sensitivity in the IR region over 1000 nm, thus the lowest-energy LSP mode in the largest (550-nm) triangle was not observed. The spatial distribution for the two first modes in the three specimens

coincides with that predicted for the dipolar ($m = 1$) and hexapolar ($m = 2$) modes [2, 13, 23–29]. The first two modes ($m = 1$ and $m = 2$) indicate similar spatial distribution in the energy-filtered images for both techniques, but slight difference in their resonant energy position. Significantly, for both modes, the resonant energy positions in STEM-CL spectra are located at higher energies than those in STEM-EELS spectra, as listed in Table 6.1 [22]. They noticed that this shift was opposite to the main tendency discovered in Ref. [13] on small Au prisms (60-nm) but coincides with simulations on Ag nano-rods made in Ref. [29, 22]. In large triangles, the signal of the higher order modes can be observed. In practice, in addition to the $m = 1$ and $m = 2$ modes, another peak is observed near 2.0 – 2.1 eV in the STEM-EELS spectrum of the 555-nm prism triangle (Fig. 6.9c, area 2). Similarly, a peak near 1.8 eV could be observed in the STEM-CL spectra [22]. In this case, the peak position was determined by the Gaussian lineshape fitting in Fig. 6.9c [22], this peak was detected near the hexapolar mode ($m = 2$), and it was difficult to divide its position. Here, the resonant peak position in STEM-CL (1.8 eV) was observed at an energy level lower than that in STEM-EELS (2.0 eV), which assigns to an opposite trend in the lower-order modes ($m = 1$ and 2) [22]. Kawasaki et al. clarified the cause of this disagreement in the energy shift between lower- and higher-order LSP modes, by performing detailed numerical simulations [22].

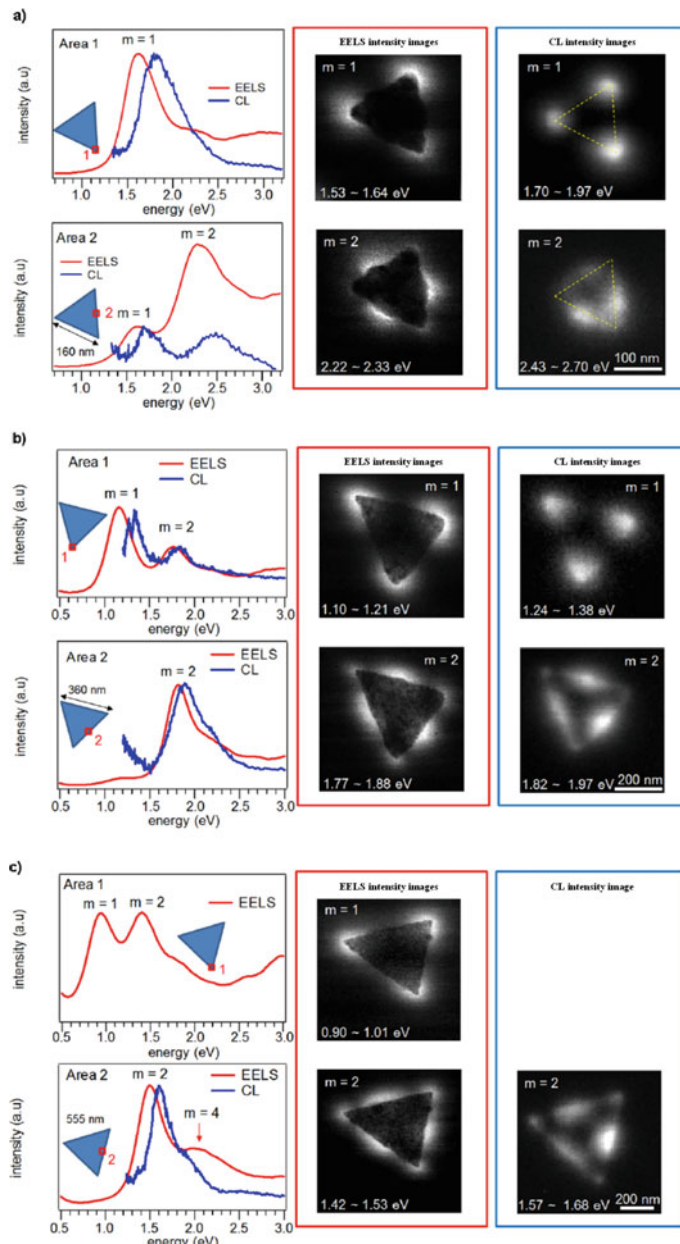


Fig. 6.9 STEM-EELS (red) and -CL (blue) spectra from the corner (area 1) and the middle between two corners (area 2) of **a** 160-nm, **b** 360-nm, and **c** 555-nm Ag triangles. The STEM-EELS and -CL energy-filtered images around the resonant energy positions are also illustrated in **a**, **b**, and **c** [22]. (Reprinted (adapted) with permission from Ref. [22]. Copyright (2016) American Chemical Society.)

Table 6.1 Resonant Energy Positions in 160-, 360-, and 555-nm Ag triangles for dipole and hexapole modes of localised surface plasmons obtained by STEM-EELS and -CL [22]. (Reprinted (adapted) with permission from Ref. [22]. Copyright (2016) American Chemical Society.)

Size (nm)	m = 1 (dipole)	m = 2 (hexapole)
160	1.6 eV (EELS), 1.8 eV (CL)	2.3 eV (EELS), 2.5 eV (CL)
360	1.2 eV (EELS), 1.3 eV (CL)	1.8 eV (EELS), 1.9 eV (CL)
555	1.0 eV (EELS)	1.5 eV (EELS), 1.6 eV (CL)

References

- Kawasaki, N., and Yoshikawa, M., (unpublished).
- Losquin, A., Zagone, L. F., Myroshnychenko, V., Rodríguez-González, B., Tencé, M., Scarbelli, L., Förstner, J., Liz-Marzán, L. M., Javier García de Abajo, F., Stéphan, O., & Kociak, M. (2015). Unveiling nanometer scale extinction and scattering phenomena through combined electron energy loss spectroscopy and cathodoluminescence measurements. *Nano Letter*, *15*, 1229–1237.
- Yoshikawa, M., Kunzer, M., Wagner, J., Obloh, H., Schlotter, P., Schmidt, R., Herres, N., & Kaufmann, U. (1999). Band-gap renormalization and band filling in Si-doped GaN films studied by photoluminescence spectroscopy. *Journal of Applied Physics*, *86*, 4400.
- Sugie, R., Yoshikawa, M., & Harima, H. 2003. Characterization of Threading Dislocation in Si-doped GaN Films by High Spatial Resolution Cathodoluminescence Spectroscopy. In: *International Conference on Solid State Devices and Materials*, Tokyo.
- Calleja, E., Sanchez, F. J., Basak, D., Sanchez-Garcia, M. A., Munoz, E., Izpura, I., Calle, F., Tijero, J. M. G., Sanchez-Rojas, J. L., Beaumont, B., Lorenzini, P., & Gibart, P. (1997). Yellow luminescence and related deep states in undoped GaN. *Physical Review B*, *55*, 4689.
- Schubert, E. F., Goepfert, I. D., & Redwing, J. M. (1997). Evidence of compensating centres as origin of yellow luminescence in GaN. *Applied Physics Letters*, *71*, 3224.
- Rieger, W., Metzger, T., Angerer, H., Dimitrov, R., Ambacher, O., & Stutzmann, M. (1996). Influence of substrate-induced biaxial compressive stress on the optical properties of thin GaN films. *Applied Physics Letters*, *68*, 970.
- Kucheyev, S. O., Toth, M., Phillips, M. R., Williams, J. S., & Jagadish, C. (2001). Effects of excitation density on cathodoluminescence from GaN. *Applied Physics Letters*, *79*, 2154–2157.
- Behr, D., Wagner, J., Ramakrishnan, A., Obloh, H., & Bachem, K.-H. (1998). Evidence for compositional inhomogeneity in low In content (InGa)N obtained by resonant Raman scattering. *Applied Physics Letters*, *73*, 241.
- Yoshikawa, M., Matsuda, K., Yamaguchi, Y., Matsunobe, T., Nagasawa, Y., Fjino, H., & Yamane, T. (2002). Characterization of ZnO nanoparticles by resonant Raman scattering and cathodoluminescence spectroscopies. *Journal of Applied Physics*, *92*, 7153.
- Katherine, E. M. (2016). The use of annular dark-field scanning transmission electron microscopy for quantitative characterisation. *Johnson Matthey Technol. Rev.*, *60*(2), 117–131.
- Egerton, R. F. Ed. (2011). *Electron Energy-Loss Spectroscopy in the Electron Microscope*. Springer.
- Collins, S. M., Nicoletti, O., Rossouw, D., Ostasevicius, T., & Midgley, P. A. (2014). Excitation dependent Fano-like interference effects in plasmonic silver nanorods. *Physical Review B*, *90*, 155419.
- de la Peña, F., Berger, M.-H., Hochepied, J.-F., Dynys, F., Stephan, O., & Walls, M. (2011). Mapping titanium and tin oxide phases using EELS: An application of independent component analysis. *Ultramicroscopy*, *111*, 169–176.

15. Lin, C.-J. (2007). Projected gradient methods for nonnegative matrix factorization. *Neural Computation*, *19*, 2756–7279.
16. Nicoletti, O., de la Peña, F., Leary, R. K., Holland, D. J., Ducati, C., & Midgley, P. A. (2013). Three-dimensional imaging of localized surface plasmon resonances of metal nanoparticles. *Nature (London)*, *502*, 80–84.
17. Guiton, B. S., Iberi, V., Li, S., Leonard, D. N., Parish, C. M., Kotula, P. G., Varela, M., Schatz, G. C., Pennycook, S. J., & Camden, J. P. (2011). Correlated optical measurements and plasmon mapping of silver nanorods. *Nano Letters*, *11*, 3482–3488.
18. Iberi, V., Bigelow, N. W., Mirsaleh-Kohan, N., Griffin, S., Simmons, P. D., Guiton, B. S., Masiello, D. J., & Camden, J. P. (2014). Resonance rayleigh scattering and electron energy-loss spectroscopy of silver nanocubes. *Journal of Physical Chemistry C*, *118*, 10254–10262.
19. Rossouw, D., Couillard, M., Vickery, J., Kumacheva, E., & Botton, G. A. (2011). Multipolar plasmonic resonances in silver nanowire antennas imaged with a subnanometer electron probe. *Nano Letters*, *11*, 1499–1504.
20. See Supplemental Material at <http://link.aps.org/supplemental/> for further details of NMF processing, a discussion of the effects of the substrate and instrumental broadening, an evaluation of dipole discretisation, additional internal damping calculations, additional spectral amplitude modulation fitting, additional simulations examining the role of rod length, and additional comments on related systems.
21. Nicoletti, O., de la Peña, F., Leary, R. K., Holland, D. J., Ducati, C., & Midgley, P. A. (2013). Three-dimensional imaging of localized surface plasmon resonances of metal nanoparticles. *Nature (London)*, *502*, 80–84.
22. Kawasaki, N., Meuret, S., Weil, R., Lourenço-Martins, H., Stéphan, O., & Kociak, M. (2016). Extinction and scattering properties of high-order surface plasmon modes in silver nanoparticles probed by combined spatially resolved electron energy loss spectroscopy and cathodoluminescence. *ACS Photonics*, *3*(9), 1654–1661.
23. Nelayah, J., Kociak, M., Stéphan, O., Javier García de Abajo, F., Tencé, M., Henrard, L., Taverna, D., Pastoriza-Santos, I., Liz-Marzán, M., Colliex, C. (2007). Mapping surface plasmons on a single metallic Nanoparticle. *Nature Physics*, *3*, 348–353.
24. Sherry, L. J., Jin, R., Mirkin, C. A., Schatz, G. C., & Van Duyne, R. P. (2006). Localized surface plasmon resonance spectroscopy of single silver triangular nanoprisms. *Nano Letters*, *6*, 2060–2065.
25. Nelayah, J., Kociak, M., Stéphan, O., Geuquet, N., Henrard, L., García de Abajo, F. J., Pastoriza-Santos, I., Liz-Marzan, L. M., Colliex, C. (2010). Two-dimensional quasistatic stationary short range surface plasmons in flat nanoprisms. *Nano Letters*, *10*, 902–907.
26. Gu, L., Sigle, W., Koch, C., Ögüt, B., van Aken, P., Talebi, N., Vogelgesang, R., Mu, J., Wen, X., Mao, J. (2011). Resonant wedge-plasmon modes in single-crystalline gold nanoplatelets. *Physical Review B: Condensed Matter and Materials Physics*, *83*, 195433.
27. Schmidt, F. P., Ditlbacher, H., Hofer, F., Krenn, J. R., & Hohenester, U. (2014). Morphing a Plasmonic Nanodisk into a Nanotriangle. *Nano Letters*, *14*, 4810–4815.
28. Keast, V. J., Walhout, C. J., Pedersen, T., Shahcheraghi, N., Cortie, M. B., & Mitchell, D. R. G. (2016). Higher order plasmonic modes excited in Ag triangular nanoplates by an electron beam. *Plasmonics*, *11*, 1–6.
29. Losquin, A., & Kociak, M. (2015). Link between cathodoluminescence and electron energy loss spectroscopy and the radiative and full electromagnetic local density of states. *ACS Photonics*, *2*, 1619–1627.

Chapter 7

Topics



7.1 DUV, UV, and NIR Raman Spectroscopy

Although Raman spectroscopy is a powerful tool for characterising the crystalline quality, stress, and bonding structures of semiconductors, Raman measurement has been limited to the visible region (400–800 nm). However, the Raman measurement range was extended recently from the DUV and UV regions to the NIR region by the development of highly sensitive InGaAs multichannel detectors. DUV and UV Raman spectroscopy have the following advantages;

- (1) An increase in Raman intensity due to the ν^4 rule

Shorter-wavelength lasers generally afford stronger Raman scattering owing to the ν^4 increase in the Raman scattering cross sections, Eq. (2.6) in Sect. 2.1, where ν is the reciprocal of the excitation wavelength of the incident light.

- (B) A decrease in the penetration depth of semiconductors (for example, see Ref. [1])

The penetration depth of most semiconductors decreases with decreasing excitation wavelength λ because the absorption coefficient of semiconductors increases with decreasing λ .

Figure 7.1 shows a photograph and a schematic of a DUV and UV Raman instrument. The Raman spectra of materials, such as semiconductors, polymers, and biological specimens, can be measured using the 266 nm (fourth harmonic) line of a Nd:YAG laser and the 364 nm line of an Ar⁺ ion laser [2–5].

Figure 7.2 shows the dependence of the Si penetration depth on the excitation wavelength, which was calculated using the absorption efficient (α) of Si. The penetration depth was calculated using the equation for $(1/2\alpha)$ of Holtz et al. [6].

Figure 7.3a-c show the penetration depth for various excitation wavelengths, and the UV Raman spectra of a Si wafer under excitations by the 325 nm line of a He–Cd laser, and by the 457.9 nm line of an Ar⁺ laser [7]. The surface of the Si wafer was treated by mechanical polishing using Al₂O₃ particles, a mechanical

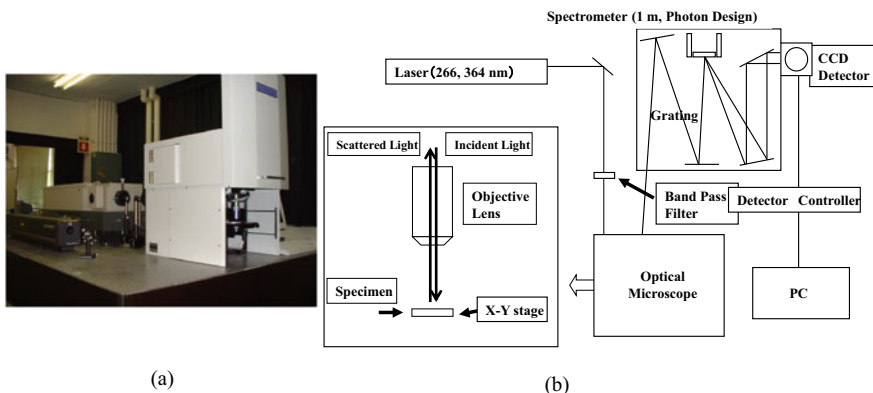
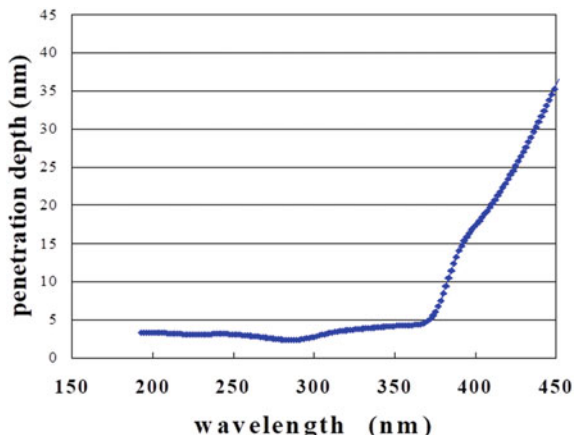


Fig. 7.1 **a** Photograph and **b** schematic of our DUV and UV Raman instrument

Fig. 7.2 Dependence of Si penetration depth on excitation wavelength [7]



polishing machine, irradiation by Ga^+ ions using a focused ion beam (FIB) instrument, Ar^+ -ion etching using an ion milling apparatus, or cleaving; it was then excited by the 457.9 nm line of an Ar^+ ion laser for comparison [7]. As shown in Fig. 7.3b, although the Raman spectrum of the cleaved surface of the Si wafer is almost the same as that of the Ar^+ -ion-etched surface, there is no Raman signal because the FIB process causes the greatest damage [7]. In the spectrum of the polished surface of the Si wafer, the Raman line at 520 cm^{-1} is blue-shifted compared with that of the cleaved surface on the 325 nm excitation, indicating compressive stress in the polished surface [7]. By contrast, the Raman spectrum of the Ar^+ -ion-etched surface is in good agreement with that of the cleaved surface on the 325 nm excitation [7]. However, as shown in Fig. 7.3c, the Raman spectrum of the Ar^+ -ion-etched surface

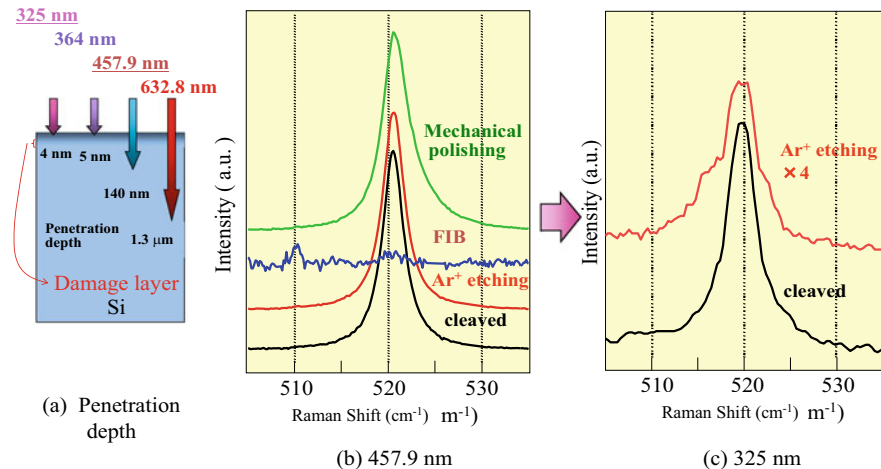


Fig. 7.3 **a** Penetration depth for various excitation wavelengths, **b** visible Raman spectra of surface of Si wafer after mechanical polishing, FIB treatment, Ar⁺ etching, or cleaving under excitation by the 457.9 nm line of an Ar⁺ laser for comparison, and **c** Raman spectra of surfaces under excitation by the 325 nm line of a He–Cd laser [7]

is broader than that of the cleaved surface on the 325 nm excitation. This result indicates that the crystalline quality of the surface is degraded within the region of less than 4 nm by Ar⁺-ion etching on the 325 nm excitation [7].

Figure 7.4 shows the Raman spectrum of a 4H-SiC wafer under excitation by the 266 nm line of a Nd:YAG laser [7]. The penetration depth of the 4H-SiC wafer is estimated to be ~200 nm using the absorption efficient α of 4H-SiC and the $(1/2\alpha)$ equation. The longitudinal optical (LO) and transverse optical (TO) phonons are observed at 790 and 970 cm⁻¹, respectively.

Figure 7.5 shows the Raman spectra of P⁺-implanted 4H-SiC wafer under excitation by the 266 nm line of a Nd:YAG laser. As shown in Fig. 7.5, although the Raman

Fig. 7.4 Raman spectrum of a 4H-SiC wafer under excitation by the 266 nm line of a Nd:YAG laser [7]

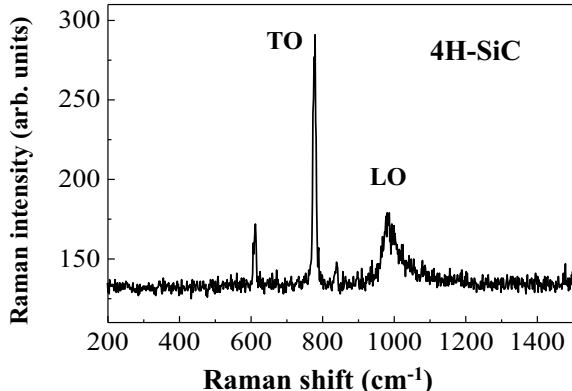
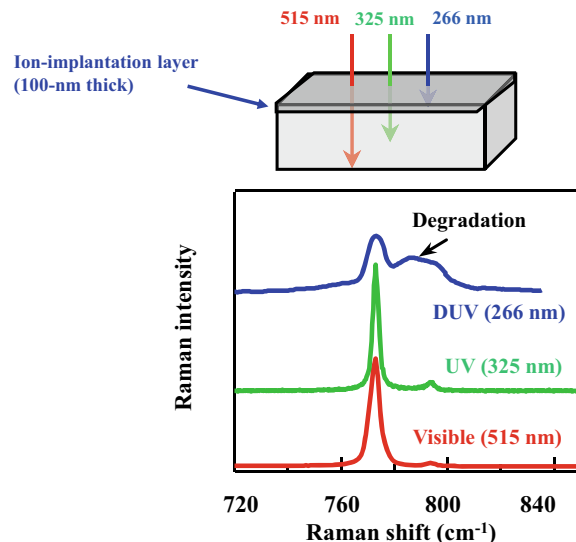


Fig. 7.5 Raman spectra of P⁺-implanted 4H-SiC wafer under excitation by the 266 nm line of a Nd:YAG laser, the 325 nm line of a He-Cd laser, and the 515 nm line of Ar⁺ laser [7]



spectrum excited by the 515 nm line of an Ar⁺ laser is almost the same as that by the 325 nm line of a He-Cd laser, the Raman spectrum of the P⁺ ion-implanted 4H-SiC surface wafer (100-nm thick) under the 266 nm excitation is found to dramatically become broader than those excited by the 515 and 325 nm lines. This means that the crystalline quality of the top surface is degraded by P⁺ ion-implantation [7]. DUV and UV Raman spectroscopy are a sensitive method of analysing the crystallinity of the surface of semiconductors.

NIR Raman spectroscopy, which can be used to obtain the Raman spectra of all materials at 900–1700 nm, has the following characteristics [7];

(1) Ability to acquire Raman spectra without specimen luminescence

Almost semiconductors do not emit luminescence during measurement because the excitation energy of NIR lasers (for example, a YAG laser: 1064 nm wavelength) is too low to excite the electronic states associated with luminescence.

(B) Ability to obtain high-intensity Raman spectra using an InGaAs multichannel detector

The Raman spectra of semiconductors can generally be measured with good sensitivity because the penetration depth of semiconductors increases with increasing excitation wavelength owing to a decrease in the absorption coefficient. For carbon nanotubes (CNTs), we can observe resonant Raman scattering [7].

Figure 7.6 shows a photograph and a schematic of a NIR Raman instrument we developed [7]. It was designed exclusively for NIR Raman measurement using a specialised optical microscope and an InGaAs array detector to obtain high sensitivity in the NIR region. Figure 7.7 shows photographs of the Nd:YAG laser and the spectrometer with InGaAs array detector [7].

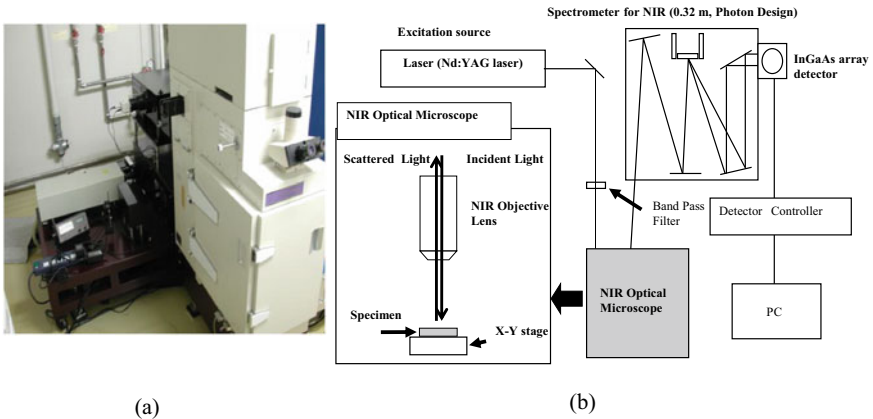


Fig. 7.6 **a** Photograph and **b** schematic of our NIR Raman setup [7]

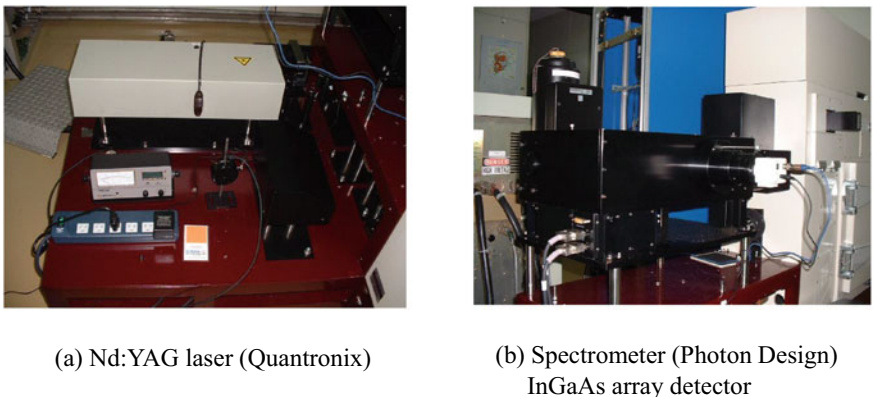


Fig. 7.7 Photographs of **a** Nd:YAG laser and **b** our spectrometer with InGaAs array detector (Photon Design) [7]

Figure 7.8 shows the Raman spectra of a low- κ film measured using this NIR instrument [7]. A low- κ material has a small relative dielectric constant compared to silicon dioxide [8]. Low- κ (dielectric material) implementation technique is one of several strategies used to allow continued scaling of microelectronic devices and low- κ materials are necessary to separate the conducting parts (wire interconnects and MOS transistors) from one another in digital circuits [8]. The Raman spectrum of the low- κ film was obtained without specimen luminescence under excitation by the 1064 nm line of a Nd:YAG laser. As a result, we can analyse the chemical structures of dielectric materials in more detail.

Figure 7.9 shows the Raman spectra of Si-doped GaAs wafers with different Si contents. LO and TO phonons were observed at 268 and 292 cm⁻¹, respectively, in the undoped GaAs wafer [7]. In a polar semiconductor such as GaAs or GaP,

Fig. 7.8 Raman spectra of a low- κ film under excitation by the 514.5 nm line of an Ar⁺ ion laser, the 632.8 nm line of a He–Ne laser, and the 1064 nm line of a Nd:YAG laser [7]

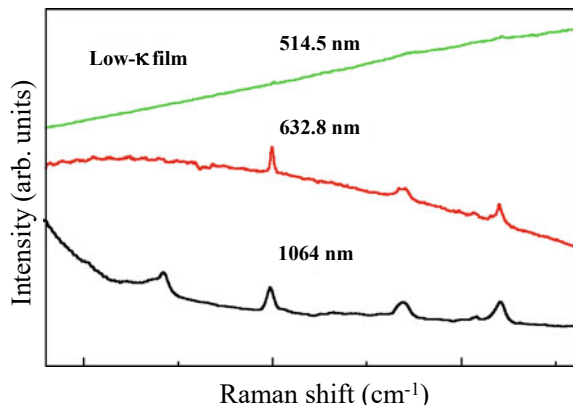
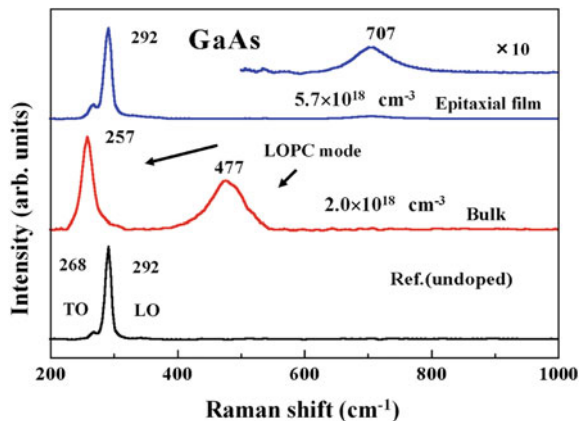


Fig. 7.9 Raman spectra of Si-doped and undoped GaAs wafers implanted at different Si doses under excitation by the 1064 nm line of a Nd:YAG laser [7]



the collective excitation of free carriers (a plasmon) interacts with the LO phonon through their macroscopic electric fields to form the LO phonon–plasmon coupled (LOPC) mode [9–11]. The LOPC modes are broad, and their peaks shift to higher frequency with increasing the number of free carriers. The carrier density dependence of the LOPC modes in *n*-type GaAs, and GaP was reported by Klein et al. [10, 11]. In Fig. 7.9, the LOPC modes of Si-doped GaAs (epitaxial) wafers at a fluence of $2.0 \times 10^{18} \text{ cm}^{-3}$ and at a fluence of $5.8 \times 10^{18} \text{ cm}^{-3}$ appear at 477 and 707 cm⁻¹, respectively.

The Raman spectrum of the undoped GaAs wafer is very weak because the penetration depth of the incident light is shallow [7]. In addition, we cannot increase the Raman intensity by increasing the laser power for GaAs specimens, because GaAs wafers are prone to irradiation damage from the excitation laser [7]. Further, the Raman band in the Si-doped GaAs becomes much weaker with increasing Si dose. Consequently, it takes 10–20 min to measure the Raman spectra of undoped and doped GaAs (epitaxial) wafers. However, the Raman spectra of undoped and

Si-doped GaAs can be obtained in several minutes using NIR Raman spectroscopy [7].

NIR Raman spectroscopy is a useful technique for measuring the Raman spectra of materials, such as semiconductors, polymers, and biological specimens, using the 1064 nm line of a Nd:YAG laser [7]. In particular, the Raman signals of narrow-gap semiconductors such as InN, InP, and AlAs in addition to GaAs, which are used in optical communication devices, are very weak in the standard visible Raman spectroscopy because of their shallow penetration depths [7]. I anticipate that NIR Raman spectroscopy will soon be used to characterise the stresses, carrier density, and crystallinity of narrow-gap semiconductor devices.

7.2 AFM-Raman and AFM-IR Spectroscopy

7.2.1 *AFM-Raman Spectroscopy*

Atomic force microscopy (AFM)-Raman spectroscopy involves the use of scanning near-field optical microscopy (SNOM), and tip-enhanced Raman scattering (TERS) by a localised surface plasmon (LSP) resonance [12]. AFM-Raman spectroscopy combines the chemical sensitivity of surface-enhanced Raman spectroscopy (SERS) and the high spatial resolution of AFM or scanning tunnelling microscope (STM), and allows chemical imaging of surfaces at the nanometre level. AFM-Raman spectroscopy has been rapidly developed into a non-destructive scanning probe microscopy tool for surface chemical characterisation [13] and has opened opportunities to study single macromolecules with subnanometre spatial resolution [14]. The technique has been recently used to study problems in biology [15], photovoltaics [16] and catalysis [17], and for investigations of semiconductors [18], carbon nanotubes (CNTs) [19], graphene [20], and single molecule detection [14].

In SNOM, the excitation laser light is focused through the SNOM-probe, resulting in an evanescent field (the near-field) on the far side of the aperture. As a specimen is moved on a piezo-driven scanning stage, the transmitted light is spectroscopically detected point by point and line by line to generate a hyperspectral image. The optical resolution of the transmitted light is limited only by the diameter of the aperture. When a beam reflection setup like that in the contact-mode AFM is used, the cantilever is always in contact with the specimen. Thus, the topography of the specimen is recorded simultaneously with the near-field Raman measurement. A schematic diagram of a SNOM system is shown in Fig. 7.10.

Figure 7.11 illustrates the principle of tip-enhanced Raman spectroscopy (TERS) [21–24]. There are two types of TERS setups: transmission and reflection TERS systems. The transmission-type TERS systems have significantly higher spatial resolutions due to the use of the objective lens with a numerical aperture (N.A.) larger than 1.0 and are more commonly used than the reflection-type ones. However, these systems require transparent specimens on transparent substrates. On the other hand,

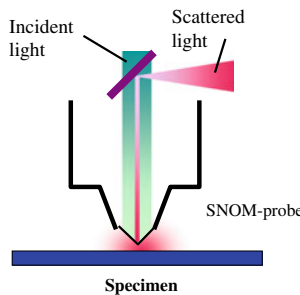


Fig. 7.10 Schematic diagram of our SNOM system

the reflection-type system can easily remove the Rayleigh scattering and far-field Raman scattering signals from specimens. Moreover, the reflection-type system can use the gap-mode TERS configuration to acquire strong TERS signals, in which the enhanced TERS signal was estimated to be up to 10^6 , and the metal substrate–tip gap forms an optical cavity where localised surface plasmons could be excited by a laser.

A sharp metal (Ag, Au, etc.) or metal-coated AFM-tip is positioned at the centre of the laser focus, and the electromagnetic (EM) field at the tip-apex is confined and enhanced owing to a combination of LSP resonance and the lightning rod effect. This increase in the EM field enhances the Raman signal from the specimen near the tip-apex and enables nanoscale vibrational imaging of the surface; thus, this technique is not subject to the diffraction limit, in contrast to SERS and the conventional Raman spectroscopy. The signal enhancement sensitivity and resolution of TERS are interpreted mainly in terms of an EM enhancement mechanism [21], although signal enhancement due to chemical interaction of a TERS-tip with the specimen has also been reported [22, 23]. The observed EM enhancement at the tip-apex arises

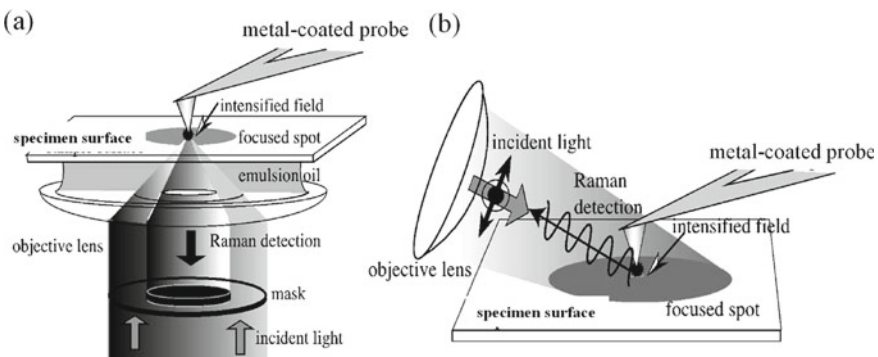


Fig. 7.11 Schematic diagram of **a** transmission-type TERS system and **b** reflection-type TERS system

from a combination of LSP resonance and the antenna effect, which results in a locally confined and enhanced electric field, as shown in Fig. 7.11.

Even greater localised electrical field enhancement is observed at the tip-apex when the LSP wavelength of the tip-apex matches the wavelength of the excitation laser. Further details on tip enhancement can be found in the book by Kawata and Shalaev [24]. The LSP wavelength of the TERS-tip can be tuned by selecting the material, radius, or roughness of the tip-apex so that the LSP wavelength matches the wavelength of the excitation laser. At resonance, the observed electrical field at the tip-apex is several orders of magnitude stronger than that off-resonance; the maximum enhancement factor is 10^6 . Although LSP resonance has been observed in many metal nano-particles, only Ag and Au are resonant with lasers in the visible region. The LSP wavelength of a silver TERS-tip generally falls in the blue and green regions [25].

The EM enhancement near the tip-apex arising from LSP resonance has been used to detect several materials, such as CNTs and graphene. To obtain the strongest SERS signals, or hot spots, localised EM fields in nanoscale gap junctions between the metallic nanoparticles have been used [26, 27]. Similarly, a sharp metallic tip can generate a hot spot when placed near a metallic surface, resulting in EM near-field enhancement at the tip-apex [28–30]. This gap-mode TERS has been extensively used for nanoscale imaging and single molecule detection [31, 32]. Au and Ag are typical metallic gap-mode TERS substrates.

Futamata et al. evaluated the local electric field and scattering cross section on Ag nanoparticles using the finite-difference time-domain (FDTD) method to investigate the single-molecule sensitivity of SERS [33].

Yang et al. used 3D FDTD simulations to investigate the field enhancement factor in TERS and identify the optimal geometric parameters of the metal-tip and metal substrate under side illumination at certain excitation wavelengths [34]. The simulation results indicate that plasmon coupling effects between the metal-tip and metal substrate play a key role in TERS enhancement, and the enhancement decreases dramatically as the distance between the tip and the substrate increases [34]. The spatial resolution of TERS depends mainly on the radius of curvature of the tip-end. The use of a sharp tip with a small radius of curvature can drastically increase the spatial resolution of TERS [34]. Increasing the tip–substrate distance or using a dielectric substrate instead of a metallic substrate decreases the spatial resolution. The TERS enhancement depends on the incident angle and polarisation of the laser beam, the size of the tip, and the substrate composition [34].

Moreover, Yang et al. modelled a double-tip with a 50-nm diameter Au nanoparticle, as the second tip on the smooth gold substrate, and found by FDTD simulation that the double-tip showed the field enhancement by a factor of 251 and induces the tip-enhanced Raman scattering by a factor of 4×10^9 [34], which was in good agreement with the experimental data reported elsewhere [35].

In standard Raman microscopy, the spatial resolution is limited by the diffraction limit of the incident laser. To overcome this limitation, a near-field optical Raman microscope was equipped with an optical fibre probe [36]. However, the performance of this instrument is limited by problems, such as those associated with obstruction

of weak Raman signals from the specimen by the strong luminescence and Raman lines of the fibre probe, the low fibre probe transmittance (on the order of 10^{-3}), and signal weakness owing to the low penetration depth of the near-field light (<100 nm) [36].

Anisotropic stresses are thought to occur around real trench structures owing to the dependence of the oxidation speed and dislocation on the orientation [37]. It is necessary to know which stress component is measured by Raman spectroscopy when experimental data are compared with stress simulations. Polarised Raman spectroscopy can give direct information about the direction and distribution of the stresses [37]. Polarised Raman spectra have been measured around trenches formed on a (100) silicon wafer; the peak-frequency shift was found to vary with the polarisation configuration, which suggests that anisotropic stresses occurred around the trenches [37].

Furthermore, tapping-mode scanning near-field optical Raman microscopy (SNOM) using a hollow pyramidal probe based on UV resonant Raman scattering has been developed and used to measure the stress distribution of Si very large-scale integration (VLSI) standards.

Resonant Raman scattering occurs when the excitation energy coincides with the electronic transition energy of the material. For Si, the direct band gap at the Γ point is approximately 3.4 eV (~ 363.8 nm) [1, 38]. Indeed, the resonance in Si results in strong enhancement of the Raman scattering cross-section (by a factor of approximately 100), and the optical penetration depth decreases under the resonant condition. The optical penetration depth of Si at an excitation wavelength of 363.8 nm is 5 nm [39]. Recently, we remodelled SNOM apparatus at an excitation wavelength of 355 nm (3.49 eV).

Figure 7.12 shows a 5000×5000 nm 2 topographic image of a VLSI standard measured by a commercially available bent-fibre probe with an aperture of 20 nm [40, 41]. The figure depicts the 200-nm-wide areas covered by SiO₂ layer, and some of the 1600 nm 2 area of the Si (100) substrate that is not covered [40, 41].

Figure 7.13a, b illustrate AFM (topographic) image, and typical SNOM spectra, respectively, of the VLSI standard measured using the pyramidal probe (we call SNOM-probe hereafter) with an aperture of approximately 150 nm [38]. The near-field Raman signal of Si could be detected only when the incident light was focused on the aperture of the SNOM-probe by the UV objective lens. Although the SNOM-probe separation in the area covered by the SiO₂ layer is 180 nm, the SNOM-probe may be buried in the SiO₂ layer owing to the use of the tapping mode and the difference in hardness between the silicon nitride (SiN) probe and the SiO₂ layer.

The Raman band of Si generally shifts to higher and lower frequencies under compressive and tensile stresses, respectively. In Fig. 7.13b, the peak frequency is $0\text{--}0.6$ cm $^{-1}$ lower in the area covered by SiO₂, while it is $0\text{--}0.2$ cm $^{-1}$ higher in the area without SiO₂ (centre or edge in Fig. 7.13b) [38]. This result indicates that the areas covered and not covered by SiO₂ are under tensile and compressive stresses, respectively [38]. The tensile stress is attributed to the difference in thermal expansion coefficients of silicon and SiO₂, which affected the wafer as it was cooled from the deposition temperature to room temperature. Moreover, the compressive stress is

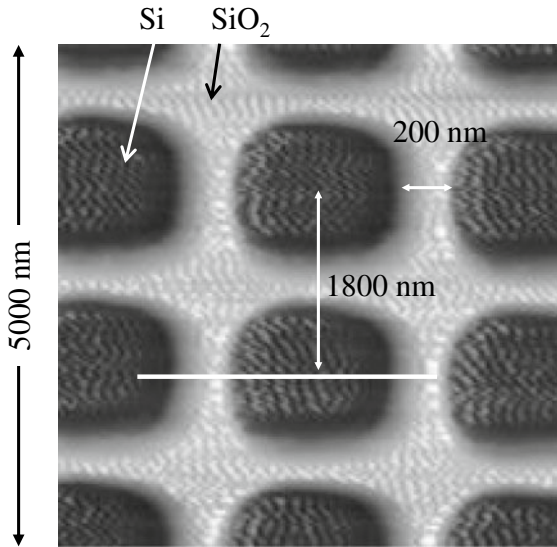


Fig. 7.12 Topographic image ($5000 \times 5000 \text{ nm}^2$) of a VLSI standard [40]. (Reproduced with permission from Ref. [40]. Copyright (2006) The Japan Society of Applied Physics.)

attributed to a trade-off between the compressive and tensile stresses [38]. As shown in Fig. 7.13b, the compressive stress is concentrated at the interface between the areas covered and not covered by SiO₂. The compressive stress can be estimated from the observed peak-frequency shift using Eq. (7.1) in Ref. [40] or Eq. (5.2). Compressive stresses of approximately 0.46 GPa/cm² were found to be concentrated at the interface between the areas covered and not covered by SiO₂, using Eq. 5.2 [38].

Figure 7.14a, b illustrate images of the peak intensity, and peak frequency, respectively, of the VLSI standard measured with and without the pyramidal cantilever [38].

The area covered by the SiO₂ layer in Fig. 7.14(a, higher figure) becomes broader than that in Fig. 7.14(b, higher figure) [38]. Moreover, the distribution of the peak frequency in Fig. 7.14a is homogeneous and out of focus compared to that in Fig. 7.14b, respectively. This difference is attributed to the difference in spatial resolution [38]. The peak frequency in the areas not covered by SiO₂ in Fig. 7.14(b, lower figure) (especially, ring of each circle in Fig. 7.14b) shifts largely than that in Fig. 7.14(a, lower figure). A comparison of 7.14a, b suggests that the spatial resolution in Fig. 7.14b is much higher in Fig. 7.14a [38].

Figure 7.15a shows a schematic of Si nano-dot structures formed by the nano-imprinting method [71]. Figure 7.15b, c show intensity images of the $500 \times 500 \text{ nm}^2$ area measured without and with the SNOM-probe (diameter of 100 nm), respectively. The Raman intensity of the structures was obtained by moving an $x-y$ piezoelectric scanner in 50 nm steps [41]. The intensity image measured with the SNOM-probe

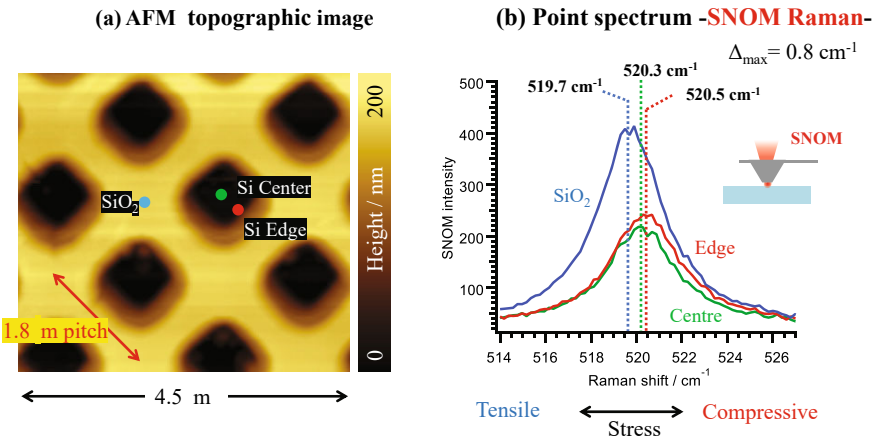


Fig. 7.13 **a** AFM topographic image, and **b** Near-field Raman spectra of the VLSI standard measured at an excitation wavelength of 355 nm (3.49 eV), using a SNOM-probe with a diameter of 150 nm (our original data) [38]

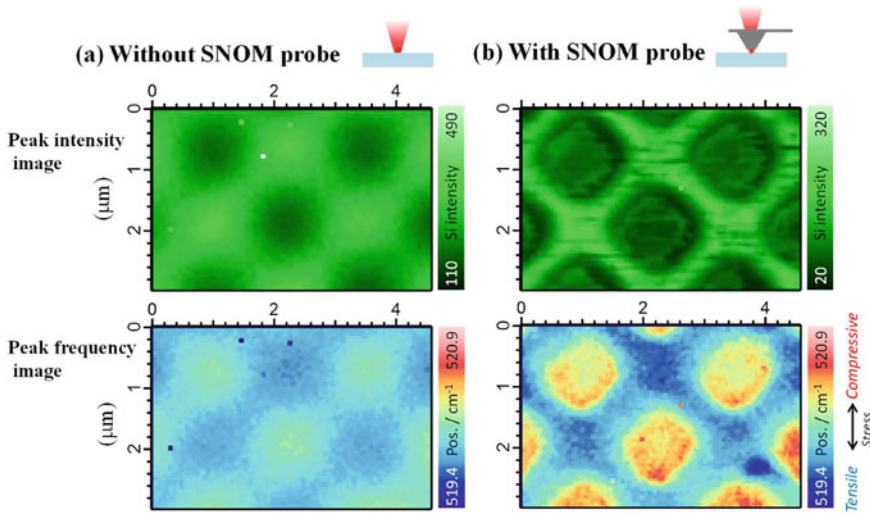


Fig. 7.14 Images of **a** peak intensity, and **b** peak frequency of VLSI standard measured, respectively, without and with the pyramidal cantilever. The upper and lower images in Fig. 7.14a, b depict the peak-intensity and peak-frequency images, respectively (our original data) [38]

shows a periodic pattern with a period of approximately 100 nm [41]. When the SNOM-probe was not used, the periodic pattern was not observed. This finding means that the spatial resolution of SNOM is higher than 100 nm [41].

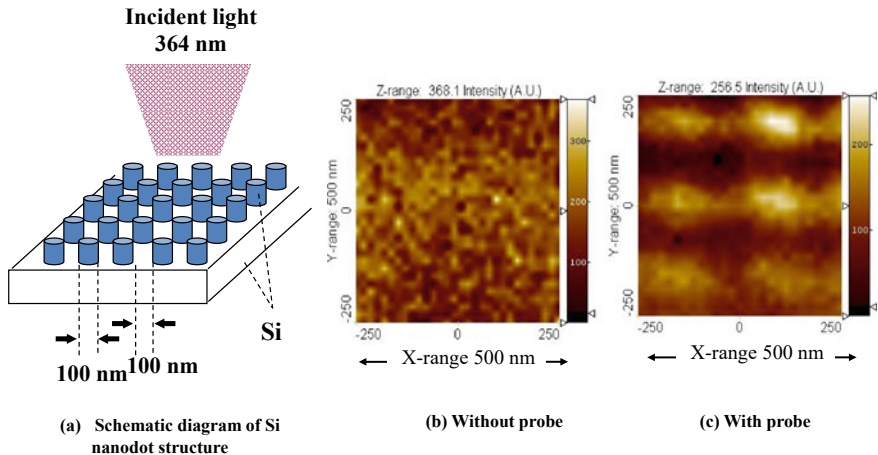
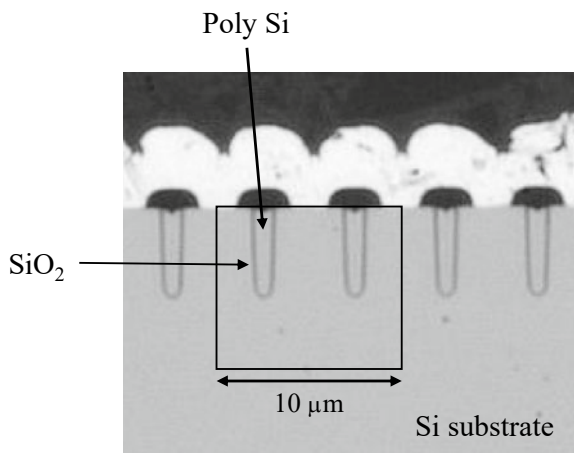


Fig. 7.15 **a** Schematic diagram of Si nano-dot structure and intensity images measured **b** without and **c** with the SNOM-probe (aperture size of 100 nm) [41] (Reproduced with permission from Ref. [41]. © AIP Publishing, 2007.)

Fig. 7.16 Cross-sectional photograph of commercially available Si trench MOSFET [38]



Currently, almost all power electronics converters use Si-based power semiconductor devices. However, in recent years, a large effort has been devoted on the development of SiC-based and GaN-based power semiconductor switches. Figure 7.16 shows a cross-sectional photograph of commercially available Si trench MOSFET [38]. The deep trenches were filled with polycrystalline silicon and coated by silicon dioxide (SiO₂) with thickness of less than approximately 100 nm [38].

To sensitively detect stresses in Si, SiC or GaN devices, we developed a new SNOM apparatus. Figure 7.17a shows photograph and a schematic of the SNOM apparatus we newly developed [38]. There are three lasers consisting of the 355 nm

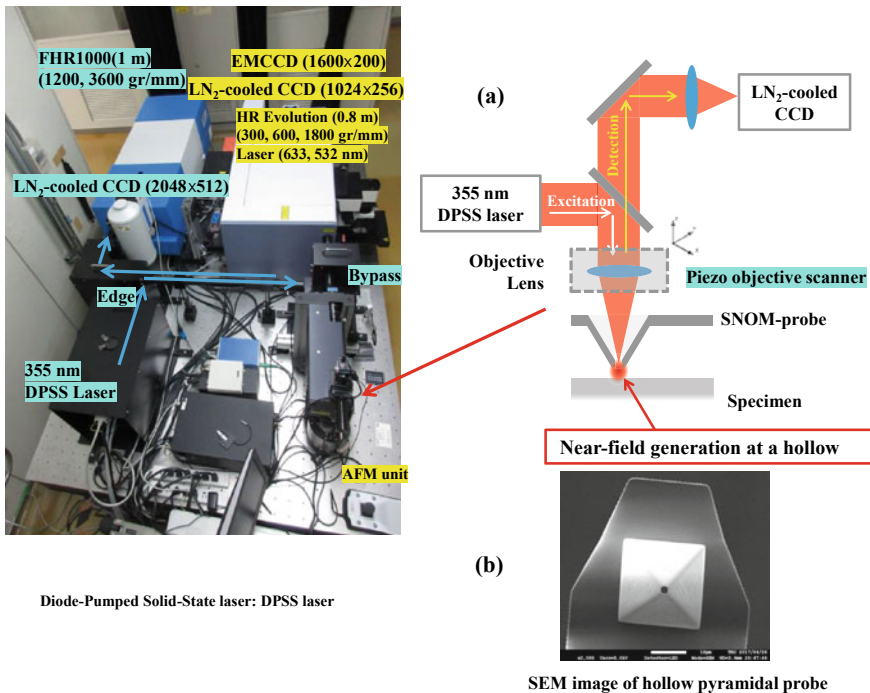


Fig. 7.17 **a** Photograph and schematic of SNOM apparatus; **b** SEM image of the SNOM-probe [38]

line of a diode-pumped solid-state laser (DPSS) laser, the 532 line of a semiconductor laser, and the 633 nm of a semiconductor laser. Horiba Jobin Yvon single monochromators with focal lengths of 0.8 m and 1 m are employed. Furthermore, a piezoelectric scanner is used as the x - y stage. Figure 7.17b shows a SEM image of the SNOM-probe in the SNOM apparatus.

Figure 7.18a–c show stress images of the cross-sectional Si trench MOSFET, measured (a) without and (b) with the SNOM-probe, and (c) near-filed Raman spectra of points 1–3 in Fig. 7.18b, measured using a SNOM-probe with a diameter of 150 nm [38]. Raman spectra of the cross-section of the Si trench MOSFET were measured at room temperature using the 355 nm line of a DPSS laser. The x - y piezoelectric scanner was moved in 105 nm steps [38]. Generally, the Raman band of Si shifts to higher and lower frequencies under compressive and tensile stresses, respectively [37]. As seen in Fig. 7.18c, the peak frequency shifts to low frequency around the sidewalls of trenches, while it shifts to a high frequency at the bottoms of the trenches. Consequently, in 7.18a, b, the sidewalls of trenches and the bottoms are under tensile and compressive stresses, respectively [38]. The tensile stress is attributed to the difference in thermal expansion coefficients of silicon and SiO₂, which affected the wafer as it was cooled from the deposition temperature to room temperature [38].

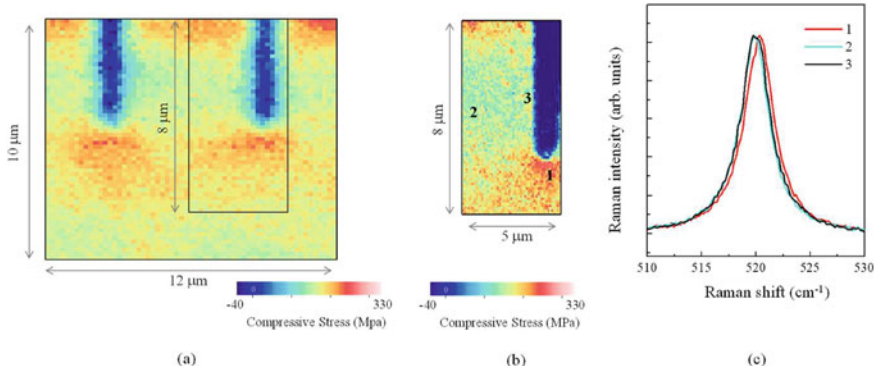


Fig. 7.18 **a** Intensity images measured **a** without and **b** with the SNOM-probe, and **c** near-filed Raman spectra of points 1–3 in Fig. 7.18b, measured at an excitation wavelength of 355 nm (3.49 eV) for commercially available Si trench MOSFET, using the SNOM-probe with a diameter of 150 nm [38]

Moreover, the compressive stress is attributed to a trade-off between the compressive and tensile stresses [38]. This result agrees well with a previous work [37].

The stress distribution in Fig. 7.18a is blurrier than that in Fig. 7.18b [38]. This difference is obviously attributed to the difference in spatial resolution. A comparison of Fig. 7.18a, b means that the new SNOM apparatus we developed in Fig. 7.17a has an extensively high spatial resolution [38].

Although many studies on stress estimation in Si devices have been reported, there has been no research on stress estimation in SiC devices. The stress induced at the interface between thermal oxide (SiO_2) and the 4H-SiC epitaxial substrate was studied using SNOM [42].

Next, we measured stresses induced in the SiC epitaxial layer near the interface between thermal silicon oxide and 4H-SiC epitaxial substrate, using a near-field optical Raman microscope equipped with a SNOM-probe (aperture size: approximately 250 nm) [42]. Epitaxial layers nearly 10-μm thick were grown via chemical vapour deposition on a 4° off-axis 4H-SiC (0001) Si face [44]. After being cleaned in accordance with the RCA cleaning process, the layers were thermally oxidised in dry O_2 at 1280 °C for 30 min. The oxide layer thickness was approximately 50–60 nm. Two types of specimens were prepared for FT-IR spectroscopy. The specimen labelled No. 1 was not subjected to post-oxidation annealing (POA), while that labelled No. 2 was subjected to POA in a N_2O atmosphere maintained at 1280 °C for 75 min. Specimen No. 1 was used for Raman microscopy measurements with a SNOM-probe (aperture size: approximately 250 nm) [42].

A Horiba Jobin Yvon single monochromator with a focal length of 0.8 m was employed to record the Raman spectra of the cleaved (01–1 0) cross-section of the epitaxial SiC substrate at room temperature using the 633 nm line of a semiconductor laser [42]. The x–y piezoelectric scanner was moved in 105 nm steps. A spectrometer equipped with a 1600 × 200 EMCCD detector was employed [42]. All the Raman

spectra were measured using a power of less than 0.4 mW [42]. Each spectrum was measured at an exposure time of 90 s. The peak-frequency shift ($\Delta\nu$) was measured with respect to that of the Raman line at a position far from the SiO_2/SiC interface (approximately 20 μm) [42]. The peak frequency was determined by fitting a Lorentzian lineshape to the spectra, and an accuracy of approximately $\pm 0.04 \text{ cm}^{-1}$ was obtained [42].

Figure 7.19a, b show Raman spectra of the epitaxial 4H-SiC substrate obtained using a backscattering configuration, and a schematic plan view of a SiO_2 film grown on a 4H-SiC epitaxial substrate, respectively [42]. The strongest peaks contain those of the E_2 [folded transverse optical (FTO)] phonon mode at 776 cm^{-1} , the A_1 (FTO) phonon mode at 783 cm^{-1} , and the E_1 (folded longitudinal optical (FLO)) phonon mode at 964.0 cm^{-1} [44]. The E_2 (FTO) phonon mode is referred to as the E_2 phonon mode hereafter.

E_2 phonon mode generally shifts to higher and lower frequencies under compressive and tensile stresses, respectively [42, 44]. The following equation is used for the E_2 phonon mode [43].

$$\sigma (\text{MPa}) = -321\Delta\nu(\text{cm}^{-1}) \quad (7.1)$$

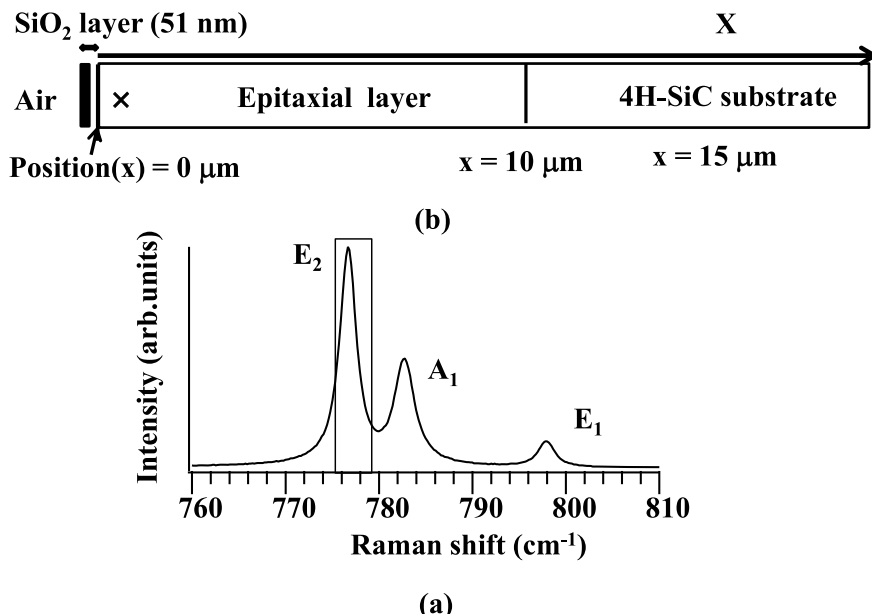


Fig. 7.19. **a** Raman spectrum of epitaxial 4H-SiC substrate measured in backscattering configuration and **b** schematic plan view of $\text{SiO}_2/4\text{H}-\text{SiC}$ interface of SiO_2 film on 4H-SiC epitaxial layer [42]. (Reproduced with permission from Ref. [42]. © SAGE Publications, 2019.)

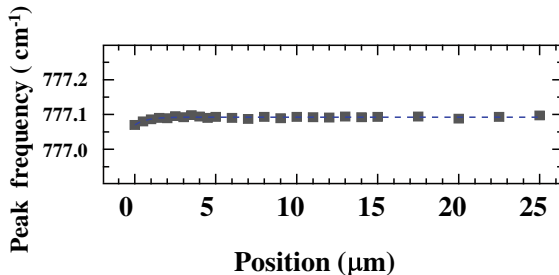


Fig. 7.20 Dependence of E_2 phonon frequency (detected using standard Raman microprobe without SNOM-probe) on oxide-layer thickness. The peak frequency was determined by fitting a Lorentzian lineshape to the spectra; an accuracy of approximately $\pm 0.04\text{ cm}^{-1}$ was obtained [42] (Reproduced with permission from Ref. [42]. © SAGE Publications, 2019.)

Figure 7.20 shows the dependence of the E_2 phonon frequency (detected using a standard Raman microprobe without the SNOM-probe) on the oxide-layer thickness. The E_2 phonon mode is red-shifted by only 0.02 cm^{-1} as the oxide-layer thickness decreases from 3 to 0 μm [42].

Figure 7.21a shows the dependence of the E_2 phonon frequency, measured using the Raman microprobe with the SNOM-probe (aperture size: approximately 250 nm) on the oxide-layer thickness [42]. Figure 7.21b shows a schematic plan view of the $\text{SiO}_2/4\text{H-SiC}$ interface. As shown in Fig. 7.21a, the E_2 phonon exhibits a dramatical red-shift of 0.17 cm^{-1} as the oxide-layer thickness decreases from 300 to 0 nm. The E_2 phonon-frequency shift ($\Delta\nu$) of -0.17 cm^{-1} in Fig. 7.21a can, therefore, be assigned to the tensile stress at the $\text{SiO}_2/4\text{H-SiC}$ interface. Equation (7.1) indicates that the thermal oxide layer at the $\text{SiO}_2/4\text{H-SiC}$ interface is under a tensile stress on the order of 50 MPa [42]. This tensile stress is originating from a difference in the thermal expansion coefficients of the SiO_2 film and 4H-SiC substrate, which affects the specimen when it is cooled from the process temperature ($1280\text{ }^\circ\text{C}$) to room temperature [42].

The 2D stress distributions across the cleaved cross-sectional interfaces between SiO_2 and 4H-SiC were calculated with the finite element method (FEM). The calculated stress distributions are plotted in Fig. 4a, b of Ref. [44]. The agreement between the results of the Raman measurement and the FEM calculations means that the effect of stress relaxation by cross-sectional cleavage of the epitaxial SiC substrate is small [44].

FT-IR spectra were measured using a single-reflection ATR attachment in combination with a FT-IR spectrometer with an IR polariser to generate *s*-polarised IR light [43]. The incident angle was set to 60° , and a Ge crystal was utilised as the ATR element. A 1% diluted hydrofluoric acid solution was used for oxide-layer etching. ATR measurements were carried out on unetched specimens with various oxide-layer thicknesses by repeated ATR measurements and wet etching. FT-IR spectra of SiO_2 films on a Si wafer revealed features at approximately 1072 and 1257 cm^{-1} that indicated TO and LO phonons, respectively [45, 46]. Figure 7.22 illustrates the

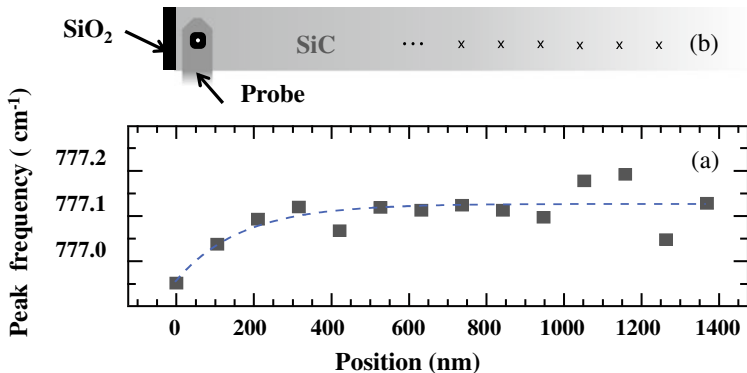
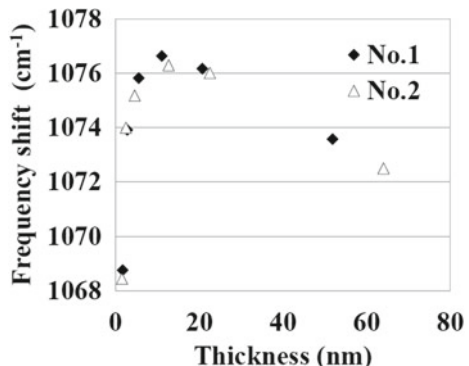


Fig. 7.21 **a** Dependence of E_2 phonon frequency (measured using standard Raman microprobe with the SNOM-probe; aperture size: approximately 250 nm) on oxide-layer thickness and **b** schematic plan view of $\text{SiO}_2/4\text{H-SiC}$ interface [42]. (Reproduced with permission from Ref. [42]. © SAGE Publications, 2019)

TO phonon-frequency dependence of specimens No. 1 and No. 2 on the oxide-layer thickness [43]. The TO phonon shifted by approximately 5 cm^{-1} as the oxide-layer thickness decreased from 65 to 10 nm. Stress characterisation of 4H-SiC MOSFETs by FT-IR spectroscopy indicates that the observed blue-shift is a result of the compressive stress across the $\text{SiO}_2/4\text{H-SiC}$ interface induced by the differences in thermal expansion coefficients and elastic moduli of SiO_2 and the SiC substrate [43].

Hirai and Kita [47] measured the FT-IR spectra of thermal oxides on the 4H-SiC (0001) Si and C faces and found that the peak frequency of the TO phonons is nearly constant for thicker oxides (5–30 nm thick); this result is only slightly different from that described above, which coincides well with that reported by Seki et al. [48]. It has also been suggested [42], on the basis of a two-plate model consisting of a thin SiO_2 layer on a 4H-SiC epitaxial layer, that the observed blue-shift could be caused by a compressive stress of approximately 0.44 GPa across the SiO_2/SiC interface [42].

Fig. 7.22 Plots of TO phonon frequency as a function of the oxide-layer thickness [43]. (Reproduced with permission from Ref. [43] © Trans Tech Publications, 2018.)



Moreover, when SNOM was used, a relatively low tensile stress (approximately 50 MPa) was observed at a 250 nm position from the interface between the SiO₂ and SiC layers. A comparison of the results obtained by Raman and FT-IR measurements reveals the following [42]:

- (1) Within a SiO₂ layer with a thickness in the range from 10 to 65 nm, oxygen vacancy centres (OVCs) were generated to relax the strong compressive stress of ~0.44 GPa observed by FT-IR spectroscopy [42].
- (2) The number of OVCs tended to increase in the vicinity of the interface between the SiO₂ and SiC epitaxial layer as the oxide-layer thickness decreased from 10 nm to 1.5–1.7 nm, increasing the SiO₂ inhomogeneity and resulting in the formation of SiO_{2-x} [42].
- (3) The FT-IR spectra illustrate that the TO phonon frequency exhibits a dramatic red-shift, which is accompanied by an increase in SiO₂ inhomogeneity (SiO_{2-x} formation) [42], which greatly reduces the strong compressive stress within the oxide layer. The large red-shift of the TO phonon is observed near the SiO₂/Si interface [45, 46, 48].
- (4) Equilibrium between the compressive and tensile stresses is indicated by a relatively low tensile stress (on the order of 50 MPa) within the SiC epitaxial layer and nearly 250 nm from the interface between the SiO₂ and epitaxial SiC layer, which was observed using SNOM [42].

This model is supported by an increase in the CL intensity, which has been assigned to the OVCs. [42] We believe that the tensile stress at the SiO₂/4H-SiC interface, which is greater than that at the SiO₂/Si interface, is one of the reasons that the D_{it} and Q_{eff} values at the SiO₂/4H-SiC interface are one to two orders of magnitude higher than those at the SiO₂/Si interface [42]. The SNOM instrument presented here affords a powerful method of practical characterisation of the stresses induced at the SiO₂, metal, and SiC substrate interfaces in SiC power devices such as 4H-SiC MOSFETs [42].

Carbon nanotubes (CNTs) and graphene have noteworthy electrical properties, such as excellent carrier mobility, typical ambipolar behaviour, and a distinctive energy band structure, which can be applied in FETs, radio frequency circuits, sensors, and memories. CNTs are potential candidates for use as via hole and wire materials in nanoscale VLSI circuits. By eliminating the electromigration reliability concerns that plague today's Cu interconnects, isolated (single and multiwall) CNTs can carry current densities in excess of 1000 MA/cm² without electromigration damage [49].

Single-walled nanotubes (SWNTs) are promising candidates for miniaturisation of electronics. The most basic building block of these systems is an electric wire, and SWNTs with diameters on the order of a nanometre can be excellent conductors [50, 51]. SWNTs can be usefully applied in the development of the first intermolecular FETs. Furthermore, graphene is also highly flexible and transparent; thus, it is attractive for use in flexible electronics such as smartphones and tablets. As graphene is both highly conductive and transparent, it has great potential for use as a material

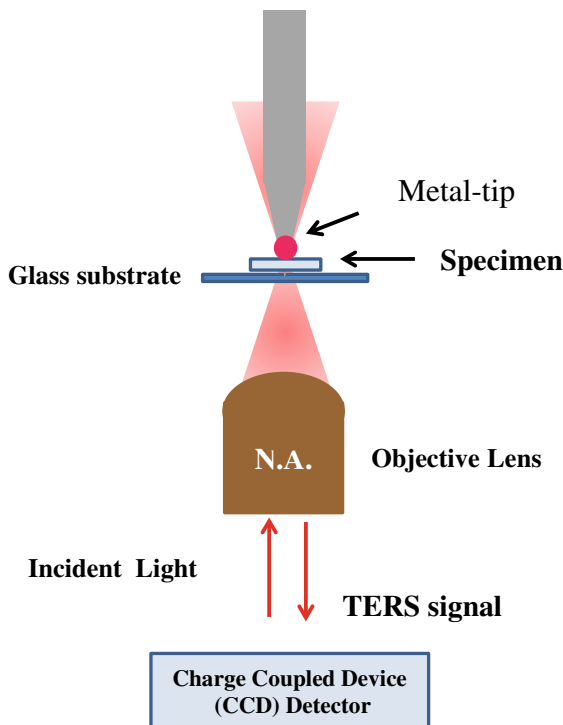
in solar cells. Furthermore, owing to its high conductivity, graphene can be used in semiconductors to greatly increase the speed at which information travels.

The giant optical nonlinearities of graphene oxide (GO) have been proved useful for a number of applications [52]. For example, the optical limiting in GO is indispensable for protecting sensitive instruments from laser-induced damage. In addition, the saturable absorption can be used for pulse compression, mode-locking, and Q-switching. Moreover, nonlinear refraction (the Kerr effect) is crucial for various functionalities, including all-optical switching, signal regeneration, and fast optical communication. The use of GO as a flexible free-standing battery anode material for room temperature lithium-ion [53] and sodium-ion batteries has been demonstrated [54]. It is also being studied as a high-surface-area conducting agent in lithium-sulphur battery cathodes. The functional groups on GO can serve as sites for chemical modification and immobilisation of active species. This approach allows for the creation of electrode materials with hybrid architectures. Recent examples have been implemented in lithium-ion batteries, which are rechargeable but have low-capacity limits. GO-based composites functionalised with metal oxides and sulphides have been shown to enhance battery performance.

Figure 7.23 shows schematic of a typical transparent TERS system [55–57].

The TERS setup shown in Fig. 7.23 is based on an inverted optical microscope equipped with an x - y piezo-scan stage for raster-scanning a specimen on a transparent

Fig. 7.23 Schematic of a typical transparent TERS configuration. A sharp Au-tip is scanned with a strongly focused laser beam. The optical signal is detected either by a photodiode or by a combination of a spectrograph and a CCD detector



substrate. An objective with a high numerical aperture ($N.A. = 1.4$) is used to focus a radially polarised laser beam on the surface of the transparent substrate. A sharp metal-tip (Au or Ag is typically used) is positioned in the focus of the incident laser beam. The tip is attached to a quartz tuning fork, and it is kept ~ 2 nm from the specimen surface by a sensitive shear-force feedback mechanism [58]. The scattered light is collected by the same objective (in the backscattering geometry) and then detected by a single-photon avalanche photodiode (APD), or by a combination of a spectrograph and a cooled CCD detector [58]. When the APD is used, the scattered beam is passed through a low-pass filter and also a narrow band-pass filter to remove the Rayleigh component and select the wavelength range of interest [58]. When the signal is detected by the CCD detector, the scattered beam is filtered by a notch filter, which removes the Rayleigh scattered light. In both cases, the tip-enhanced Raman image and topographic image are obtained simultaneously by raster-scanning the specimen [58].

Yano et al. studied the distribution of single-walled carbon nanotubes (SWNTs), using a transparent TERS system [59]. They measured the radial breathing mode (RBM) of SWNTs in the TERS spectra, which corresponded to the diameters of various SWNTs in the immediate vicinity of the tip. Moreover, they obtained a colour TERS image of the RBM that reflected the diameter distribution of SWNTs within a bundle and then, measured TERS image of an isolated SWNT bundle at three different frequencies of RBM pre-selected from a TERS spectrum of the bundle [59]. A topographic image of the specimen is shown in Fig. 7.24a (the dotted line). The dotted line indicates the bundle selected for their study [59]. The spectrometer was fixed at frequencies of 195 cm^{-1} (diameter: 1.23 nm), 244 cm^{-1} (diameter: 0.97 nm), and 278 cm^{-1} (diameter: 0.85 nm), and the TERS images were obtained, which are shown in Fig. 7.24b–d, respectively [59]. Figure 7.24b indicates that the SWNTs with a diameter of 1.23 nm are localised at both edges of the bundle. Figure 7.24c depicts that the SWNTs with a diameter of 0.97 nm are dominantly distributed towards the central and upper portion of the bundle, and Fig. 7.24d shows that the SWNTs with a diameter of 0.85 nm are distributed mainly towards the lower portion of the bundle [59]. Figure 7.24e is a combination of the Fig. 7.24b–d, which compares with the topographic image in Fig. 7.24a. Figure 7.24e shows colour-coded diameter distribution of the SWNTs within the bundle and might give much more information than Fig. 7.24a [59].

We investigated the microstructure of the semiconducting and metallic carbon nanotubes (CNTs) on nanometre-scale using a reflection-type TERS system. Figure 7.25a–c show two simultaneously acquired images: a phase-contrast AFM image and a schematic of topographic AFM image of Fig. 7.25a, and RBM spectra of CNTs 1–3. CNTs 1 and 3 are semiconducting CNTs with sizes of 1.65 and 1.8 nm, respectively, whereas CNT 2 is a CNT bundle (CNT bundle 2) consisting of a 0.7 and a 1.65 nm semiconducting CNTs and a metallic 1.4 nm CNT [60–63].

Figure 7.26a–g depict a topographic image of the CNTs, the super-resolved intensity images of the D, G, and 2D bands, the merged colour image obtained by combining the three images in (b), (c), and (d), the relative intensity of the D band

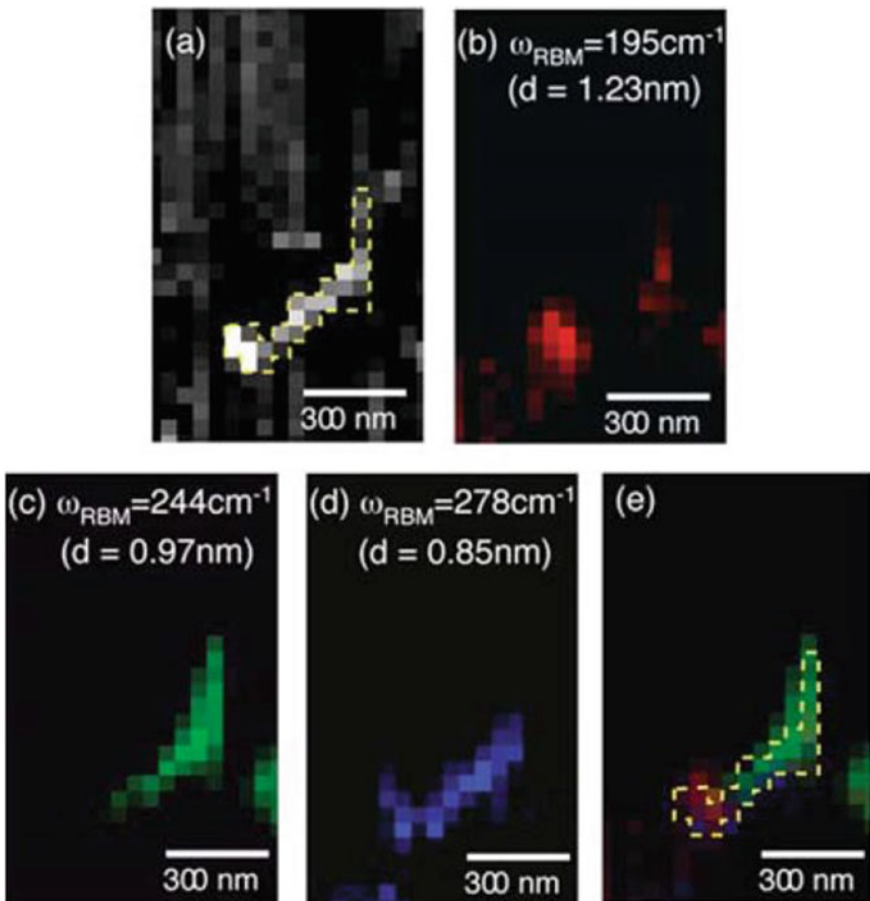


Fig. 7.24 A topographic image of **a** a SWNT bundle and TERS images at **b** 195 cm^{-1} , **c** 244 cm^{-1} , **d** 278 cm^{-1} , and **e** the mixed colour image illustrated by combining the three images in **(b)**, **(c)**, and **(d)** [59]. (Reproduced with permission from Ref. [59]. © AIP Publishing, 2006.)

normalised by that of the G band (I_D/I_G), and TERS spectra of the positions 1-3 in Fig. 7.26f, respectively [60].

A comparison between Figs. 7.25a and 7.26e indicates that CNT 1 comes into contact with CNTs 2 and 3 at the CNT intersection. The relative intensity (I_D/I_G) image in Fig. 7.26f, which shows a crystalline defect distribution in the CNTs, becomes higher at the CNT intersection. This result suggests a dramatic decrease in crystalline quality at the CNT intersection [60].

Figure 7.26g shows the TERS spectra of CNT1 (position 1), CNT2 (position 2), and the intersection (position 3) of CNTs 1 and 2 in Fig. 7.25a, and 7.26f. The D band splits into several peaks at this intersection; the 2D band becomes broader than

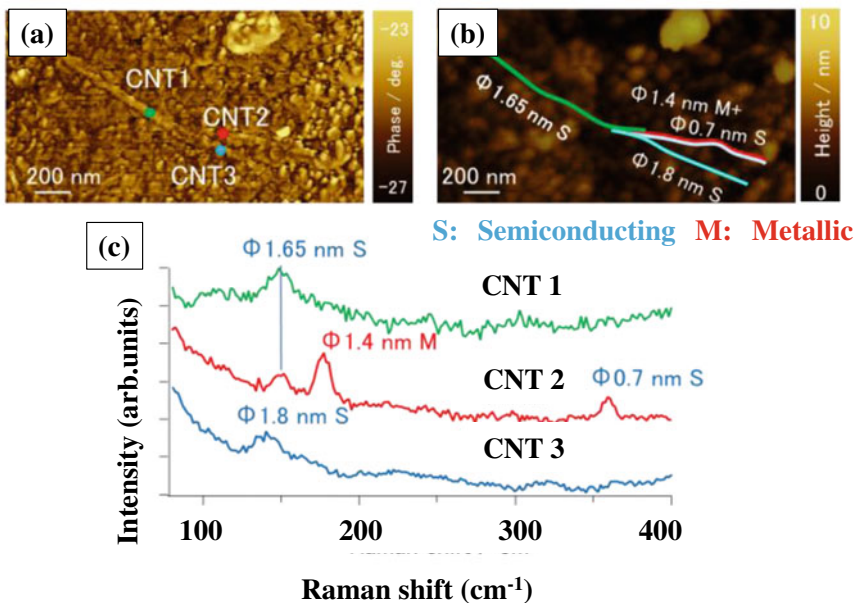


Fig. 7.25 **a** Phase-contrast AFM image of CNTs 1–3, **b** schematic of topographic AFM image of semiconducting and metallic CNT bundles on an Au substrate in Fig. 7.25a, and **c** RBM spectra of CNTs 1–3 [60]

those of CNTs 1 and 2 and then shifts to a lower frequency. These results indicate a decrease in the crystalline quality at the intersection of the CNTs [60].

Graphene features two characteristic Raman modes centred at $\sim 1580 \text{ cm}^{-1}$ (G band) and $\sim 2700 \text{ cm}^{-1}$ (2D band), and the disorder in graphene is indicated by the appearance of a $\sim 1350 \text{ cm}^{-1}$ resonance (D band) [64].

TERS is particularly sensitive to the conditions at plasmonic tip–specimen nanojunctions, where the incident and scattered optical fields may be localised and optimally enhanced. However, the enhanced local electric fields in this so-called gap-mode TERS configuration are nominally orthogonal to the specimen plane. Therefore, the polarisability derivative tensor elements of any Raman active vibrational eigenstate must be projected along the specimen normal to be detectable via TERS. The faint TERS signals observed from two prototypical systems, pristine graphene and GO, are a typical example of the rather restrictive TERS selection rule.

Figure 7.27 shows our reflection-type AFM-Raman (TERS) system. Semiconductor lasers with excitation wavelengths of 532 and 633 nm are used.

Figure 7.28 shows a topographic AFM image, a cross-sectional topographic AFM image, a TERS image (D band) and standard Raman image (D band) of a GO flake on an Au substrate [65]. A comparison of Fig. 7.28b and the Raman spectrum of GO confirms that the GO measured here approximately consists of one layer. As shown in Fig. 7.28c, d, the intensity image of the D band obtained by TERS has a much higher spatial resolution than that obtained using a standard Raman microscope.

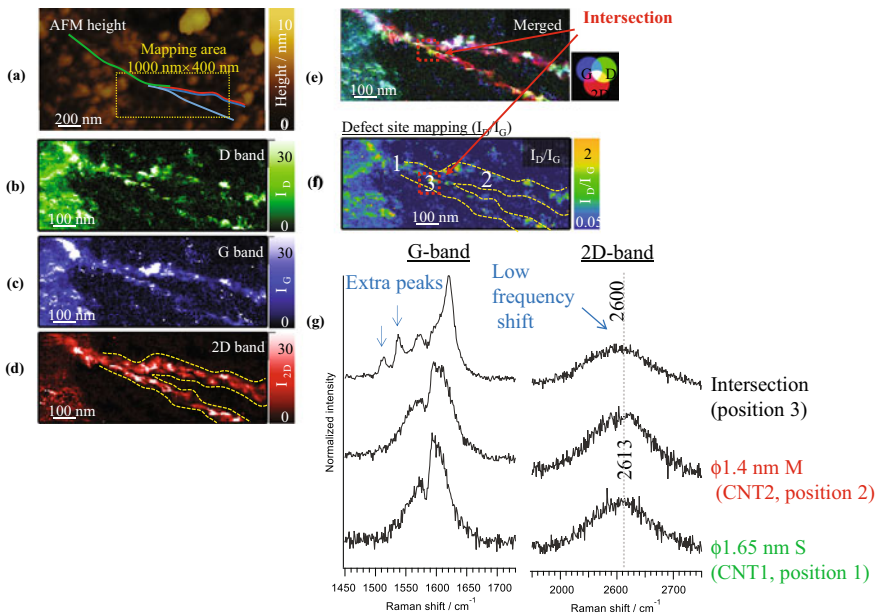


Fig. 7.26 **a** Topographic image; the intensity images of **b** D, **c** G, and **d** 2D bands ($1000\text{ nm} \times 400\text{ nm}$ square); **f** super resolved merged colour image obtained by combining the three images in **(b)**, **(c)**, and **(d)**; **f** relative intensity (I_D/I_G) image; and **g** TERS spectra of the positions 1-3 in **(f)**. Raman images were obtained using the 633 nm line of a semiconductor laser, moving the x-y piezoelectric scanner in steps of 6.6 nm [60]

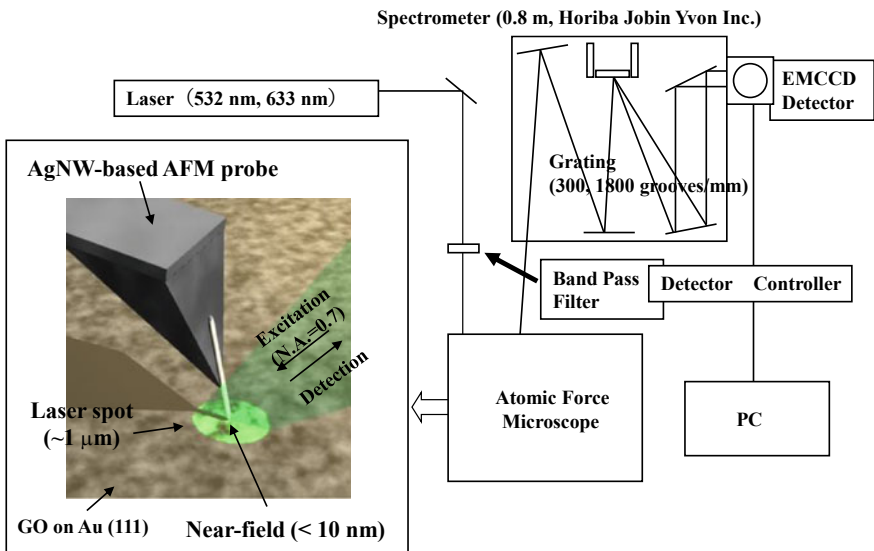


Fig. 7.27 Our reflection-type AFM-Raman (TERS) system [60]

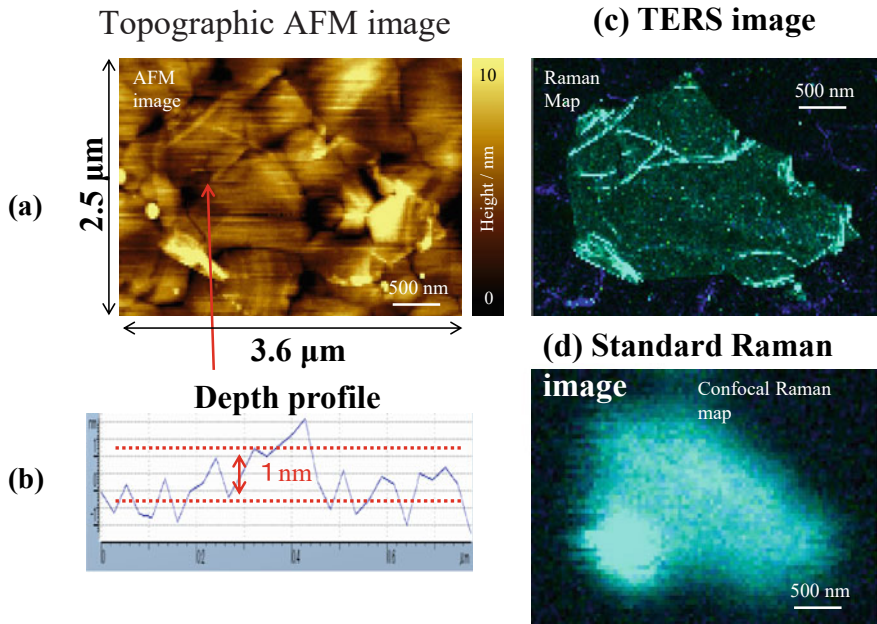


Fig. 7.28 **a** Topographic AFM image, **b** cross-sectional topographic AFM image, **c** TERS image (D band), and **d** standard Raman image (D band) of a GO flake on an Au substrate [65]

Figure 7.29a–e show absolute intensity images of the D band, the relative intensity of the D band normalised by that of the G band (I_D/I_G), and the Raman spectra of points 1 and 2, respectively [65]. Figure 7.29b shows a magnified version of the absolute intensity image in Fig. 7.29a. I_D/I_G depends on the position in the GO plane, and the C–H stretching mode at approximately 2900 cm^{-1} was observed at some positions in the GO plane. These results suggest that the GO plane consists of inhomogeneous structures. As shown in these examples, AFM-Raman spectroscopy is an outstanding technique for characterising the nanostructure of graphene, GO, and CNTs [60, 65].

7.2.2 AFM-IR Spectroscopy

The AFM-IR system overcomes the resolution limits of conventional IR spectroscopy by using the tip of an AFM probe to measure the IR absorption [66, 67]. A typical AFM-IR system is shown in Fig. 7.30. In this system, a pulsed, tuneable IR source is used to excite molecular or lattice vibrations in a thin film mounted on an ATR prism with a high refractive index. The IR beam is focused on the specimen using ATR techniques. As the specimen absorbs the radiation, its temperature increases, resulting in

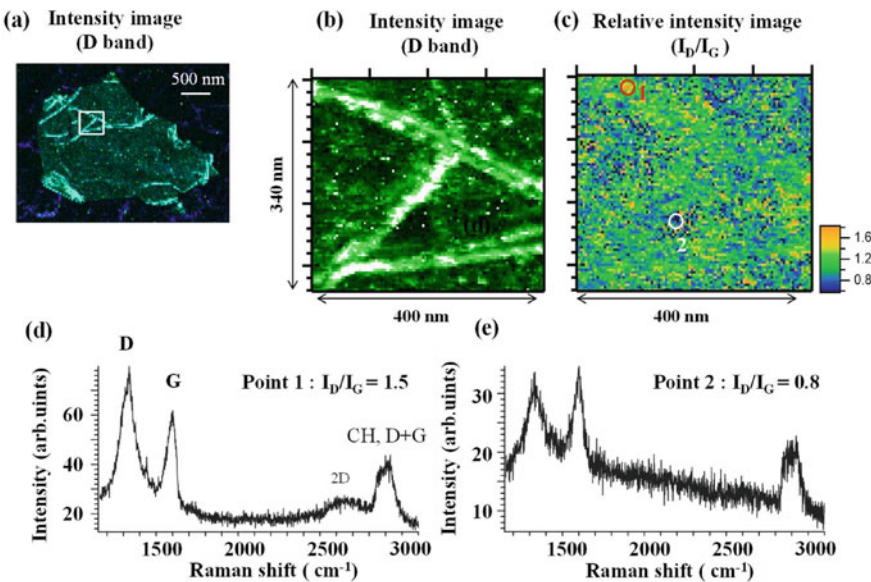


Fig. 7.29 **a** Absolute intensity image of D band, **b** magnified view of (a), **c** relative intensity image of D band normalised by that of G band (I_D/I_G), and Raman spectra of **d** point 1 and **e** point 2 [65]

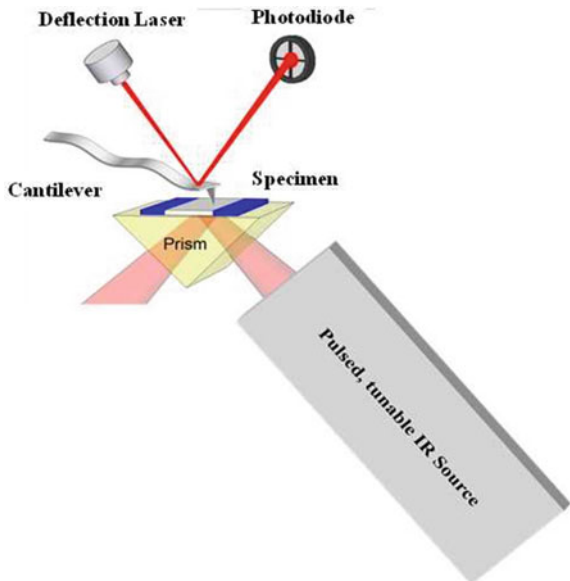
rapid thermal expansion. Consequently, resonant oscillations of the cantilever (ring-down oscillations) occur. By measuring the amplitudes of the cantilever oscillation as a function of the source wavelength, we can obtain the IR absorption spectra of the specimen, in addition to the mechanical properties and images of the surface topography.

In the AFM-IR system, an AFM-tip is used to measure the local thermal expansion resulting from the absorption of IR light. Even though the IR irradiation spot size is on the order of many microns, the thermal expansion can be spatially resolved by the AFM-tip on scales well below the optical diffraction limit. Although AFM-IR spectroscopy is used to characterise polymers and biomaterials [66, 67], there are few reports on its application to semiconductors.

Felts et al. measured the near-field absorption in heavily Si-doped InAs micro-particles using an AFM-IR system [68]. Figure 7.31a shows a schematic diagram of this system [68]. A 10 ns laser pulse from a tuneable IR laser is travelled through a ZnSe prism to irradiate the specimen. The specimen absorbs the incident IR light and undergoes rapid thermal expansion [68]. An AFM cantilever in constant contact with the specimen detects this expansion. By measuring the specimen expansion while scanning the laser wavelength, a qualitative IR absorption spectrum localised at the tip/specimen contact can be obtained [68].

Figure 7.31b depicts a topographic AFM image of the specimen, which consists of an array of heavily Si-doped InAs microparticles, with a height and diameter of 1.0 μm and a pitch of 3.4 μm [68]. The Si-doped InAs film was prepared on

Fig. 7.30 Schematic illustrating the principle of the AFM-IR technique

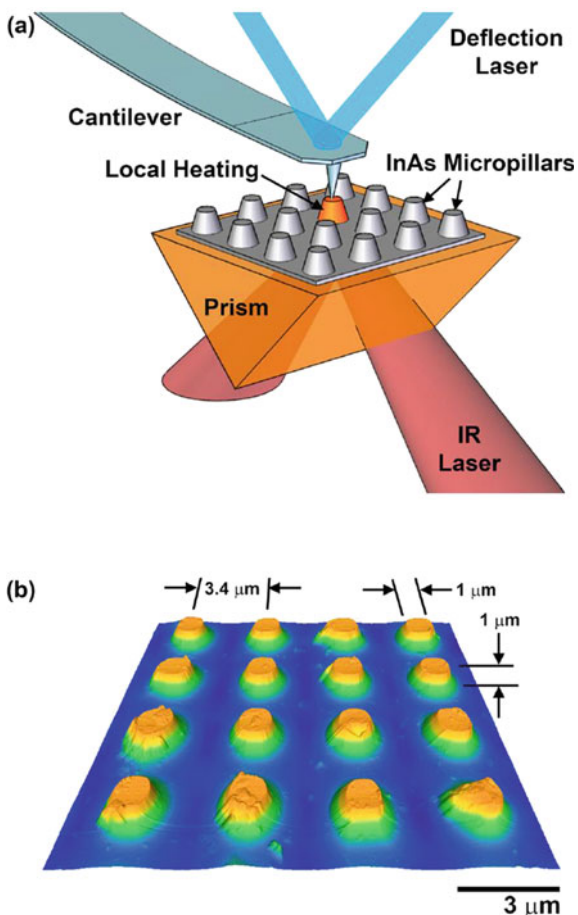


an undoped InAs buffer layer on a GaAs substrate. The films were then patterned using standard photolithographic techniques [68]. The film formation condition is explained in more detail by Ref. [68]. The microparticle film had a doping density of $9.5 \times 10^{19} \text{ cm}^{-3}$; consequently, a localised surface plasmon resonance (LSPR) appeared in the particles at $5.75 \mu\text{m}$ [69].

The AFM-IR near-field measurements were compared with far-field optical measurements. Figure 7.32 adepicts far-field transmission and reflection spectra obtained by FT-IR spectroscopy, which possess dips in both the reflection and transmission near $5.75 \mu\text{m}$ [68]. The locations of the measured peaks coincide well with predictions, although the experimental transmission is lower than predicted, owing to dislocations within the specimen [68]. The reflection-dip is slightly red-shifted and attenuated relative to the transmission-dip; this result was detected previously and assigned to the differences in absorption and scattering resonant wavelengths and the scattering solid angles [69].

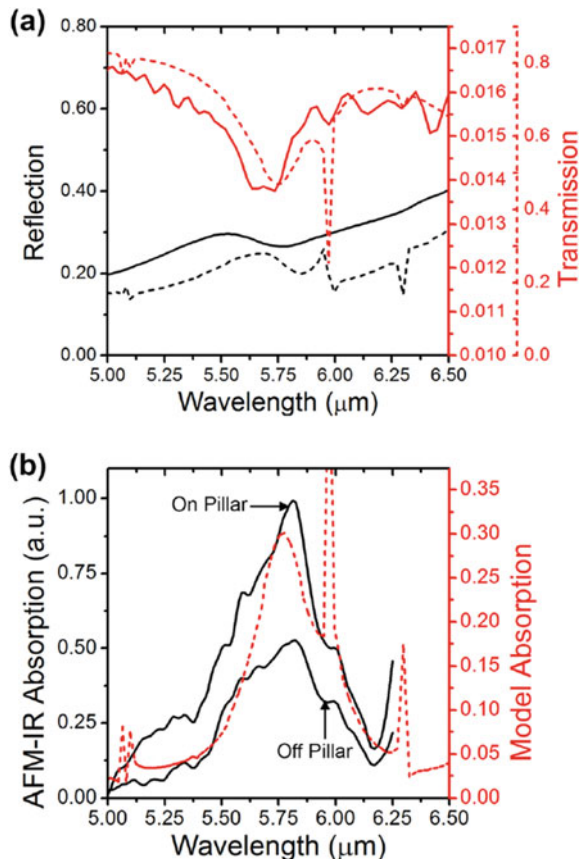
Figure 7.32b displays the AFM-IR absorption spectrum of a single InAs micro-particle, which shows a peak at $5.75 \mu\text{m}$ [68]. The absorption peak measured by the AFM-tip away from the micro-particle is much lower, suggesting that the localised heating is confined within the micro-particles [68]. The peak observed away from the micro-particle is due to pressure waves incident on the AFM-tip from nearby absorbing micro-particles [68]. To clarify this phenomenon, a 3D FEM was used to solve the Maxwell equations of the structure. The calculation result provides the microscopic field distributions across the specimen, as well as the far-field reflection and transmission spectra [68]. Their calculations indicate that the optical spectrum consists of a broad resonance near $5.75 \mu\text{m}$ overlain by a set of sharp resonances

Fig. 7.31 **a** Schematic diagram of AFM-IR absorption measurement of heavily Si-doped InAs micro-particles. **b** Topographic AFM image of an array of InAs micro-particles [68]. (Reproduced with permission from Ref. [68]. © AIP Publishing, 2013.)



[68]. Further analysis of the spatial field profile confirms that the broad resonance at $5.75\text{ }\mu\text{m}$ originates from an LSPR in a single micro-particle, whereas the sharp ‘satellite’ resonances result from the coupling of normally incident light into guided modes supported by the undoped InAs buffer layer [68]. The simulated transmission and reflection results agree well with the far-field data in Fig. 7.32a [68]. The measured transmission was much lower than the simulated transmission owing to defects in the undoped InAs buffer layer, an effect that has been observed in other research on similar materials [70]. The increase in absorption near $6.25\text{ }\mu\text{m}$ in Fig. 7.32b results from a laser stage transition, and it is not believed to be a waveguide resonance. A comparison of the simulated and measured near-field absorption in Fig. 7.32b illustrates that the measured near-field absorption peak, which is localised to the micro-particle, coincides with the simulated LSPR peak [68].

Fig. 7.32 **a** Far-field reflection (solid black) and transmission (solid red) measurements of the InAs micro-particle array, and near-field calculations (dashed lines) for a single micro-particle. **b** AFM-IR near-field absorption both on and off of a micro-particle (black line), and speculated micro-particle absorption (dashed red line) [68]. (Reproduced with permission from Ref. [68]. © AIP Publishing, 2013.)



7.2.3 Optical Photothermal IR and Raman Spectroscopy

Anasys Instruments recently developed a new optical-photothermal infrared (O-PTIR) spectroscopy combined with Raman spectrometer, which can simultaneously measure several specimens using submicron IR and Raman microscopy at a spectral resolution of less than 500 nm. This instrument uses a reflection-type AFM-IR system. Figures 7.33 and 7.34 show a photograph and schematic, respectively, of the O-PTIR spectroscopy.

In reflection-type AFM-IR spectroscopy, a material is irradiated by a pulsed tuneable IR laser and a visible (532.0 nm) laser. When molecular or lattice vibrations in a bulk material are excited by a pulsed, tuneable IR source under simultaneous irradiation by a visible semiconductor laser with a wavelength of 532.0 nm, the temperature of the material increases owing to the fundamental molecular or lattice vibrations, resulting in thermal expansion. Then the visible light with a spot size of

Fig. 7.33 Photograph of O-PTIR spectroscopy instrumentation, which includes a Raman spectrometer [71]

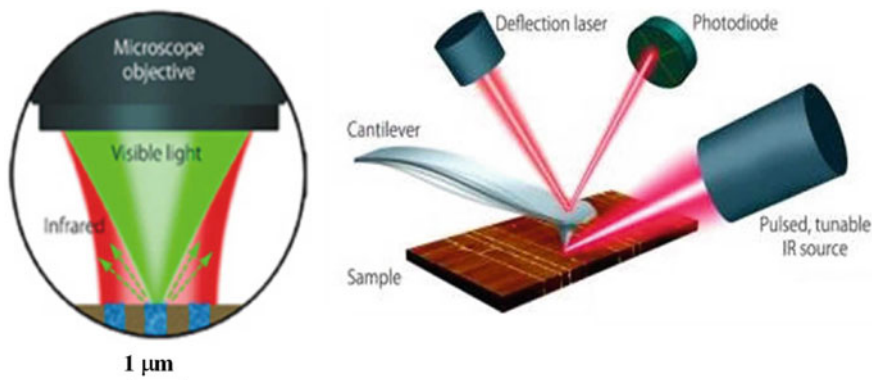
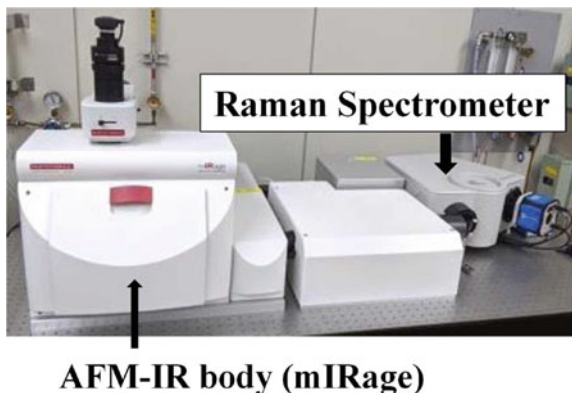


Fig. 7.34 Schematic of O-PTIR spectroscopy mechanism [71]

approximately 500 nm is reflected toward a different direction. We can measure the AFM-IR and Raman spectra of the materials by detecting changes in the direction of the visible light and Raman scattering light from them simultaneously. Unfortunately, there are few reports of applications of this instrument to semiconductors, but the characterisation of semiconductors by this method is anticipated.

Figure 7.35 shows the result of O-PTIR spectroscopy of a hydrolysed polyimide (PI) film after alkali treatment. PL films are used for various applications such as capacitors, insulation films, and printed circuit for electronic devices. First, the hydrolysed PI film was embedded in epoxy resin and then polished by a polishing machine.

The IR peaks at 1380 and 1520 cm^{-1} in Fig. 7.35c are assigned to the vibrational mode of the imide group and C = C bonding of the aromatic imide ring in PI, respectively, whereas the IR peak at 1580 cm^{-1} is attributed to the C = O bonding vibration of the hydrolysed PI. As shown in Fig. 7.35b, the intensity of the

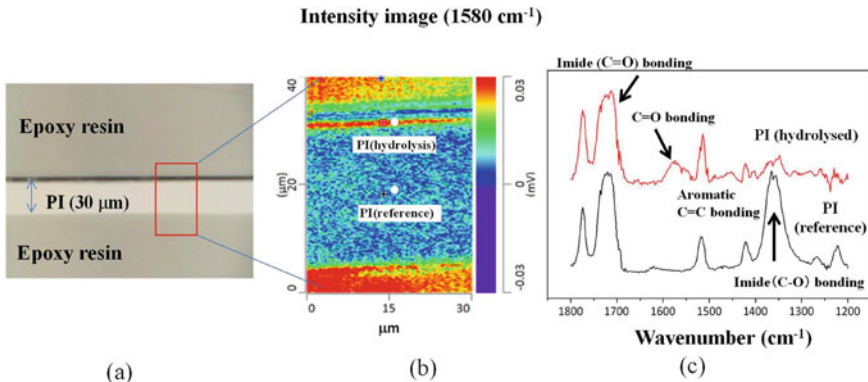


Fig. 7.35 **a** Cross-sectional photograph, **b** absolute intensity image at 1580 cm⁻¹, and **c** O-PTIR spectra of hydrolysed PI film [71]

1580 cm⁻¹ peak increases at approximately 0.1 μm position from the surface of the PI. This result shows that this area was hydrolysed by the alkali treatment. As I mentioned above, although O-PTIR spectroscopy is a superior method to simultaneously measure polymer structures with a special resolution of less than 500 nm, there are few applications for semiconductors. In the near future, I am expecting an increase in analytical applications of semiconductor devices, for example, failure analysis of semiconductor devices, using O-PTIR spectroscopy.

7.3 Terahertz Time-Domain Spectroscopy (THz-TDS)

Terahertz (THz) waves have frequencies of 0.1–10 THz, which correspond to wavelengths of 3000 to 30 μm. THz waves are non-destructive and penetrate many materials to penetration depths greater than those of microwave radiation [72]. THz radiation is very sensitive to various types of resonances, such as vibrational, translational, rotational, torsional, and conformational states; thus, it can provide information on molecules or semiconductors that cannot be obtained using other analytical and imaging techniques [72]. These unique characteristics make it suitable for identifying, analysing, or imaging various materials. Unlike the case for Raman and IR spectroscopy, techniques for generating, manipulating, and detecting THz radiation are still being developed [72]. Although THz time-domain spectroscopy (TDS) has an excellent potential, it has fewer applications at present, especially applications to semiconductors, than Raman and IR spectroscopy.

A THz-TDS system consists of a laser, an emitter, a detector, and a delay device. Specifically, THz-TDS requires the generation of an ultrafast (and thus high-bandwidth) THz pulse from an even faster femtosecond optical pulse, typically from a Ti:sapphire laser [72].

Figure 7.36 shows a schematic of our experimental setup for a THz-TDS system. A mode-locked amplified Ti: sapphire laser ($\lambda = 800$ nm) produces ~ 130 fs pulses at a repetition rate of 1 kHz. The laser beam is divided into a pump and a probe. The pump beam is focused on a ZnTe crystal. The generated THz radiation is collimated and focused on a specimen by a pair of off-axis parabolic mirrors. The THz radiation transmitted through the specimen is collimated and focused again on a detector by a second pair of off-axis parabolic mirrors. Another ZnTe crystal is used in an electro-optic (EO) sampling setup for the detection of THz radiation. The temporal profile of the THz field is obtained by varying the delay between the pump and probe pulses.

There have been a few reports on characterisation of semiconductors by THz spectroscopy until now: for example, characterisation of the complex electric conductivity and dielectric response of GaN [73].

Zhang et al. performed the characterisation of the complex electric conductivity and dielectric response of a GaN freestanding crystal (180- μm thick) at frequencies of 0.1 to 4.0 THz using THz-TDS [73]. The complex spectrum of the transmitted pulse, $E_0(\omega)$, is obtained by taking the product of the input spectrum $E_i(\omega)$ and the total transmission function of the specimen [73]:

$$E_0(\omega) = E_i(\omega) \frac{t_{12}t_{21} \exp(ikL) \exp(-\alpha L/2)}{1 + r_{12}r_{21} \exp(-\alpha L) \exp(i2kL)} \quad (7.2)$$

where $E_i(\omega) = E_R(\omega) \exp(-ik_0L)$ ($E_R(\omega)$ is the reference spectrum, and the phase correction k_0L accounts for the free space occupied by the specimen); t_{12} , t_{21} and r_{12} , r_{21} are the frequency-dependent complex Fresnel transmission and reflection coefficients, respectively; α is the power absorption coefficient; k is the specimen wave vector ($k = 2\pi n/\lambda_0$), and L is the specimen thickness. Consequently, the total

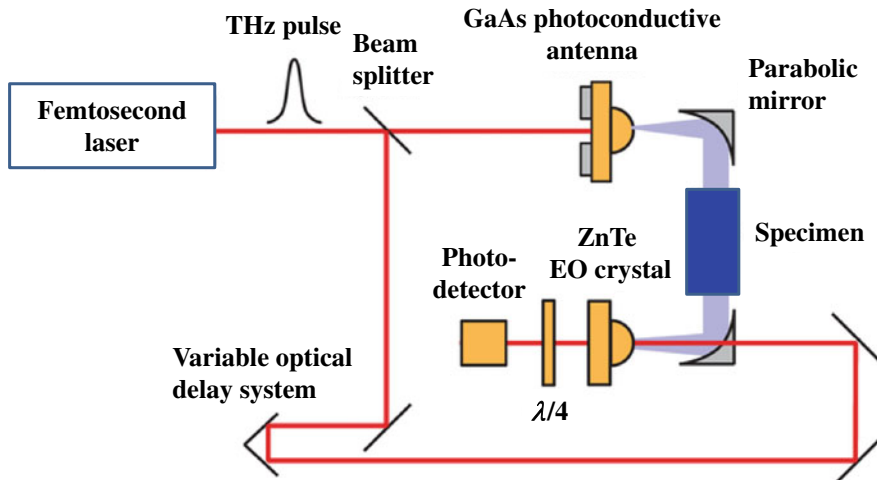


Fig. 7.36 Schematic of our THz-TDS system [72]

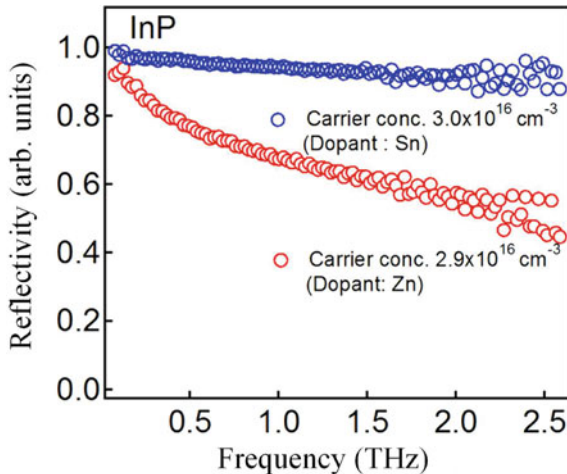


Fig. 7.37 Reflectivity of Sn or Zn doped InP wafers with carrier concentrations of $3.0 \times 10^{16} \text{ cm}^{-3}$ and $2.9 \times 10^{16} \text{ cm}^{-3}$

reflectivity function of the specimen is obtained as follows;

$$R(\omega) = 1 - \frac{E_0(\omega)}{E_i(\omega)} \quad (7.3)$$

We measured terahertz spectra of Sn or Zn doped InP wafers with carrier concentrations of $3.0 \times 10^{16} \text{ cm}^{-3}$ and $2.9 \times 10^{16} \text{ cm}^{-3}$, and calculated the reflectivity of these wafers [74]. Figure 7.37 indicated the reflectivity of two InP wafers. As seen in Fig. 7.37, the reflectivity of the InP wafer with a carrier concentration of $2.9 \times 10^{16} \text{ cm}^{-3}$ is dramatically lower than that of the wafer with a carrier concentration of $3.0 \times 10^{16} \text{ cm}^{-3}$. The different reflectivity of two specimens is mainly caused by a difference of mobilities between two dopant ions in the InP wafers. This result indicates that terahertz spectroscopy is an important technique to characterise the electronic property of carriers of semiconductors.

Although it is a useful technique for inspecting drugs, toxic materials, and medicines with various polytypes *in situ* and non-destructively at airports worldwide, there are only a few applications of semiconductors, using THz spectroscopy. I expect its spectroscopic applications to increase when problems such as low sensitivity, low spatial resolution, and the high cost of the instrument are solved.

7.4 SIMS-OES/-CL Spectroscopy

When a solid specimen is sputtered by the primary ions of a low-keV energy, a fraction of the particles emitted from the target is ionised. The ions generated by

this process form the secondary beam and are subsequently transmitted within a continuous high vacuum environment to a mass spectrometer. Secondary Ion Mass Spectrometry (SIMS) gives us some information about the elemental, isotopic, and molecular composition of its uppermost atomic layers, by analysing these secondary ions with a mass spectrometer. Secondary ions emitted from a solid surface under primary ion bombardment supply information about the elemental, isotopic, and molecular composition of its uppermost atomic layers.

On the other hand, optical emission spectrometry (OES) involves applying electrical energy in the form of a spark generated between an electrode and a metal, whereby the vaporised atoms are brought to a high-energy state within a discharged plasma. Then, these excited atoms and ions in the discharged plasma yield a unique emission spectrum specific to each element. Thus, a single element generates numerous characteristic emission spectral lines. When we irradiated the primary ions of a low-keV energy on an Si wafer, using an SIMS instrument attached to a spectrometer, we found the emission spectrum ascribed to Si in the SIMS chamber. We called this apparatus “SIMS-OES” [75].

After this observation, we noticed that with the irradiation of accelerated ions to the specimen surface in a vacuum, atoms on and in the vicinity of the specimen surface were stirred, with some of them released into the vacuum (sputtering phenomenon) yielding an atomic emission that was discovered in the 1970s and named surface composition by analysis neutral and ion impact radiation (SCANIIR) [76].

Figure 7.38 shows a schematic for SIMS-OES. The SIMS-OES apparatus consists of SIMS optics, an electronic spray gun that neutralises an ionic charge of a specimen caused by the ion irradiation, and a spectrometer.

Figure 7.39 shows the observation results of a light-emitting state when primary ions were irradiated on the solid specimen surface. The photograph shows a light-emitting state when O_2^+ ions were irradiated on an AlGaInP specimen by 5 keV and 100 nA in vertical direction from the ion source in SIMS4550 of CAMECA. It is a photograph taken with 5 min of exposure time, using a digital camera, and taken within the equipment.

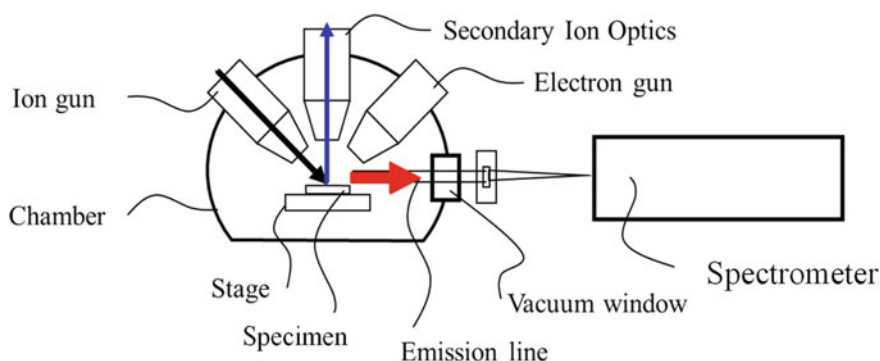


Fig. 7.38 Schematic for SIMS-OES [75]

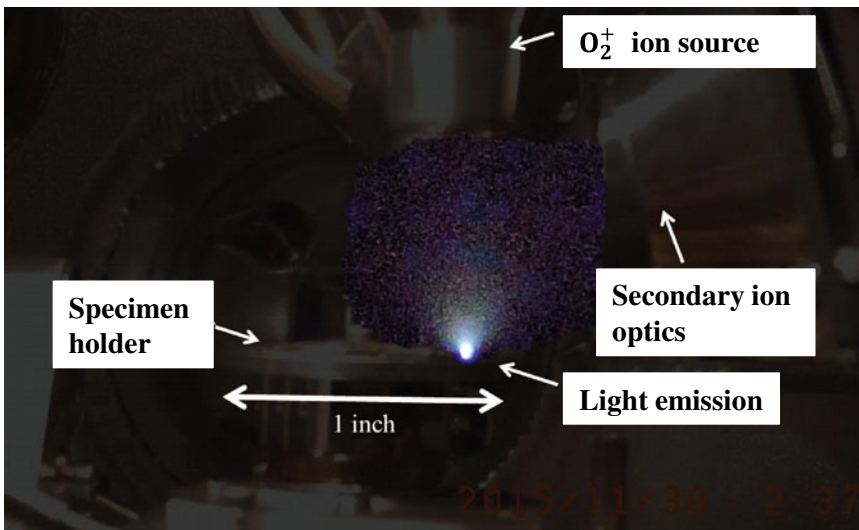


Fig. 7.39 Optical photograph of light-emitting state when O_2^+ ions were irradiated on an AlGaInP specimen by 5 keV and 100 nA in the vertical direction from the ion source in SIMS4550 of CAMECA [75]

Figure 7.40 depicts an emission spectrum of AlGaInP obtained by using the established system. It is possible to identify atomic emission lines of the constituent elements, i.e., Al, Ga, and In. This equipment makes it possible to monitor secondary ions based on SIMS and atomic emission, simultaneously, and is called SIMS-OES (Optical Emission Spectrometry) [75]

The optical system we developed was designed by suppressing the chromatic aberration within the wavelength region from 120 to 800 nm as much as possible. Therefore, it is impossible to observe atomic emission spectrum of some of the elements in a vacuum ultraviolet region of 120 nm or less. It is impossible to observe P of AlGaInP because of the impact. If it becomes possible to measure the composition quantitatively based on atomic emission spectrum with this equipment, a new analytical approach in combination with impurity analysis based on SIMS will also become available.

Figure 7.41 shows the result of measuring quantity using this formula for laminate structure specimens with different InAlGaP compositions. Thin film laminate specimens, in which the composition ratio of Al and Ga differs in each layer, were adopted for analysis, presented by Ref. [76]. As seen in Fig. 7.41, this result shows a significantly better consistency with a given Al/Ga ratio in the upper and lower layers in the three-layer construction. SIMS-OES is a useful technique for analysing the composition of Al and Ga by using the atomic emission intensity [75].

In the SIMS system, the electron spray gun is used to neutralise the ionic charge of a specimen caused by ion irradiation. Using the electron spray gun, we can acquire

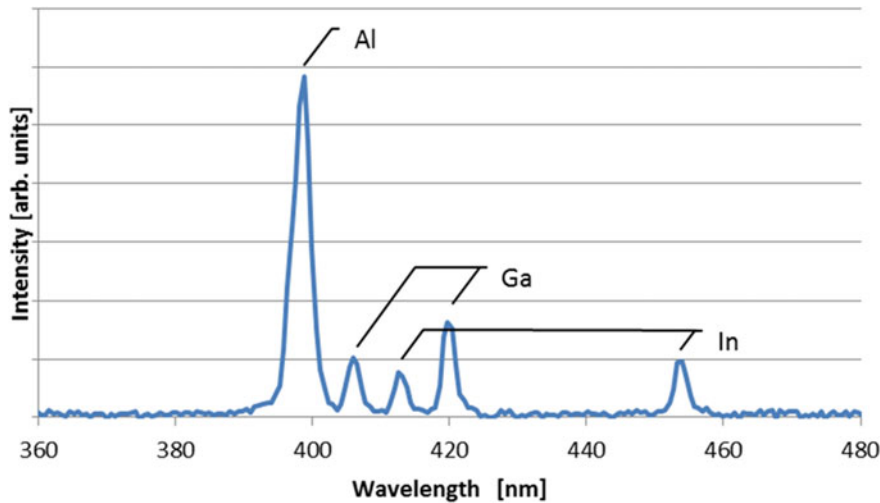


Fig. 7.40 Emission spectrum of AlGaInP, obtained by using the SIMS-OES system [75]

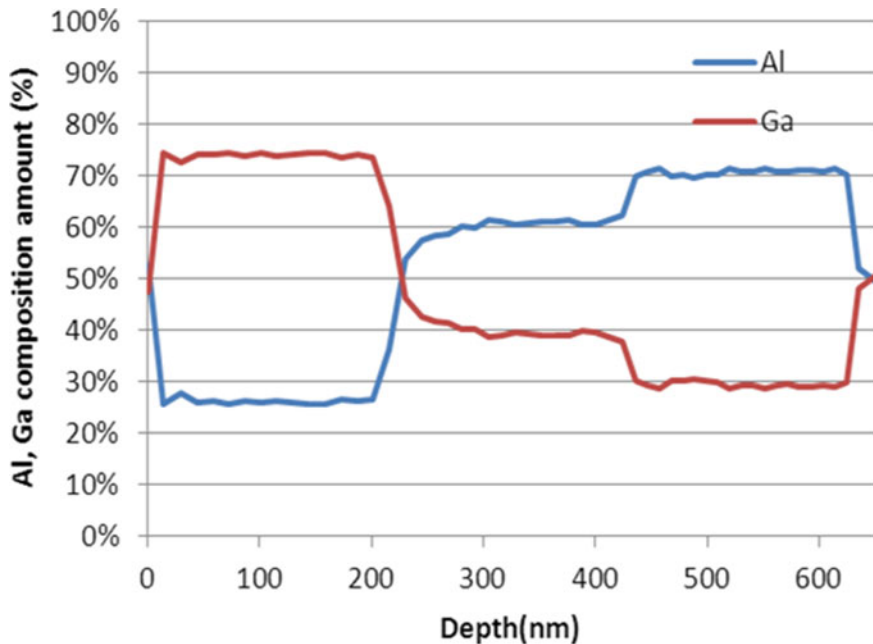


Fig. 7.41 Depth profile of InAlGaP by SIMS-OES. Layer structure of specimen is In $(\text{Al}_{0.25}\text{Ga}_{0.75})\text{P}$ /In $(\text{Al}_{0.50}\text{Ga}_{0.50})\text{P}$ /In $(\text{Al}_{0.70}\text{Ga}_{0.30})\text{P}$ /GaAs substrate (Al/Ga ratio is designed value) [75]

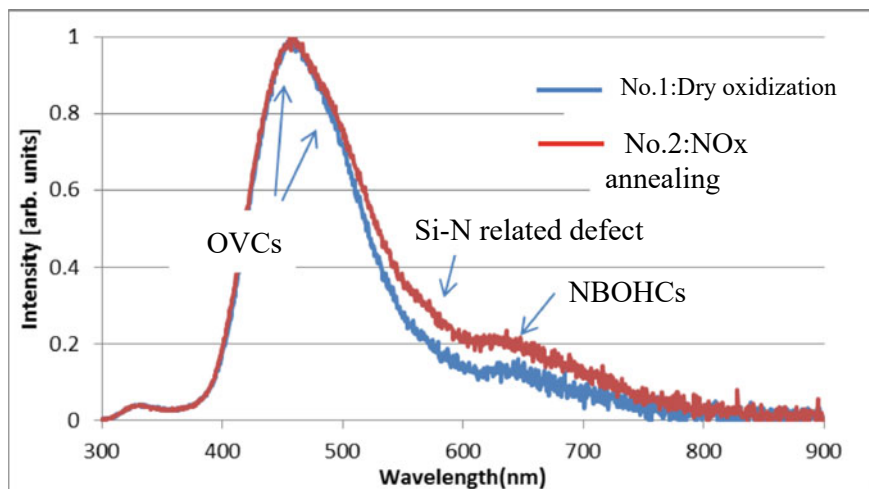


Fig. 7.42 CL spectra of SiO_2 films (specimens No. 1 and 2) measured at a low acceleration voltage of 500 V [75]

CL spectra of the same position at the same time, measuring the SIMS depth profiling of a specimen.

Figure 7.42 depicts the CL spectra of SiO_2 films (specimens No. 1 and 2) measured at a low acceleration voltage of 500 V. Specimens No. 1 and 2 correspond to the SiO_2 films (40-nm thick) on a 4H-SiC epitaxial substrate, which were made by dry oxidation and annealed in ambient N_2O , respectively. The CL peaks at 460 and 490 nm are attributed to OVCs, whereas the CL peaks at 600 nm and 670 nm are attributed to the Si–N bonding structures and non-bridging oxidation hole centres (NBOHCs) [77–79]. As seen in Fig. 7.42, the CL peak at 580 nm, related to the Si–N bonding structures in No. 2, becomes stronger than that in No. 1. As discussed in Sect. 5.7.2, this result suggested that more dangling bonds at the SiO_2/SiC interface in No. 2 were terminated by the N atom than those in No. 1 [75].

7.5 Time-Resolved CL Spectroscopy

Up to now, time-resolved cathodoluminescence (TR-CL) has been developed to provide quantitative information on the transfer/recombination dynamics of free, donor-bound, and basal stacking fault (BSF)-bound excitons in semiconductors, but it has not been successful in sufficiently characterising nanomaterials with a spatial

resolution at the nanometre level. Picosecond and femtosecond spectroscopy give detailed information about carrier dynamics in nanomaterials [80–82].

There are two types of methods that generate electron-gun pulses: one method is to use a commercial beam blanker, and the other is to use a photocathode plate. Moerland et al. used commercial hardware in a standard SEM and developed a pulse electron gun that generated electron pulses of 80–90 ps through beam blanking [83]. Meanwhile, Merano et al. used the classical hairpin tungsten electron gun of a SEM with an Au photocathode plate and generated a pulsed electron beam by illuminating the photocathode by an UV mode-locked laser [84].

TR-CL spectroscopy possesses several characteristics. The multimode image by CL spectroscopy enables the correlation between optical properties (via CL) and surface morphology (secondary electron image) at the nanometre level. The broad energy range of the electrons can excite wide-bandgap materials, such as diamond-, GaN-, InGaAs/AlGaAs pyramidal quantum structures, and Yttrium-Aluminum-Garnet (YAG) structures without damage caused by electron irradiation [81–84].

Figure 7.43 depicts the setup of Moerland et al. [83]. They used a commercially available blanker which is inserted into the column of an FEI Quanta FEG 200 SEM. Their apparatus features electron pulses of 80–90 ps, generated through beam blanking, which permits probing emitters within a large range of decay rates and a resolution better than $\lambda /10$ [83].

On the other hand, Merano et al. [84] have replaced the classical hairpin tungsten electron gun of a JEOL 6360 SEM (Fig. 7.44a) with a 20-nm-thick Au photocathode deposited on a quartz plate. By irradiating the photocathode with an UV mode-locked laser (266 nm in wavelength, 200 fs, 80.7 MHz repetition rate, spot size of 3 μm), they generated a pulsed electron beam, brilliant enough (average brightness of $2 \times 10^3 \text{ Acm}^{-2} \text{ steradians}^{-1}$, 1–100 pA at the specimen surface) to acquire secondary electron images. A streak camera mounted behind a monochromator (spectral resolution better than 200 meV) was utilised as a time-resolved detector [84]. A liquid N₂ cryostat was used to cool the specimen to 90 K. As can be seen in Fig. 7.44b, the observation of a specimen made of Au particles deposited on an amorphous carbon (a-C) film believed that this remodelled SEM has a spatial resolution of less than 50 nm [84].

From the rising time of the signal in Fig. 7.44c, the temporal resolution of the electron pulse was estimated to be approximately 10 ps [84]. The average number of electrons per pulse is generally lower than ten.

Merano et al. measured the TR-CL spectra of the InGaAs/AlGaAs pyramidal quantum dot (QD) structure, using their TR-CL system [84]. The specimens were prepared on a GaAs substrate by a low-pressure organometallic CVD [84]. The growth process gives rise to the formation of different nano-structures, as illustrated in Fig. 7.45. All measurements were conducted at 90 K and with an acceleration voltage of 10 kV [84].

The TR-CL spectrum of a single pyramid (obtained with a pulsed excitation and with a time integrated detection) and TR-CL images taken at energies that match the different recombination channels are shown in Fig. 7.46 [84]. The several peaks in the spectrum were attributed based on Ref. [85]. The TR-CL images in Fig. 7.46 relative

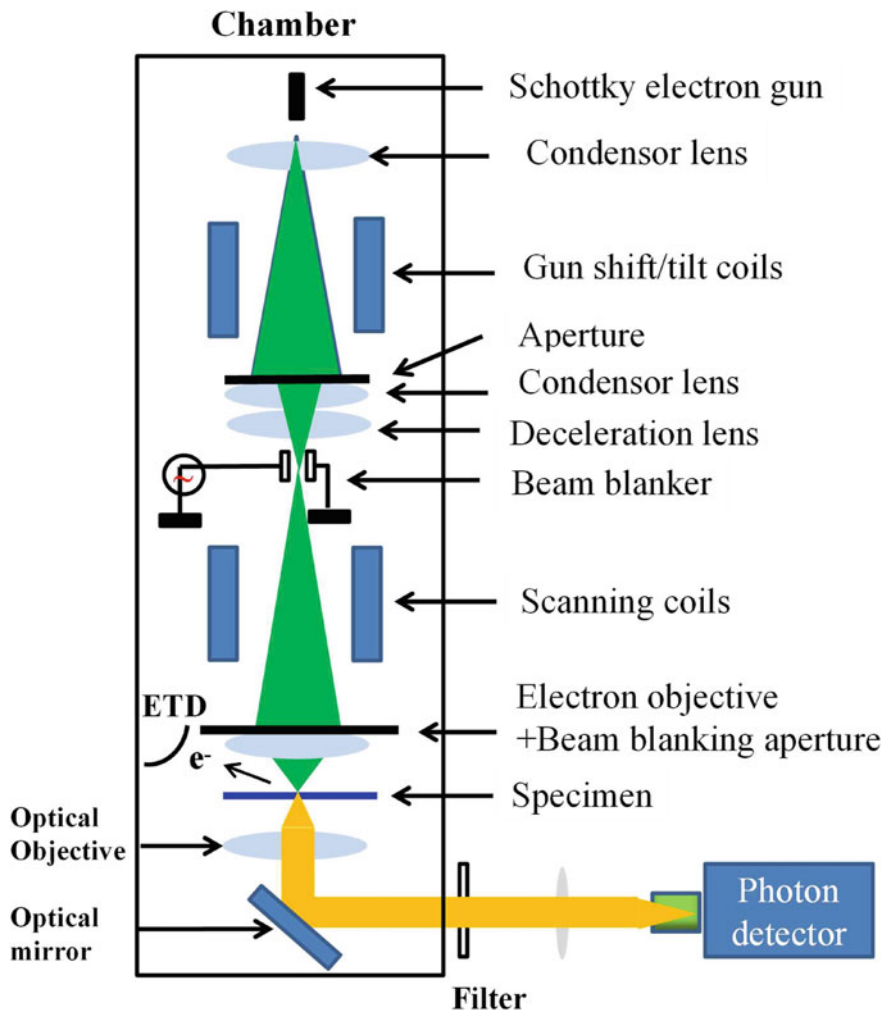


Fig. 7.43 Schematic diagram of beam blanking typed TR-CL

to QDs, quantum wires (QWRs), and vertical quantum wires (VQWRs) shown in Fig. 7.45 cannot be directly connected to the nano-structure location at the origin of the CL signal [84]. They found that the CL pattern spans the entire pyramid. This suggests that the carriers generated at any point on the pyramid diffuse towards the dot [84]. One of the important advantages of TR-CL is to clarify the specificities of the carrier transport [84].

GaN is one of the most important candidates for the emission of visible to UV light by optoelectronic devices, as introduced in more detail in Sect. 5.6 [86]. The presence in heterostructures of high built-in electric fields along the c -axis [87] increases the number of non-radiative centres at room temperature [88]. The growing

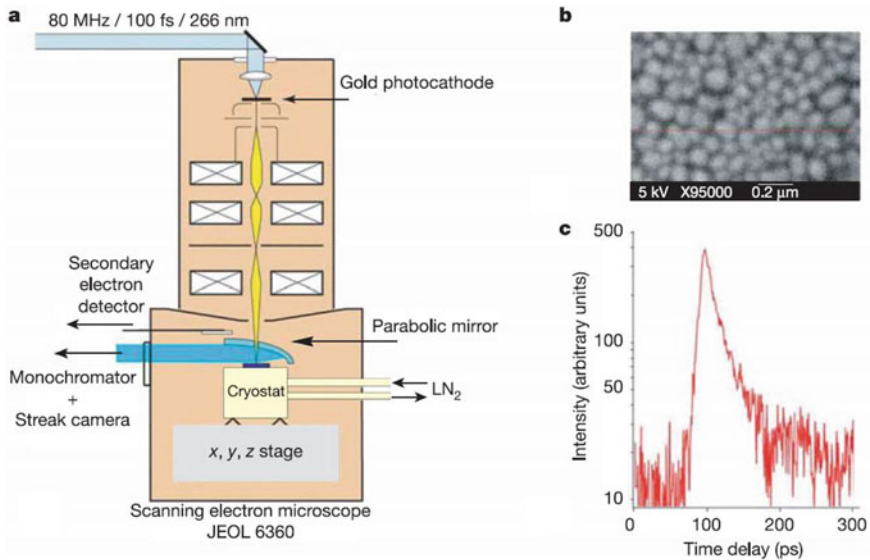


Fig. 7.44 TR-CL system developed by Merano et al. **a** Schematic of their TR-CL system. **b** SEM image of Au nanoparticles deposited on an a-C film. **c** TR spectrum of a GaN specimen at room temperature [84]. (Reproduced with permission from Ref. [84]. © Springer Nature, 2005.)

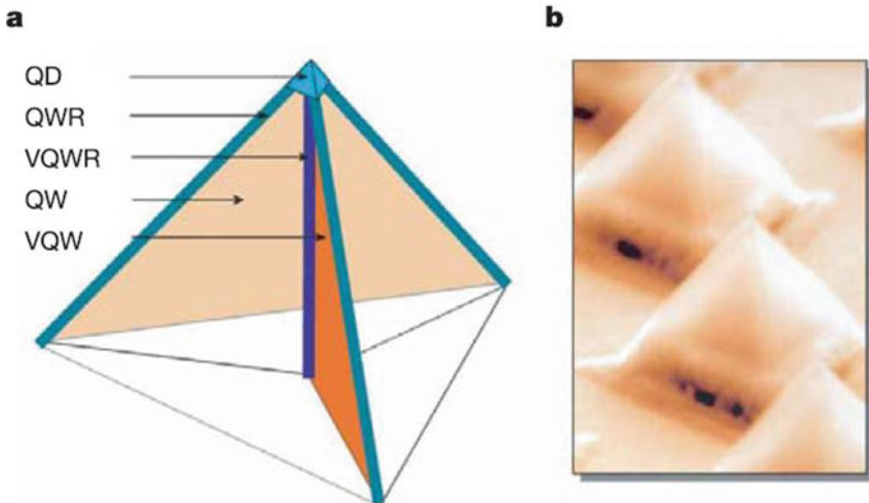


Fig. 7.45 InGaAs/AlGaAs pyramidal quantum structures. **a** schematic of the five heterostructures in an InGaAs/AlGaAs pyramid (the AlGaAs cap layer), an InGaAs quantum dot (QD; approximately 30 nm in lateral size) connected to several types of low-dimensional barriers: three InGaAs quantum wires (QWRs) on the pyramid edges, three InGaAs quantum wells (QWs) on the pyramid faces, and three vertical quantum wells (VQWs), with a vertical quantum wire (VQWR) located at the intersection of the VQWs. **b** The pyramid SEM image (the tops of the pyramids are separated by 5 μm) [84]. (Reproduced with permission from Ref. [84]. © Springer Nature, 2005.)

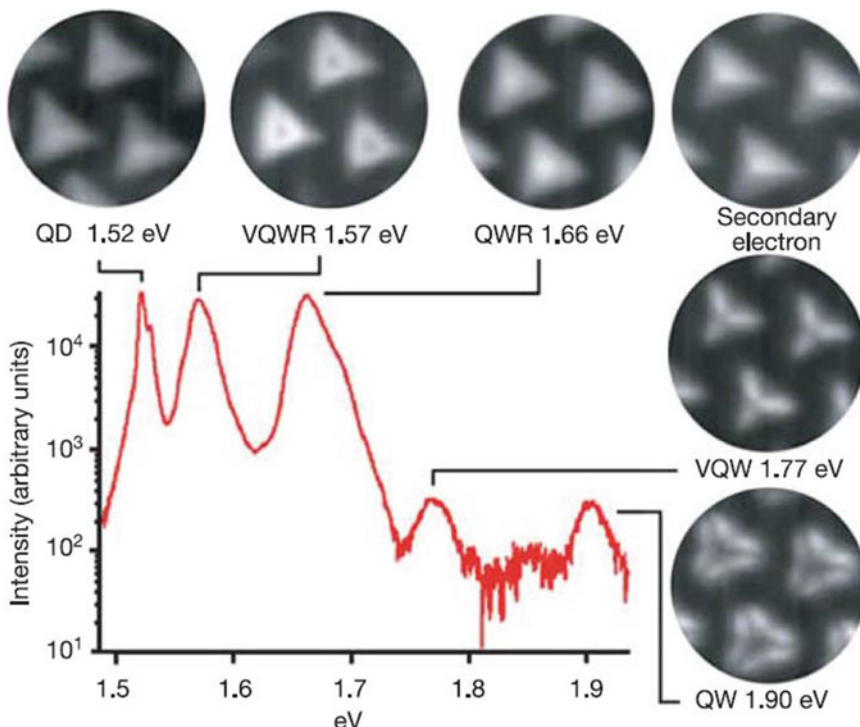


Fig. 7.46 CL spectrum and images at each energy position originating from the pyramidal structures. The CL spectrum depicts five peaks equivalent to the five main structures in the pyramid [84]. (Reproduced with permission from Ref. [84]. © Springer Nature, 2005.)

of nitride heterostructures along the a -axis, which corresponds to a nonpolar direction perpendicular to the c -axis, is one of the approaches to overcome the quantum-confined Stark effect [89] and to increase the radiative efficiency of GaN-related devices. Hence, the growing of a -plane GaN with high quality is difficult and causes high densities of extended defects [90–92]. Particularly, basal stacking faults (BSFs) produce extended defects with optical activity [93–97]. They are considered narrow (a few atomic monolayers) type-II QWs made of cubic-like GaN surrounded by wurtzite GaN barriers. Lately, CL studies on epitaxial lateral overgrowth (ELO) a -plane GaN have indicated that I_1 -type BSFs tend to gather into dense bundles, resulting in position-dependent morphologies [97].

Several groups have reported on the fabrication of a -plane GaN templates using the ELO technique with improved surface morphology and material quality in the two types of so-called “wing” areas that grow along the $+c$ (Ga-face) and $-c$ (N-face) directions [97]. Corfdir et al. measured picosecond-TR-CL spectra of a -plane GaN grown by ELO at 27 K [97]. They investigated the relaxation and recombination mechanisms of excitons (free or bound to neutral donors or bound to I_1 -type BSFs) correlated to the local density in BSFs in more detail [97].

Figure 7.47a depicts time-integrated CL spectra of the specimen studied by Corfdir et al. [97]. Beyond Ref. [96], the higher CL lies at 3.471 eV and is assigned to the recombination of donor-bound excitons (D^0X), while the 3.417 eV transition arises from the recombination of excitons bound to the so-called I_1 basal stacking faults (BSFs) [97]. I_1 -type BSFs consist of the stacking sequences: if the fault starts on a Bb layer, the stacking sequence is then ... $AaBbAaBbCcBbCcBbAaBb$ The CL peak ascribed to free exciton A (FX) on the high energy side of D^0X was observed at 3.478 eV [97]. Figure 7.47b displays the top-view time-integrated CL image of the ELO GaN epitaxial layer at $T = 27$ K, measured at the CL energy position of I_1 -BSFs [97]. Despite of the higher density in BSF in the $-c$ wings, the BSF emission in these areas was weak, related to high local densities of non-radiative defects dominating the recombination mechanisms [97]. They found the difference between the images in the $+c$ wings of the bright bundles and the diluted zones. In the diluted zones, the CL spectrum, and dynamics (Fig. 7.47a, c) remain absolutely unchanged in terms of the distance of a few hundred nanometres to several micrometres, that is, the distance between the excitation spot and the nearest bundle [97]. Particularly, the rising times of the CL peak at 3.417 eV ascribed to the donor- and BSF-bound excitons depend very little on this distance. This result suggests that BSFs are homogeneously present in those areas [97].

Furthermore, Corfdir et al. proposed a one-dimensional diffusion model for excitons along the c -axis, i.e., perpendicular to the BSF planes, and examined in detail the mechanisms of exciton relaxation and recombination involving BSFs in an a -plane GaN epitaxial layer grown by the ELO method, using the low-temperature picosecond TR-CL technique [97]. Finally, Corfdir et al. concluded that the BSFs exhibited two types of spatial distributions. In the areas where they are diluted, the relaxation of excitons toward them, at $T = 27$ K, affects the donors via a type of

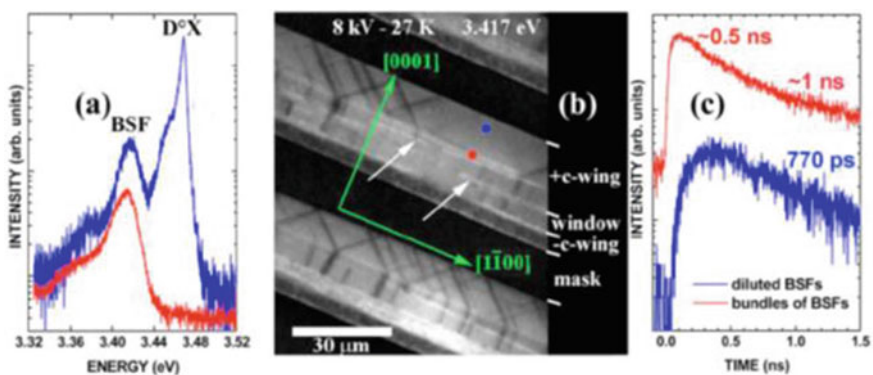


Fig. 7.47 Blue and red curves correspond, respectively, to CL spectra, away from bundles of BSFs, as illustrated in (b), by a blue and red dot. **a** Time-integrated CL spectra (upper curve is blue). **b** Top-view CL image at 3.417 eV. White arrows depict the occurrence of bundles of BSFs. **c** Time decays of the 3.417 eV CL peak (upper curve is red) [97]. (Reproduced with permission from Ref. [97]. © AIP Publishing, 2009.)

hopping process [97]. In the areas in which they are concentrated into bundles, the exciton relaxation is much faster but not instantaneous. The CL decay dynamics related to BSFs were also found to be different, being dependent on whether the excitation area is small or has a high density of BSFs [97].

As described above, TR-CL allows us to study the carrier dynamics inside the nanostructures of semiconductors and obtain precise knowledge of the photoexcited carrier path toward the lower-energy state at the tip of the pyramid. Furthermore, TR-CL can yield information about soft and bio-materials avoiding damage caused by electron irradiation. I expect that TR-CL will be used as a tool to measure efficacy of medicine, for example, a drug enclosed into a drug delivery system (DDS), such as ribosome, throughout the human body.

References

1. Renucci, J. B., Tyte, R. N., & Cardona, M. (1975). Resonant Raman scattering in silicon. *Physical Review B*, *11*, 3885.
2. Yoshikawa, M., Murakami, M., Matsuda, K., Sugie, R., Ishida, H., & Shimizu, R. (2006). Stress characterization of Si by a scanning Near-field optical Raman microscope with spatial resolution and with penetration depth at the nanometer level, using resonant Raman scattering. *Japanese Journal of Applied Physics*, *45*, L486.
3. Yoshikawa, M., & Murakami, M. (2006). Stress characterization of Si by near-field raman microscope using resonant scattering. *Applied Spectroscopy*, *60*, 479.
4. Yoshikawa, M., Murakami, M., & Ishida, H. (2007). Characterization of Si nanostructures using a noncontact mode scanning near-field optical Raman microscope, with 100 nm spatial resolution and 5 nm depth resolution, using ultraviolet resonant Raman scattering. *Applied Physics Letters*, *91*, 131908.
5. Yoshikawa, M., Murakami, M., & Ishida, H. (2008). Highly sensitive detection of near-field Raman scattered light from strained Si/SiGe heterostructures by scanning near-field optical Raman microscope using ultraviolet resonant Raman scattering. *Applied Physics Letters*, *92*, 091903.
6. Holtz, M., Duncan, W. M., Zollner, S., & Lie, R. (2000). Visible and ultraviolet Raman scattering studies of $\text{Si}_{1-x}\text{Ge}_x$ alloys. *Journal of Applied Physics*, *88*, 2523.
7. Yoshikawa, M., (unpublished).
8. Yoshikawa, M., Iwagami, K., Morita, N., Matsunobe, T., & Ishida, H. (1997). Characterization of fluorine-doped silicon dioxide film by Raman spectroscopy. *Thin Solid Films*, *310*, 167.
9. Yoshikawa, M. (2018). Infrared spectroscopy and Raman spectroscopy of semiconductor. In *Encyclopedia of analytical chemistry*. John Wiley & Sons, Ltd.
10. Klein, M. V., Ganguly, B. N., & Colwell, P. J. (1972). Theoretical and experimental study of Raman scattering from coupled LO-phonon-plasmon modes in silicon carbide. *Physical Review B*, *6*, 2380.
11. Klein, M. V. (1982). In M. Cardona (Eds.), *Light scattering in solids I*, (vol. 147). Springer-Verlag.
12. Kumar, N., Mignuzzi, S., & Roy, W. S. D. (2015). Tip-enhanced Raman spectroscopy: Principles and applications. *EPJ Techniques and Instrumentation*, *2*(9), 1–23.
13. Blum, C., Opilik, L., Atkin, J. M., Braun, K., Kammer, S. B., & Kravtsov, V. (2014). Tip-enhanced Raman spectroscopy—an interlaboratory reproducibility and comparison study. *Journal of Raman Spectroscopy*, *45*, 22–31.
14. Zhang, R., Zhang, Y., Dong, Z. C., Jiang, S., Zhang, C., & Chen, L. G. (2013). Chemical mapping of a single molecule by Plasmon-enhanced Raman scattering. *Nature*, *498*, 82–86.

15. Najjar, S., Talaga, D., Schue, L., Coffinier, Y., Szunerits, S., & Boukherroub, R. (2014). Tip-enhanced Raman spectroscopy of combed double-stranded DNA bundles. *Journal of Physical Chemistry C*, *118*, 1174–1181.
16. Wang, X., Zhang, D., Braun, K., Egelhaaf, H. J., Brabec, C. J., & Meixner, A. J. (2010). High-resolution spectroscopic mapping of the chemical contrast from nanometer domains in P3HT: PCBM organic blend films for solar-cell applications. *Advanced Functional Materials*, *20*, 492–499.
17. Van Schrojenstein Lantman, E. M., Deckert-Gaudig, T., Mank, A. J. G., Deckert, V., Weckhuysen, B. M. (2012). Catalytic processes monitored at the nanoscale with tip-enhanced Raman spectroscopy. *Nature Nanotechnology*, *7*, 583–586.
18. Lee, N., Hartschuh, R. D., Mehtani, D., Kisliuk, A., Maguire, J. F., & Green, M. (2007). High contrast scanning nano-Raman spectroscopy of silicon. *Journal of Raman Spectroscopy*, *38*, 789–796.
19. Okuno, Y., Saito, Y., Kawata, S., & Verma, P. (2013). Tip-enhanced Raman investigation of extremely localized semiconductor-to-metal transition of a carbon nanotube. *Physical Review Letters*, *111*, 216101.
20. Su, W., & Roy, D. (2013). Visualizing graphene edges using tip-enhanced Raman spectroscopy. *Journal of Vacuum Science and Technology B*, *31*, 041808.
21. Richards, D., Milner, R. G., Huang, F., & Festy, F. (2003). Tip-enhanced Raman microscopy: Practicalities and limitations. *Journal of Raman Spectroscopy*, *34*, 663–667.
22. Hayazawa, N., Watanabe, H., Saito, Y., & Kawata, S. (2006). Towards atomic site-selective sensitivity in tip-enhanced Raman spectroscopy. *The Journal of Chemical Physics*, *125*, 244706.
23. Asghari-Khiavi, M., Wood, B. R., Hojati-Talemi, P., Downes, A., McNaughton, D., & Mechler, A. (2012). Exploring the origin of tip-enhanced Raman scattering: preparation of efficient TERS probes with high yield. *Journal of Raman Spectroscopy*, *43*, 173–180.
24. Kawata, S., & Shalaev, V. M. (2007). *Tip enhancement*. Elsevier.
25. Zhang, M., Wang, R., Zhu, Z., Wang, J., & Tian, Q. (2013). Experimental research on the spectral response of tips for tip-enhanced Raman spectroscopy. *Journal of Optics*, *15*, 055006.
26. Kneipp, K., Moskovits, M., & Kneipp, H. (2006). Surface-enhanced Raman scattering. In *Physics and applications* (Vol. 103). Springer Science & Business Media.
27. Ru, E. L., & Etchegoin, P. (2008). *Principles of surface-enhanced Raman spectroscopy*. Elsevier.
28. Anderson, M. S. (2000). Locally enhanced Raman spectroscopy with an atomic force microscope. *Applied Physics Letters*, *76*(21), 3130–3132.
29. Nieman, L. T., Krampert, G. M., & Martinez, R. E. (2001). An apertureless near-field scanning optical microscope and its application to surface-enhanced Raman spectroscopy and multiphoton fluorescence imaging. *Review of Scientific Instruments*, *72*(3), 1691–1699.
30. Pettinger, B., Picardi, G., Schuster, R., & Ertl, G. (2002). Surface-enhanced and STM-tip-enhanced Raman spectroscopy at metal surfaces. *Single Molecules*, *3*(5–6), 285–294.
31. Hartschuh, A., Sánchez, E. J., Xie, X. S., & Novotny, L. (2003). High-resolution near-field Raman microscopy of single-walled carbon nanotubes. *Physical Review Letter*, *90*(9), 095503.
32. Zhang, W., Yeo, B. S., Schmid, T., & Zenobi, R. (2007). Single molecule tip-enhanced Raman spectroscopy with silver tips. *Journal of Physical Chemistry C*, *111*(4), 1733–1738.
33. Futamata, M., Maruyama, Y., & Ishikawa, M. (2003). Local electric field and scattering cross section of Ag nanoparticles under surface plasmon resonance by finite difference time domain method. *The Journal of Physical Chemistry B*, *107*, 7607–7617.
34. Yang, Z., Aizpurua, J., & Xu, H. (2009). Electromagnetic field enhancement in TERS configurations. *Journal of Raman Spectroscopy*, *40*, 1343–1348.
35. Chen, J. N., Yang, W. S., Dick, K., Deppert, K., Xu, H. Q., Samuelson, L., & Xu, H. X. (2008). Tip-enhanced Raman scattering of p-thiocresol molecules on individual gold nanoparticles. *Applied Physics Letters*, *92*, 093110.
36. Ohtsu, M. (Ed.). (1998). *Near-field nano/atom optics and technology*. Springer-Verlag.
37. Yoshikawa, M., Maegawa, M., Katagiri, G., & Ishida, H. (1995). Characterization of anisotropic stress around Si trenches by polarized Raman spectroscopy. *Journal of Applied Physics*, *78*(2), 941–944.

38. Murakami, M., Fujita, Y., & Yoshikawa, M. (to be published).
39. Holts, M., Duncan, W. M., Zollner, S., & Lie, R. (2000). Visible and ultraviolet Raman scattering studies of $\text{Si}_{1-x}\text{Ge}_x$ alloys. *Journal of Applied Physics*, *88*, 2523.
40. Yoshikawa, M., Murakami, M., & Ishida, H. (2006). Stress characterization of Si by a scanning near-field optical Raman microscope with spatial resolution and with penetration depth at the nanometer level, using resonant Raman scattering. *Japanese Journal of Applied Physics*, *45*(17–19), L486–L489.
41. Yoshikawa, M., Murakami, M., & Ishida, H. (2007). Characterization of Si nanostructures using a noncontact mode scanning near-field optical Raman microscope, with 100 nm spatial resolution and 5 nm depth resolution, using ultraviolet resonant Raman scattering. *Applied Physics Letter*, *91*, 131908.
42. Yoshikawa, M., Fujita, Y., & Murakami, M. (2019). Stress characterization of the interface between thermal oxide and the 4H-SiC epitaxial layer using near-field optical Raman microscopy. *Applied Spectroscopy*, *73*(10), 1193–1200.
43. Yoshikawa, M., Inoue, K., Sameshima, J., & Seki, H. (2018). Characterization of inhomogeneity in thermal oxide SiO_2 films on 4H-SiC epitaxial substrates by a combination of Fourier transform infrared spectroscopy and cathodoluminescence spectroscopy. *Materials Science Forum*, *924*, 273–276.
44. Yoshikawa, M., Kosaka, K., Seki, H., & Kimoto, T. (2016). Stress characterization of 4H-SiC metal-oxide-semiconductor field-effect transistor (MOSFET) using Raman spectroscopy and the finite element method. *Applied Spectroscopy*, *70*(7), 1209–1213.
45. Martinet, C., & Devine, R. A. B. (1995). Analysis of the vibrational mode spectra of amorphous SiO_2 films. *Journal of Applied Physics*, *77*(9), 4343–4349.
46. Queeney, K. T., Weldon, M. K., Chang, J. P., Chabal, Y. J., Gurevich, A. B., Sapjeta, J., & Opila, R. L. (2000). Infrared spectroscopic analysis of the Si/ SiO_2 interface structure of thermally oxidized silicon. *Journal of Applied Physics*, *87*(3), 1322–1331.
47. Hirai, H., & Kita, K. (2013). Structural difference between near interface oxides grown on Si and C faces of 4H-SiC characterized by infrared spectroscopy. *Applied Physics Letters*, *103*, 132106.
48. Seki, H., Yoshikawa, M., Kobayashi, T., Kimoto, T., & Ozaki, Y. (2017). Characterization of thermal oxides on 4H-SiC epitaxial substrates using fourier-transform infrared spectroscopy. *Applied Spectroscopy*, *71*(5), 911–918.
49. Lienig, J., & Thiele, M. (2018). Mitigating electromigration in physical design. In *Fundamentals of electromigration-aware integrated circuit design* (pp. 138–140). Springer.
50. Mintmire, J. W., Dunlap, B. I., & White, C. T. (1992). Are fullerene tubules metallic. *Physical Review Letters*, *68*(5), 631–634.
51. Dekker, C. (1999). Carbon nanotubes as molecular quantum wires. *Physics Today*, *52*(5), 22–28.
52. Zheng, X., Jia, B., Chen, X., & Gu, M. (2014). In situ third-order non-linear responses during laser reduction of graphene oxide thin films towards on-chip non-linear photonic devices. *Xiaorui Zheng*, *26*(17), 2699–2703.
53. Coxworth, B. (2012). Graphene paper anodes pave way for faster charging Li-ion batteries. www.gizmag.com. Retrieved 26 Sept 2015.
54. David, L., & Singh, G. (2014). Reduced graphene oxide paper electrode: opposing effect of thermal annealing on Li and Na cyclability. *Journal of Physical Chemistry C*, *118*(49), 284041–328408.
55. Deckert-Gaudig, T., Taguchi, A., Kawata, S., & Deckert, V. (2017). Tip-enhanced Raman spectroscopy—from early developments to recent advances. *Chemical Society Reviews*, *44*, 4077–4110.
56. Zhang, Z., Sheng, S., Wang, R., & Sun, M. (2016). Tip-enhanced raman spectroscopy. *Nano Letters*, *88*, 9328–9346.
57. Stockle, R. M., Suh, Y. D., Deckert, V., & Zenobi, R. (2000). Nanoscale chemical analysis by tip-enhanced Raman spectroscopy. *Chemical Physics Letters*, *318*, 131–136.

58. Karrai, K., & Grober, R. D. (1995). Piezoelectric tip-sample distance control for near field optical microscopes. *Applied Physics Letters*, *66*, 1842.
59. Yano, T., Verma, P., & Kawata, S. (2006). Diameter-selective near-field Raman analysis and imaging of isolated carbon nanotube bundles. *Applied Physics Letters*, *88*, 093125.
60. Yoshikawa, M., Fujita, Y., & Murakami, M. (2022). Structural characterization of intersections between semiconducting and metallic carbon nanotubes using tip-enhanced Raman spectroscopy. *Journal of Raman Spectroscopy*, *53*, 1048–1054.
61. Jorio, A., Dresselhaus, M. S., & Dresselhaus, G. (2008). Carbon nanotubes: Advanced topics in synthesis, properties, and applications. In *Topics in applied physics* (Vol. 111). Springer.
62. Jorio, A., Saito, R., Hafner, J. H., Lieber, C. M., Hunter, M., McClure, T., Dresselhaus, G., & Dresselhaus, M. S. (2001). Structural (n, m) determination of isolated single-wall carbon nanotubes by resonant Raman scattering. *Physical Review Letters*, *86*, 1118.
63. Araujo, P. T., Maciel, I. O., Pesce, P. B. C., Pimenta, M. A., Doorn, S. K., Qian, H., Hartschuh, A., Steiner, M., Grigorian, L., Hata, K., & Jorio, A. (2008). Nature of the constant factor in the relation between radial breathing mode frequency and tube diameter for single-wall carbon nanotubes. *Physical Review B*, *77*, 241403.
64. Bhattacharai, A., Krayev, A., Temiryazev, A., Evpov, D., Crampton, K. T., Hess, W. P., & El-Khoury, P. Z. (2018). Tip-enhanced raman scattering from nanopatterned graphene and graphene oxide. *Nano Letters*, *18*, 4029–4033.
65. Yoshikawa, M., Fujita, Y., & Murakami, M. (2022). Characterization of inhomogeneity at edges of graphene oxide films using tip-enhanced Raman spectroscopy. *Journal of Raman Spectroscopy*, *53*, 1394–1401.
66. Dazzi, A., Prater, C. B., Hu, Q., Chase, D. B., Rabolt, J. F., & Marcott, C. (2012). AFM-IR: Combining atomic force microscopy and infrared spectroscopy for nanoscale chemical characterization. *Applied Spectroscopy*, *66*(12), 1366–1384.
67. Dazzi, A., & Prater, C. B. (2017). AFM-IR: Technology and applications in nanoscale infrared spectroscopy and chemical imaging. *Chemical Review*, *117*(7), 5146–5173.
68. Felts, J. R., Law, S., Roberts, C. M., Podolskiy, V., Wasserman, D. M., & King, W. P. (2013). Near-field infrared absorption of plasmonic semiconductor microparticles studied using atomic force microscope infrared spectroscopy. *Applied Physics Letters*, *102*, 152110.
69. Law, S., Adams, D. C., Taylor, A. M., & Wasserman, D. (2012). Mid-infrared designer metals. *Optics Express*, *20*, 12155–12165.
70. Adams, D. C., Inampudi, S., Ribaudo, T., Slocum, D., Vangala, S., Kuhta, N. A., Goodhue, W. D., Podolskiy, V. A., & Wasserman, D. (2011). Funneling light through a subwavelength aperture with epsilon-near-zero materials. *Physical Review Letters*, *107*, 133901.
71. Mitsuhashi, K., Fujita, Y., Aoki, Y., & Yoshikawa, M. (unpublished).
72. Nishizawa, S., Sakai, K., Hangyo, M., Nagashima, Mitsuo, T., Takeda, W., Tominaga, K., Oka, A., Tanaka, K., & Morikawa, O. (2005). Terahertz time-domain spectroscopy. In K. Sakai (Eds.). Springer.
73. Zhang, W., Azad, A. K., & Grischkowsky, D. (2003). Terahertz studies of carrier dynamics and dielectric response of n-type, freestanding epitaxial GaN. *Applied Physics Letters*, *82*, 2841–2843.
74. Kato, F., Kumazawa, R., & Yoshikawa, M. (unpublished).
75. Miyamoto, T., Numao, S., Sameshima J., Nakagawa, Y., Mizoguchi, K., & Yoshikawa, M. (to be published).
76. White, C. W., Simms, D. L., & Tolk, N. H. (1972). Surface composition determined by analysis of impact radiation. *Science*, *177*, 481–486.
77. Yoshikawa, M., Seki, H., Inoue, K., Matsuda, K., Tanahashi, Y., Sako, H., Nanen, Y., Kato, M., & Kimoto, T. (2011). Characterization of silicon dioxide films on a 4H-SiC Si(0001) face by Fourier transform infrared (FT-IR) spectroscopy and cathodoluminescence spectroscopy. *Applied Spectroscopy*, *65*, 543–548.
78. Yoshikawa, M., Ogawa, S., Inoue, K., Seki, H., Tanahashi, Y., Sako, H., Nanen, Y., Kato, M., & Kimoto, T. (2012). Characterization of silicon dioxide films on 4H-SiC Si (0001) face by cathodoluminescence spectroscopy and x-ray photoelectron spectroscopy. *Applied Physics Letters*, *100*, 082105.

79. Yoshikawa, M., Inoue, K., Seki, H., Nanen, Y., Kato, M., & Kimoto, T. (2013). Characterization of silicon dioxide films on 4H-SiC (0001) Si, (1 00) M, and (11 0) A faces by cathodoluminescence spectroscopy. *Applied Physics Letters*, *102*, 051612.
80. Shah, J. (ed.). (1999). *Ultrafast spectroscopy of semiconductors and semiconductor nanostructures*. Springer-Verlag.
81. Corfdir, P., Ristić, J., Lefebvre, P., Zhu, T., Martin, D., Dussaigne, A., Ganière, J. D., Grandjean, N., & Deveaud-Plédran, B. (2009). Low-temperature time-resolved cathodoluminescence study of exciton dynamics involving basal stacking faults in *a*-plane GaN. *Applied Physics Letters*, *94*, 201115.
82. Lipatov, E. I., Lisitsyn, V. M., Oleshko, V. I., Polisadova, E. F., Tarasenko, V. F., & Baksht, E. H. (2012). Pulsed cathodoluminescence of natural and synthetic diamonds excited by nanosecond and subnanosecond electron beams. www.intechopen.com
83. Moerland, R. J., Gerward, I., Weppelman, C., Garming, M. W. H., Kruit, P., & Hoogenboom, J. P. (2016). Time-resolved cathodoluminescence microscopy with sub-nanosecond beam blanking for direct evaluation of the local density of states. *Optics Express*, *24*(21), 24760–24772. <https://doi.org/10.1364/OE.24.024760>
84. Merano, M., Sonderegger, S., Crottini, A., Collin, S., Renucci, P., Pelucchi, E., Malko, A., Baier, M. H., Kapon, E., Deveaud, B., & Ganife, J.-D. (2005). Probing carrier dynamics in nanostructures by picosecond cathodoluminescence. *Nature Letters*, *438*, 479–482.
85. Leifer, K., Hartmann, A., Ducommun, Y., & Kapon, E. (2000). Probing carrier dynamics in nanostructures by picosecond cathodoluminescence. *Applied Physics Letters*, *77*(24), 3923–3925.
86. Nakamura, S., Mukai, T., & Senoh, A. (1994). *p*-type gallium nitride by reactive ion-beam molecular beam epitaxy with ion implantation, diffusion, or coevaporation of Mg. *Applied Physics Letters*, *64*, 1687.
87. Lefebvre, P., Morel, A., Gallart, M., Taliercio, T., Allègre, J., Gil, B., Mathieu, H., Damilano, B., Grandjean, N., & Massies, J. (2001). High internal electric field in a graded-width InGaN/GaN quantum well: Accurate determination by time-resolved photoluminescence spectroscopy. *Applied Physics Letters*, *78*, 1252.
88. Lefebvre, P., Morel, A., Gallart, M., Taliercio, T., Allègre, J., Gil, B., Mathieu, H., Damilano, B., Grandjean, N., & Massies, J. (2001). Effects of GaAIN barriers and of dimensionality on optical recombination processes in InGaN quantum wells and quantum boxes. *Applied Physics Letters*, *78*, 1538.
89. Akopian, N., Bahir, G., Gershoni, D., Craven, M. D., Speck, J. S., & DenBaars, S. P. (2005). Optical evidence for lack of polarization in (11–20) oriented GaN/(AlGaN) quantum structures. *Applied Physics Letters*, *86*, 202104-1–202104-3.
90. Johnston, C. F., Kappers, M. J., Barnard, J. S., & Humphreys, C. J. (2008). Morphological study of non-polar (11–20) GaN grown on *r*-plane (1–102) sapphire. *Physica Status Solidi C*, *5*, 1786.
91. Ni, X., Özgür, Ü., Fu, Y., Biyikli, N., Xie, J., Baski, A. A., Morkoç, H., & Liliental-Weber, Z. (2006). Defect reduction in (11–20) *a*—plane GaN by two-stage epitaxial lateral overgrowth. *Applied Physics Letters*, *89*, 262105.
92. Imer, B., Wu, F., DenBaars, S. P., & Speck, J. S. (2006). Improved quality (11–20) *a*—plane GaN with sidewall lateral epitaxial overgrowth. *Applied Physics Letters*, *88*, 061908.
93. Stampfl, C., & Van de Walle, C. G. (1998). Energetics and electronic structure of stacking faults in AlN, GaN, and InN. *Physical Review B*, *57*, R15052.
94. Rebane, Y. T., Shrater, Y. G., & Albrecht, M. (1997). Stacking faults as quantum wells for excitons in Wurtzite GaN. *Physica Status Solidi A*, *164*, 141.
95. Salviati, G., Albrecht, M., Zanotti-Fregonara, C., Armani, N., Mayer, M., Shrater, Y., Guzzi, M., Melnik, Y. V., Vassilevski, K., Dmitiev, V. A., & Strunk, H. P. (1999). Cathodoluminescence and transmission electron microscopy study of the influence of crystal defects on optical transitions in GaN. *Physica Status Solidi A*, *171*, 325.
96. Liu, R., Bell, A., Ponce, F. A., Chen, C. Q., Yang, J. W., & Khan, M. A. (2005). Luminescence from stacking faults in gallium nitride. *Applied Physics Letters*, *86*, 021908.

97. Corfdir, P., Lefebvre, P., Levrat, J., Dussaigne, A., Ganière, J.-D., Martin, D., Ristic, J., Zhu, T., Grandjean, N., & Deveaud-Plédran, B. (2009). Low-temperature time-resolved cathodoluminescence study of exciton dynamics involving basal stacking faults in *a*-plane GaN. *Journal of Applied Physics*, *94*, 043102.

Paper List

Author	Title	Journal
Masanobu Yoshikawa, Masataka Murakami, Yasuhiko Fujita	Characterization of inhomogeneity at edges of graphene oxide films using tip-enhanced Raman spectroscopy	Journal of Raman Spectroscopy 53, 1394 (2022)
Masanobu Yoshikawa, Masataka Murakami, Yasuhiko Fujita	Structural characterization of intersections between semiconducting and metallic carbon nanotubes using tip-enhanced Raman spectroscopy	Journal of Raman Spectroscopy 53, 1048 (2022)
Masanobu Yoshikawa, Yasuhiko Fujita, and Masataka Murakami	Stress characterization of interface between thermal oxide and 4H-SiC epitaxial layer using near-field optical Raman microscopy	Applied Spectroscopy Vol. 73(10) 1193–1200, 2019
J. Sameshima, and M. Yoshikawa	An effect of residual gas component on detected secondary ions during TOF-SIMS depth profiling and a method to estimate contained component	Surface and Interface Analysis, 50, 8, pp. 802–806, (2018)
Masanobu Yoshikawa	Infrared spectroscopy and Raman spectroscopy of semiconductor	Encyclopedia of Analytical Chemistry (John Wiley & Sons Ltd), 2018

(continued)

(continued)

Author	Title	Journal
Masanobu Yoshikawa, Keiko Inoue, Junichiro Sameshima, and Hirohumi Seki	Characterization of inhomogeneity in thermal oxide SiO ₂ films on 4H-SiC epitaxial substrates by a combination of Fourier transform infrared spectroscopy and cathodoluminescence spectroscopy	Materials Science Forum Vol. 924, pp 273–276, 2018
Hirofumi Seki, Masanobu Yoshikawa, Takuma Kobayashi, Tsunenobu Kimoto, and Yukihiro Ozaki	Characterization of thermal oxides on 4H-SiC epitaxial substrates using Fourier-transform infrared spectroscopy	Applied Spectroscopy, 2016, Vol. 71(5) 911–918
Masanobu Yoshikawa, Kenichi Kosaka, Hirohumi Seki, and Tsunenobu Kimoto	Stress characterization of 4H-SiC metal–oxide–semiconductor field-effect transistor (MOSFET) using Raman spectroscopy and the finite element method	Applied Spectroscopy, 2016, Vol. 70(7) 1209–1213
M. Yoshikawa	Abnormal Raman spectral variation with excitation wavelength in boron-doped single-crystalline diamond	Materials Science Forum Vol. 858, pp 1158–1161, 2015
M. Yoshikawa, H. Seki, K. Inoue, Y. Nanen, T. Kimoto	Characterization of inhomogeneity in silicon dioxide films on 4H-silicon carbide epitaxial substrate using a combination of Fourier transform infrared and cathodoluminescence spectroscopy	Applied Spectroscopy, 2014, Vol. 68(10) 1176–1180
M. Yoshikawa, K. Inoue, J. Sameshima, and H. Seki	Characterization of inhomogeneity in SiO ₂ films on 4H-SiC epitaxial substrate by a combination of Fourier transform infrared and cathodoluminescence spectroscopy	Materials Science Forum 924, 273–276 (2018)
M. Yoshikawa, H. Seki, T. Yamane, Y. Nanen, M. Kato, T. Kimoto	Abnormal behavior of LO phonon in silicon dioxide films on 4H-SiC bulk epitaxial substrate by Fourier transform infrared (FT-IR) spectroscopy	Applied Spectroscopy, Vol. 67(5), pp. 542–545, 2013

(continued)

(continued)

Author	Title	Journal
M. Yoshikawa, K. Inoue, H. Seki, Y. Nanen, M. Kato, and T. Kimoto	Characterization of silicon dioxide films on 4H-SiC (0001) Si, (1-100)M, and (11-20) A faces by cathodoluminescence spectroscopy	Applied Physics Letters, 102, 051612 (2013)
M. Yoshikawa, S. Ogawa, K. Inoue, H. Seki, Y. Tanahashi, H. Sako, K. Matsuda, Y. Nanen, M. Kato, and T. Kimoto	Characterization of silicon dioxide films on 4H-SiC Si (0001) face by cathodoluminescence spectroscopy and X-ray photoelectron spectroscopy	Applied Physics Letters, 100, 082105 (2012)
M. Yoshikawa, H. Seki, K. Inoue, Y. Tanahashi, H. Sako, Y. Nanen, M. Kato, and T. Kimoto	Characterization of silicon dioxide films on 4H-SiC Si(0001) face by Fourier transform infrared spectroscopy and cathodoluminescence spectroscopy	Applied Spectroscopy, Vol. 65(5), pp. 543–548, 2011
Naoki Muraki, Takeshi Miyamoto, and Masanobu Yoshikawa	Depth profile analysis of organic multi-layer device with nanometer resolution using surface-enhanced Raman spectroscopy	Chem. Phys. Lett., 499, pp. 158–160, spectra of InGaN single quantum well films
Naoki Muraki, and Masanobu Yoshikawa	Characterization of the interface between metal and tris (8-hydroxyquinoline) aluminum using surface-enhanced Raman scattering with glass cap encapsulation	Chem. Phys. Lett., 496, pp. 91–93, 2010
R. Sugie, M. Takeshi, Masanobu Yoshikawa, et al	Cathodoluminescence Microcharacterization of Radiative Recombination Centers in Lifetime-Controlled Insulated Gate Bipolar Transistors	Jpn. J. Appl. Phys., 49, pp. 04DP15.1–04DP15.4, 2010
M. Yoshikawa, M. Murakami, H. Ishida and H. Harima ¹ (1: Kyoto Institute of Technology)	Characterizing nanometer-sized V-defects in InGaN single quantum well films by high-spatial-resolution cathodoluminescence spectroscopy	Applied Physics Letters, 94, 131908 (2009)
M. Yoshikawa, et al	Characterization of V-defects in InGaN single-quantum-well films at nanometer level by high spatial resolution cathodoluminescence spectroscopy	Materials Science Forum, Vols. 600–603, pp. 1305–1308 (2009)

(continued)

(continued)

Author	Title	Journal
Takeshi Mitani, Ryo Hattori, and Masanobu Yoshikawa	Depth profiling of Al ion-implantation damage in SiC crystals by cathodoluminescence spectroscopy	Materials Science Forum, Vols. 600–603, pp. 615–618, 2009
Ryuichi Sugie, Masanobu Yoshikawa, Shin Harada, and Yasuo Namikawa	Expansion of stacking faults by electron-beam irradiation in 4H-SiC diode structure	Materials Science Forum, Vols. 600–603, pp. 353–356, 2009
M. Yoshikawa	Stress characterization of nano-polycrystalline silicon films and silicon and by near-field and far-field Raman microscope, using UV resonant scattering	Trends in nanotechnology, 2008
M. Yoshikawa, et al	Characterization of V-defects in InGaN single quantum well films at the nanometer level by high-spatial-resolution cathodoluminescence spectroscopy	Applied Spectroscopy, 62, 86 (2008)
M. Yoshikawa, et al	Characterization of ZnO nanoparticles by resonant Raman scattering and cathodoluminescence spectroscopies	Applied Physics Letters, 92, 113115 (2008)
M. Yoshikawa, et al	Highly sensitive detection of the near-filed Raman scattered light from strained Si/SiGe heterostructures by scanning near-field optical Raman microscope, using ultraviolet resonant Raman scattering	Applied Physics Letters, 92, 091903 (2008)
M. Yoshikawa, et al	Stress characterization of Si by near-field Raman microscope, using resonant scattering	Applied Spectroscopy, 62, 86 (2008)
M. Yoshikawa, et al	Characterization of Si nanostructures using a noncontact mode, scanning near-field optical Raman microscope, with 100 nm spatial resolution and 5 nm depth resolution, using ultraviolet resonant Raman scattering	Applied Physics Letters, 91, 131908 (2007)

(continued)

(continued)

Author	Title	Journal
M. Yoshikawa, et al	Stress characterization of Si by a scanning Near-field optical Raman microscope with spatial resolution and with penetration depth at the nanometer level, using resonant Raman scattering	Jpn. J. Appl. Phys., 45, L486 (2006)
M. Yoshikawa, et al	Defect characterization of Si-doped GaN films by a scanning near-field optical microscope-induced photoluminescence using an ultra violet laser and by high spatial resolution cathodoluminescence spectroscopy	Applied Physics Letters, 88, 161905 (2006)
Ryuichi Sugie, Masanobu Yoshikawa, et al	Investigation of stress-induced defects in shallow trench isolation by cathodoluminescence and Raman spectroscopies	J. Appl. Phys., 100, p.064504–064504-5, 2006
M. Yoshikawa, et al	Characterization of Si nano-polycrystalline films at the nanometer level using resonant Raman scattering	Journal of Applied Physics, 98, 063531 (2005)
M. Yoshikawa, et al	Resonant Raman scattering from N-doped and Si-doped diamondlike amorphous carbon films	Phys. Rev. B, 69, 045410R (2004)
Naoki Muraki, N. Matoba, T. Hirano, M. Yoshikawa	Determination of thermal stress distribution in a model microelectronic device encapsulated with alumina filled epoxy resin using fluorescence spectroscopy	Polymer, 43, pp. 1277–1285, 2002
M. Yoshikawa, et al	Characterization of silicon dioxide film by high spatial resolution cathodoluminescence spectroscopy	Journal of Applied Physics, vol. 92, No. 12, 7153 (2002)
M. Yoshikawa, et al	Resonant Raman scattering from buried Al _x Ga _{1-x} N(x < 0.17) layers in (Al, Ga, In)N heterostructures	Journal of Applied Physics, 87, 2583 (2000)

(continued)

(continued)

Author	Title	Journal
M. Yoshikawa, et al	Band-gap renormalization and band filling in Si-doped GaN films studied by photoluminescence spectroscopy	Journal of Applied Physics, 86, 4400 (1999)
M. Yoshikawa, et al microprobe	Characterization of carrier concentration and stress in GaAs metal–semiconductor field-effect transistor by cathodoluminescence spectroscopy	Applied Physics Letters, 57(5), 428 (1990)
M. Yoshikawa, et al	Raman spectra of diamondlike amorphous carbon films	Science and Technology of New Diamond, 1, 445 (1990)
M. Yoshikawa	Raman spectra of diamondlike amorphous carbon films	New Diamond, 1, 54 (1990)
I. Nagai, A. Ishitani, H. Kuroda, Masanobu Yoshikawa, N. Nagai	Preparation of diamondlike carbon films by electron cyclotron resonance chemical vapor deposition	J. Appl. Phys., 67, pp. 2890–2893, 1990
M. Yoshikawa, et al	Characterization of crystalline quality of diamond films by Raman spectroscopy	Applied Physics Letters, 55(25), 2608 (1989)
Naoto Nagai, M. Yoshikawa et al	FT-IR study on microstructure of diamondlike amorphous carbon films	Proc. SPIE Int. Soc. Opt. Eng., 1145, pp. 496–497, 1989
M. Yoshikawa	Raman spectra of diamondlike amorphous carbon films	Mater. Sci. Forum, 52–53, 365 (1989)
M. Yoshikawa, et al	Raman spectra of diamondlike amorphous carbon films	Solid State Communications, 66, 1177 (1988)
M. Yoshikawa, et al	Raman spectra of diamondlike amorphous carbon films	Journal of Applied Physics, 64, 6464 (1988)
M. Yoshikawa, et al	Resonant Raman scattering of diamondlike amorphous carbon films	Applied Physics Letters, 52, 1639 (1988)
M. Yoshikawa, et al	Raman spectra of NH ₄ -TCNQ-I and -II	Journal of The Physical Society of Japan, Vol. 55, No. 4, pp. 1177–1187 (1986)
M. Yoshikawa, et al	Raman spectra of thin TCNQ films deposited on silver films	Journal of Raman Spectroscopy, Vol. 17, 369–371 (1986)
M. Yoshikawa, et al	Pressure Raman effect in TCNQ salts	Solid State Communications, Vol. 48, No. 1, pp.13–16 (1983)

Proceeding

M. Yoshikawa, et al	Raman spectra of diamondlike amorphous carbon films	Xth International Conference on Raman Spectroscopy	Sept. 6, London, UK, 1988
M. Yoshikawa, et al	Raman spectra of diamondlike amorphous carbon films	1st International Conference on the New Diamond	Oct. 24, Tokyo, 1988
M. Yoshikawa, et al	Origin of Raman bands of a-C films	XIIth International Conference on Raman Spectroscopy	August 13–17, USA, 1990
M. Yoshikawa, et al	Determination of anisotropic refractive indices of a single-crystal organic thin film by attenuated total reflection Raman spectroscopy	XIIth International Conference on Raman Spectroscopy	August 13–17, USA, 1990
M. Yoshikawa, et al	Determination of anisotropic refractive indices of a single-crystal organic thin film by attenuated total reflection Raman spectroscopy	XIIth International Conference on Raman Spectroscopy	August 13–17, USA, 1990
M. Yoshikawa, et al	Characterization of carrier and stress distributions in semiconductor devices by cathodoluminescence spectroscopy and Raman microprobe	Inst. Phys. Conf. Ser. No165, Symposium 1, 2nd Conf. Int. Union Microbeam analysis societies	Kailua-Kona, Hawaii, 9–13 July 2000, p27 (invited)
M. Yoshikawa, et al	Resonant Raman scattering from Si doped and N doped a-C:H films	Proceedings of the XVIIth International Conference on Raman Spectroscopy,	Edited by J. Mink, G. Jalovszky and G. Keresztry (Wiley, England, 2002), p. 487
Yasuhide Aoki, Naoki Mura-ki, Masanobu Yoshikawa	A micro-Raman study of natural rubber with YAG laser excitation	19th International Conference on Raman Spectroscopy	8–13 August, Australia, 2004
T. Hayashi, H. Seki, N. Muraki, N. Nagai and M. Yoshikawa	Chemical structure analysis of OLED device using IR microspectroscopy and micro-MS spectrometry	The Third International Conference on Advanced Vibrational Spectroscopy(ICAVS-3)	USA, 2005

(continued)

(continued)

Ryuichi Sugie, Keiko Matsuda, Naoto Nagai, Tsuneo Ajioka, Masanobu Yoshikawa, Toshikazu Mizukoshi, Katsuhiko Shibusawa, and Shoji Yo	Characterization of crystalline defects and stress in shallow trench isolation by cathodoluminescence and Raman spectroscopies	2005 International Conference on Solid State Devices and Materials (SSDM)	Japan, 2005
M. Yoshikawa, M. Murakami, T. Fujita, K. Inoue, K. Matsuda, H. Ishida and H. Harima	Characterization of V-defects in InGaN single-quantum-well films at nanometer level by high spatial resolution cathodoluminescence spectroscopy	International Conference on Silicon Carbide and Related Materials 2007	Japan, 2005
Masataka Murakami, Keiko Matsuda, Ryuichi Sugie, Masanobu Yoshikawa	Characterization of silicon nanostructures by near-field Raman spectroscopy	Characterization of Silicon nanostructures by Near-Field Raman Spectroscopy	8/17–24 Brunel University/London, 2008
M. Yoshikawa	Characterization of Si by a tapping mode-scanning near-field optical Raman microscope (SNORM)	20th International Conference on Raman Spectroscopy	Invited speaker, Sep. 21–25th, 2006
T. Mitani, S. Nakashima, H. Okumura	Characterization of Process-Induced Defects in SiC Crystals by Micro-Raman Mapping	20th International Conference on Raman Spectroscopy	Sep. 21–25th, 2006
Y. Aoki, N. Muraki, M. Yoshikawa	Characterization of Nafion membrane using Raman spectroscopy	20th International Conference on Raman Spectroscopy	Sep. 21–25th, 2006
K. Matsuda, R. Miyoshi, H. Seki, H. Hashimoto and M. Yoshikawa	Depth analysis of annealed SiOC thin films by Raman Spectroscopy	20th International Conference on Raman Spectroscopy	Sep. 21–25th, 2006
K. Inoue, K. Okada, M. Yoshikawa and N. Hasuike, H. Harima	Raman scattering from nanometer-sized zinc oxide	20th International Conference on Raman Spectroscopy	Sep. 21–25th, 2006

(continued)

(continued)

M. Murakami, K. Matsuda, R. Sugie and M. Yoshikawa	Determination of residual stress distribution in silicon by near-field Raman spectroscopy	20th International Conference on Raman Spectroscopy	Sep. 21–25th, 2006
M. Yoshikawa, et al	Characterization of V-defects in InGaN single-quantum-well films at nanometer level by high spatial resolution cathodoluminescence spectroscopy	International Conference on Silicon Carbide and Related Materials	October 14–19th, 2007
T. Mitani, R. Hattori, M. Yoshikawa	Diffusion of point defects from ion implanted 4H-SiC: cathodoluminescence observation	European Conference on Silicon Carbide and Related Materials	9/8, Barcelona, 2008
H. Seki, H. Hashimoto, M. Yoshikawa	Characterization of low-k films between narrow Cu lines using infrared microscopy	Sixth International Conference on Advanced Vibrational Spectroscopy (ICAVS-6)	6/16, USA, 2011
Ryuichi Sugie, Kensuke Inoue, and Masanobu Yoshikawa	Semi-quantitative determination of radiative recombination centers in silicon power devices by cross-sectional cathodoluminescence	SSDM2011 (International Conference on Solid State Devices and Materials 2011)	9/28 Nagoya, Japan, 2011
M. Yoshikawa, et al	Raman spectra of diamondlike amorphous carbon films	Xth international conference on Raman spectroscopy	Sept. 6, London, UK, 1988
M. Yoshikawa, et al	Characterization of inhomogeneity in SiO ₂ films on 4H-SiC epitaxial substrate by a combination of Fourier transform infrared spectroscopy and cathodoluminescence spectroscopy	European Conference on Silicon Carbide & Related Materials (ECSCRM 2014)	September 21–25, 2014, Grenoble, France
M. Yoshikawa	Abnormal Raman spectral variation with excitation wavelength in boron-doped single-crystalline diamond	16th International Conference on Silicon Carbide and Related Materials	Italy, October 4–9, 2015

(continued)

(continued)

M. Yoshikawa, K. Inoue, J. Sameshima, and H. Seki	Characterization of inhomogeneity in thermal oxide SiO ₂ films on 4H-SiC epitaxial substrates by a combination of Fourier transform infrared spectroscopy and cathodoluminescence spectroscopy	International Conference on Silicon Carbide and Related Materials (ICSCRM 2017)	USA, Washington, D.C., September 17–22, 2017
M. Yoshikawa, Y. Fujita, M. Murakami, K. Inoue, J. Sameshima, and H. Seki	Stress characterization of 4H-SiC epitaxial substrates by scanning near-field optical Raman microscope, with 250-nm spatial resolution	European Conference on Silicon Carbide and Related Materials (ECSCRM)	UK, Birmingham, September 2–7, 2018
M. Yoshikawa, Y. Fujita, and M. Murakami	Characterization of inhomogeneity in thermal oxide films on 4H-SiC epitaxial substrates by a combination of infrared, Raman and cathodoluminescence spectroscopy	Energy Materials and Nanotechnology 2018 (Invited speaker)	Austria, Vienna, June 18–22, 2018
M. Yoshikawa, and N. Kawasaki	Defect characterization of GaN by SEM-CL and STEM-CL	Energy Materials and Nanotechnology Barcelona Meeting on Semiconductor (Invited speaker)	Spain, Barcelona, August 19–23, 2019
M. Yoshikawa, K. Inoue, Y. Fujita, and M. Murakami	Characterization of inhomogeneity at the interface between SiO ₂ and 4H-SiC substrate by infrared, Raman and cathodoluminescence spectroscopy	International Conference on Advanced Materials Science and Engineering (AMSE) (Invited speaker)	Vienna, Austria, July 22–25, 2020

Raman, infrared and cathodoluminescence spectroscopy of advanced semiconductors and related materials	2021	“Raman, infrared and cathodoluminescence spectroscopy of advanced semiconductors and related materials”, edited by M. Yoshikawa, (cambridgescholars.com, UK, 2021)
Handbook of vibrational spectroscopy	2002	“Handbook of vibrational spectroscopy”, edited by J. M. Chalmers and P. R. Griffiths, (Wiley, Chichester, 2002), p. 259

(continued)

(continued)

Raman spectra of diamondlike amorphous carbon films	1990	Properties and characterization of amorphous carbon films ed. by J. J. Pouch and S. A. Alterovitz 52&53, p. 365 (Materials Science Forum)
---	------	--

Index

A

- Absorption efficient (α), 157
Adolf Smekal, 3
AFM-IR, 181, 182, 184
AFM-tip, 164
AlAs, 64, 126
AlAs in addition to GaAs, 163
 $(\alpha E)^{1/2}$, 110
AlGaInP, 190, 191
AIN, 70
Aluminium Gallium Arsenide (AlGaAs), 65
Amorphous Carbon (a-C), 102
Anti-Stokes scattering, 4
Ar⁺ laser, 14
As Non-radiative Recombination Centres (NRRCs) like GaN, 146
At 1257 and 1072 cm⁻¹, 86
At approximately 0.1 μm, 187
Attenuated total reflection Raman spectroscopy, 211
anisotropic refractive indices of a single-crystal organic thin film, 211
crystallographic orientations in the diamond film on cubic boron nitride, 210
Atomic Force Microscopy (AFM), 40, 58, 163
Atomic Layer Deposition (ALD), 118
ATR crystal, 12
Attenuated Total Internal Reflectance (ATR), 89
Attenuated Total Reflection (ATR), 86
Auger electrons, 33
Avalanche Photodiode (APD), 177

B

- Band-Edge Emission (BEE), 41, 44
Band-gap, 33
Basal Stacking Fault (BSF), 193, 197
Berreman effect, 86
Berreman method, 64
Biaxial stress (σ), 57
Blackbody, 19
Boltzmann factor, 5
Brillouin zone, 107
Burstain–Moss shift, 66

C

- 3C-SiC, 76, 78
 C_6V^4 ($P6_3mc$), 95
CaF₂, 22
CAMECA, 190
Capacitance–Voltage (C – V), 89
Carbon Nanotubes (CNTs), 163, 175, 177
RBM, 177
Cartesian coordinate, 5
Catastrophic Optical Damage (COD), 67
Cathodoluminescence and Raman spectroscopies, 209
carrier and stress distributions, 211
nhomogeneity in thermal oxide films on 4H-SiC #, 214
shallow trench isolation, 209, 212
stress-induced defects in shallow trench isolation, 209
Cathodoluminescence (CL), 33
InGaN single quantum well films, 208
silicon power devices, 213
V-defects in InGaN, 207

V-defects in InGaN
single-quantum-well films, 207, 212, 213
ZnO, 208
Cathodoluminescence spectroscopy, 208
Al ion-implantation damage in SiC, 208
4H-SiC, 208
GaAs metal–semiconductor field-effect transistor, 206
InGaN single quantum well films, 208
ion implanted 4H-SiC, 213
silicon dioxide film, 209
V-defects in InGaN, 207
ZnO nanoparticles, 208
Cathodoluminescence spectroscopy and X-ray photoelectron spectroscopy, 207
silicon dioxide films on 4H-SiC Si (0001) face, 207
CdSe, 127
CdSe Quantum Dots (QDs), 127
Channel Mobility (CM), 76, 89, 90
Charge-Coupled Device (CCD), 17
Charge-Coupled Device (CCD) detector, 16
Chemical Mechanical Polishing (CMP), 60–62
Circuits, 161
CL spectroscopy, 34
Complementary Metal Oxide Silicon (CMOS), 57
Compressive stresses, 70
Confocal Raman microscope, 14
Critical angle, θ_c , 12
Crystallite size, 107
 $\text{Cs}_i\text{-SiC}$, 82
Cu/low- k , 54
Cubic Boron Nitride (c-BN), 100, 101
Czerny–Turner (CT) monochromator, 16

D

3D FDTD, 165
D1, D2, D3, and D4, 47
 $D^\circ X$, 198
Dark Spot Defects (DSDs), 68
D band, 179, 181
Dc p-CVD, 100
Deep Ultraviolet (DUV), 78–80
Defect-related broad luminescence, 43
Density Of States (DOS), 105–107
Deuterated Triglycine Sulfate (DTGS), 21
Diamond, 99, 106
Diamond-Like amorphous Carbon (DLC), 99

D_I center, 82, 85
Dielectric, 161
Diffracted light, 15
Diffuse reflectance, 12
Disordered (D), 109
 D_{it} , 89
D lines, 62
Donor–Acceptor Pair (DAP), 85
Drug Delivery System (DDS), 199
DUV, 157, 158. *See also* 00

E

E' centres, 51
ECR p-CVD, 111, 112
EELS spectra, 110, 111
Effective fixed-charge densities (Q_{eff}), 76
EL, 81
Electromagnetic (EM), 164, 165
Electromagnetic phenomenon, 40
Electron Backscatter Diffraction (EBSD), 35
Electron Beam (EB), 54
Electron Beam Induced Current (EBIC), 57, 58
Electron-Energy-Loss Spectroscopy (EELS), 110
Electronic polarisability, 5
Electronic polarisability tensor, 4
Electron penetration (Re), 34, 41, 49
Electron Probe Micro-Analyser (EPMA), 35
Electron Spin Resonance (ESR), 54–56
Electro-Optic (EO), 188
Ellipsoidal and parabolic mirrors, 37
Energy-Dispersive X-ray Spectrometry (EDS), 35
Epitaxial Lateral Overgrowth (ELO), 197, 198

Evanescence wave, 11
Excitonic luminescence (EX(TO)), 47
Extensively, 22
EX(TO) observed at 1.1 eV, 57

F

Fano, 104
Far-IR (FIR), 11
Field-Emission (FE), 36
Finite-Difference Time-Domain (FDTD), 165
 $FLO(\pm x)$, 79
Float-Zone (FZ), 47
Fluorescence spectroscopy, 209

- thermal stress distribution in a model microelectronic device, 209
- Fluorine-doped silicon-dioxide (SiOF), 51
- Focal Plane Arrays (FPAs), 22
- Focused Ion Beam (FIB), 158
- Folded Longitudinal Acoustic (FLA), 78
- Folded Longitudinal Optical (FLO), 78
- Folded Transverse Acoustic (FTA), 78
- Fourier transform infrared and
cathodoluminescence spectroscopy, 206
- inhomogeneity in SiO₂ films on 4H-SiC epitaxial substrate, 206
- silicon dioxide films on 4H-SiC (0001) Si, (1-100)M, and (11-20) A faces, 207
- silicon dioxide films on 4H-SiC Si(0001) face, 207
- Fourier Transform Infrared (FT-IR), 1, 54
- Fourier Transform Infrared (FT-IR) spectroscopy, 1
- diamondlike amorphous carbon films, 210
- LO phonon in silicon dioxide films, 206
- low-k films, 213
- silicon dioxide films on 4H-silicon carbide epitaxial substrate, 206
- SiO₂ films on 4H-SiC epitaxial substrate, 206
- thermal oxide SiO₂ films on 4H-SiC, 206
- Free exciton (FXA), 39
- FTA ($\pm x$), 79
- FT-IR spectrometer, 11
- Full Width at Half-Maximum (FWHM), 95
- G**
- GaAs, 9, 64, 65, 162
- GaAs MESFET, 65
- GaAs wafer, 34
- Gallium arsenide and related devices, 63
- GaN, 70
- GaP, 64
- Gap-mode TERS, 179
- Gaussian, 107, 113
- Glassy Carbon (GC), 99, 109
- Globar, 19
- Golay detector, 19
- Graphene Oxide (GO), 176
- Graphite, 107
- Grating, 14
- Grazing incidence, 89
- Group III–V compound semiconductors, 64
- GaP, 64
- Group III–V zinc-blende semiconductors, 63
- AlAs, 64
- H**
- 3H-SiC, 30
- 4H, 77
- 4H-polytype Silicon Carbide (4H-SiC), 28, 29
- 6H, 77
- 8H-SiC polytype, 29
- He–Cd laser, 14
- He–Ne laser, 14
- He cooling cryostat, 39
- Heterojunction Bipolar Transistor (HBT), 64
- Hexagonal (H), 76
- Hg_{1-x}Cd_xTe, 22
- HgCdTe, 22
- High Angle Annular Dark Field (HAADF), 143
- High-Density Plasma Chemical Vapor Deposition (HDP-CVD), 60
- Highly Oriented Pyrolytic Graphite (HOPG), 99
- Hydrogenated diamond-like amorphous carbon (a-CH), 109
- Hydrogens bonded to sp² and sp³ carbons, 115
- I**
- InAs, 64, 126, 182
- InAs/AlAs, 126
- Indium antimonide (InSb), 22
- Indium Phosphate (InP), 67
- Infrared (IR), 1
- Silicon dioxide (SiO₂), 49, 50, 51, 55, 60
- SiO₂ films, 206
- thermal oxides on 4H-SiC epitaxial substrates, 206, 214
- Infrared (IR) spectroscopy, 11
- Infrared, Raman and cathodoluminescence spectroscopy, 214
- advanced semiconductors and related materials, 214
- inhomogeneity at the interface between SiO₂ and 4H-SiC, 214
- Infrared spectroscopy and Raman spectroscopy, 205

vibrational spectroscopy, 214
 InGaAs/AlGaAs, 194
 InGaAs arrays, 17
 InGaAsP, 68
 InGaAsP/InP, 68
 InGaAsP/InP Multi-Quantum-Layer (MQW), 68
 InGaN/InGaN Single Quantum Wells (SQWs), 74
 Inhomogeneity, 205
 In-grown Frank-type SFs, 30
 InN, 70
 InP, 64, 65, 163
 InSb, 64
 Insulated Gate Bipolar Transistors, 207
 Interconnects, 161
 Interface (IF), 126
 Interface (IF) phonons, 126
 Interface trap densities (D_{it}), 76
 Internal reflectance, 11
 Interstitials (C_i), 82
 Intrinsic defect complex, 82
 IR microspectroscopy and micro-MS spectrometry, 211
 OLED device, 211

J

JEOL, 35, 36

K
 Kanaya–Okayama model, 60
 Kr⁺ laser, 14
 Kramers–Heisenberg–Dirac (KHD), 5, 6
 KRS-5, 12
 Krishnan, K. S., 3
 Kubelka–Munk, 13

L
 L₁ line, 82
 L₁ lines related to D₁ centers, 85
 Large-Scale Integrated (LSI), 56, 60
 Laser Diodes (LDs), 70
 Light-Emitting Diodes (LEDs), 70
 Liquid helium (He), 39
 Lithium Tantalate (LiTaO₃), 21
 Localised Surface Plasmon (LSP), 163, 165
 Local Vibrational Modes (LVMs), 95
 Longitudinal Optical (LO), 64
 Lorentzian, 107
 Low- k , 54
 Luminescence, 33

Luminescent, 40
 Lyddane–Sachs–Teller (LST), 64

M
 Magnetoresistance (MR), 109
 Marzena B. Zaczek, 5
 Metal–Oxide–Semiconductor (MOS), 89
 Metal–Oxide–Semiconductor Field-Effect Transistors (MOSFETs), 174
 Metal-Semiconductor Field-Effect Transistor (MESFET), 64
 Michelson interferometer, 20
 Mid-IR (MIR), 11
 Monochromator, 15
 Monoclinic gallium oxide (β -Ga₂O₃), 117
 Monte Carlo simulation, 34, 43
 Multiple Quantum Well (MQW), 68, 74

N
 3nR, 77
 Nd:YAG laser, 14
 Near-field, 41
 Near-field and far-field Raman microscope, 208
 Si nanostructures, 208
 strained Si/SiGe, 208
 Stress characterization of nano-polycrystalline silicon films, 208
 Stress characterization of Si, 209
 Near-field optical microscope-induced photoluminescence, 209
 defect characterization of Si-doped GaN films, 209
 Near-Field PL (NFP), 41
 Near-IR (NIR), 11, 163
 Near-field Raman microscope, 208
 Si, 208
 silicon nanostructures, 212
 stress characterization of 4H-SiC, 206, 214
 stress distribution in silicon, 213
 NIR Raman spectroscopy, 160
 nH, 77
 Non-Bridging Oxidation Hole Centre (NBOHC), 54, 55, 91, 193
 Non-Negative Matrix Factorisation (NMF), 149–151
 Non-Radiative Recombination Centres (NRRCs), 44, 83

O

- OH, 54
 O_h , 100
OH/Si-O, 54
Optical, 40
Optical absorption coefficient (α), 40
Optical gaps, 110, 111
Optical Penetration Depth (OPD), 40
Optical-Photothermal Infrared (O-PTIR),
 185
 O-PTIR, 186
Oxford instruments, 39
Oxygen vacancy, 55
Oxygen Vacancy Centres (OVCs), 51, 54,
 55, 89, 175, 193
Oxygen Vacancy Defects (OVDs), 97
Oxygen vacancy–interstitial pairs, 55

P

- Peak-frequency shift ($\Delta\nu$), 57
Penetration depth d_p , 12
Perkin-Elmer Infracord, 19
Phosphor, 40
Photoluminescence (PL), 27, 33
 Band-gap renormalization, 210
 Si-doped GaN films, 210
Photomultiplier Tube (PMT), 17
Photon, 33
Plasma-Chemical Vapor Deposition
 (p -CVD), 54, 99
Plasma-enhanced Atomic Layer Deposition
 (ALD), 118
Polarized Raman spectroscopy, 209–213
 anisotropic stress around Si trenches,
 166
Polyimide (PI), 186
Post-Oxidation Annealing (POA), 76, 89
Potassium Bromide (KBr), 22
Pressure Raman effect, 210
 TCNQ salts, 210
Pyramidal probe, 41
Pyrolytic, 99
Pyrolytic Graphite (PG), 99
 P - n junction, 64, 65

Q

- Q-switching, 176
Quantum Dots (QDs), 126, 128
Quantum Well (QW), 68, 70
Quantum Wires (QWRs), 195
Quartz glass, 55

R

- 15R, 77
Radial Breathing Mode (RBM), 177
Radiative Recombination Centres (RRCs),
 47
Raman, C. V., 1, 3, 110, 111
 strained silicon, 57, 208
Raman effect, 3
Raman microanalysis, 13
 Defects in SiC Crystals, 212
Raman microprobe
 diamond film on the (100) surface of
 cubic boron nitride, 210
 SiOC thin films, 212
 natural rubber, 211
Raman scattering, 208, 209, 210
 nanometer-sized diamond, 207, 212
 diamond particles, 208
 sp₂ carbon clusters, 208
Raman spectroscopy, 1, 210
 4H-SiC metal–oxide–semiconductor
 field-effect transistor (MOSFET), 206
 a-C films, 211
 boron-doped single-crystalline
 diamond, 206
 crystalline quality of diamond films, 210
 diamondlike amorphous carbon films,
 210
 diamondlike carbon films, 210
 Nafion membrane, 212
 nanometer-sized zinc oxide, 212
 NH4-TCNQ-I and -II, 210
 SiGe, 48
 anisotropic refractive indices of a
 single-crystal organic thin film, 211
 TCNQ films, 210
Rayleigh, 4
Rayleigh scattered, 3
Rayleigh scattering, 3, 5
RCA, 171
Refractive index, 12
Resonant Raman scattering, 209
 Al_xGa_{1-x}N ($x < 0.17$) layers in (Al, Ga,
 In)N heterostructures, 209
 diamondlike amorphous carbon films,
 210
 N-doped and Si-doped diamondlike
 amorphous carbon films, 209
 Si doped and N doped a-C:H films, 211
 Si nano-polycrystalline films, 209
Retardation (optical path difference), 20
Rhombohedral (R), 76
Roman S. Czerruszewicz, 5

- S**
- Scanning Capacitance Microscopy (SCM), 83, 121
 - Scanning Electron Microscopy (SEM), 34–36
 - Scanning Near-Field Optical Microscopy (SNOM), 40, 41, 163, 166, 175
 - Scanning Transmission Electron Microscope (STEM), 36
 - Scanning Tunnelling Microscopy (STM), 40
 - Schottky-Emission Scanning Electron Microscopy (SE-SEM), 41
 - Secondary Electrons (SEs), 33
 - Secondary Ion Mass Spectrometry (SIMS), 121, 190
 - Secondary Ion Mass Spectroscopy (SIMS)-Optical Emission Spectroscopy (OES)/-CL SiO₂ films, 193
 - SEM-CL, 38
 - SEM-CL and STEM-CL, 214
 - GaN, 209, 210, 214,
 - Semiconductor laser, 14
 - SE-SEM-CL, 41
 - Shallow Trench Isolation (STI), 60, 61
 - Shockley-type Stacking Faults (SFs), 80
 - Si, 34
 - Si-C, 77
 - Si-CH₃, 54
 - Si-CH₃/Si-O, 54
 - Si-H/Si-O, 54
 - Silicon, 47
 - Si-O, 54
 - SiC Metal–Oxide–Semiconductor Field-Effect Transistors (MOSFETs), 83
 - Silicon Carbide (SiC), 76
 - Silicon dioxide (SiO₂), 51
 - Silicon-On-Insulator (SOI), 57
 - SIMS-OES, 190, 192
 - In(Al0.25Ga0.75)P/In(Al0.50Ga0.50)P/In(Al0.70Ga0.30)P/GaAs Raman scattering (TERS), 192
 - SIMS, 205
 - Single, double, or triple monochromator, 16
 - Single Shockley SFs, 30
 - Single-Walled Carbon Nanotubes (SWNTs), 177
 - Single-walled nanotubes (SWNTs), 175
 - SWNTs, 175
 - SNOM, 166
 - SNOM-probe, 169
 - SNOM-PL, 40, 41
 - Sp² carbon, 99, 102
 - Spatial resolution 100 nm, 35
 - Spectrometer, 15
 - Sputtering (SP), 54
 - Stacking Faults (SFs), 28
 - STEM-EELS, 149
 - Stokes, 4
 - Stranski–Krastanov (S–K) mode, 127
 - Stress characterization, 9
 - Substitutional carbon and self-interstitial silicon (Cs–Si), 61
 - Surface Composition by Analysis Neutral and Ion Impact Radiation (SCANIRR), 190
 - Surface-enhanced Raman scattering, 207
 - Surface-Enhanced Raman Spectroscopy (SERS), 163, 164, 207
 - Surface Plasmon Resonances (SPRs), 147
 - Surface Plasmons (SPs), 147
 - Surface Polaritons (SPPs), 87, 90
- T**
- TEOS (CVD), 54
 - Terahertz (THz), 1, 187
 - Terahertz Time-Domain Spectroscopy (THz-TDS), 188
 - Tetraethoxysilane (TEOS), 51
 - Thermal effects and two-photon absorption (TPA), 67
 - Thermal Oxidation (TO), 54
 - Threading Dislocations (TDs), 44
 - Threading-Edge Dislocations (TEDs), 81
 - Three-fold and four-fold ring defects, 51
 - THz time-Domain Spectroscopy (TDS), 1, 187
 - Ti:sapphire laser, 187
 - Time-Resolved Cathodoluminescence (TR-CL), 193, 194, 198, 199
 - InGaAs/AlGaAs pyramidal quantum dot (QD) structure, 194
 - Tip-Enhanced Raman Scattering (TERS), 163
 - 4H-SiC, 205
 - carbon nanotubes, 205
 - graphene oxide, 205
 - Journal of Raman Spectroscopy 53, 1394 (2022), 205
 - TERS, 164
 - Tip-Enhanced Raman Spectroscopy (TERS), 163–165, 179
 - metal-tip, 177
 - Transistors, 161

Transmission Electron Microscopy (TEM),

[29, 40](#)

Transverse Optical (TO) phonon, [47, 64](#)

Travel, [14](#)

Triangular defects, [28](#)

U

Ultraviolet (UV), [41, 58, 78, 157, 158](#)

V

Vanadium oxide, [22](#)

V-defect, [74](#)

Vertical Quantum Wires (VQWRs), [195](#)

Very Large-Scale Integration (VLSI), [166, 167](#)

V_o , [55](#)

$(V_o; (O_2)_i)$, [55](#)

W

Wide-gap semiconductors:Silicon carbide
and related materials, [76](#)

X

X-ray Fluorescence spectroscopy (XRF), [54](#)

X-ray Photoelectron Spectroscopy (XPS),
[90](#)

X-rays, [33](#)

XRD, [103](#)

Y

Yellow Luminescence (YL), [43, 44](#)

Yttrium-Aluminum-Garnet (YAG), [194](#)

Z

Zero-Loss Peak (ZLP), [148, 149, 151](#)

Zinc Oxide (ZnO), [94](#)

Zinc selenide ($ZnSe$), [12](#)

ZnSe, [22](#)